INAUGURAL - DISSERTATION

zur Erlangung der Doktorwürde der
Naturwissenschaftlich-Mathematischen Gesamtfakultät der
Ruprecht–Karls-Universität
Heidelberg

vorgelegt von
Mikael Scott

Tag der mündlichen Prüfung: 15.12.2021

Linear and nonlinear spectroscopies exploiting the algebraic-diagrammatic construction scheme

Mikael Scott

im November 2021

Gutachter:

Prof. Dr. Andreas Dreuw

Dr. Tiago Buckup

“Don’t ever, for any reason, do anything, to anyone, for any reason, ever, no matter what, no matter where, or who, or who you are with, or where you are going, or where you’ve been, ever, for any reason whatsoever.”

Michael Scott (The Office)

Abstract

This dissertation deals with theoretical methods to simulate the linear and nonlinear absorption of circularly polarized light. Specifically, expressions for the rotatory strength in the intermediate state representation (ISR) of the algebraic-diagrammatic construction (ADC) scheme up to third order are detailed in both the length and velocity gauge, and are used to simulate electronic circular dichroism (ECD) spectra. The well-known origin-dependence inherent to the prediction of magnetic properties within approximate theories is explored related to ECD using the ADC method. The ECD spectra of methyloxirane, methylthiirane and their dimethylated counterparts, H_2O_2 and H_2S_2 are calculated at the ADC(2) and ADC(3) levels of theory and compared to the same spectra calculated at CC2, CCSD and CC3 level of theory. The simulated ECD spectra of the bicyclic ketones, camphor, norcamphor and fenchone are analysed at ADC(3) level and compared against experimental gas-phase ECD spectra. Solvent effects are addressed by the use of a polarizable continuum model (PCM) on the simulated ECD spectra of solvated epinephrine.

The time-resolved counterpart to ECD, namely excited-state electronic circular dichroism (ESECD) is further derived within the ADC/ISR formalism, replacing the ground state with an excited-state, to obtain excited-state rotatory strengths. The quality of the simulated ESECD spectra of norcamphor at ADC(3) level is compared with those same spectra calculated at time-dependent density functional theory (TDDFT) with several exchange-correlation functionals. Furthermore, the ESECD spectrum of binol in the energetically lowest singlet excited state (S_1-ESECD) is computed at the ADC(2) level of theory.

The simultaneous absorption of two-photons where at least one of them is circularly polarized, so-called "two-photon circular dichroism" (TPCD), is derived within the ADC/ISR formalism. In this case, three formulations of the TPCD rotatory strength are employed and used to simulate the TPCD spectra of methyloxirane and methylthiirane. The chiroptical properties of a twisted biphenyl molecule is subsequently evaluated in terms of their linear (ECD) and nonlinear (TPCD) spectra. The impact the polarization-propagation of the two light beams have on the simulated TPCD spectra of norcamphor is further demonstrated.

Next, expressions for the first-order hyperpolarizability are derived and used to calculate the second harmonic generation (SHG) and hyper-Rayleigh scattering (HRS) within the ADC/ISR formalism. The static first-order hyperpolarizability of several organic and inorganic molecules is then compared at ADC(n) and CC levels of theory. The dynamic, SHG, signal strength of several molecules is subsequently evaluated at ADC(n) levels of theory with respect to experimental measurements. Lastly, the HRS of ammonia is evaluated at ADC(2) and ADC(3) levels of theory.

Zusammenfassung

Diese Dissertation beschäftigt sich mit theoretischen Methoden zur Simulation der linearen und nichtlinearen Absorption von zirkular polarisiertem Licht. Insbesondere werden Ausdrücke für die Rotationsstärke in der *intermdiate state representation* (ISR) des algebraisch-diagrammatischen Konstruktionsschemas (ADC) bis zur dritten Ordnung sowohl im Längen- und Geschwindigkeitsmaß detailliert beschrieben und zur Simulation des elektronischen Zirkulardichroismus (ECD) verwendet. Spektren. Die bekannte Ursprungsabhängigkeit, die der Vorhersage magnetischer Eigenschaften in Näherungstheorien inhärent ist, wird im Zusammenhang mit ECD und ADC untersucht. Die ECD-Spektren von Methyloxiran, Methylthiiran und ihren dimethylierten Derivaten, sowie H_2O_2 und H_2S_2 werden auf dem ADC(2)- und ADC(3)-Theorieniveau berechnet und mit verglichen Spektren berechnet auf CC2-, CCSD- und CC3-Theorieniveau verglichen. Die simulierten ECD-Spektren der bicyclischen Ketone Campher, Norcampher und Fenchon werden auf ADC(3)-Niveau analysiert und mit experimentellen Gasphasen-ECD-Spektren verglichen. Lösungsmitteleffekte werden durch die Verwendung eines polarisierbaren Kontinuumsmodells (PCM) auf die simulierten ECD-Spektren von solvatisiertem Adrenalin behandelt.

Das zeitaufgelöste Gegenstück zur ECD, nämlich der elektronische Zirkulardichroismus (ESECD) im angeregten Zustand, wird im ADC/ISR-Formalismus hergeleitet, wobei der Grundzustand durch einen angeregten Zustands ersetzt wird, um die Rotationsstärken des angeregten Zustands zu erhalten. Die Qualität der simulierten ESECD-Spektren von Norcampher auf ADC(3)-Niveau wird mit den entsprechenden Spektren verglichen, die mit der zeitabhängigen Dichtefunktionaltheorie (TDDFT) mit mehreren Austauschkorrelationsfunktionalen berechnet wurden. Darüber hinaus wird das ESECD-Spektrum von Binol im energetisch niedrigsten angeregten Singulett-Zustand (S_1-ESECD) auf ADC(2)-Niveau berechnet.

Die gleichzeitige Absorption von Zweiphotonen, bei denen mindestens eines zirkular polarisiert ist, der sogenannte Zweiphotonen-Zirkulardichroismus (TPCD), wird im ADC/ISR-Formalismus abgeleitet. In diesem Fall werden drei Formulierungen der TPCD-Rotationsstärke verwendet und genutzt, um die TPCD-Spektren von Methyloxiran und Methylthiiran zu simulieren. Die chiroptischen Eigenschaften eines verdrillten Biphenylmoleküls werden anschließend hinsichtlich ihrer linearen (ECD) und nichtlinearen (TPCD) Spektren bewertet. Der Einfluss der Polarisationsausbreitung der beiden Lichtstrahlen auf die simulierten TPCD-Spektren von Norcampher wird weiter untersucht.

Als nächstes werden Ausdrücke für die Hyperpolarisierbarkeit erster Ordnung abgeleitet und verwendet, um die Frequenzverdopplung (SHG) und die Hyper-Rayleigh-Streuung (HRS) innerhalb des ADC/ISR-Formalismus zu berechnen. Die statische Hyperpolarisierbarkeit erster Ordnung mehrerer organischer Moleküle wird dann auf den Theorieebenen ADC(n) und CC verglichen. Die dynamische SHG-Signalstärke mehrerer Moleküle

wird anschließend auf ADC(n)-Niveau in Bezug auf experimentelle Messungen bewertet. Schließlich wird die HRS von Ammoniak auf den Theorie-Niveaus ADC(2) und ADC(3) bewertet.

Contents

Abbreviations

ADC	algebraic-diagrammatic construction
ADC(1)	first-order ADC matrix and transition moments
ADC(2)	second-order ADC matrix and transition moments
ADC(3)	third-order ADC matrix and second-order transition moments
BO	Born-Oppenheimer approximation
CASSCF	complete active space self-consistent field
CC	coupled cluster
CCS	coupled cluster singles
CC2	coupled cluster singles and approximate doubles
CC3	coupled cluster singles, doubles and approximate triples
CCSD	coupled cluster singles and doubles
CCSD(T)	coupled cluster singles, doubles and perturbative triples
CC-LR	coupled cluster linear response
CES	correlated-excited states
CI	configuration interaction
CID	configuration interaction doubles
CIS	configuration interaction singles
CISD	configuration interaction singles and doubles
CISDT	configuration interaction singles, doubles and triples
COEBS	complete one-electron basis set
DFG	differential frequency generation
DFT	density-functional theory
ECD	electronic circular dichroism
ESA	excited-state absorption
ES-ECD	excited state electronic circular dichroism

EFISH	electric-field-induced second-harmonic generation
EOM-CC	equations-of-motion coupled cluster
FF	finite field
FWHM	full width at half maximum
GIAO	gauge including atomic orbitals
HF	Hartree-Fock
HRS	hyper-Rayleigh scattering
HWHM	half width at half maximum
ICD	induced circular dichroism
IS	intermediate states
ISR	intermediate state representation
LR	linear response
MCD	magnetic circular dichroism
MP	Møller–Plesset perturbation theory
NLO	nonlinear optics
OR	optical retification
PCM	polarizable continuum model
RF	response function
RPA	random-phase approximation
SCF	self-consistent field
SFG	sum-frequency generation
SHG	second-harmonic generation
SOS	sum-over-states
VCD	vibrational circular dichroism
VES	vertically excited state
TD-DFT	time-dependent density-functional theory
TD-HF	time-dependent Hartree-Fock
TISE	time-independent Schrödinger equation
TI	translationally invariant
THG	third harmonic generation
TPCD	two-photon circular dichroism
TPA	two-photon absorption

QR-DFT	quadratic-response density functional theory
xc	exchange-correlation

Chapter 1

Introduction

The absorption of light is the fundamental process studied in optical spectroscopy where molecular systems are interrogated providing insight into physical processes.[1] By the use of linear polarized plane waves as the light source, one obtains information about the electronic structure of the investigated molecular system. However, this does not yield information about the absolute stereochemistry of the system. Using circularly polarized light, where the tip of the vector potential rotates in a counter or anti-counter clockwise motion results in the preferential absorption by enantiomers, thus providing information about the absolute stereochemistry of the system. This preferential absorption is measured in electronic circular dichroism (ECD) spectroscopy.[2–9]

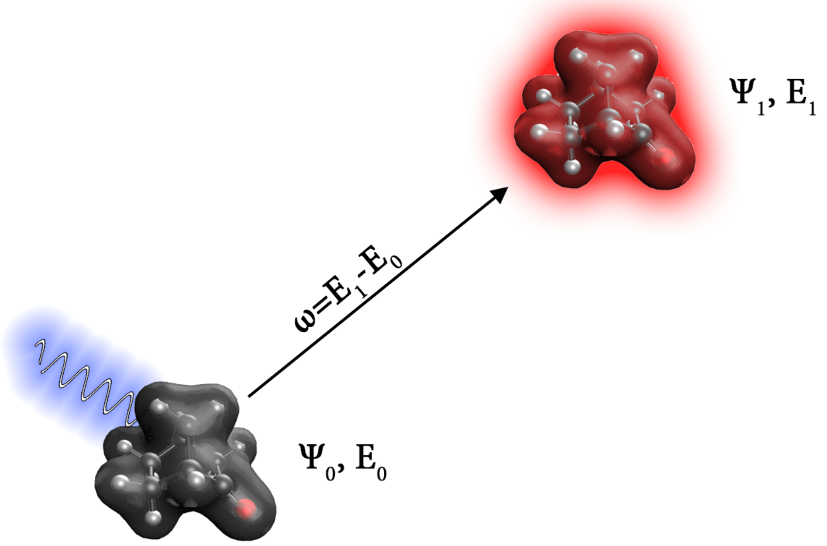

FIGURE 1.1: Absorption.

On a theoretical level, various methods have been developed over the last century, chiefly, the development of quantum mechanics allowed molecular systems to be described using a wave function, containing all the information about the system described therein.[10] Properties can then be obtained as solutions to the time-independent Schrödinger equation (TISE) equation.[11–15] Analytical solutions are not available for systems containing more than two particles, and several approximations have been employed to keep the computational effort minimal while providing the most accurate quantities. The starting point is often Hartree-Fock (HF) which neglects the motion of individual electrons, instead treating their interaction in an average fashion.[16–20] Perturbation theory can then be used to recover electron correlation with the most common being the Møller–Plesset perturbation theory (MP) method.[21–27] The wave function can also be expanded in terms of excited determinants where inclusion of all possible determinants fully correlates the motions of the electrons, providing the exact solution to the TISE within a given one-electron basis set, referred to as configuration interaction (CI).[28]

The algebraic-diagrammatic construction (ADC) scheme is formally derived from Greens function theory and can be viewed as a combination of a configuration interaction expansion of the wave function with a MP treatment of the matrix elements.[29,30] While ADC has proven high accuracy in the simulation of UV/VIS spectroscopy,[31] it has not yet been applied to simulate chiroptical spectroscopies, which is the main focus of this dissertation.

The first of these chiroptical spectroscopies is electronic circular dichroism (ECD) (commonly called CD), where the difference in absorption of left- and right-handed circularly polarized light is measured.[3,4,32] Since a difference in absorption is measured, a negative or positive signal can be recorded where enantiomers produce mirror-like spectra. A common usage of ECD spectroscopy is the determination of secondary structures of proteins,[5,33–36] as well as in pharmaceutical synthesis as a control for enantiomeric purity.[37] ECD is typically measured in solution and hence solvent molecules arranging themselves around a solute can give rise to a signal though a processes referred to as induced circular dichroism (ICD).[38–43] Quantum mechanically, the ECD signal arising from an electronic transition is described by the Rosenfeld equation as the scalar product of the electric and magnetic transition dipole moments between the ground state Ψ_0 and nth excited state Ψ_n, a quantity referred to as the rotatory strength

$$R_{n0} = \vec{\mu}_{n0} \cdot \vec{m}_{n0}. \tag{1.1}$$

Several methods have been used to calculate rotatory strengths, for molecules on the

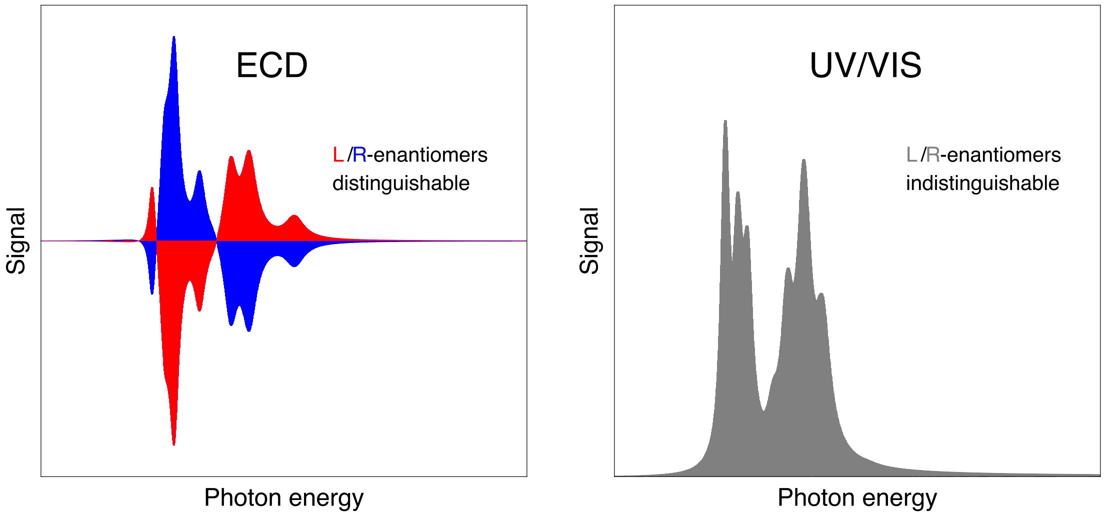

FIGURE 1.2: Additional information obtained by ECD compared to UV/VIS spectroscopy. Enantiomers are clearly distinguishable and determination of absolute configuration is possible using ECD where circularly polarized light is used.

order of hundreds of atoms, time-dependent Hartree-Fock (TD-HF)[44–46] and time-dependent density-functional theory (TD-DFT)[47–51] has been used. For molecules on the order of tens of electrons, CI[52] as well as linear response (LR) based on a complete active space self-consistent field (CASSCF) reference[53] and equations-of-motion coupled cluster (EOM-CC)[54,55] and the similar coupled cluster linear response (CC-LR) approach[56–59] has been employed.

The Rosenfeld equation, need not be restricted to describe excitations from the ground state, but can in principle describe rotatory strengths corresponding to excitations from an excited-state

$$R_{nk} = \vec{\mu}_{nk} \cdot \vec{m}_{nk}. \tag{1.2}$$

The resulting process is then referred to as excited state electronic circular dichroism (ES-ECD) which is a nonlinear absorption process analogous to pump-probe UV/VIS.[60–63] ES-ECD has been theoretically explored at the TD-HF and TD-DFT levels of theory, where the rotatory strength from an excited-state was evaluated through the double residue of a quadratic response function.[64] However, ES-ECD has yet not been implemented using the ADC formalism, as will be presented for the first time in this work.

Another important nonlinear spectroscopy is two-photon absorption (TPA), here, two-photons are absorbed simultaneously, acting as a single photon with the sum of their individual frequencies.[65–68] Analogous to how ECD complements UV/VIS spectroscopy, two-photon circular dichroism (TPCD) complements TPA spectroscopy, providing information about the absolute stereochemistry of molecular system.[69–78] Here, two-photons where at least one is circularly polarized are simultaneously absorbed through a so-called "virtual state", in a preferential manner depending on the absolute stereochemistry of the system.[79] The unique benefit TPA offers, specifically, high temporal and spatial resolution, owing to the nonlinear optics (NLO) process, as well as the use of lower frequency light, are both inherent to the TPCD process.[80,81] While TPA has been explored theoretically at several levels of theory including ADC,[82] TPCD has only been evaluated at TD-HF, TD-DFT, CC2 and CCSD levels of theory.[78,79,83] Hence, another milestone of this dissertation is to implement and simulate TPCD spectra within the ADC/intermediate state representation (ISR) formalism.

Of equal importance in this work is the static and dynamic first-order hyperpolarizability, specifically, the dispersion process of second-harmonic generation (SHG).[84–92] While conceptually similar to TPA, here, two photons are dispersed through a virtual excited state and re-emitted at the combined frequency of both. Measured in SHG spectroscopy is thus the dynamic first-order hyperpolarizability of the molecular system, which has been used to analyse collagen fibrillar structure,[93–95], cell imaging[96] and cancers.[97] Here, systems with large hyperpolarizabilities are sought after in the development of several exotic materials for use in displays, medicinal imaging, etc.[98–104] Furthermore, the SHG process is constrained through symmetry to only produce signals from centrosymmetric media, thus the method is commonly applied to the study of surface phenomena.When the first-order hyperpolarizability is measured from liquid samples, the hyper-Rayleigh scattering (HRS) is processes is exploited, where the signal is isotropic, incoherent and dephasing.[105] Theoretically, the first-order hyperpolarizability and thus SHG and HRS, have been evaluated at various levels of theory, e.g., TD-DFT, CISD and coupled cluster singles and doubles (CCSD), but not yet using the ADC method.

Implementation and evaluation of these spectroscopies novel to the ADC method is what will be presented in this dissertation. In Chapter 3, expressions for the rotatory strength is used to simulate ECD spectra within the ADC/ISR formalism.[106] In Chapter 4 expressions for rotatory strengths arising from transitions from excited states are used to simulate ES-ECD spectra.[107] In 5 expressions for the two-photon rotatory strength are derived within the used to simulate TPCD spectra. Lastly, in Chapter 6, expressions for the static first-order hyperpolarizability tensor, SHG and HRS within the ADC/ISR formalism are used to calculate hyperpolarizabilities. Other projects that have been published in collaboration with other groups are not included in this thesis but are listed in the end.

Chapter 2

Theory

This chapter begins with a discussion of the molecular TISE and its approximate solution starting with the Hartree-Fock method. In Section 2.2, one of the most fundamental correlated methods, namely CI, is described. Section 2.3 continues the discussion of correlated methods, here, Rayleigh-Schrödinger and Møller-Plesset (MP) perturbation theory are described. In Section 2.4, linear and circularly polarized plane wave light are described as well as the absorption of both. Next, in Section 2.5 response theory will be described as related to the absorption of linear and circularly polarized light, electric-dipole polarizability and the first-order electric-dipole hyperpolarizability as well as two-photon absorption. Lastly, in Section 2.6 the algebraic-diagrammatic construction (ADC) scheme for the polarization propagator in the intermediate state representation is described and applied to electronic circular dichroism, two-photon circular dichroism and second harmonic generation.

2.1 Hartree-Fock

Hartree-Fock (HF) is arguably the most fundamental approximate method of electronic structure theory and forms the basis of molecular orbital theory where each electron's motion is described by a single-particle (orbital) function and every electron is unresponsive to the motion of the others.[16,17] The method arose in the pursuit to solve the electronic Schrödinger equation or more precisely, the time-independent Schrödinger equation TISE after the Born-Oppenheimer approximation (BO) (considering the nuclei as fixed in space) has been invoked. Using $\mathbf{r}$ and $\mathbf{R}$ to denote the coordinates (in atomic units) of the electrons and nuclei, respectively, the TISE is then written as,[15]

$$\left[-\frac{1}{2}\sum_{i}\nabla_i^2-\sum_{A,i}\frac{Z_A}{r_{Ai}}+\sum_{A>B}\frac{Z_AZ_B}{R_{AB}}+\sum_{i>j}\frac{1}{r_{ij}}\right]\Psi(\mathbf{r};\mathbf{R})=E_{\mathrm{el}}\Psi(\mathbf{r};\mathbf{R}). \tag{2.1}$$

The total N-electron wave function is then separated into products of one-electron wave function (orbitals), resulting in a form known as a Hartree-product (HP). However, this form does not satisfy the *antisymmetry principle*, which states that fermions need to be antisymmetric with respect to an interchange of any set of spatial and spin coordinates $\mathbf{x} = \{\mathbf{r}, \omega\}$. Here, one introduces notations for spatial orbitals as $\phi(r)$ and spin orbitals as $\chi(x) = \phi(r)\alpha(\omega)$ or $\chi(x) = \phi(r)\beta(\omega)$. To ensure the *antisymmetry principle* is obeyed, the wave function is then parameterized using a Slater determinant, which for N-electrons is written as

$$\Psi = \frac{1}{\sqrt{N!}} \begin{vmatrix} \chi_1(\mathbf{x}_1) & \chi_2(\mathbf{x}_1) & \cdots & \chi_N(\mathbf{x}_1) \\ \chi_1(\mathbf{x}_2) & \chi_2(\mathbf{x}_2) & \cdots & \chi_N(\mathbf{x}_2) \\ \vdots & \vdots & \ddots & \vdots \\ \chi_1(\mathbf{x}_N) & \chi_2(\mathbf{x}_N) & \cdots & \chi_N(\mathbf{x}_N) \end{vmatrix}, \tag{2.2}$$

where $\frac{1}{\sqrt{(N!)}}$ is a normalization factor.[20] One consequence of using a Slater determinant is that each electron is indistinguishable and contributes to every orbital, however small that contribution might be. With this form for the wave function one proceeds towards simplifying the Hamiltonian. Defining first a one-electron operator h,

$$h(i) = -\frac{1}{2}\nabla_i^2 - \sum_A \frac{Z_A}{r_{iA}}, \tag{2.3}$$

and a two-electron operator $v(i,j)$,

$$v(i,j) = \frac{1}{r_{ij}}. \tag{2.4}$$

The electronic Hamiltonian can then be written more compactly as,

$$\hat{H}_{\text{el}} = \sum_i h(i) + \sum_{i<j} v(i,j) + V_{NN}, \tag{2.5}$$

where V_{NN} is a fixed constant dependent only on the fixed set of nuclear coordinates $\mathbf{R}$ (BO approximation). The energy can then be obtained as an expectation value,

$$E_{\text{el}} = \left\langle \Psi \middle| \hat{H}_{\text{el}} \middle| \Psi \right\rangle, \tag{2.6}$$

which in the case of the HF energy satisfies the *variational theorem* which ensures that the energy is necessarily an upper bound to the exact (minimal) energy. Because of this, the parameters of Ψ can be varied until a minimum is obtained with the resulting molecular orbitals (MOs) referred to as canonical MOs, i.e., those that minimizes E_{el} within the HF-approximation. By simple rearrangement and making use of *braket* notations, the

HF energy can be written in terms of integrals over the one- and two-electron operators,

$$E_{\mathrm{HF}} = \sum_i \langle i|h|i\rangle + \frac{1}{2}\sum_{ij}\left([ii|jj] - [ij|ji]\right), \tag{2.7}$$

where the one electron integral is,

$$\langle i|h|j\rangle = \int d\mathbf{x}_1 \chi_i^*\left(\mathbf{x}_1\right) h\left(\mathbf{r}_1\right) \chi_j\left(\mathbf{x}_1\right), \tag{2.8}$$

and the two electron integral is,

$$[ij|kl] = \int d\mathbf{x}_1 d\mathbf{x}_2 \chi_i^*\left(\mathbf{x}_1\right) \chi_j\left(\mathbf{x}_1\right) \frac{1}{r_{12}} \chi_k^*\left(\mathbf{x}_2\right) \chi_l\left(\mathbf{x}_2\right), \tag{2.9}$$

for which there are numerous efficient integration algorithms. Hence, the HF-method yields approximate solutions to the TISE assuming the wave function is constituted by a single Slater determinant with each electron occupying a single spin orbital. To minimize the HF energy one wants to change the orbital parameters $\chi_i \to \chi_i + \delta\chi_i$, while keeping the spinorbitals orthonormal to one and other. This is accomplished by Langrange's method of undetermined multipliers, where one uses a functional $\mathcal{L}$,

$$\mathcal{L}\left[\{\chi_i\}\right] = E_{\mathrm{HF}}\left[\{\chi_i\}\right] - \sum_{ij} \epsilon_{ij}\left(\langle i|j\rangle - \delta_{ij}\right). \tag{2.10}$$

Here ϵ_{ij} are undetermined Langrange multipliers, $\langle i|j\rangle$ is the overlap of spin orbitals i and j. One then proceeds by setting the first variation to zero, $\delta\mathcal{L} = 0$, to arrive at the Hartree-Fock equations,

$$\begin{aligned} h\left(\mathbf{x}_1\right)\chi_i\left(\mathbf{x}_1\right) + &\sum_{j\neq i}\left[\int d\mathbf{x}_2 \left|\chi_j\left(\mathbf{x}_2\right)\right|^2 r_{12}^{-1}\right]\chi_i\left(\mathbf{x}_1\right) - \sum_{j\neq i}\left[\int d\mathbf{x}_2 \chi_j^*\left(\mathbf{x}_2\right)\chi_i\left(\mathbf{x}_2\right) r_{12}^{-1}\right]\chi_j\left(\mathbf{x}_1\right) \\ &= \epsilon_i \chi_i\left(\mathbf{x}_1\right), \end{aligned} \tag{2.11}$$

where ϵ_i is the energy associated with orbital χ_i. One may solve these equations numerically (exact HF) or in a space spanned by a set of basis functions (Hartree-Fock-Roothan equations), in either case some initial guess for the orbitals are required which are then iterated upon. Because of this requirement of iteration on an initial guess the procedure is referred to as a self-consistent field (SCF) method or approach. The second term in Equation 2.11 describes the Coulomb interaction of an electron occupying spin orbital χ_i, with the integral producing the average interaction to other electrons, i.e. "mean field". This *Coulomb term* can then be defined by the Coulomb operator as,

$$\mathcal{J}_j\left(\mathbf{x}_1\right) = \int d\mathbf{x}_2 \left|\chi_j\left(\mathbf{x}_2\right)\right|^2 r_{12}^{-1}. \tag{2.12}$$

The Coulomb operator thus describes the average local potential at point $\mathbf{x}_1$ arising from the charge distribution of spin-orbital χ_j. The second term is referred to as the "*exchange term*" has no classical analogue and arises from the antisymmetric condition, it likewise is defined by the Exchange operator as,

$$\mathcal{K}_j\left(\mathbf{x}_1\right)\chi_i\left(\mathbf{x}_1\right)=\left[\int d\mathbf{x}_2\chi_j^*\left(\mathbf{x}_2\right)r_{12}^{-1}\chi_i\left(\mathbf{x}_2\right)\right]\chi_j\left(\mathbf{x}_1\right). \tag{2.13}$$

Using these notations and lifting the $j \neq i$ condition of the summations, one can define the Fock operator as,

$$f\left(\mathbf{x}_1\right)=h\left(\mathbf{x}_1\right)+\sum_j \mathcal{J}_j\left(\mathbf{x}_1\right)-\mathcal{K}_j\left(\mathbf{x}_1\right), \tag{2.14}$$

Equation 2.11 can then be written compactly as,

$$f\left(\mathbf{x}_1\right)\chi_i\left(\mathbf{x}_1\right)=\epsilon_i\chi_i\left(\mathbf{x}_1\right). \tag{2.15}$$

To obtain the Roothan equations the orbitals are expressed in terms of one-particle (orbital) basis functions with the expansion,

$$\chi_i=\sum_{\mu=1}^{K}C_{\mu i}\tilde{B}_\mu, \tag{2.16}$$

where $\tilde{B}_\mu$ is the spatial function spanning the i-th orbital with expansion cofficient $C_{\mu i}$. Within the given basis set $\{B\}$, Equation 2.15 takes the form,

$$f\left(\mathbf{x}_1\right)\sum_\nu C_{\nu i}\tilde{B}_\nu\left(\mathbf{x}_1\right)=\epsilon_i\sum_\nu C_{\nu i}\tilde{B}_\nu\left(\mathbf{x}_1\right) \tag{2.17}$$

and after left multiplication and integration,

$$\sum_\nu C_{\nu i}\int d\mathbf{x}_1\tilde{B}_\mu^*\left(\mathbf{x}_1\right)f\left(\mathbf{x}_1\right)\tilde{B}_\nu\left(\mathbf{x}_1\right)=\epsilon_i\sum_\nu C_{\nu i}\int d\mathbf{x}_1\tilde{B}_\mu^*\left(\mathbf{x}_1\right)\tilde{B}_\nu\left(\mathbf{x}_1\right). \tag{2.18}$$

Lastly, one defines the overlap **S** and Fock **F** matrices as,

$$S_{\mu\nu}=\int d\mathbf{x}_1\tilde{B}_\mu^*\left(\mathbf{x}_1\right)\tilde{B}_\nu\left(\mathbf{x}_1\right), \tag{2.19}$$

$$F_{\mu\nu}=\int d\mathbf{x}_1\tilde{B}_\mu^*\left(\mathbf{x}_1\right)f\left(\mathbf{x}_1\right)\tilde{B}_\nu\left(\mathbf{x}_1\right), \tag{2.20}$$

and finally the Hartree-Fock-Roothaan equations are written as,

$$\sum_\nu F_{\mu\nu}C_{\nu i}=\epsilon_i\sum_\nu S_{\mu\nu}C_{\nu i}, \tag{2.21}$$

or in matrix notations,

$$\mathbf{FC}=\mathbf{SC}\epsilon. \tag{2.22}$$

After transformation into the basis of **S**, one obtains a simple eigenvalue equation.

2.2 Configuration interaction

In the Hartree-Fock approximation one finds the energetically lowest single determinant wave function in a given one-electron basis set, neglecting correlation of electrons with opposite spin. Correlation can then be recaptured by an expansion of the HF wave function with excited determinants,[15]

$$\Psi_{\text{CI}} = a_o \Phi_{\text{HF}} + \sum_S a_S \Phi_S + \sum_D a_D \Phi_D + \sum_T a_T \Phi_T + \cdots = \sum a_i \Phi_i. \tag{2.23}$$

where a_i are expansion coefficients of the Φ_i excited determinant constructed by permutations of the occupied and virtual orbitals. Including permutations of one- (singles, S), two- (doubles, D) and three-pairs (triples, T) are the most common inclusions. A hierarchy of methods are thus configuration interaction singles (CIS), configuration interaction doubles (CID), configuration interaction singles and doubles (CISD), configuration interaction singles, doubles and triples (CISDT) etc. Inclusion of all possible determinants is referred to as Full-CI (FCI) which captures all correlation in a given basis set. To obtain state and excitation energies one introduces the Lagrangian L, where λ are Lagrange multipliers,

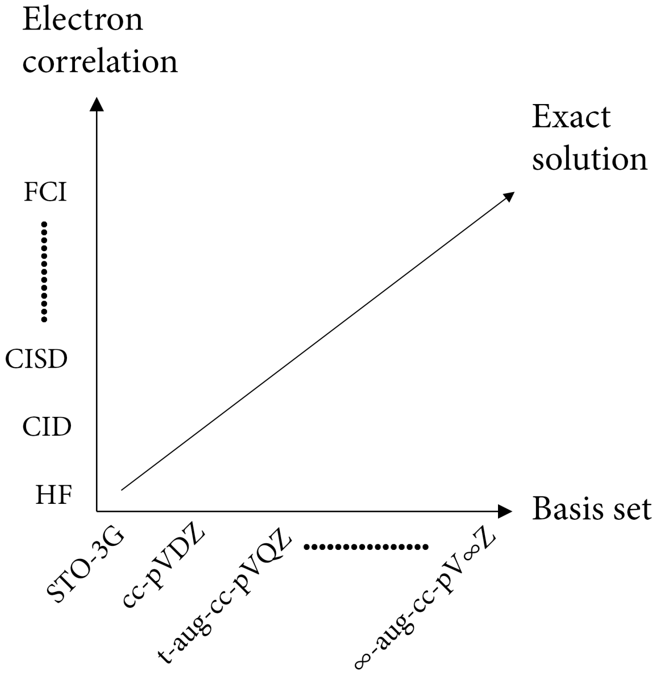

FIGURE 2.1: The relation of the completeness of the one-electron basis set and the inclusion of excited determinants in the CI expansion. The diagonal arrow points towards the exact solution to the TISE.

$$L = \langle \Psi_{\text{CI}} | H | \Psi_{\text{CI}} \rangle - \lambda(\langle \Psi_{\text{CI}} | \Psi_{\text{CI}} \rangle - 1). \tag{2.24}$$

This then yields a set of variational secular equations by the eigenvalue equation,

$$\begin{pmatrix} H_{00}-E & H_{01} & \cdots & H_{0i} \\ H_{10} & H_{11}-E & \cdots & H_{1i} \\ \vdots & \vdots & \ddots & \vdots \\ H_{i0} & \vdots & \cdot & H_{ii}-E \end{pmatrix} \begin{pmatrix} a_0 \\ a_1 \\ \vdots \\ a_i \end{pmatrix} = \begin{pmatrix} 0 \\ 0 \\ \vdots \\ 0 \end{pmatrix}. \tag{2.25}$$

The lowest and second lowest eigenvalues corresponds to the ground state and first excited state energies, the corresponding eigenvectors contains the expansion coefficients (a_i) of Equation 2.23. Simplifications are made possible by the *Slater-Condon* rules, which state that CI elements with more than two different MOs are necessarily zero. Moreover, *Brillouin's thereom* states that matrix elements containing the HF reference and singly excited determinants vanish and hence the first correlation correction is obtained at the CID level.

2.3 Perturbation theory

In this section, time-independent perturbation theory will be discussed as a method to describe electron correlation. Specifically, obtaining corrections to the energy and wave function using Rayleigh-Schrödinger perturbation theory. Next, Møller-Plesset perturbation theory is described where the fock operator is used as the unperturbed reference state.

2.3.1 Rayleigh-Schrödinger perturbation theory

This section will describe Rayleigh-Schrödinger perturbation theory (RSPT). Here, the aim is to find approximate solutions to the TISE

$$\hat{H}\psi_n = E_n\psi_n. \tag{2.26}$$

While these solutions aren't known, one assumes that the solutions to a conceptually "simpler" system $\psi_n^{(0)}$ with the Hamiltonian $\hat{H}^{(0)}$ are known exactly

$$\hat{H}^{(0)}\psi_n^{(0)} = E_n^{(0)}\psi_n^{(0)} \tag{2.27}$$

and that this simpler system is not significantly different such that the difference between $\hat{H}$ and $\hat{H}^{(0)}$ can be viewed as a small perturbation. All quantities of the system described by $\hat{H}$ can then be expanded as a Taylor series in terms of a parameter λ,

$$\hat{H} = \hat{H}^{(0)} + \lambda\hat{H}^{(1)} + \lambda^2\hat{H}^{(2)} + \ldots \tag{2.28}$$

$$\psi_n = \psi_n^{(0)} + \lambda\psi_n^{(1)} + \lambda^2\psi_n^{(2)} + \ldots \tag{2.29}$$

$$E_n = \hat{E}_n^{(0)} + \lambda E_n^{(1)} + \lambda^2 E_n^{(2)} + \ldots \tag{2.30}$$

Here, the $\psi_n^{(1)}$ and $E_n^{(1)}$ terms are the first corrections to the wave function and energy, respectively, $\psi_n^{(2)}$ and $E_n^{(2)}$ are the second order corrections to the same and so on. If the perturbation is turned off, $\lambda \to 0$, then $\hat{H} \to \hat{H}^{(0)}$, $\psi_n \to \psi_n^{(0)}$ and $E_n \to E_n^{(0)}$, the equations above revert to the original unperturbed system, whose properties are already known. The goal of perturbation theory is then to determine energies and wave functions up to a given order. This can be done by insertion of Equations. (2.28)-(2.30) into the TISE, Equation 2.26, and sorting the terms by order of λ,

$$\hat{H}^{(0)}\psi_n^{(0)} = E_n^{(0)}\psi_n^{(0)} \tag{2.31}$$

$$\left(\hat{H}^{(0)} - E_n^{(0)}\right)\psi_n^{(1)} = \left(E_n^{(1)} - \hat{H}^{(1)}\right)\psi_n^{(0)} \tag{2.32}$$

$$\left(\hat{H}^{(0)} - E_n^{(0)}\right)\psi_n^{(2)} = \left(E_n^{(2)} - \hat{H}^{(2)}\right)\psi_n^{(0)} + \left(E_n^{(1)} - \hat{H}^{(1)}\right)\psi_n^{(1)} \tag{2.33}$$

$$\vdots$$

From now on more its more convenient to use bra-ket notation

$$\psi_n^{(0)} \equiv \left|\psi_n^{(0)}\right\rangle, \quad \psi_n^{(1)} \equiv \left|\psi_n^{(1)}\right\rangle, \ldots \tag{2.34}$$

Next, to obtain the first order correction to the energy, $E^{(1)}$, Equation 2.32 is multiplied by $\left\langle\psi_n^{(0)}\right|$ from the left which gives

$$\left\langle\psi_n^{(0)}\left|\left(\hat{H}^{(0)} - E_n^{(0)}\right)\right|\psi_n^{(1)}\right\rangle = \left\langle\psi_n^{(0)}\left|\left(E_n^{(1)} - \hat{H}^{(1)}\right)\right|\psi_n^{(0)}\right\rangle \tag{2.35}$$

$$\left\langle\psi_n^{(0)}\left|\hat{H}^{(0)}\right|\psi_n^{(1)}\right\rangle - E_n^{(0)}\left\langle\psi_n^{(0)}\middle|\psi_n^{(1)}\right\rangle = E_n^{(1)}\left\langle\psi_n^{(0)}\middle|\psi_n^{(0)}\right\rangle - \left\langle\psi_n^{(0)}\left|\hat{H}^{(1)}\right|\psi_n^{(0)}\right\rangle \tag{2.36}$$

Furthermore, by using the fact that $\hat{H}^{(0)}$ is an Hermitian operator and that the eigenvalues of $H^{(0)}$ are orthonormal

$$\left\langle\psi_n^{(0)}\left|\hat{H}^{(0)}\right|\psi_n^{(1)}\right\rangle = \left\langle\left(\hat{H}^{(0)}\psi_n^{(0)}\right)\middle|\psi_n^{(1)}\right\rangle = \left\langle\left(E_n^{(0)}\psi_n^{(0)}\right)\middle|\psi_n^{(1)}\right\rangle = E_n^{(0)}\left\langle\psi_n^{(0)}\middle|\psi_n^{(1)}\right\rangle. \tag{2.37}$$

Equation 2.36 becomes,

$$E_n^{(0)}\left\langle\psi_n^{(0)}\middle|\psi_n^{(1)}\right\rangle - E_n^{(0)}\left\langle\psi_n^{(0)}\middle|\psi_n^{(1)}\right\rangle = E_n^{(1)} - \left\langle\psi_n^{(0)}\left|\hat{H}^{(1)}\right|\psi_n^{(0)}\right\rangle \tag{2.38}$$

$$0 = E_n^{(1)} - \left\langle\psi_n^{(0)}\left|\hat{H}^{(1)}\right|\psi_n^{(0)}\right\rangle \tag{2.39}$$

Thus, according to Equation 2.39, the first order correction to the energy is,

$$E_n^{(1)} = \left\langle\psi_n^{(0)}\left|\hat{H}^{(1)}\right|\psi_n^{(0)}\right\rangle \tag{2.40}$$

which is the expectation value of the first order Hamiltonian in the state ${\psi_\psi}_n^{(0)}$ of the unperturbed system. To find the first order correction to the wave function, one proceeds in a similar manner, here left multiplying Equation 2.32 by $\left\langle \psi_k^{(0)} \right|$, where $k \neq n$,

$$\left\langle \psi_k^{(0)} \middle| \hat{H}^{(0)} - E_n^{(0)} \middle| \psi_n^{(1)} \right\rangle = \left\langle \psi_k^{(0)} \middle| E_n^{(1)} - \hat{H}^{(1)} \middle| \psi_n^{(0)} \right\rangle \tag{2.41}$$

$$\left(E_k^{(0)} - E_n^{(0)} \right) \left\langle \psi_k^{(0)} \middle| \psi_n^{(1)} \right\rangle = - \left\langle \psi_k^{(0)} \middle| \hat{H}^{(1)} \middle| \psi_n^{(0)} \right\rangle \tag{2.42}$$

$$\left\langle \psi_k^{(0)} \middle| \psi_n^{(1)} \right\rangle = \frac{\left\langle \psi_k^{(0)} \middle| \hat{H}^{(1)} \middle| \psi_n^{(0)} \right\rangle}{E_n^{(0)} - E_k^{(0)}} \tag{2.43}$$

where going from Equation 2.41 to Equation 2.42, the orthogonality of the zeroth-order wave function have been exploited, i.e. $\left\langle \psi_k^{(0)} \middle| \psi_n^{(0)} \right\rangle = 0$. Furthermore, Equation 2.43 is only valid when the unperturbed system is assumed to be non-degenerate. To find $\left| \psi_n^{(1)} \right\rangle$, one may introduce the identity operator, $\hat{1}$, which is defined in terms of the eigenfunctions of the unperturbed system

$$\left| \psi_n^{(1)} \right\rangle = \hat{1} \left| \psi_n^{(1)} \right\rangle = \sum_k \left| \psi_k^{(0)} \right\rangle \left\langle \psi_k^{(0)} \middle| \psi_n^{(1)} \right\rangle \tag{2.44}$$

What remains is a simple insertion of Equation 2.43 into Equation 2.44, although the summations over k must here be different such that $k \neq n$, which is imposed by using intermediate normalisation

$$\left\langle \psi_n^{(0)} \middle| \psi_n \right\rangle = 1. \tag{2.45}$$

With this normalization condition established, insertion of Equation 2.43 into Equation 2.44 yields the first order correction to the wave function as,

$$\left| \psi_n^{(1)} \right\rangle = \sum_{k \neq n} \left| \psi_k^{(0)} \right\rangle \frac{\left\langle \psi_k^{(0)} \middle| \hat{H}^{(1)} \middle| \psi_n^{(0)} \right\rangle}{E_n^{(0)} - E_k^{(0)}} = \sum_{k \neq n} \left| \psi_k^{(0)} \right\rangle \frac{H_{kn}^{(1)}}{E_n^{(0)} - E_k^{(0)}} \tag{2.46}$$

where, $H_{kn}^{(1)}$ is a shorthand notation for the matrix element $\left\langle \psi_k^{(0)} \middle| \hat{H}^{(1)} \middle| \psi_n^{(0)} \right\rangle$.

As mentioned above, the first order correction to the energy was simply the expectation value of the unperturbed Hamiltonian. To obtain the second order correction, one multiplies Equation 2.33 by $\left\langle \psi_n^{(0)} \right|$ from the left, and use the fact that $\left\langle \psi_n^{(0)} \middle| \psi_n^{(1)} \right\rangle = 0$. This results in

$$\begin{aligned} \left\langle \psi_n^{(0)} \middle| \hat{H}^{(0)} - E_n^{(0)} \middle| n^{(2)} \right\rangle &= \left\langle \psi_n^{(0)} \middle| E_n^{(2)} - \hat{H}^{(2)} \middle| \psi_n^{(0)} \right\rangle + \left\langle \psi_n^{(0)} \middle| E_n^{(1)} - \hat{H}^{(1)} \middle| \psi_n^{(1)} \right\rangle \\ 0 &= E_n^{(2)} - \left\langle \psi_n^{(0)} \middle| \hat{H}^{(2)} \middle| \psi_n^{(0)} \right\rangle - \left\langle \psi_n^{(0)} \middle| \hat{H}^{(1)} \middle| \psi_n^{(1)} \right\rangle. \end{aligned} \tag{2.47}$$

Then, solving for $E_n^{(2)}$ one finds

$$E_n^{(2)} = \left\langle \psi_n^{(0)} \middle| \hat{H}^{(2)} \middle| \psi_n^{(0)} \right\rangle + \left\langle \psi_n^{(0)} \middle| \hat{H}^{(1)} \middle| \psi_n^{(1)} \right\rangle = H_{nn}^{(2)} + \left\langle \psi_n^{(0)} \middle| \hat{H}^{(1)} \middle| \psi_n^{(1)} \right\rangle, \tag{2.48}$$

which when inserted into Equation 2.46 yields the the second-order correction to the energy as,

$$E_n^{(2)} = H_{nn}^{(2)} + \sum_{k \neq n} \frac{H_{nk}^{(1)} H_{kn}^{(1)}}{E_n^{(0)} - E_k^{(0)}} \tag{2.49}$$

2.3.2 Møller-Plesset perturbation theory

While the above discussion of Rayleigh-Schrödinger perturbation theory was rather general, a more concrete case is when one wishes to improve upon the Hartree-Fock approximation. Writing the Hamiltonian of the form,

$$\begin{aligned}\hat{H} &= \sum_{i=1}^{N_e}\left[\frac{\hbar^2}{2m_e}\nabla_i^2 - \sum_{I=1}^{N_N}\frac{Z_I e^2}{4\pi\varepsilon_0\left|\mathbf{r}_I - \mathbf{r}_i\right|}\right] + \frac{1}{2}\sum_{i,ji\neq j}^{N_e}\frac{e^2}{4\pi\varepsilon_0\left|\mathbf{r}_i - \mathbf{r}_j\right|} \\ &= \sum_{i=1}^{N_e}\hat{f}_i + \frac{1}{2}\sum_{i,ji\neq j}^{N_e}\frac{e^2}{4\pi\varepsilon_0\left|\mathbf{r}_i - \mathbf{r}_j\right|}\end{aligned} \tag{2.50}$$

where we again made the separation into a one-electron operator $\hat{h}_i$ and a two electron operator. Next, one defines the zeroth order Hamiltonian as a sum of Fock operators $\hat{f}_i$ for each electron i

$$\hat{H}^{(0)} = \sum_{i=1}^{N_e}\left(\hat{h}_i + \hat{v}_i^{\mathrm{HF}}\right) = \sum_{i=1}^{N_e}\hat{f}_i. \tag{2.51}$$

Where the HF potential for electron i is defined as,

$$\hat{v}_i^{\mathrm{HF}} = \sum_{a=1}^{N_e}\left(\hat{\mathcal{J}}_a(i) - \hat{\mathcal{K}}_a(i)\right) \tag{2.52}$$

here $\mathrm{N_e}$ is the number of occupied spinorbitals and $\hat{\mathcal{J}}$ and $\hat{\mathcal{K}}$ are the familiar Coulomb and exchange operators, Equation 2.12 and Equation 2.13, respectively. Using this choice as the unperturbed Hamiltonian, the first correction is given by,

$$\hat{H}^{(1)} = \hat{H} - \hat{H}^{(0)} = \frac{1}{2}\sum_{i,j}^{N_e}\frac{e^2}{4\pi\varepsilon_0\left|\mathbf{r}_i - \mathbf{r}_j\right|} - \sum_{i=1}^{N_e}\hat{v}_i^{\mathrm{HF}}. \tag{2.53}$$

This choice of $H^{(0)}$ as the Fock operator, is known as Møller-Plesset (MP) perturbation theory. Next, to see how this will improve the energy description of the ground state, one first observes that any Slater determinant that is a solution Equation 2.22 is an eigenfunction of $\hat{H}^{(0)}$ and hence

$$\begin{aligned}\hat{H}^{(0)}\Phi_0^{(0)} &= \hat{H}^{(0)}\left|\chi_a(1)\chi_b(2)\ldots\chi_z\left(N_e\right)\right| \\ &= \left(\varepsilon_a + \varepsilon_b + \ldots + \varepsilon_z\right)\left|\chi_a(1)\chi_b(2)\ldots\chi_z\left(N_e\right)\right|\end{aligned} \tag{2.54}$$

where Φ_0 is the ground state determinant. The zeroth order energy is then read from Equation 2.54 as the sum of the energies of the spinorbitals of $\Phi_0^{(0)}$

$$E_0^{(0)} = \epsilon_a + \epsilon_b + \ldots + \epsilon_z. \tag{2.55}$$

The first order energy, Equation 2.40, is

$$E_0^{(1)} = \left\langle\Phi_0^{(0)}\middle|\hat{H}^{(1)}\middle|\Psi_0^{(0)}\right\rangle. \tag{2.56}$$

Here, an important observation can be made, namely that the sum $E_0^{(0)} + E_0^{(1)}$ is just equal to the HF energy

$$E_0^{(0)} + E_0^{(1)} = \left\langle \Psi_0^{(0)} \middle| \hat{H}^{(0)} + \hat{H}^{(1)} \middle| \Psi_0^{(0)} \right\rangle = \left\langle \Psi_0^{(0)} \middle| \hat{H} \middle| \Psi_0^{(0)} \right\rangle = E_0^{\mathrm{HF}} \tag{2.57}$$

Importantly, Equation 2.57 implies that to obtain any improvement on the HF energy, the second order energy correction must be computed, i.e. correlation is obtained at second order. This method to obtain second order energy correction is referred to as MP2, which according to Equation 2.49 is

$$E_0^{(2)} = \sum_{J \neq 0} \frac{\left\langle \Phi_0^{(0)} \middle| \hat{H}^{(1)} \middle| \Phi_J^{(0)} \right\rangle \left\langle \Phi_J^{(0)} \middle| \hat{H}^{(1)} \middle| \Phi_0^{(0)} \right\rangle}{E_0^{(0)} - E_J^{(0)}} \tag{2.58}$$

To calculate $E_0^{(2)}$, the matrix elements $\left\langle \Phi_0^{(0)} \middle| \hat{H}^{(1)} \middle| \Phi_J^{(0)} \right\rangle$ must be evaluated. Here, one can make use of the orthogonality property of different Slater determinants, for $J \neq 0$

$$\left\langle \Phi_0^{(0)} \middle| \hat{H}^{(0)} \middle| \Phi_J^{(0)} \right\rangle = \left\langle \Phi_0^{(0)} \middle| E_J^{(0)} \middle| \Phi_J^{(0)} \right\rangle = E_J^{(0)} \left\langle \Phi_0^{(0)} \mid \Phi_J^{(0)} \right\rangle = 0 \tag{2.59}$$

which yields

$$0 = \left\langle \Phi_0^{(0)} \middle| \hat{H}^{(0)} \middle| \Phi_J^{(0)} \right\rangle \Leftrightarrow 0 = \left\langle \Phi_0^{(0)} \middle| \hat{H} - \hat{H}^{(1)} \middle| \Phi_J^{(0)} \right\rangle \Leftrightarrow \left\langle \Phi_0^{(0)} | \hat{H} | \Phi_J^{(0)} \right\rangle = \left\langle \Phi_0^{(0)} \middle| \hat{H}^{(1)} \middle| \Phi_J^{(0)} \right\rangle \tag{2.60}$$

The above result demonstrates that the matrix elements of the $\hat{H}$ and $\hat{H}^{(1)}$ operators are in fact identical for $J \neq 0$. Using this result as well as the SC rules, i.e., $\left\langle \Phi_0^{(0)} \middle| \hat{H}^{(1)} \middle| \Phi_J^{(0)} \right\rangle$ is nonzero when $\Phi_J^{(0)}$ and $\Phi_0^{(0)}$ differs by two excitations (spinorbitals), one arrives at the following result for the energy at second-order MP

$$E_0^{(2)} = \frac{1}{4} \sum_{x,y} \sum_{r,s} \frac{\langle xy \| rs \rangle \langle rs \| xy \rangle}{\varepsilon_x + \varepsilon_y - \varepsilon_r - \varepsilon_s}. \tag{2.61}$$

This is often enough to describe electron correlation, usually capturing 80-90%, and higher order MP is rarely used. One important point is that in contrast to CI, MP is not variational, it is however *size-extensive*. Moreover, if a molecular system's electronic structure is poorly described using a single Hartree-Fock reference, then likewise the perturbation treatment on top will be poor.

2.4 Polarization and absorption of plane waves

In this section, the polarization of plane waves is illustrated. Next, the absorption of plane waves as measured in the UV/VIS and ECD spectroscopies is derived from the perspective of electric and magnetic fields.

2.4.1 Linear and circular polarized plane wave light

Maxwell's equations yield plane wave solutions,[32]

$$\vec{F} = \vec{F}_0 e^{i(\vec{k}\cdot\vec{x}-\omega t)}, \quad \vec{B} = \vec{B}_0 e^{i(\vec{k}\cdot\vec{x}-\omega t)}, \tag{2.62}$$

where $\vec{F}_0$ and $\vec{B}_0$ are the electric and magnetic polarization vectors both 3-dimensional complex vectors, ω is the real angular frequency, $\vec{k}$ is the real wavevector ($\omega = c|\vec{k}|$, in vacuo). Furthermore, Maxwell's equations show that the electric and magnetic fields are orthogonal to each other

$$\vec{B}_0 = \frac{1}{\omega}\left(\vec{k} \times \vec{F}_0\right). \tag{2.63}$$

Equation 2.63 implies that the magnetic field depends on the electric field with magnitude $\left|\vec{F}_0\right| = c\left|\vec{B}_0\right|$. Thus, the electric field in propagating in the z-direction can be written as

$$\vec{F} = \vec{F}_0 e^{i\omega\left(\frac{z}{c}-t\right)}, \quad \vec{F}_0 = (F_x, F_y, 0). \tag{2.64}$$

Here, F_x and F_y are complex numbers,

$$F_x = |F_x|\, e^{i\phi_x}, \quad F_y = |F_y|\, e^{i\phi_y}, \tag{2.65}$$

where ϕ denotes the phase of the field. When in-phase, Equations 2.64 and 2.65 describe linear polarization in the z-direction. If the components are out of phase ($\phi_x \neq \phi_y$) with equal magnitudes ($|F_x| = |F_y|$) the resulting polarization is said to be elliptical or circular. Specifically, $\phi_x - \phi_y = +\frac{\pi}{2}$ denotes left-handed circularly polarized light and $\phi_x - \phi_y = -\frac{\pi}{2}$ describes right-handed circularly polarized light. Hence,

$$\vec{F}_0 = \left(F_0, F_0 e^{i\frac{\pi}{2}}, 0\right) = (F_0, iF_0, 0) \qquad \text{left-handed circularly polarized light.} \tag{2.66}$$

$$\vec{F}_0 = \left(F_0, F_0 e^{-i\frac{\pi}{2}}, 0\right) = (F_0, -iF_0, 0) \qquad \text{right-handed circularly polarized light.} \tag{2.67}$$

Since the electric field is real, the vector potential of left-handed circularly polarized light propagating in the z-direction is

$$\mathrm{Re}(\vec{F}) = (F_0\cos(kz-\omega t), -F_0\sin(kz-\omega t), 0). \tag{2.68}$$

Linearly and circularly polarized light as described by the above equations can be illustrated by plotting the individual components of the vector potential as well as the tip of the vector potential, as shown in Fig. 2.2. Here, the tip of the vector potential oscillates in a straight path along the axis of propagation (linear, *left figure*) or spins in around the axis of propagation (circular, *right figure*). As is trivial to see from the above equations, addition of left and right-handed circularly polarized light yields linearly polarized light again,

$$\vec{F}_0 = (F_0, iF_0, 0) + (F_0, -iF_0, 0) = (2F_0, 0, 0). \tag{2.69}$$

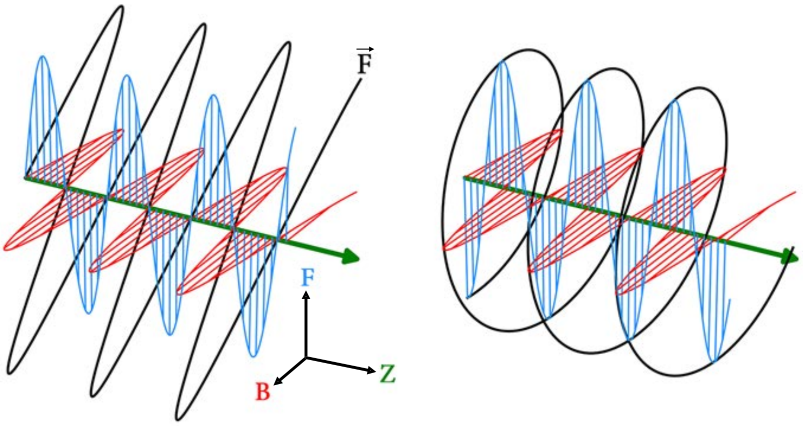

FIGURE 2.2: The electric (*blue*) and magnetic (*red*) oscillating fields and the tip of the vector potential (black) of in-phase, linear polarized light (*left*) and out out-of-phase, circular polarization light (*right*).

2.4.2 Absorption

Absorption occurs when the frequency of incoming light passing through a molecule matches the energy difference ω_{k0} between two quantum states $|\Psi_0\rangle$ and $|\Psi_k\rangle$. The transition rate of the absorption is then described by Fermi's golden rule,[108]

$$P_{k0}(\omega) = \frac{\pi}{2\hbar^2} |\langle\Psi_0| \hat{V}(t) |\Psi_k\rangle|^2 \delta(\omega - \omega_{k0}), \tag{2.70}$$

where δ is Dirac's delta function, ensuring that a transition only occurs when the incoming frequency matches the difference between the quantum states. $\hat{V}(t)$ is the gauge-dependent interaction operator which describes the interaction of the the system with the fields. One may then partition the time-dependent Hamiltonian $\hat{H}(t)$ as,

$$\hat{H}(t) = \hat{H}_0 + \hat{V}(t), \tag{2.71}$$

In Equation 2.71, $\hat{H}_0$ is the unperturbed Hamiltonian, which when used in the TISE (2.1) yields quantum states $|n\rangle$ as eigenfunctions and state energies E_n as eigenvalues.

In the Coulomb gauge, the interaction operator may be expressed as a multipole expansion in terms of an external electric field,[32]

$$\hat{V}(t) = -F_0(i_F \cdot \hat{\mu}) - B_0(i_B \cdot \hat{m}) - \frac{\nabla F_0}{2}(i_z \cdot \hat{\theta} \cdot i_F) + \dots \tag{2.72}$$

where i_F, i_B, i_z are unit vectors for the electric and magnetic vector of the polarized field and the unit-vector in the direction of propagation, $\hat{\mu}$ is the electric dipole operator, $\hat{m}$ is the magnetic dipole operator and $\hat{\theta}$ is the traceless quadrupole operator defined as

$$\hat{\mu} = \sum_{i}^{N_{\text{el}}} q_i \hat{r}_i, \tag{2.73}$$

$$\hat{m} = \sum_{i}^{N_{\text{el}}} \frac{q_i}{2m_i} (\hat{r}_i \times \hat{p}_i) \tag{2.74}$$

$$\hat{\theta} = \sum_{i}^{N_{\text{el}}} q_i \hat{r}_i \hat{r}_i. \tag{2.75}$$

Here, $\hat{r}$ is the position operator, $\hat{p}$ is the linear momentum operator, and q_i is the charge of the ith particle.

The absorption of a molecular species is linearly proportional to its concentration (outside of dispersion effects), as described by the Beer-Lambert law,[109]

$$A = \epsilon(\omega) c l \tag{2.76}$$

where $\epsilon(\omega)$ is the molar absorption coefficient at frequency ω, c is the concentration of the sample, l is the path length light traverses. The molar absorption coefficient is related to Fermi's rule as

$$\epsilon(\omega) = \frac{N_{\text{A}} \pi \omega}{1000 \times \ln(10) \times 2\hbar I_0} \sum_{k0} g_{k0}(\omega) |\langle \Psi_0 | \hat{V} | \Psi_k \rangle|^2, \tag{2.77}$$

where, N_{A} is Avogradro's number, I_0 is the intensity of light and g_{k0} is a function accounting for spectral broadening. There are several reasons for spectral broadening, e.g., collisions of molecules, scattering of light, vibrational effects, and more. These effects are not trivial to include in the Hamiltonian and as such it is common practice to simulate the impact they have by inclusion of $g_{k0}(\omega)$ centered at ω_{k0}. When the chief contribution of spectral broadening is spontaneous emission g_{k0} is taken to be a Lorentzian function,[110]

$$g_{k0}(\omega) = \frac{1}{\pi} \frac{\gamma_{k0}}{(\omega - \omega_{k0})^2 + \gamma_{k0}^2} \tag{2.78}$$

with γ_{n0} being inversely proportional to the lifetime of the nth excited state. Equation 2.77 can be used to derive expressions for the absorption processes of many different spectroscopic techniques. For instance, using linear polarization for the oscillating electric field in the multipole expansion leads to expressions for UV/VIS spectroscopy. Using the left- and right handed circularly polarized light in the same expansion and taking the difference will yield expressions for ECD as shall be discussed next.

Absorption of linear polarized light: UV/VIS spectroscopy

For a randomly oriented sample, the molar absorption coefficient is dominated by the lowest term in the multipole expansion and thus given by

$$\epsilon(\omega) = \frac{4\pi^2 N_{\text{A}} \omega}{3 \times 1000 \times \ln(10)(4\pi\epsilon_0) n\hbar c} \sum_{k0} g_{k0}(\omega) \sum_{i=x,y,z} \left| \langle \Psi_0 | \hat{\mu}_i | \Psi_k \rangle \right|^2, \tag{2.79}$$

which is measured in UV/VIS spectroscopy. However, for theoretical methods, it is convenient to use the dimensionless oscillator strength

$$f^r_{k0} = \frac{2m_e\omega_{k0}}{3\hbar e^2} \sum_{i=x,y,z} |\langle\Psi_0| \hat{\mu}_i |\Psi_k\rangle|^2 \tag{2.80}$$

where the superscript r denotes the length-gauge i.e., the use of the position operator (2.73). In atomic units, the oscillator strength is given by

$$f^r_{k0} = \frac{2\omega_{k0}}{3} \left(\vec{\mu}_{0k} \cdot \vec{\mu}_{k0}\right) \tag{2.81}$$

Absorption of circularly polarized light: ECD spectroscopy

When the electric and magnetic fields are out of phase by $\pm\frac{\pi}{2}$, the difference in absorption between them considering only electronic transitions, form the basis of ECD spectroscopy. Denoting the left and right circularly polarized light as ϵ_L and ϵ_R, respectively, the difference

$$\Delta\epsilon(\omega) = \epsilon_\mathrm{L}(\omega) - \epsilon_\mathrm{R}(\omega), \tag{2.82}$$

for a randomly oriented sample, using Equation 2.77, is

$$\Delta\epsilon(\omega) = \frac{N_\mathrm{A}\pi\omega}{1000 \times \ln(10) \times 2\hbar I_o} \sum_{k0} g_{k0}(\omega)\Big(\left|(V^L)_{k0}\right|^2 - \left|(V^R)_{k0}\right|^2 \Big). \tag{2.83}$$

By using Equations 2.66 and 2.67 for the fields, after insertion into Equation 2.83, one obtains, [111]

$$\begin{aligned} \left|(V^L)_{k0}\right|^2 - \left|(V^R)_{k0}\right|^2 =& \frac{1}{2}\,\mathrm{Im}\left[(\mu_x)_{k0}(m_y)_{k0} + (\mu_y)_{k0}(m_x)_{k0}\right] F_0 B_0 \\ &+ \frac{i}{4}\mathbf{i}_z \cdot (\mu_{k0} \times \mu_{k0})F_0^2 + \frac{i}{4}\mathbf{i}_z \cdot (m_{k0} \times m_{k0})B_0^2 + \dots\ . \end{aligned} \tag{2.84}$$

The last two terms in Equation 2.84 are nonzero in the presence of an external magnetic field and are relevant for magnetic circular dichroism (MCD), but are zero in the case of ECD. One can now express the molar coefficient describing the difference in absorption between left and right circularly polarized light as,

$$\Delta\epsilon(\omega) = \frac{16\pi^2 N_\mathrm{A}\omega}{3 \times 1000 \ln(10)\,(4\pi\epsilon_0)\,\hbar c^2} \sum_{k0} g_{k0}(\omega)\,\mathrm{Im}\,\big(\langle\Psi_0| \hat{\mu} |\Psi_k\rangle \langle\Psi_k| \hat{m} |\Psi_0\rangle\big). \tag{2.85}$$

Analogous to the oscillator strength, it is here convenient to introduce the rotatory strength

$$R^r_{k0} = \mathrm{Im}\,\langle\Psi_0| \hat{\mu} |\Psi_k\rangle \langle\Psi_k| \hat{m} |\Psi_0\rangle \tag{2.86}$$

where the superscript r again denotes the length-gauge formulation.Unlike the oscillator, the rotatory strength is not a dimensionless quantity, but has units of 10^{-40} esu · cm · erg/G or 10^{-40} c.g.s. units. [112] Equation 2.86 was first derived in a similar manner by Rosenfeld in 1929 and is thus known as the Rosenfeld equation. [113] R^r_{k0} is only nonzero for molecular systems without a primary axis of rotation, hence chiral molecules, where at least one component of the scalar product of the electric and magnetic transition dipole moments overlap.

2.5 Response theory

Exact response theory may be viewed as a particular scheme of time-dependent perturbation theory whereby explicit summations are avoided, instead solving algebraic equations in a transferable manner, i.e., properties can be retrieved from a wave function, independent of the parameterization of the wave function itself.[114,115]

Response theory begins with an examination of the expectation value of some arbitrary operator of interest, $\hat{A}$. Denoting the time-dependent reference state $|\tilde{0}(t)\rangle$ and considering only Hermitian (time-dependent) perturbation operators $\hat{V}$, the response functions are obtained as Fourier coefficients in the time dependent-expectation value of $\hat{A}$ as

$$\begin{aligned}\langle\tilde{0}(t)|\hat{A}|\tilde{0}(t)\rangle =& \langle 0|\hat{A}|0\rangle \\ &+\int_{-\infty}^{\infty}\langle\langle\hat{A};\hat{V}^{\omega_1}\rangle\rangle e^{-i\omega_1 t}d\omega_1 \\ &+\frac{1}{2}\int_{-\infty}^{\infty}\int_{-\infty}^{\infty}\left\langle\left\langle\hat{A};\hat{V}^{\omega_1},\hat{V}^{\omega_2}\right\rangle\right\rangle e^{-i(\omega_1+\omega_2)t}d\omega_1 d\omega_2 \\ &+\frac{1}{6}\int_{-\infty}^{\infty}\int_{-\infty}^{\infty}\int_{-\infty}^{\infty}\left\langle\left\langle\hat{A};\hat{V}^{\omega_1},\hat{V}^{\omega_2},V^{\omega_3}\right\rangle\right\rangle e^{-i(\omega_1+\omega_2+\omega_3)t}d\omega_1 d\omega_2 d\omega_3+\cdots,\end{aligned} \tag{2.87}$$

here each V^{ω_i} corresponds to a time-dependent perturbation operator and the infinitesimal factors which ensure that the perturbations are turned on adiabatically, and vanish as $t \to \infty$, are omitted. Each response function is denoted $\langle\langle\hat{A};\hat{B}^{\omega_2},\ldots,\hat{X}^{\omega_i}\rangle\rangle$ where $\hat{A}$ is the observable, and $\hat{B}^{\omega_1}\ldots\hat{X}^{\omega_i}$ are the perturbation operators at ω_i frequency. This perturbational treatment is only valid when the perturbations are small compared to the interatomic potential.[116] While Equation 2.87 describes response functions for both static and dynamic fields, frequency-dependent response functions can only be used with approximate methods that provide the time-dependent expectation value of $\hat{A}$, and hence methods that only provide the energy but not the wave function, e.g., coupled cluster singles, doubles and perturbative triples (CCSD(T)), are not applicable to this approach. However, static response functions can be used for these methods. The methods that can be used with frequency-dependent response functions are thus HF, DFT, MCSCF, etc, where the ground state $|0\rangle$ is taken as the reference (zeroth-order), and frequency-dependent response functions are calculated “on top”.

The first, second and higher order responses in Equation 2.87 are determined in a way consistent with the TISE and in general have the matrix form

$$[\mathcal{H}-\omega\mathcal{S}]\lambda^{(n)}(\omega) = -\mathcal{V}^{(n)}(\omega), \tag{2.88}$$

where $\lambda^{(n)}(\omega)$ is a vector containing the nth order ($n > 0$) wave function parameters. Here, $\mathcal{H}$ and $\mathcal{S}$ depend only on the unperturbed ground state, whereas the vector on the right-hand side depends on the lower-order wave function parameters ($\lambda^{(1)}$, $\lambda^{(2)}$, $\lambda^{(3)}$,. . .,$\lambda^{(n-1)}$) and on the perturbation operator $\mathcal{V}^{(n)}(\omega)$. This means that to solve an nth order response function, the $(n-1)$th order must already have been solved for. The formal solution to Equation 2.88 is trivial, namely

$$\lambda^{(n)}(\omega) = -[\mathcal{H} - \omega\mathcal{S}]^{-1}\mathcal{V}^{(n)}(\omega), \tag{2.89}$$

where $[\mathcal{H} - \omega\mathcal{S}]^{-1}$ is a nonsingular matrix. Since $\mathcal{H}$ and $\mathcal{S}$ depend only on the unperturbed ground state, they can in principle be computed directly. Subsequently, the inverse would be calculated followed by matrix-vector multiplication to obtain a solution. However, in practice the inverse is often too computationally expensive to compute directly due to the sizes of $\mathcal{H}$ and $\mathcal{S}$.

Furthermore, when $[\mathcal{H} - \omega\mathcal{S}]^{-1}$ is non-invertible, occurs when ω_k is identical to one of the eigenvalues of the system, i.e., $\omega_{k0} = \omega_k,\ k = 1, 2, 3, \ldots$, which can be used to identify the excitation energies of the system. Finding these eigenvalues corresponds to solving the eigenvalue problem

$$(\mathcal{H} - w_k\mathcal{S})\,\mathbf{X}_k = 0, \tag{2.90}$$

where $\mathbf{X}_k$ is the eigenvector corresponding to w_k. Equation 2.90 has no perturbational dependence and as such can be solved directly to obtain the excitation energies $\omega_{k0} = w_k,\ k = 1, 2, 3, \ldots$ without explicit knowledge of the excited-state wave function, which is one of the attractive features of response theory. Since the ground state energy is known from the unperturbed calculation, the excited-state energy is then also known by

$$E_k = E_0 + \hbar\omega_{k0}. \tag{2.91}$$

The computational advantage of the response approach is thus that explicit knowledge of the excited-state wave functions is required, rather, the solutions of the response functions in Equation 2.88 for each perturbation operator $\mathcal{V}(\omega)$ are needed.

2.5.1 Linear response functions

Considering only exact states, the zeroth-order response function in Equation 2.87 is the expectation value of operator $\hat{A}$ in the unperturbed reference state $|\Psi_0\rangle$, $\langle\Psi_0|\,\hat{A}\,|\Psi_0\rangle$. The first-order, linear response function in the sum-over-states (SOS) or spectral representation is [117,118]

$$\langle\langle \hat{A}^{\omega_\sigma}; \hat{B}^{\omega_1}\rangle\rangle_{\omega_1} = -\frac{1}{\hbar}\mathcal{P}\sum_k \frac{\langle\Psi_0|\hat{A}^{\omega_\sigma}|\Psi_k\rangle\langle\Psi_k|\hat{B}^{\omega_1}|\Psi_0\rangle}{\omega_k - \omega_1,} \tag{2.92}$$

where $\hbar\omega_k = E_k - E_0$ is the transition energy from the ground state to the kth excited state. Here $\mathcal{P}$ denotes a permutation operator with implicit summation of the permutations, i.e., $\mathcal{P}$ above is the sum of the permutations of $(\hat{A}^{\omega_\sigma}, \omega_\sigma)$ and $(\hat{B}^{\omega_1}, \omega_1)$. Writing the above equation without the permutation operator is thus

$$\langle\langle \hat{A}^{\omega_\sigma}; \hat{B}^{\omega_1}\rangle\rangle_{\omega_1} = -\frac{1}{\hbar}\sum_k \left[\frac{\langle\Psi_0|\hat{A}^{\omega_\sigma}|\Psi_k\rangle\langle\Psi_k|\hat{B}^{\omega_1}|\Psi_0\rangle}{\omega_k - \omega_1} + \frac{\langle\Psi_0|\hat{B}^{\omega_1}|\Psi_k\rangle\langle\Psi_k|\hat{A}^{\omega_\sigma}|\Psi_0\rangle}{\omega_k + \omega_1}\right]. \tag{2.93}$$

In the following equations the superscript for the operator frequencies are implicit. Since the poles of Equation 2.92 correspond to excitation energies, the residues can be used to obtain transition moments

$$\lim_{\omega\to\omega_k} \hbar\,(\omega-\omega_k)\,\langle\langle\hat{A};\hat{B}\rangle\rangle_{\omega_1} = \langle\Psi_0|\hat{A}|\Psi_k\rangle\langle\Psi_k|\hat{B}|\Psi_0\rangle \tag{2.94}$$

$$\lim_{\omega\to-\omega_k} \hbar\,(\omega+\omega_k)\,\langle\langle\hat{A};\hat{B}\rangle\rangle_{\omega_1} = -\langle\Psi_0|\hat{B}|\Psi_k\rangle\langle\Psi_k|\hat{A}|\Psi_0\rangle \tag{2.95}$$

where $\langle\Psi_0|\,\hat{A}\,|\Psi_k\rangle$ corresponds to a transition moment between the ground state and the kth excited state. This is commonly expressed in terms of the kth eigenvector of Equation 2.90 and the matrix representation of operator $\hat{A}$. Using the excitation energies and transition moments obtained from Equation 2.90 and 2.94, in SOS expression including all states, is equivalent to Equation 2.88.

Furthermore, the linear response functions defined by Equation 2.92 obey the permutation and conjugation rules

$$\langle\langle\hat{A};\hat{B}\rangle\rangle_{\omega_1} = \langle\langle\hat{B};\hat{A}\rangle\rangle_{-\omega_1} \tag{2.96}$$

$$\langle\langle\hat{A};\hat{B}\rangle\rangle^*_{\omega_1} = \langle\langle\hat{A}^\dagger;\hat{B}^\dagger\rangle\rangle_{-\omega_1} \tag{2.97}$$

In approximate theories, Equation 2.92, is only valid in off-resonance regions, i.e., far away from the poles, since the lifetime of the kth excited state is assumed to be infinite. To correct for this, one may introduce a broadening constant, γ_k, which is inversely proportional to the lifetime of the kth excited state ($\tau_k = 1/\gamma_k$). The exact *damped* linear response function will then be of the form,[116]

$$\langle\langle\hat{A};\hat{B}\rangle\rangle_{\omega} = \frac{1}{\hbar}\sum_{k\neq 0}\left(\frac{\langle\Psi_0|\hat{A}|\Psi_k\rangle\langle\Psi_k|\hat{B}|\Psi_0\rangle}{\omega-\omega_{k0}+i\gamma_k/2} - \frac{\langle\Psi_0|\hat{B}|\Psi_k\rangle\langle\Psi_k|\hat{A}|\Psi_0\rangle}{\omega+\omega_{k0}-i\gamma_k/2}\right). \tag{2.98}$$

While the lifetime of the individual excited states of a molecular system will in principle be different for each state, it is very difficult to account for this in approximate theories using Equation 2.88. Instead, an identical lifetime for all excited states are used ($\gamma_1 = \gamma_2 = \ldots = \gamma$). The spectral form of Equation 2.98 is then a Lorentzian function.

2.5.2 Quadratic response functions

The second-order, exact quadratic response function is defined as

$$\langle\langle\hat{A};\hat{B},\hat{C}\rangle\rangle_{\omega_1,\omega_2} = -\frac{1}{\hbar^2}\mathcal{P}\sum_{k,f}\frac{\langle\Psi_0|\hat{A}|\Psi_k\rangle\langle\Psi_k|\hat{B}|\Psi_f\rangle\langle\Psi_f|\hat{C}|\Psi_0\rangle}{(\omega_k-\omega_\sigma)\,(\omega_f-\omega_2)}, \tag{2.99}$$

where ω_σ is the sum of the perturbation frequencies ($\omega_\sigma = \sum_i \omega_i$). $\mathcal{P}$ permutes the three frequency-operator pairs as described for Equation 2.92. When the ground state $|0\rangle$ is omitted from the sum in Equation 2.99, one obtains operators of the form $\bar{\hat{B}} = \hat{B} - \langle 0|\,\hat{B}\,|0\rangle$, i.e., the operator shifted by the exact ground-state expectation value, referred to as the “fluctuation operator”.[118] From the quadratic and higher-order response functions, multiple residues are possible. Among the most important is the single residue of a quadratic response function

$$\lim_{\omega_2 \to \omega_f} \hbar\,(\omega_2 - \omega_f)\,\langle\langle \hat{A}; \hat{B}, \hat{C} \rangle\rangle_{\omega_1,\omega_2} = -\frac{1}{\hbar}\left[\mathcal{P}\sum_k \frac{\langle\Psi_0|\hat{A}|\Psi_k\rangle\langle\Psi_k|\hat{B}|\Psi_f\rangle}{(\omega_k - \omega_\sigma)}\right]\langle\Psi_f|\hat{C}|\Psi_0\rangle, \tag{2.100}$$

which can be used to obtain two-photon transition matrix elements which are relevant for TPA and TPCD as will be described later. Another important residue is the double residue of a quadratic response function

$$\begin{aligned} &\lim_{\omega_1 \to -\omega_k} \hbar\,(\omega_1 + \omega_k) \lim_{\omega_2 \to \omega_f} \hbar\,(\omega_2 - \omega_f)\,\langle\langle \hat{A}; \hat{B}, \hat{C} \rangle\rangle_{\omega_1,\omega_2} \\ &= -\langle\Psi_0|\hat{B}|\Psi_k\rangle\langle\Psi_k|(\hat{A} - \langle\Psi_0|\hat{A}|\Psi_0\rangle)|\Psi_f\rangle\langle\Psi_f|\hat{C}|\Psi_0\rangle, \end{aligned} \tag{2.101}$$

which allows for the determination of transition moments between two excited states $|\Psi_k\rangle$ and $|\Psi_f\rangle$ (having only knowledge of the reference state $|\Psi_0\rangle$). Importantly, with the choice of $|\Psi_k\rangle = |\Psi_d f\rangle$ one obtains,

$$\begin{aligned} &\lim_{\omega_1 \to -\omega_k} \hbar\,(\omega_1 + \omega_k) \lim_{\omega_2 \to \omega_k} \hbar\,(\omega_2 - \omega_k)\,\langle\langle \hat{A}; \hat{B}, \hat{C} \rangle\rangle_{\omega_1,\omega_2} \\ &= -\langle\Psi_0|\hat{B}|\Psi_k\rangle \Big(\langle\Psi_k|\hat{A}|\Psi_k\rangle - \langle\Psi_0|\hat{A}|\Psi_0\rangle \Big) \langle\Psi_k|\hat{C}|\Psi_0\rangle. \end{aligned} \tag{2.102}$$

Here, the state specific expectation value $\langle\Psi_k|\,\hat{A}\,|\Psi_k\rangle$, is recovered.

2.5.3 Linear polarizability

Insertion of $\hat{A} = \hat{\mu}$ and $\hat{V}^{\omega} = \hat{\mu} \cdot F^{\omega}$ into Equation 2.87 yields the exact linear response function which describes the first-order induced electric dipole moment in the presence of an oscillating electric field. With these operators, Equation 2.92 defines the elements of the frequency-dependent electric dipole polarizability

$$\alpha_{\alpha\beta}(-\omega;\omega) = -\,\langle\langle \hat{\mu}_\alpha; \hat{\mu}_\beta \rangle\rangle_\omega\,. \tag{2.103}$$

Here, the subscripts i, j denote the Cartesian spatial components of the electric dipole operator $\hat{\mu}$. From the permutation and conjugation rules (2.96 and 2.97) inherent to the linear response function, it follows that the electric dipole polarizability is an even function of frequency and is symmetric with respect to permutations of the indices

$$\alpha_{\alpha\beta}(-\omega;\omega) = \alpha_{\alpha\beta}(\omega;-\omega) \tag{2.104}$$

$$\alpha_{\alpha\beta}(-\omega;\omega) = \alpha_{\beta\alpha}(-\omega;\omega), \tag{2.105}$$

which demonstrates that α possesses six linearly independent components.

Another important quantity is the mixed electric - magnetic dipole polarizability, which can be evaluated from the linear response function

$$G'_{\alpha\beta}\,(\omega_k) = -\,\mathrm{Im}\,\langle\langle \hat{\mu}_\alpha; \widehat{m}_\beta \rangle\rangle_{\omega_k}\,. \tag{2.106}$$

The residues of Equation 2.103 and 2.106 are related to the oscillator and rotatory strengths (2.80 and 2.86), which shows how response approach can be used to obtain these spectroscopy-relevant quantities, as will be discussed in the next section.

Common properties accessible from the linear response function and its residue are summarized in Table 2.1.

TABLE 2.1: Properties obtained by the linear response function and its residue.

Response fnc.	Residue	Property
$\langle\langle\hat{\mu};\hat{\mu}\rangle\rangle_\omega$	–	Linear electric dipole polarizability.
	$\omega = \omega_{f0}$	One-photon transition matrix elements between the ground state $\|0\rangle$ and the excited state $\|f\rangle$.
$\langle\langle\hat{\mu};\hat{m}\rangle\rangle_\omega$	–	Linear mixed electric-magnetic dipole polarizability.
	$\omega = \omega_{f0}$	One-photon rotatory strength elements between the ground state $\|0\rangle$ and the excited state $\|f\rangle$.

2.5.4 Oscillator and rotatory strengths

For the following sections, the properties derived will be presented in atomic units.

Oscillator strength

In approximate theories, the one-photon absorption intensity, oscillator strength f, Equation 2.80, is obtained from the residue of the frequency-dependent electric dipole polarizability. By Equation 2.103, in the length-gauge is written

$$\begin{aligned} f^r_{k0} &= -\frac{2\omega_{k0}}{3}\sum_{\alpha}^{x,y,z}\lim_{\omega\to\omega_{k0}}(\omega-\omega_{k0})\,\langle\langle\hat{\mu}_\alpha;\hat{\mu}_\alpha\rangle\rangle_\omega \\ &= \frac{2\omega_{k0}}{3}\sum_{\alpha}^{x,y,z}\lim_{\omega\to\omega_{k0}}(\omega-\omega_{k0})\,\alpha_{\alpha\alpha}(-\omega;\omega) \\ &= \frac{2\omega_{k0}}{3}\langle\Psi_0|\,\hat{\mu}\,|\Psi_k\rangle\langle\Psi_k|\,\hat{\mu}\,|\Psi_0\rangle\ . \end{aligned} \tag{2.107}$$

It is important to consider the relation between the position and momentum operator which are related by the hypervirial relationship

$$\langle\Psi_0|\,\hat{p}_\alpha\,|\Psi_k\rangle = i\omega_{k0}\,\langle\Psi_0|\,\hat{r}_\alpha\,|\Psi_k\rangle\ . \tag{2.108}$$

By replacing the electric dipole operator by the linear momentum operator using Equation 2.108 allows for the oscillator strength to be expressed in the so-called "velocity-gauge" as

$$\begin{aligned} f_{k0}^{\nabla} &= \frac{2\omega_{k0}}{3} \sum_{\alpha}^{x,y,z} \lim_{\omega \to \omega_{k0}} (\omega - \omega_{k0}) \langle\langle \hat{p}_\alpha ; \hat{p}_\alpha \rangle\rangle_\omega \\ &= \frac{2}{3\omega_{k0}} \langle \Psi_0 | \, \hat{p} \, | \Psi_k \rangle \langle \Psi_k | \, \hat{p} \, | \Psi_0 \rangle \ , \end{aligned} \tag{2.109}$$

where the ∇ superscript denotes the that the linear momentum operator has been used ($\hat{p} = -i\nabla$). Furthermore, the oscillator strength can be expressed in the so-called mixed length-velocity gauge,[3]

$$\begin{aligned} f_{k0}^{r\nabla} &= -\frac{2i}{3} \sum_{\alpha}^{x,y,z} \lim_{\omega \to \omega_{k0}} (\omega - \omega_{k0}) \langle\langle \hat{\mu}_\alpha ; \hat{p}_\alpha \rangle\rangle_\omega \\ &= -\frac{2i}{3} \langle \Psi_0 | \, \hat{\mu} \, | \Psi_k \rangle \langle \Psi_k | \, \hat{p} \, | \Psi_0 \rangle \ . \end{aligned} \tag{2.110}$$

While these formulations are formally identical, they are in fact only equivalent when Equation 2.108 is fully upheld, which is only the case when the TISE is solved exactly. Hence for approximate theories, differences between these formulations will occur. Approximate methods can further be divided into "gauge-invariant" and "gauge-variant" categories, where gauge-invariant methods produce equivalent oscillator strengths in all formulation for a complete one-electron basis set (COEBS). For such methods, the mixed-gauge representation can be used to measure the completeness of the one-electron basis set in combination with the other two formulations (Equation 2.107 and 2.110).[119] A common gauge-invariant method is random-phase approximation (RPA) and gauge-variant methods include CCS, CC2, CCSD etc, as well as ADC. However, even for relatively small basis sets these methods usually yield small difference between the gauges. Furthermore, there is no "good" reason to believe that one or the other of these formulations is more accurate and as such there is little reason to compute one over the other. However, this is not the case for the optical rotatory strength as shall be discussed next.

Rotatory strength

As was the case for the oscillator strength, the rotatory strength, Equation 2.86, can be obtained as the residue of the mixed electric - magnetic dipole polarizability, Equation 2.106

$$R_{k0}^{r} = \sum_{\alpha}^{x,y,z} \lim_{\omega \to \omega_{k0}} (\omega_{k0} - \omega) \, \mathrm{Im} \, \langle\langle \hat{\mu}_\alpha ; \hat{m}_\alpha \rangle\rangle_\omega \tag{2.111}$$

Equation 2.111 corresponds to the length-gauge formulation of the rotatory strength. This form of the rotatory strength has an *unphysical* origin-dependence. Specifically, this means that if the molecular coordinates are transformed, the calculated property, i.e., the corresponding rotatory strength, will likewise change. To see why this is the case, consider a change in gauge-origin along a vector $\mathbf{O}$ such that such that the position of the nuclei and electrons are shifted $\mathbf{r}^{\mathrm{O}} \to \mathbf{r}^{\mathrm{O}} - \mathbf{O}$, the electric-magnetic dipole polarizability then changes accordingly as

$$G'(-\omega;\omega) \to G'(-\omega;\omega) + \frac{1}{2} \, \mathrm{Im} \left[\langle\langle \hat{\mu} ; \hat{p} \rangle\rangle_\omega \times \mathbf{O} \right] \tag{2.112}$$

which shows that the tensor is indeed origin dependent. Furthermore, this origin dependence arises solely from the magnetic dipole operator which transforms as

$$\hat{m} \rightarrow \hat{m} - \frac{1}{2}\hat{p} \times \mathbf{O} \tag{2.113}$$

with a shift in origin. This is where the gauge transformation introduced in Equation 2.108 shows its usefulness. When the electric dipole operator is replaced with the linear momentum operator, one obtains the rotatory strength in the velocity-gauge as

$$\begin{aligned} R_{k0}^{\nabla} &= -\frac{1}{\omega_{k0}} \sum_{\alpha}^{x,y,z} \lim_{\omega \rightarrow \omega_{k0}} \left(\omega_{k0} - \omega\right) \langle\langle \hat{p}_{\alpha}; \hat{m}_{\alpha} \rangle\rangle_{\omega} \\ &= -\frac{1}{\omega_{k0}} \langle \Psi_0 | \hat{p} | \Psi_k \rangle \langle \Psi_k | \hat{m} | \Psi_0 \rangle \ . \end{aligned} \tag{2.114}$$

This form of the rotatory strength is inherently origin-*independent*, even for approximate theories. As such, it can be argued that velocity-gauge rotatory strengths are more reliable than length-gauge rotatory strength and they are often preferred in calculations. However it should be emphasized that these two formulations are equivalent in exact theory, i.e., the length-gauge formulation is origin-independent when the TISE is solved exactly. An alternative approach to obtain origin-independent rotatory strengths is by using magnetic-field gauge including atomic orbitals (GIAO), also referred to as London orbitals.[48,120–127]

While the expressions for the oscillator and rotatory strengths discussed so far correspond to excitations from the ground state, they can in principle be used to describe excitations from excited states. For approximate theories where excited state transition moments can be obtained, e.g., $\langle \Psi_n | \hat{\mu} | \Psi_f \rangle$, $\langle \Psi_n | \hat{p} | \Psi_f \rangle$ and $\langle \Psi_n | \hat{m} | \Psi_f \rangle$, one can express the oscillator and rotatory strengths corresponding to excitations from the nth to kth excited states using the matrix elements. For the oscillator strengths

$$f_{kn}^{r} = \frac{2\omega_{kn}}{3} \langle \Psi_n | \hat{\mu} | \Psi_k \rangle \langle \Psi_k | \hat{\mu} | \Psi_n \rangle \tag{2.115}$$

$$f_{kn}^{\nabla} = \frac{2}{3\omega_{kn}} \langle \Psi_n | \hat{p} | \Psi_k \rangle \langle \Psi_k | \hat{p} | \Psi_n \rangle \tag{2.116}$$

$$f_{kn}^{r\nabla} = -\frac{2i}{3} \langle \Psi_n | \hat{\mu} | \Psi_k \rangle \langle \Psi_k | \hat{p} | \Psi_n \rangle \tag{2.117}$$

and for the rotatory strengths

$$R_{kn}^{r} = \operatorname{Im} \langle \Psi_n | \hat{\mu} | \Psi_k \rangle \langle \Psi_n | \hat{m} | \Psi_k \rangle \tag{2.118}$$

$$R_{kn}^{\nabla} = -\frac{1}{\omega_{kn}} \langle \Psi_n | \hat{p} | \Psi_k \rangle \langle \Psi_k | \hat{m} | \Psi_n \rangle . \tag{2.119}$$

For approximate methods, where frequency-dependent response functions can be used, these quantities can be obtained either using linear response functions (replacing the ground state with an excited-state wave function) or alternatively by the residues of a quadratic response function as demonstrated in Section 2.5.2.

Described above are the processes that encompass the one-photon absorption of linear and circularly polarized plane wave light which are summarized in Table 2.2.

Table 2.2: Oscillator and rotatory strengths for one-photon processes and their associated spectroscopies.

Symbol	Formula	n $(k > n)$	Associated spectroscopy	Origin dependence[1]
		linear polarization		
f_{kn}^{r}	$\frac{2m_e\omega_{kn}}{3\hbar e^2}\left\langle\Psi_n\right\|\hat{\mu}\left\|\Psi_k\right\rangle\left\langle\Psi_k\right\|\hat{\mu}\left\|\Psi_n\right\rangle$	$n = 0$	UV/VIS	no
		$n > 0$	pump-probe	no
f_{kn}^{∇}	$\frac{2}{3\hbar m_e\omega_{kn}}\left\langle\Psi_n\right\|\hat{p}\left\|\Psi_k\right\rangle\left\langle\Psi_k\right\|\hat{p}\left\|\Psi_n\right\rangle$	$n = 0$	UV/VIS	no
		$n > 0$	pump-probe	no
$f_{kn}^{r\nabla}$	$-\frac{2i}{3\hbar e}\left\langle\Psi_n\right\|\hat{p}\left\|\Psi_k\right\rangle\left\langle\Psi_k\right\|\hat{\mu}\left\|\Psi_n\right\rangle$	$n = 0$	UV/VIS	no
		$n > 0$	pump-probe	no
		circular polarization		
R_{kn}^{r}	$\mathrm{Im}\left\langle\Psi_n\right\|\hat{\mu}\left\|\Psi_k\right\rangle\left\langle\Psi_k\right\|\hat{m}\left\|\Psi_n\right\rangle$	$n = 0$	ECD	yes
		$n > 0$	ES-ECD	yes
R_{kn}^{∇}	$-\frac{\hbar}{m_e\omega_{kn}}\left\langle\Psi_n\right\|\hat{p}\left\|\Psi_k\right\rangle\left\langle\Psi_k\right\|\hat{m}\left\|\Psi_n\right\rangle$	$n = 0$	ECD	no
		$n > 0$	ES-ECD	no

---

[1] For approximate theories without using GIAOs.

2.5.5 First-order electric dipole hyperpolarizability and second harmonics

When the electric dipole operator is chosen for $\hat{A}$, $\hat{B}$ and $\hat{C}$, Equation 2.99 yields the first-order electric dipole hyperpolarizability

$$\beta_{\alpha\beta\gamma}\left(-\omega_\sigma;\omega_1,\omega_2\right) = -\left\langle\left\langle\hat{\mu}_\alpha;\hat{\mu}_\beta,\hat{\mu}_\gamma\right\rangle\right\rangle_{\omega_1,\omega_2}, \tag{2.120}$$

which is only physically relevant when $\omega_\sigma = \omega_1 + \omega_2$. One can associate Equation 2.120 with several different nonlinear processes, depending on the dynamic fields, as listed in Table 2.3. Inherent to the definition of the quadratic response function, Equation 2.99, are symmetry with respect to permutation of operators,

$$\beta_{\alpha\beta\gamma}\left(-\omega_\sigma;\omega_1,\omega_2\right) = \beta_{\alpha\gamma\beta}\left(-\omega_\sigma;\omega_2,\omega_1\right), \tag{2.121}$$

$$\beta_{\alpha\beta\gamma}\left(-\omega_\sigma;\omega_1,\omega_2\right) = \beta_{\beta\alpha\gamma}\left(\omega_1;-\omega_\sigma,\omega_2\right). \tag{2.122}$$

TABLE 2.3: Processes described by first-order electric dipole hyperpolarizability.

Process	Symbol	Frequencies	Response function
Second harmonic generation (SHG)	$\beta^{\mathrm{SHG}}_{\alpha\beta\gamma}$	$(-2\omega;\omega,\omega)$	$\langle\langle\hat{\mu}_\alpha;\hat{\mu}_\beta,\hat{\mu}_\gamma\rangle\rangle_{\omega,\omega}$
Electro-Optic Pockels Effect (EOPE)	$\beta^{\mathrm{EOPE}}_{\alpha\beta\gamma}$	$(-\omega;\omega,0)$	$\langle\langle\hat{\mu}_\alpha;\hat{\mu}_\beta,\hat{\mu}_\gamma\rangle\rangle_{\omega,0}$
Optical Retification	$\beta^{\mathrm{OR}}_{\alpha\beta\gamma}$	$(0;-\omega,\omega)$	$\langle\langle\hat{\mu}_\alpha;\hat{\mu}_\beta,\hat{\mu}_\gamma\rangle\rangle_{\omega,-\omega}$

Furthermore, by assuming that one can interchange the indices of the incoming light, without changing the corresponding frequencies

$$\beta_{\alpha\beta\gamma}\left(-\omega_\sigma;\omega_1,\omega_2\right)\approx\beta_{\alpha\gamma\beta}\left(-\omega_\sigma;\omega_1,\omega_2\right), \tag{2.123}$$

the number of linearly independent components of β is further reduced, an assumption known as Kleinman's symmetry.[128] This relation is fully upheld at static frequency, although, often used as a good approximation in dynamic and especially low-frequency regions. In the case of the first-order electric dipole hyperpolarizability, the experimentally relevant quantity is the vector component of β in the direction of the permanent dipole moment in the direction of the molecular z-axis. The isotropic averages are then defined as

$$\beta_{||}=\frac{1}{5}\sum_{\eta}^{x,y,z}\left(\beta_{z\eta\eta}+\beta_{\eta z\eta}+\beta_{\eta\eta z}\right), \tag{2.124}$$

$$\beta_{\perp}=\frac{1}{5}\sum_{\eta}^{x,y,z}\left(2\beta_{z\eta\eta}-3\beta_{\eta z\eta}+2\beta_{\eta\eta z}\right), \tag{2.125}$$

where the same sequence of optical frequencies are used for the laboratory and molecular axes. The number of linearly independent elements of β depends on the frequency combination applied as well as on the symmetry of the molecule. In the case of SHG, the signal is related to the isotropic values as

$$\beta_{\mathrm{SHG}}=\beta_{||}(-2\omega;\omega,\omega),\quad \omega>0. \tag{2.126}$$

An often employed experimental method to measure β is HRS which owes its prominence due to allowing measurements in solutions. The SHG intensity associated with an HRS measurement is

$$I_{2\omega}=g\sum_{s}\mathcal{N}_s\beta^2_{\mathrm{HRS}}I_o^2, \tag{2.127}$$

where $\mathcal{N}_s$ is the number density of the sth molecular species, I_o is the intensity of the incoming field at frequency ω. β_{HRS} in the laboratory axes frame is related to the molecular axes reference by

$$\beta_{\mathrm{HRS}}=\sqrt{\langle\beta^2_{iii}\rangle+\langle\beta^2_{jii}\rangle} \tag{2.128}$$

where $\langle \beta_{iii}^2 \rangle$ and $\langle \beta_{jii}^2 \rangle$ are orientational averages of β in the molecular axes as

$$\begin{aligned}
\langle \beta_{iii}^2 \rangle = &+ \frac{1}{7} \sum_{\alpha}^{x,y,z} \beta_{\alpha\alpha\alpha}^2 + \frac{4}{35} \sum_{\alpha\neq\beta}^{x,y,z} \beta_{\alpha\alpha\beta}^2 + \frac{2}{35} \sum_{\alpha\neq\beta}^{x,y,z} \beta_{\alpha\alpha\alpha}\beta_{\alpha\alpha\beta} + \frac{4}{35} \sum_{\alpha\neq\beta}^{x,y,z} \beta_{\beta\alpha\alpha}\beta_{\alpha\alpha\beta} \\
&+ \frac{4}{35} \sum_{\alpha\neq\beta}^{x,y,z} \beta_{\alpha\alpha\alpha}\beta_{\beta\beta\beta} + \frac{1}{35} \sum_{\alpha\neq\beta\neq\gamma}^{x,y,z} \beta_{\beta\alpha\alpha}^2 + \frac{4}{105} \sum_{\alpha\neq\beta\neq\gamma}^{x,y,z} \beta_{\alpha\alpha\beta}\beta_{\beta\gamma\gamma} \\
&+ \frac{1}{105} \sum_{\alpha\neq\beta\neq\gamma}^{x,y,z} \beta_{\beta\alpha\alpha}\beta_{\beta\gamma\gamma} + \frac{4}{105} \sum_{\alpha\neq\beta\neq\gamma}^{x,y,z} \beta_{\alpha\alpha\beta}\beta_{\gamma\gamma\beta} + \frac{2}{105} \sum_{\alpha\neq\beta\neq\gamma}^{x,y,z} \beta_{\alpha\beta\gamma}^2 \\
&+ \frac{4}{105} \sum_{\alpha\neq\beta\neq\gamma}^{x,y,z} \beta_{\beta\alpha\gamma}\beta_{\alpha\beta\gamma}
\end{aligned} \tag{2.129}$$

$$\begin{aligned}
\langle \beta_{jii}^2 \rangle = &+ \frac{1}{7} \sum_{\alpha}^{x,y,z} \beta_{\alpha\alpha\alpha}^2 + \frac{4}{105} \sum_{\alpha\neq\beta}^{x,y,z} \beta_{\alpha\alpha\beta}\beta_{\alpha\beta\beta} - \frac{2}{35} \sum_{\alpha\neq\beta}^{x,y,z} \beta_{\alpha\alpha\alpha}\beta_{\beta\beta\alpha} + \frac{8}{105} \sum_{\alpha\neq\beta}^{x,y,z} \beta_{\beta\alpha\alpha}^2 \\
&+ \frac{3}{35} \sum_{\alpha\neq\beta}^{x,y,z} \beta_{\alpha\beta\beta}^2 - \frac{2}{35} \sum_{\alpha\neq\beta\neq\gamma}^{x,y,z} \beta_{\alpha\alpha\beta}\beta_{\beta\alpha\alpha} + \frac{1}{35} \sum_{\alpha\neq\beta\neq\gamma}^{x,y,z} \beta_{\alpha\beta\beta}\beta_{\alpha\gamma\gamma} \\
&- \frac{2}{105} \sum_{\alpha\neq\beta\neq\gamma}^{x,y,z} \beta_{\alpha\alpha\beta}\beta_{\beta\beta\gamma} - \frac{2}{105} \sum_{\alpha\neq\beta\neq\gamma}^{x,y,z} \beta_{\alpha\alpha\beta}\beta_{\beta\gamma\gamma} + \frac{2}{35} \sum_{\alpha\neq\beta\neq\gamma}^{x,y,z} \beta_{\alpha\beta\gamma}^2 \\
&- \frac{2}{105} \sum_{\alpha\neq\beta\neq\gamma}^{x,y,z} \beta_{\alpha\beta\gamma}\beta_{\beta\alpha\gamma}.
\end{aligned} \tag{2.130}$$

In Equation 2.129 and 2.130 the molecular system is assumed to have the ground state dipole moment aligned along the positive z-axis.

2.5.6 Two-photon absorption

Two-photon absorption is formally obtained from the cubic response function, however, in the vicinity of two-photon resonance it is sufficient to use the single residue of the quadratic response function. The two-photon probability is then,[129,130]

$$\delta_{k0}^{\mathrm{TPA}} (\omega_1, \omega_2) = \mathbf{F}\delta_F (\omega_1, \omega_2) + \mathbf{G}\delta_G (\omega_1, \omega_2) + \mathbf{H}\delta_H (\omega_1, \omega_2), \tag{2.131}$$

where **F**, **G** and **H** are constants that depend on the polarization of the two photons and the geometrical setup of the measurement. The other three quantities, δ_F, δ_F and δ_F are

$$\delta_F (\omega_1, \omega_2) = S_{\alpha\alpha}^{k0} (\omega_1, \omega_2) S_{\beta\beta}^{k0,*} (\omega_1, \omega_2) \tag{2.132}$$

$$\delta_G (\omega_1, \omega_2) = S_{\alpha\beta}^{k0} (\omega_1, \omega_2) S_{\alpha\beta}^{k0,*} (\omega_1, \omega_2) \tag{2.133}$$

$$\delta_H (\omega_1, \omega_2) = S_{\alpha\beta}^{k0} (\omega_1, \omega_2) S_{\beta\alpha}^{k0,*} (\omega_1, \omega_2) \tag{2.134}$$

The two-photon tensor, $S_{\alpha\beta}$, can be obtained from Equation 2.100 when the electric dipole operator is used

$$S^{k0}_{\alpha\beta}\left(\omega_1,\omega_2\right)=\frac{1}{\hbar}\sum_m\left\{\frac{\langle\Psi_0|\hat{\mu}_\alpha|\Psi_m\rangle\langle\Psi_m|\hat{\mu}_\beta|\Psi_k\rangle}{\omega_{k0}-\omega_1}+\frac{\langle\Psi_0|\hat{\mu}_\beta|\Psi_m\rangle\langle\Psi_m|\hat{\mu}_\alpha|\Psi_k\rangle}{\omega_{k0}-\omega_2}\right\}. \tag{2.135}$$

With the condition that both photons are linearly polarized and have the same frequency, i.e., using a monochromatic light source one can express $S_{\alpha\beta}$ as

$$S^{k0}_{\alpha\beta}\left(\omega\right)=\frac{1}{\hbar}\sum_m\left\{\frac{\langle\Psi_0|\hat{\mu}_\alpha|\Psi_k\rangle\langle\Psi_k|\hat{\mu}_\beta|\Psi_m\rangle}{\omega_{m0}-\frac{1}{2}\omega}+\frac{\langle\Psi_0|\hat{\mu}_\beta|\Psi_k\rangle\langle\Psi_k|\hat{\mu}_\alpha|\Psi_m\rangle}{\omega_{m0}-\frac{1}{2}\omega}\right\}. \tag{2.136}$$

For this experimental setup, the coefficients are $\mathbf{F}=\mathbf{G}=\mathbf{H}=2$ and Equation 2.131 simplifies significantly,

$$\delta^{\mathrm{TPA}}_{k0}=-S^{k0}_{\alpha\alpha}S^{k0,*}_{\mu\mu}+3S_{\alpha\beta}S^{k0,*}_{\alpha\beta} \tag{2.137}$$

Equation 2.136 may be evaluated using the SOS expression, although many states are often needed to ensure convergence. When circularly polarized light is used, the coefficients depending on the experimental setup are listed in Table 2.4.

Table 2.4: Coefficients for experimental configurations reproduced from Ref. 131

Polarization		Propagation	F	G+H
1.	Two co-rotating circularly polarized	Parallel	-2	6
		Perpendicular	-1/4	13/4
2.	One circularly polarized;	Parallel	1/2	7/2
	one linear polarized in plane of circle	Perpendicular	1/2	7/2
3.	One circularly polarized;	Perpendicular	-1	3
	one linear polarized			
	perpendicular to plane of circle			

2.5.7 Two-photon circular dichroism

When the difference between left and right circularly polarized light is measured, i.e., in TPCD spectroscopy, with both photons being of equal frequency the difference is

$$\delta^{\mathrm{TP}}_{L}-\delta^{\mathrm{TP}}_{R}=\frac{4}{15}\frac{(2\pi)^2N_A\omega^2g(2\omega)}{c_0^3\left(4\pi\epsilon_0\right)^2}R^{\mathrm{TP}}(\omega) \tag{2.138}$$

with $g(2\omega)$, denotes a normalized line shape. is Avogadro's number, c_0 is the speed of light in vacuo and ϵ_0 is the vacuum permittivity. Here R^{TP} is the two-photon rotatory strength, analogous to the rotatory strength describing preferential absorption in ECD,[78]

$$ {}^{f}R^{\mathrm{TP}}_{\omega_0}(\omega) = -ib_1\mathcal{B}_1^{\omega_0}(\omega) + b_2\mathcal{B}_2^{\omega_0}(\omega) - ib_3\mathcal{B}_3^{\omega_0}(\omega). \tag{2.139} $$

Here, the superscript f denotes a transition from the ground state to an excited-state Ψ_f, b_1, b_2 and b_3 are coefficients depending on the polarization and propagation of light in the experimental setup analogous to **F**, **H** and **G** in Equation 2.131. The coefficients for various experimental setups are listed in Table 2.5.

TABLE 2.5: Coefficients for different experimental configurations reproduced from Ref. 131.

Polarization		Propagation	b_1	b_2	b_3
1.	Two left circularly polarized	Parallell	6	2	-2
		Antiparallell	1	-1	3
		Perpendicular	13/4	-1/4	-1/4
2.	One left circularly polarized; one linear polarized in plane of circle	Parallell	3	1	-1
		Antiparallell	1/2	-1/2	3/2
		Perpendicular	7/4	1/4	1/4
3.	One left circularly polarized; one linear polarized perpendicular to plane of circle	Perpendicular	3/2	-1/2	-1/2

The other three quantities, $\mathcal{B}_1^{\omega_0}$, $\mathcal{B}_2^{\omega_0}$ and $\mathcal{B}_3^{\omega_0}$, are analogous to the three terms constituting $\delta_{n0}^{\mathrm{TPA}}$ (2.132, 2.133 and 2.134), and are constructed as

$$ \mathcal{B}_1^{\omega_0}(\omega) = \sum_{\rho\sigma} M^{0f}_{\rho\sigma}(\omega) S^{f0^*}_{\rho\sigma}(\omega), \tag{2.140} $$

$$ \mathcal{B}_2^{\omega_0}(\omega) = \frac{\omega}{2}\sum_{\rho\sigma} Q^{0f}_{\rho\sigma}(\omega) S^{f0*}_{\rho\sigma}(\omega), \tag{2.141} $$

$$ \mathcal{B}_3^{\omega_0}(\omega) = \left[\sum_{\rho} M^{0f}_{\rho\rho}(\omega)\right]\left[\sum_{\sigma} S^{0f}_{\sigma\sigma}(\omega)\right], \tag{2.142} $$

where ω is the one-photon excitation energy and $\rho, \sigma \in x, y, z$. Here S, M and Q are the two-photon tensors corresponding to the electric dipole-electric dipole, electric dipole-magnetic dipole and electric dipole - electric quadrupole,

$$S^{0f}_{\alpha\beta}\left(\omega_\beta\right) = \frac{1}{\hbar}\mathcal{P}\sum_{n\neq 0}\frac{\langle\Psi_0|\,\hat{\mu}_\alpha\,|\Psi_n\rangle\,\langle\Psi_n|\,\hat{\mu}_\beta\,|\Psi_f\rangle}{\omega_\alpha-\omega_{0n}}, \tag{2.143}$$

$$M^{0f}_{\alpha\beta}\left(\omega_\beta\right) = \frac{1}{\hbar}\mathcal{P}\sum_{n\neq 0}\frac{\langle\Psi_0|\,\hat{\mu}_\alpha\,|\Psi_n\rangle\,\langle\Psi_n|\,\hat{m}_\beta\,|\Psi_f\rangle}{\omega_\alpha-\omega_{0n}}, \tag{2.144}$$

$$Q^{0f}_{\alpha\beta}\left(\omega_\beta\right) = \frac{1}{\hbar}\varepsilon_{\beta\gamma\delta}\mathcal{P}\sum_{n\neq 0}\frac{\langle\Psi_0|\,\hat{q}_{\alpha\gamma}\,|\Psi_n\rangle\,\langle\Psi_n|\,\hat{\mu}_\delta\,|\Psi_f\rangle}{\omega_\alpha-\omega_{0n}}, \tag{2.145}$$

where α and β are the spatial components $\alpha,\beta\in[x,y,z]$, $\epsilon_{\beta\gamma\delta}$ is the Levi-Cevitas tensor, $\mathcal{P}$ is the permutation operator acting on the operator-frequency pairs $(\mu_\alpha,\omega_\alpha)$ and (μ_β,ω_β) as described for Equation 2.92, μ_i is the electric transition dipole moment, m_i is the magnetic transition dipole moment and q_{ij} is the quadrupole transition dipole moment. Equation 2.139 can be described as the two-photon Rosenfeld equation in the length-gauge formalism and hence exhibit origin-dependence which arises solely from the $\mathcal{B}_1$ and $\mathcal{B}_3$ terms as the $\mathcal{B}_2$ term does not include the magnetic dipole operator and hence is already origin-independent.[78]

In the effort of obtaining origin-independent two-photon rotatory strengths, three velocity gauge formulations have been proposed named ω_1, ω_3, and the translationally invariant (TI)-equation. Only the ω_1 and ω_3 formulations are implemented in this work as they should yield the same values in the limit of a complete one-electron basis set and full-ADC. To arrive at the ω_1 and ω_3 formulations of the two-photon rotatory strength, one can use the commutator relationship between the position, momentum and Hamiltonian operator, Equation 2.108. However, this transformation can be applied either once or twice to $S_{\alpha\beta}$, both transformations will yield origin-invariant terms in the two-photon rotatory strengths. Applying it once is denoted $P_{\alpha\beta}$ and applying it twice is denoted $P^p_{\alpha\beta}$. Likewise, it can be applied to $M_{\alpha\beta}$ to produce $M^p_{\alpha\beta}$. Explicitly, one writes

$$S_{\alpha\beta} = \frac{1}{\hbar}\mathcal{P}\sum_{n\neq 0}\frac{\langle\Psi_0|\,\hat{\mu}_\alpha\,|\Psi_n\rangle\,\langle\Psi_n|\,\hat{\mu}_\beta\,|\Psi_f\rangle}{\omega_\alpha-\omega_{0n}} \longrightarrow P_{\alpha\beta} = \frac{1}{\hbar\omega}\mathcal{P}\sum_{n\neq 0}\frac{\langle\Psi_0|\,\hat{\mu}_\alpha\,|\Psi_n\rangle\,\langle\Psi_n|\,\hat{p}_\beta\,|\Psi_f\rangle}{\omega_\alpha-\omega_{0n}} \tag{2.146}$$

$$\longrightarrow \quad P^p_{\alpha\beta} = \frac{1}{\hbar\omega^2}\mathcal{P}\sum_{n\neq 0}\frac{\langle\Psi_0|\,\hat{p}_\alpha\,|\Psi_n\rangle\,\langle\Psi_n|\,\hat{p}_\beta\,|\Psi_f\rangle}{\omega_\alpha-\omega_{0n}} \tag{2.147}$$

$$M^{0f}_{\alpha\beta} = \frac{1}{\hbar}\mathcal{P}\sum_{n\neq 0}\frac{\langle\Psi_0|\,\hat{\mu}_\alpha\,|\Psi_n\rangle\,\langle\Psi_n|\,\hat{m}_\beta\,|\Psi_f\rangle}{\omega_\alpha-\omega_{0n}} \longrightarrow {M^p_{\alpha\beta}}^{0f} = \frac{1}{\hbar\omega}\mathcal{P}\sum_{n\neq 0}\frac{\langle\Psi_0|\,\hat{p}_\alpha\,|\Psi_n\rangle\,\langle\Psi_n|\,\hat{m}_\beta\,|\Psi_f\rangle}{\omega_\alpha-\omega_{0n}} \tag{2.148}$$

For the first transformation, one obtains the terms comprising the "ω_1" velocity-gauge two-photon rotatory strength

$$\mathcal{B}_1^{\omega_1}(\omega) = \frac{1}{\omega}\sum_{\rho\sigma} M_{\rho\sigma}^{0f}(\omega) P_{\rho\sigma}^{f0}(\omega), \tag{2.149}$$

$$\mathcal{B}_2^{\omega_1}(\omega) = \mathcal{B}_2^{\omega_0}(\omega) = \frac{\omega}{2}\sum_{\rho\sigma} Q_{\rho\sigma}^{0f}(\omega) S_{\rho\sigma}^{f0}(\omega), \tag{2.150}$$

$$\mathcal{B}_3^{\omega_1}(\omega) = \frac{1}{\omega}\left[\sum_{\rho} M_{\rho\rho}^{p,0f}(\omega)\right]\left[\sum_{\sigma} S_{\sigma\sigma}^{0f}(\omega)\right]. \tag{2.151}$$

Hence, the ω_1 formulation two-photon rotatory strength is thus

$$^{f}R_{\omega_1}^{\mathrm{TP}}(\omega) = b_1\mathcal{B}_1^{\omega_1}(\omega) + b_2\mathcal{B}_2^{\omega_1}(\omega) + b_3\mathcal{B}_3^{\omega_1}(\omega). \tag{2.152}$$

Applying the hypervirial theorem twice produces the terms comprising the "ω_3" velocity-gauge rotatory strength

$$\mathcal{B}_1^{\omega_3}(\omega) = \frac{1}{\omega^3}\sum_{\rho\sigma} M_{\rho\sigma}^{p,0f}(\omega) P_{\rho\sigma}^{p,f0^*}(\omega) \tag{2.153}$$

$$\mathcal{B}_2^{\omega_3}(\omega) = \mathcal{B}_2^{\omega_0}(\omega) = \frac{\omega}{2}\sum_{\rho\sigma} Q_{\rho\sigma}^{0f}(\omega) S_{\rho\sigma}^{f0^*}(\omega) \tag{2.154}$$

$$\mathcal{B}_3^{\omega_3}(\omega) = \frac{1}{\omega^3}\left[\sum_{\rho} M_{\rho\rho}^{p,0f}(\omega)\right]\left[\sum_{\sigma} P_{\sigma\sigma}^{p,0f}(\omega)\right] \tag{2.155}$$

hence the ω_3 formulation two-photon rotatory strength is

$$^{f}R_{\omega_3}^{\mathrm{TP}}(\omega) = -b_1\mathcal{B}_1^{\omega_3}(\omega) + b_2\mathcal{B}_2^{\omega_3}(\omega) - b_3\mathcal{B}_3^{\omega_3}(\omega) \tag{2.156}$$

For each of these transformations new energy prefactors appear in front of the $\mathcal{B}_1$ and $\mathcal{B}_3$ terms, which gives these formulations their names, ω_1 and ω_3, namely ω^{-1} and ω^{-3} dependencies.

Lastly, in the TI equation, the electric quadrupole operator is expressed in its velocity-gauge formulation as

$$T_{\alpha\beta}^{+} = \sum_{i}\frac{q_i}{m_i}\left(p_{i\alpha}r_{i\alpha} + r_{i\alpha}p_{i\alpha}\right), \tag{2.157}$$

and thus

$$\mathcal{T}_{\alpha\beta}^{+,0f}(\omega_\beta) = \frac{1}{\hbar}\varepsilon_{\beta\gamma\delta}\mathcal{P}\sum_{n\neq 0}\frac{\langle\Psi_0|\,\hat{T}_{\alpha\gamma}^{+}\,|\Psi_n\rangle\,\langle\Psi_n|\,\hat{p}_{\delta\beta}\,|\Psi_f\rangle}{\omega_\alpha - \omega_{0n}}. \tag{2.158}$$

Using this form for the electric quadrupole operator results in the following three terms comprising the TI two-photon rotatory strength

$$\mathcal{B}_1^{\mathrm{TI}}(\omega) = \mathcal{B}_1^{\omega_3} = \frac{1}{\omega^3} \sum_{\rho\sigma} M_{\rho\sigma}^{p,0f}(\omega) P_{\rho\sigma}^{p,f0^*}(\omega) \tag{2.159}$$

$$\mathcal{B}_2^{\mathrm{TI}}(\omega) = \frac{1}{2\omega^3} \sum_{\rho\sigma} \mathcal{T}_{\rho\sigma}^{+,0f}(\omega) P_{\rho\sigma}^{p,f0^*}(\omega) \tag{2.160}$$

$$\mathcal{B}_3^{\mathrm{TI}}(\omega) = \mathcal{B}_3^{\omega_3}(\omega) = \frac{1}{\omega^3} \left[\sum_{\rho} M_{\rho\rho}^{p,0f}(\omega) \right] \left[\sum_{\sigma} P_{\sigma\sigma}^{p,0f}(\omega) \right] \tag{2.161}$$

The benefit of the above approach is that each term has the same energy dependence, namely ω^{-3}. The resulting expression for the TI two-photon rotatory strength is thus

$$^{f}R^{\mathrm{TP}} = -b_1 \mathcal{B}_1^{\mathrm{TI}}(\omega) - b_2 \mathcal{B}_2^{\mathrm{TI}}(\omega) - b_3 \mathcal{B}_3^{\mathrm{TI}}(\omega). \tag{2.162}$$

To reiterate, these expressions are all equivalent for gauge-invariant methods in the limit of a complete one-electron basis set (COEBS), hence

$$-i\mathcal{B}_1^{\omega_0} \overset{\mathrm{COEBS}}{\equiv} \mathcal{B}_1^{\omega_1} \overset{\mathrm{COEBS}}{\equiv} -\mathcal{B}_1^{\omega_3} \overset{\mathrm{COEBS}}{\equiv} -\mathcal{B}_1^{\mathrm{TI}}, \tag{2.163}$$

$$\mathcal{B}_2^{\omega_0} \overset{\mathrm{COEBS}}{\equiv} \mathcal{B}_2^{\omega_1} \overset{\mathrm{COEBS}}{\equiv} \mathcal{B}_2^{\omega_3} \overset{\mathrm{COEBS}}{\equiv} -\mathcal{B}_2^{\mathrm{TI}}, \tag{2.164}$$

$$-i\mathcal{B}_3^{\omega_0} \overset{\mathrm{COEBS}}{\equiv} \mathcal{B}_3^{\omega_1} \overset{\mathrm{COEBS}}{\equiv} -\mathcal{B}_3^{\omega_3} \overset{\mathrm{COEBS}}{\equiv} -\mathcal{B}_3^{\mathrm{TI}} . \tag{2.165}$$

2.6 Algebraic-diagrammatic construction

The algebraic-diagrammatic construction (ADC) scheme provides a series of *ab initio* methods for the treatment of electronic vertically excited state (VES), combining diagonalization of a (Hermitian) secular matrix and a perturbation treatment for the matrix elements.[29,31,132? –136] It can be derived via Green's functions or propagator theory, where different propagators yield different properties, e.g., ionization potentials, electron affinities, or excitation energies. In the original derivation, ADC did not provide excited-state wave functions, but this deficiency was overcome with the development of the intermediate state representation (ISR), within which ADC may be viewed as a representation of the (shifted) Hamiltonian within a basis of explicitly constructable intermediate states (IS), giving direct access to excited-state wave functions and properties.[137] In the following sections, I will limit myself to the polarization propagator and the absorption of one or two photons.

2.6.1 ADC method

Within the ISR, excitation energies are evaluated by solving the secular equation of the shifted Hamiltonian ($\hat{H} - E_0$) within a basis of explicitly constructable intermediate-states (IS),

$$M_{IJ} = \left\langle \tilde{\Psi}_I \middle| \hat{H} - E_0 \middle| \tilde{\Psi}_J \right\rangle = \left\langle \tilde{\Psi}_I | \hat{H} | \tilde{\Psi}_J \right\rangle - E_0 \delta_{IJ}. \tag{2.166}$$

Finding solutions to this secular equation corresponds to solving an Hermitian eigenvalue equation

$$\mathbf{M}\mathbf{X} = \mathbf{X}\mathbf{\Omega}, \quad \mathbf{X}^\dagger \mathbf{X} = \mathbf{1}, \tag{2.167}$$

where $\mathbf{X}$ is a column matrix of eigenvectors X_k and Ω is a diagonal matrix of eigenvalues $\omega_k = E_k - E_0$. Ground- to excited-states transition moments are then obtained by contraction of the eigenvector $X_n^\dagger$ with an applied arbitrary operator $\hat{D}$,

$$x_n = \left\langle \Psi_n | \hat{D} | \Psi_0 \right\rangle = \mathbf{X}_n^\dagger \tilde{\mathbf{F}}(\hat{D}) = \mathbf{X}_n^\dagger \left\langle \tilde{\Psi}_I | \hat{D} | \Psi_0 \right\rangle \tag{2.168}$$

where $\tilde{\mathbf{F}}$ are so called "modified-transition moments". To construct the IS, one usually starts with so-called correlated-excited states (CES), which are obtained by applying a set of excitation operators on the exact ground state with the set of operators used depending on which propagator and hence property one desires

$$\left|\Psi_J^0\right\rangle = \hat{C}_J \left|\Psi_0\right\rangle \tag{2.169}$$

For n-particle, n-hole processes, i.e., single and double excitations etc

$$\{\hat{C}_J\} \equiv \left\{ \hat{c}_a^\dagger \hat{c}_k, \hat{c}_a^\dagger \hat{c}_b^\dagger \hat{c}_k \hat{c}_l, \ldots \right\} \qquad \text{Polarization propagator} \tag{2.170}$$

The ADC method then proceeds by replacing the exact ground state $|\Psi_0\rangle$ and its energy E_0 in a perturbation expansion,

$$|\Psi_0\rangle = \left|\Psi_0^{(0)}\right\rangle + \left|\Psi_0^{(1)}\right\rangle + \left|\Psi_0^{(2)}\right\rangle + \dots \tag{2.171}$$

$$E_0 = E_0^{(0)} + E_0^{(1)} + E_0^{(2)} + \dots \tag{2.172}$$

Using an MP partitioning of the Hamiltonian results in the zeroth-order wavefunction as the HF determinant. With this expansion of Ψ_0 and E_0, the ADC secular matrix $\mathbf{M}$ is likewise expanded in a series as

$$\mathbf{M} = \mathbf{M}^{(0)} + \mathbf{M}^{(1)} + \mathbf{M}^{(2)} + \dots \tag{2.173}$$

What results of the above expressions when including all terms up to the nth order is termed ADC(n) scheme. Moreover, when the excited-state wave function is expanded in the complete basis of IS, one can obtain excited-state wave functions and properties,

$$|\Psi_n\rangle = \sum_I |\tilde{\Psi}_I\rangle \langle\tilde{\Psi}_I \mid \Psi_n\rangle = \sum_I X_{I,n} |\tilde{\Psi}_I\rangle, \tag{2.174}$$

where $X_{I,n}$ are elements of the ADC eigenvector. Insertion of the above expansion (2.174) into the expression for the expectation value of an arbitrary operator yields the nth excited state expectation value of operator $\hat{D}$ as

$$D_n = \left\langle \Psi_n|\hat{D}|\Psi_n \right\rangle = \sum_{IJ} X_{I,n}^{*} \left\langle \tilde{\Psi}_I|\hat{D}|\tilde{\Psi}_J \right\rangle X_{J,n} = \mathbf{X}_n^{\dagger}\tilde{\mathbf{B}}\mathbf{X}_n \tag{2.175}$$

where $\tilde{B}_{IJ} = \left\langle \tilde{\Psi}_I|\hat{D}|\tilde{\Psi}_J \right\rangle$ is the matrix representation of operator $\hat{D}$ in the IS basis. Excited-state to excited-state transition moments can likewise then be obtained as

$$T_{mn} = \left\langle \Psi_m|\hat{D}|\Psi_n \right\rangle = \mathbf{X}_m^{\dagger}\tilde{\mathbf{B}}\mathbf{X}_n. \tag{2.176}$$

Next, one can decompose the matrix representation $\mathbf{B}$ of operator $\hat{D}$ in the IS basis into a ground-state and excited-state contribution

$$\tilde{B}_{IJ} = D_0\delta_{IJ} + B_{IJ} \tag{2.177}$$

where,

$$D_0 = \left\langle \Psi_0|\hat{D}|\Psi_0 \right\rangle \tag{2.178}$$

is the ground-state contribution and

$$B_{IJ} = \left\langle \tilde{\Psi}_I \middle| \hat{D} - D_0 \middle| \tilde{\Psi}_J \right\rangle \tag{2.179}$$

is the excited-state contribution, analogous to the ADC matrix. **B** can then expanded in a similar fashion to **M** as,

$$\mathbf{B} = \mathbf{B}^{(0)} + \mathbf{B}^{(1)} + \mathbf{B}^{(2)} + \ldots \tag{2.180}$$

by then writing the one-particle operator in second quantization, i.e. $\hat{D} = \sum_{pq} d_{pd} a_p^\dagger a_q^\dagger$, allows for the excited-state or state-to-state transition moments to be expressed in terms of state ρ_n and transition densities ρ_{mn} as

$$D_n = \left\langle \Psi_n | \hat{D} | \Psi_n \right\rangle = \sum_{pq} d_{pq} \sum_{IJ} X^*_{I,n} \left\langle \tilde{\Psi}_I \left| \hat{a}_p^\dagger \hat{a}_q \right| \tilde{\Psi}_J \right\rangle X_{J,n} = \sum_{pq} d_{pq} \rho_{n,pq} \tag{2.181}$$

$$T_{mn} = \left\langle \Psi_m | \hat{D} | \Psi_n \right\rangle = \sum_{pq} d_{pq} \sum_{IJ} X^*_{I,n} \left\langle \tilde{\Psi}_I \left| \hat{a}_p^\dagger \hat{a}_q \right| \tilde{\Psi}_J \right\rangle X_{J,m} = \sum_{pq} d_{pq} \rho_{mn,pq} \tag{2.182}$$

By choosing the nth order Møller-Plesset treatment of the wave function as the ground state yields nth order ADC(n) with MP2 yielding ADC(2) and so on.

Hence, ADC(1) consists of the eigenvectors of first-order **M** and **B**, ADC(2) consists of the eigenvectors of second-order **M** and **B**, consistent through order n. Another significant method is ADC(3)) which is not consistent through order n and uses the third-order **M** with the second-order **B**, which will for simplicity be referred to as ADC(3) in the coming chapters.[31,138]

2.6.2 Electronic circular dichroism

In the ADC/ISR approach, the exact states contained in the Rosenfeld equation (2.86) are replaced by the known IS states. The rotatory strength corresponding to an excitation from the ground state $|\Psi_0\rangle$ to an excited state $|\Psi_n\rangle$ is then expressed as

$$R^r_{n0} = \mathrm{Im}\left(\tilde{\mathbf{F}}^\dagger(\hat{\mu}) \mathbf{X}_n \mathbf{X}_n^\dagger \tilde{\mathbf{F}}(\hat{m})\right), \tag{2.183}$$

where $\tilde{\mathbf{F}}(\hat{\mu})$, and $\tilde{\mathbf{F}}(\hat{m})$, are the modified transition moments by the electric and magnetic dipole moment operators in the IS basis (2.168) and $\mathbf{X}_n$ is the eigenvector corresponding to state n. By using Equation 2.176, one similarly obtains an expression for the excited-state to excited-state rotatory strength as

$$R^r_{mn} = \mathrm{Im}\left(\mathbf{X}_n^\dagger \tilde{\mathbf{B}}(\hat{\mu}) \mathbf{X}_m \mathbf{X}_m^\dagger \tilde{\mathbf{B}}(\hat{m}) \mathbf{X}_n\right), \tag{2.184}$$

where $\tilde{\mathbf{B}}(\hat{\mu})$ and $\tilde{\mathbf{B}}(\hat{m})$ are the one-electron matrix representations of the electric and magnetic dipole operators in the IS basis. Hence, the ground state to excited-state and excited-state to excited-state rotatory strengths are computed as expectation values within the ISR formalism.[137] It is of course trivial to express the velocity-gauge representations of either of the two rotatory strengths as

$$R^\nabla_{n0} = \mathrm{Re}\left(\tilde{\mathbf{F}}^\dagger(\hat{p}) \mathbf{X}_n \mathbf{X}_n^\dagger \tilde{\mathbf{F}}(\hat{m})\right), \tag{2.185}$$

And, in an analogous manner,

$$R^\nabla_{mn} = \mathrm{Re}\left(\mathbf{X}_n^\dagger \tilde{\mathbf{B}}(\hat{p}) \mathbf{X}_m \mathbf{X}_m^\dagger \tilde{\mathbf{B}}(\hat{m}) \mathbf{X}_n\right), \tag{2.186}$$

2.6.3 Two-photon circular dichroism

The two-photon absorption cross-section within ADC/ISR has been derived from time-dependent response theory for exact states,[82,139] and the same methodology is applied in the derivation of two-photon circular dichroism.[78] Using quadratic response theory, the two-photon tensor of arbitrary operators $\hat{A}$ and $\hat{Z}$ can be expressed as,[82]

$$(\mathcal{A}\mathcal{Z})^{f}_{\alpha\beta} = \sum_{n\neq 0} \left(\frac{\left\langle \Psi_0 \middle| \hat{A}_\alpha \middle| \Psi_n \right\rangle \left\langle \Psi_n \middle| \overline{\hat{Z}}_\beta \middle| \Psi_f \right\rangle}{\omega_n - \omega_1} + \frac{\left\langle \Psi_0 \middle| \hat{Z}_\beta \middle| \Psi_n \right\rangle \left\langle \Psi_n \middle| \overline{\hat{A}}_\mu \middle| \Psi_f \right\rangle}{\omega_n - \omega_2} \right), \tag{2.187}$$

where the subscripts denote spatial components, i.e., $\alpha, \beta \in [x, y, z]$ and $\mathcal{A}$ and $\mathcal{B}$ here denote general operators, but are in the of TPA both electric dipole operators. Here and in the following, the short-hand notations

$$\overline{\hat{A}}_\alpha = \hat{A}_\alpha - \left\langle \Psi_0 \middle| \hat{A}_\alpha \middle| \Psi_0 \right\rangle, \tag{2.188}$$

$$\overline{\hat{Z}}_\alpha = \hat{Z}_\alpha - \left\langle \Psi_0 \middle| \hat{Z}_\alpha \middle| \Psi_0 \right\rangle, \tag{2.189}$$

are used for the $\hat{A}$ and $\hat{Z}$ operators shifted by their exact ground state expectation values. Furthermore, by using Equation 2.168 and 2.176 for the modified transition moments and matrix representation of operator $\hat{A}$ and $\hat{Z}$ in the IS basis, the secular ADC matrix $\mathbf{M}$ as well as the eigenvector $\mathbf{X}_f$ one can write Equation 2.187 in matrix notation within the ADC/ISR as[140]

$$(\mathcal{A}\mathcal{Z})^{f}_{\alpha\beta} = \tilde{\mathbf{F}}^\dagger(\hat{A}_\alpha)\left(\mathbf{M} - \omega_1 \mathbf{1}\right)^{-1} \tilde{\mathbf{B}}(\overline{\hat{Z}}_\beta)\mathbf{X}_f + \tilde{\mathbf{F}}^\dagger(\hat{Z}_\beta)\left(\mathbf{M} - \omega_2 \mathbf{1}\right)^{-1} \tilde{\mathbf{B}}(\overline{\hat{A}}_\alpha)\mathbf{X}_f. \tag{2.190}$$

With these notations, one can express the S, M, Q, M^p, P and P^p two-photon tensors within the ADC/ISR formalism. Using $\mathcal{D}$, $\mathcal{M}$, $\mathcal{Q}$ and $\mathcal{P}$ for the electric, magnetic, quadrupole and momentum dipole operators, respectively, all three formulations (2.139), (2.152) and (2.156) of the two-photon rotatory strength may be expressed as

$$ {}^{f}R^{\mathrm{TP}}_{\omega_0} = \sum_{\alpha,\beta} \Big(- i b_1 (\mathcal{D}\mathcal{M})^{f}_{\alpha\beta} (\mathcal{D}\mathcal{D})^{f*}_{\alpha\beta} + \frac{b_2\omega_n}{2} (\mathcal{Q}\mathcal{D})^{f}_{\alpha\beta} (\mathcal{D}\mathcal{D})^{f*}_{\alpha\beta} - i b_3 (\mathcal{D}\mathcal{M})^{f}_{\alpha\alpha} (\mathcal{D}\mathcal{D})^{f*}_{\beta\beta} \Big), \tag{2.191}$$

$$ {}^{f}R^{\mathrm{TP}}_{\omega_1} = \sum_{\alpha,\beta} \Big(+ \frac{b_1}{\omega_n} (\mathcal{D}\mathcal{M})^{f}_{\alpha\beta} (\mathcal{D}\mathcal{P})^{f*}_{\alpha\beta} + \frac{b_2\omega_n}{2} (\mathcal{Q}\mathcal{D})^{f}_{\alpha\beta} (\mathcal{D}\mathcal{D})^{f*}_{\alpha\beta} + \frac{b_3}{\omega_n} (\mathcal{P}\mathcal{M})^{f}_{\alpha\alpha} (\mathcal{D}\mathcal{D})^{f*}_{\beta\beta} \Big), \tag{2.192}$$

$$ {}^{f}R^{\mathrm{TP}}_{\omega_3} = \sum_{\alpha,\beta} \Big(- \frac{b_1}{\omega_n^3} (\mathcal{P}\mathcal{M})^{f}_{\alpha\beta} (\mathcal{P}\mathcal{P})^{f*}_{\alpha\beta} + \frac{b_2\omega_n}{2} (\mathcal{Q}\mathcal{D})^{f}_{\alpha\beta} (\mathcal{D}\mathcal{D})^{f*}_{\alpha\beta} - \frac{b_3}{\omega_n^3} (\mathcal{P}\mathcal{M})^{f}_{\alpha\alpha} (\mathcal{P}\mathcal{P})^{f*}_{\beta\beta} \Big). \tag{2.193}$$

The above equations describe the two-photon rotatory strength corresponding to an excitation from the ground state $|\Psi_0\rangle$ to an excited state $|\Psi_f\rangle$. All three formulations of the two-photon rotatory strengths may be calculated using their SOS expression and calculated at ADC(n) level in an identical fashion to SOS-TPA,[141] although this approach is not computationally tractable for large systems where many states may be required to achieve numerically convergent results, as explained in previous sections.

2.6.4 First-order hyperpolarizability and second harmonic generation

In this section, expressions for the linear electric dipole polarizability and the first-order electric dipole hyperpolarizability with the ADC/ISR formalism are derived. Subsequently, the isotropic dynamic first-order hyperpolarizability using frequency relations applicable for SHG and HRS are presented.

Linear polarizability within the ADC/ISR formalism

The electric dipole polarizability, Equation 2.92 and 2.103, can be expressed within the ADC/ISR formalism using Equation 2.168 for the modified transition moments of the electric dipole operator, as well as the inverse of the secular ADC matrix $\mathbf{M}$ at frequency ω, $(\mathbf{M}-\omega)^{-1}$,[142]

$$\alpha_{\alpha\beta}(-\omega;\omega) = \mathcal{P}\Big(\tilde{\mathbf{F}}^{\dagger}(\hat{\mu}_{\alpha})(\mathbf{M}-\mathbf{1}\omega)^{-1}\tilde{\mathbf{F}}(\hat{\mu}_{\beta})\Big). \tag{2.194}$$

Here, $\mathcal{P}$, permutes the $(\mu_\alpha,-\omega)$ and (μ_β,ω) pairs such that,

$$\alpha_{\alpha\beta}(-\omega;\omega) = \tilde{\mathbf{F}}^{\dagger}(\hat{\mu}_{\alpha})(\mathbf{M}-\mathbf{1}\omega)^{-1}\tilde{\mathbf{F}}(\hat{\mu}_{\beta}) + \tilde{\mathbf{F}}^{\dagger}(\hat{\mu}_{\beta})(\mathbf{M}+\mathbf{1}\omega)^{-1}\tilde{\mathbf{F}}^{\dagger}(\hat{\mu}_{\alpha})\ . \tag{2.195}$$

Evident from Equation 2.194, is that the eigenvectors corresponding to the nth excited states, are not explicitly required and that once $\tilde{\mathbf{F}}(\hat{\mu}_\alpha)$ and $(\mathbf{M}-\mathbf{1}\omega)^{-1}$ are known a solution is obtained by simple matrix-vector multiplication. These are solved for by a projection algorithm as will be described in the next section.

First-order hyperpolarizability within the ADC/ISR formalism

The first-order electric dipole hyperpolarizability, Equation 2.120 and 2.99, can be expressed within the ADC/ISR formalism using Equation 2.168 for the modified transition moments and Equation 2.176 for the matrix representation of μ in the IS basis, as well as the inverse of the secular ADC matrix $\mathbf{M}$ at frequency ω,

$$\beta_{\alpha\beta\gamma}(-\omega_\sigma;\omega_1,\omega_2) = \mathcal{P}\left(\tilde{\mathbf{F}}^{\dagger}(\hat{\mu}_{\alpha})(\mathrm{M}-\mathbf{1}\omega_\sigma)^{-1}\tilde{\mathbf{B}}(\mu_{\beta})(\mathrm{M}-\mathbf{1}\omega_2)^{-1}\tilde{\mathbf{F}}^{\dagger}(\hat{\mu}_{\gamma})\right). \tag{2.196}$$

Here, $\mathcal{P}$, permutes the $(\mu_\alpha,-\omega_\sigma)$, (μ_β,ω_1) and (μ_γ,ω_2) pairs, in an identical manner to the same operator in Equation 2.194. The above equation is the general non-damped first-order electric dipole hyperpolarizability, which describes all the processes in Table 2.3. However, specifically in the case of SHG, the frequency relation[143]

$$2\omega_1 = 2\omega_2 = \omega_\sigma = 2\omega, \tag{2.197}$$

applies, which allows for simplifications with the $\beta^{\mathrm{SHG}}_{\alpha\beta\gamma}$ -tensor expressed as

$$\beta^{\mathrm{SHG}}_{\alpha\beta\gamma}(-2\omega;\omega,\omega) = \mathcal{P}\left(\tilde{\mathbf{F}}^{\dagger}(\hat{\mu}_{\alpha})(\mathrm{M}-\mathbf{2}\omega)^{-1}\tilde{\mathbf{B}}^{(}\mu_{\beta})(\mathrm{M}-\mathbf{1}\omega)^{-1}\tilde{\mathbf{F}}(\hat{\mu}_{\gamma})\right). \tag{2.198}$$

While in principle, all the elements contained in Equation 2.198 are known. The inverse, $(\mathbf{M}{\pm}\omega)^{-1}$, is often too large to be solved for directly. Instead, one may introduce the response vector, $\mathbf{y}_\alpha^{-\omega}$

$$\boldsymbol{y}_\alpha^{-\omega} = \tilde{\mathbf{F}}^\dagger(\hat{\mu}_\alpha)(\mathbf{M} - \omega\mathbf{1})^{-1}, \tag{2.199}$$

which after rearrangement,

$$\boldsymbol{y}_\alpha^{-\omega}(\mathbf{M} - \omega\mathbf{1}) = \tilde{\mathbf{F}}^\dagger(\hat{\mu}_\alpha), \tag{2.200}$$

can be solved for using a projection algorithm, e.g., DIIS. In this case, 12 equations are required to obtain the full $\beta^{\mathrm{SHG}}_{\alpha\beta\gamma}$-tensor, which, when calculated allows for the tensor to be expressed as

$$\beta^{\mathrm{SHG}}_{\alpha\beta\gamma}(-2\omega;\omega,\omega) = \mathcal{P}\Bigg(\ \boldsymbol{y}_\alpha^{-2\omega}\tilde{\mathbf{B}}^\dagger(\mu_\beta)\boldsymbol{y}_\gamma^{-\omega}\Bigg). \tag{2.201}$$

Which is solved for by matrix-vector multiplications, once $\mathbf{y}_\alpha$ are obtained.

Chapter 3

Electronic circular dichroism

This chapter will cover electronic circular dichroism (ECD) implemented at ADC(n) levels of theory. Here, the origin dependence of the length formulation is compared with those at CC levels of theory for methyloxirane. Next, the computed rotatory strengths at ADC(2) and ADC(3) levels of theory are compared to those at CC2 and CCSD levels for enantiomers of methyloxirane, methylthiirane and their dimethylated counterparts, as well as for H_2O_2 and H_2S_2. The inclusion of solvent effects on the rotatory strengths is evaluated for L-epinephrine at the ADC(2) level using the polarizable continuum model (PCM). Lastly, the ECD spectra of an camphor, norcamphor and fenchone enantiomer is analyzed at ADC(2) and ADC(3) level of theory and compared to their experimental gas-phase ECD spectra. This chapter has already been published as Mikael Scott, Dirk R. Rehn, Sonia Coriani, Patrick Norman, and Andreas Dreuw. "Electronic circular dichroism spectra using the algebraic diagrammatic construction schemes of the polarization propagator up to third order", The Journal of Chemical Physics, 154(6):064107,2021.

3.1 Introduction

ECD is among the oldest techniques for determining the absolute configuration of chiral molecules,[32] exploiting the differential absorption of one of the two circularly polarized components of plane polarized light (Figure 2.2), resulting in a rotation of the plane of polarization, commonly measured in units of molecular ellipticity. Among the many uses, ECD has found particular employment in the detection of secondary structures of proteins,[144] as well as in pharmaceutical synthesis as a quality control tool to measure enantiomeric purity.[37] Of central importance is the sign of the measured ECD signal where enantiomers produce mirror-like ECD spectra and can thus be easily distinguished. Not only chiral molecules produce ECD spectra, non-chiral molecules interacting with a chiral system, e.g., a solvent can give rise to a CD signal through a processed referred to as induced circular dichroism (ICD). ICD thus provides information about the absolute configuration of the chiral structure be it an achiral solvent arranging itself in a structurally chiral manner or a chiral solvent doing the same.[145] The experimental setup for measuring an ECD spectrum is almost identical to a standard UV/VIS measurement with the only significant addition of a polarizer to produce left- and right-handed circularly polarized light. The measurement is then carried out twice, using only one of the two handedness each time. The difference between these two signals then define the measured ECD (commonly CD) signal at a specific wavelength ω,

$$\Delta\epsilon(\omega) = \epsilon_{\mathrm{L}}(\omega) - \epsilon_{\mathrm{R}}(\omega), \tag{3.1}$$

with $\epsilon(\omega)$ being the molar absorption coefficients and the two subscripts denoting left or right circularly polarized light. After measurement, the signal may then be related to the rotatory strength, R, by integration over a frequency range as

$$R = 22.97 \times \int_{\omega_1}^{\omega_2} \frac{\Delta\epsilon(\omega)}{\omega} d\omega, \tag{3.2}$$

where the photon energy ω is in eV and $\Delta\epsilon(\omega)$ is given in L mol^{-1} cm^{-1}. The rotatory strength, R, is in units of 10^{-40} esu · cm · erg/G or 10^{-40} c.g.s. units.[112,146] This quantity was first derived in 1929 by Rosenfeld as the scalar product of the electric and magnetic transition dipole moments (see Section 2.4.2).[147] The selection rules for ECD are obtained by simple inspection of Equation 2.86. Here, the rotatory strength is only nonzero for both electric and magnetic dipole allowed transitions, where at least one component of the transition moments overlap. This only occurs when the molecular system lacks a principal axis of rotation, hence for chiral systems, as shown in Figure 3.1. Furthermore, as is readily apparent when comparing Equation 3.2 to Equation 2.86, Equation 3.2 assumes that the signal arises from an isolated state. This is obviously rarely the case and cannot be known *a priori* before measurement.

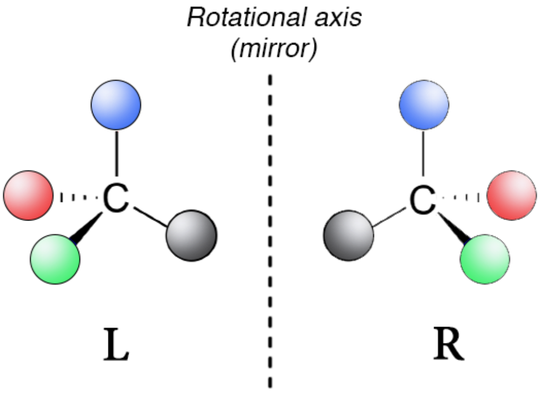

FIGURE 3.1: Chiral systems lack any principal axis of rotation and their mirror images are not superimposable.

On a theoretical level, ECD spectra have been calculated for molecules on the order of hundreds of atoms, using TD-HF[44–46] and TD-DFT[47–51], for molecules on the order of tens of electrons, CI[52] and LR based on a CASSCF reference[53] and EOM-CC[54,55] and the similar CC-LR approach[56–59] have been used.For very large systems, e.g. proteins, semi-empirical methods have also been used which can predict low-lying CD signals.

For this novel ADC(n) implementation, however, it makes most sense to compare calculated rotatory strengths directly to experiment and CC methods (coupled cluster singles (CCS), coupled cluster singles and approximate doubles (CC2), CCSD, coupled cluster singles, doubles and approximate triples (CC3)) due to the similar scaling and *ab initio* of these methods compared with the hierarchy of ADC(n) methods.

To test the robustness of the ADC(n) methods in simulating ECD spectra, methyloxirane and methylthiirane as well as their dimethylated derivatives represent excellent systems. For these molecules, highly resolved gas-phase spectra exist for comparison. Furthermore, the inherently chiral hydrogen peroxide H_2O_2 and dihydrogen disulfide H_2S_2 are likewise highly suitable due to their small size and well studied chiro-optical properties. Beside these relatively small molecules, camphor, norcamphor and fenchone constitute additional test cases whose chiroptical properties have been explored in previous work,[148–152] but have not yet been explored using a third order *ab initio* method. Furthermore, epinephrine, a common medical drug and hormone,[153] for which there are aqueous ECD solution spectra reported is likewise an excellent test case to include the effects of a solvent.[154] Thus, the ECC spectra of these molecules, Figure 3.2, will be presented in the coming sections.

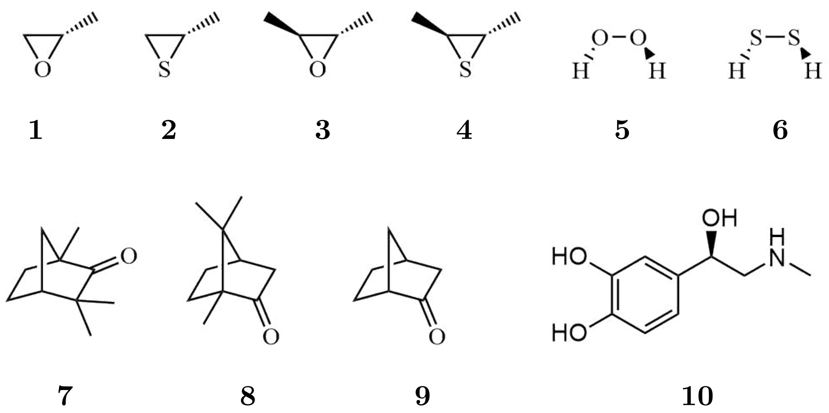

FIGURE 3.2: Chemical sketches of **1** (R)-methyloxirane, **2** (R)-methylthiirane, **3** (R,R)-dimethyloxirane, **4** (R,R)-dimethylthiirane, **5** hydrogen peroxide, **6** hydrogen persulfide, **7** (1R)-camphor, **8** (1R)-fenchone, **9** (1R)-norcamphor and **10** L-epinephrine.

3.2 Computational details

The length and velocity gauge rotatory strengths at ADC(n) levels have been implemented in a development version of Q-Chem 5.2,[155] as described in Section 2.6.2. For the length and velocity gauge rotatory strengths at CC level, Dalton2018 was used.[156] Dunning basis sets were employed throughout this chapter.[157–160] The origin for the position operator was set to the hetero atom for the oxiranes, thiiranes, camphor and its derivatives and to one of the oxygen/sulfur atoms in the symmetrical H_2O_2 and H_2S_2 molecules. Geometries of methyloxirane, dimethyloxirane, methylthiirane and dimethylthiirane were optimized using MP2/aug-cc-pVTZ and those of and at MP2/d-aug-cc-pVTZ level. For camphor, norcamphor and fenchone, DFT/CAM-B3LYP/aug-cc-pVTZ[161] was used for the geometry optimization. To simulate the ECD spectra, the rotatory strengths were converted from a.u. to 10^{-40} c.g.s. using the conversion factor of 471.44 and subsequently broadened by a Lorentzian function according to

$$\Delta\epsilon(\omega) = \sum_n \Delta\epsilon_n \frac{\gamma_n}{(\omega - \omega_{n0})^2 + \gamma_n^2} \tag{3.3}$$

$$\Delta\epsilon_n = \frac{\omega R_{n0}}{22.94\pi} \times 10^{40}, \tag{3.4}$$

where $\Delta\epsilon_n$ is the peak intensity of the nth transition given in L mol $^{-1}$ cm^{-1}, R_{n0} is the rotatory strength in 10^{-40} c.g.s., γ_n is the Lorentzian broadening factor, ω and ω_{n0} are the incident optical frequency and excitation energy in eV. The broadening factor corresponding to full width at half maximum full width at half maximum (FWHM) of $\gamma_n = 1000$ cm^{-1} is used for all spectra.[162]

3.3 Origin-dependence of length gauge rotatory strengths

As described in subsection 2.5.4, the calculated length gauge rotatory strengths (2.111), in approximate theories exhibit *unphysical* origin-dependence. Specifically, a translation of the gauge-origin of the position operator will alter the calculated rotatory strength. While Full-ADC is origin-independent, truncated ADC schemes are not, and hence will yield different rotatory and oscillator strengths in the length- and velocity gauges, which is of the order $\mathcal{O}(n)$ for ADC(n).[30]

To visualize the impact a shift in origin has on the calculated rotatory strengths in the length gauge, Figure 3.3 shows the ECD spectra of R-methyloxirane where the molecule is shifted along the spatial coordinate diagonal. Initially, the oxygen atom of R-methyloxirane is placed at the origin $\mathbf{O}_a = (0, 0, 0)$ and the entire molecule is subsequently shifted to a new origin $\mathbf{O}_b = (10, 10, 10)$ (in units of Å); through 20 uniformly spaced steps.

Evidently, Figure 3.3 clearly demonstrates the origin-dependence of Equation 2.111 while Equation 2.114 is inherently origin-independent at each of the ADC and CC levels of theory, as expected. For the specific case of R-methyloxirane, using the aug-cc-pVTZ basis set, length-gauge rotatory strengths computed using ADC(1) are less impacted than those at CCS level when subjected to a shift in origin with the latter producing a noticeable sign reversal of the energetically lowest band structure. Although, the direction of change is consistent between both methods, the magnitude is more prominent in case of CCS. At ADC(2) and CC2 levels, a similar behaviour is noted between, with the direction of change being identical for both methods. ADC(3) yields larger alterations in the computed length-gauge rotatory strengths with a shift in origin as compared to CCSD. This is likely due to the overall larger rotatory strengths of the *gauge 1* spectrum at ADC(3) compared to CCSD as well as the qualitatively different results of both methods. Using the center of charge as origin of the position operator produces near identical spectra for the two gauges which is consistent in all methods.

Furthermore, the transition moments of the electric, magnetic and momentum dipole for the lowest energetic excited state are collected in Table 3.1, where the same translation is performed, up until a distance of $(20, 20, 20)$ Å; in 20 uniform steps.

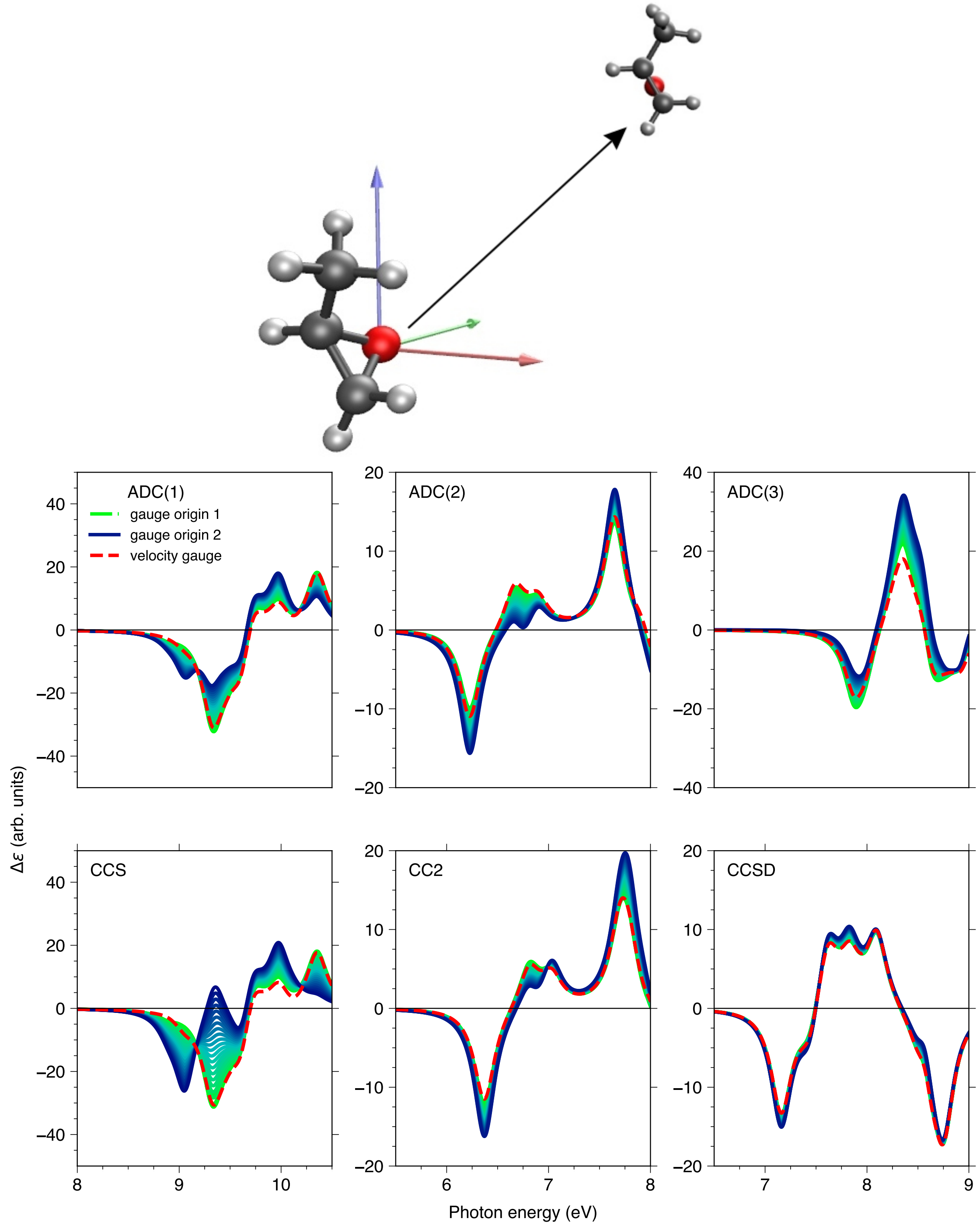

FIGURE 3.3: Simulated ECD spectra, with a shift in origin, of *R*-methyloxirane at ADC and coupled cluster (CC) levels of theory using the aug-cc-pVTZ basis set. The oxygen atom of methyloxirane is placed at $\mathbf{O}_1 = (0,0,0)$ (*gauge origin 1*) and subsequently moved to $\mathbf{O}_b = (10,10,10)$ (*gauge origin 2*) with each line creating the color-gradient is one uniform step of 0.5 Å in the direction of $\mathbf{O}_b$.

Table 3.1: Transition moment components of *R*-methyloxirane at ADC(2)/aug-cc-pVDZ level of theory for the energetically lowest singlet excited state. The molecule is shifted from $\mathbf{O}_0 = (0,0,0) \rightarrow \mathbf{O}_{20} = (20,20,20)$ Å.

$\mathbf{O}_n$	$\vec{\mu}_{10}(\times 10)$ a.u.			$\omega_{10}^{-1}\vec{p}_{10}(\times 10)$ a.u.			$\vec{L}_{10}(\times 10)$ a.u.		
n	x	y	z	x	y	z	x	y	z
0	·	·	·	·	·	·	2.9	2.6	1.5
2	·	·	·	·	·	·	0.6	1.9	4.5
4	·	·	·	·	·	·	−1.6	1.1	7.5
6	·	·	·	·	·	·	−3.9	0.3	10.6
8	·	·	·	·	·	·	−6.1	−0.4	13.6
10	−2.2	0.9	−1.6	−2.5	1.0	−1.6	−8.4	−1.2	16.6
12	·	·	·	·	·	·	−10.6	−2.0	19.6
14	·	·	·	·	·	·	−12.9	−2.7	22.6
16	·	·	·	·	·	·	−15.1	−3.5	25.6
18	·	·	·	·	·	·	−17.4	−4.3	28.6
20	·	·	·	·	·	·	−19.6	−5.0	31.7

$\mathbf{O}_n$	$R^{r}_{10}(\times 100)$ a.u.				$R^{\nabla}_{10}(\times 100)$ a.u.			
n	x	y	z	$\sum$	x	y	z	$\sum$
0	−6.4	2.5	−2.5	−6.4	−7.2	2.6	−2.5	·
2	−1.4	1.8	−7.4	−7.1	−1.5	1.8	−7.3	·
4	3.6	1.0	−12.4	−7.7	4.1	1.1	−12.2	·
6	8.7	0.3	−17.4	−8.4	9.7	0.3	−17.1	·
8	13.7	−0.4	−22.3	−9.0	15.3	−0.4	−22.0	·
10	18.7	−1.1	−27.3	−9.7	21.0	−1.2	−26.9	−7.0
12	23.7	−1.8	−32.2	−10.4	26.6	−1.9	−31.7	·
14	28.7	−2.6	−37.2	−11.0	32.2	−2.7	−36.6	·
16	33.7	−3.3	−42.2	−11.7	37.9	−3.4	−41.5	·
18	38.8	−4.0	−47.1	−12.4	43.5	−4.2	−46.4	·
20	43.8	−4.7	−52.1	−13.0	49.1	−4.9	−51.3	·

3.4 ADC and CC level rotatory strengths compared to experiment

In this section, ADC(1), ADC(2), ADC(3) will be compared directly to CCS, CC2 and CCSD, as well as CC3 when possible, in their respective ability to reproduce experimental gas-phase ECD spectra of small organic molecules.

3.4.1 ***R*-Methyloxirane and *R*-methylthiirane**

Methyloxirane, a 3-membered ring structure, is commonly used to benchmark theoretical methods in their ability to simulate ECD spectra, primarily due to its small size and readily available experimental gas-phase ECD spectrum,[163–165] as well as its well-studied electronic structure,[166] excited state properties and solution spectrum.[167–171] The importance of diffuse functions in describing the electronic structure of methyloxirane especially for the assignment of the sign of the rotatory strength has been demonstrated by other authors.[172] Furthermore Pople basis sets seem inadequate even with diffuse functions, while Dunning basis sets provide a more qualitative description.[48] Consequently, the dependence of different correlation-consistent basis sets on the calculated rotatory strengths will be assessed for *R*-methyloxirane in the following section.

Basis set impact on ***R*-methyloxirane.**

The excitation energies, length and velocity gauge rotatory strengths of *R*-methyloxirane calculated at ADC(2), ADC(3), CC2 and CCSD levels of theory are collected in Figure 3.4 - 3.5. For some large basis sets, only ADC(2) was calculated due to the computational effort required by the higher-order methods. Starting with ADC(2) and CC2, with the smallest basis of the cc-pVXZ series (X: D,T,Q), cc-pVDZ, yields nearly identical excitation energies for ADC(2) and CC2, with the first vertically excited state calculated at 8.24 eV at ADC(2) and 8.35 eV at CC2 level, which should be compared with the experimental value of 7.08 eV.[164] Increasing the basis set size from

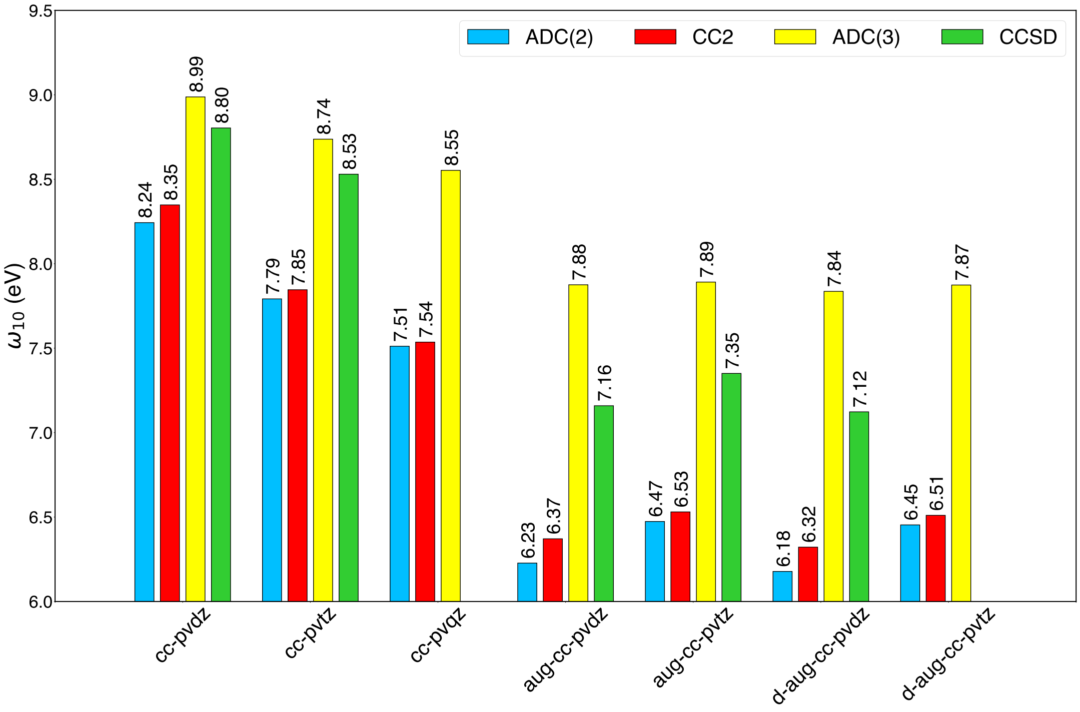

FIGURE 3.4: Excitation energies (eV) of the energetically lowest singlet electronic transition of *R*-methyloxirane calculated at the ADC(2), ADC(3), CC2 and CCSD levels of theory using Dunning basis sets.

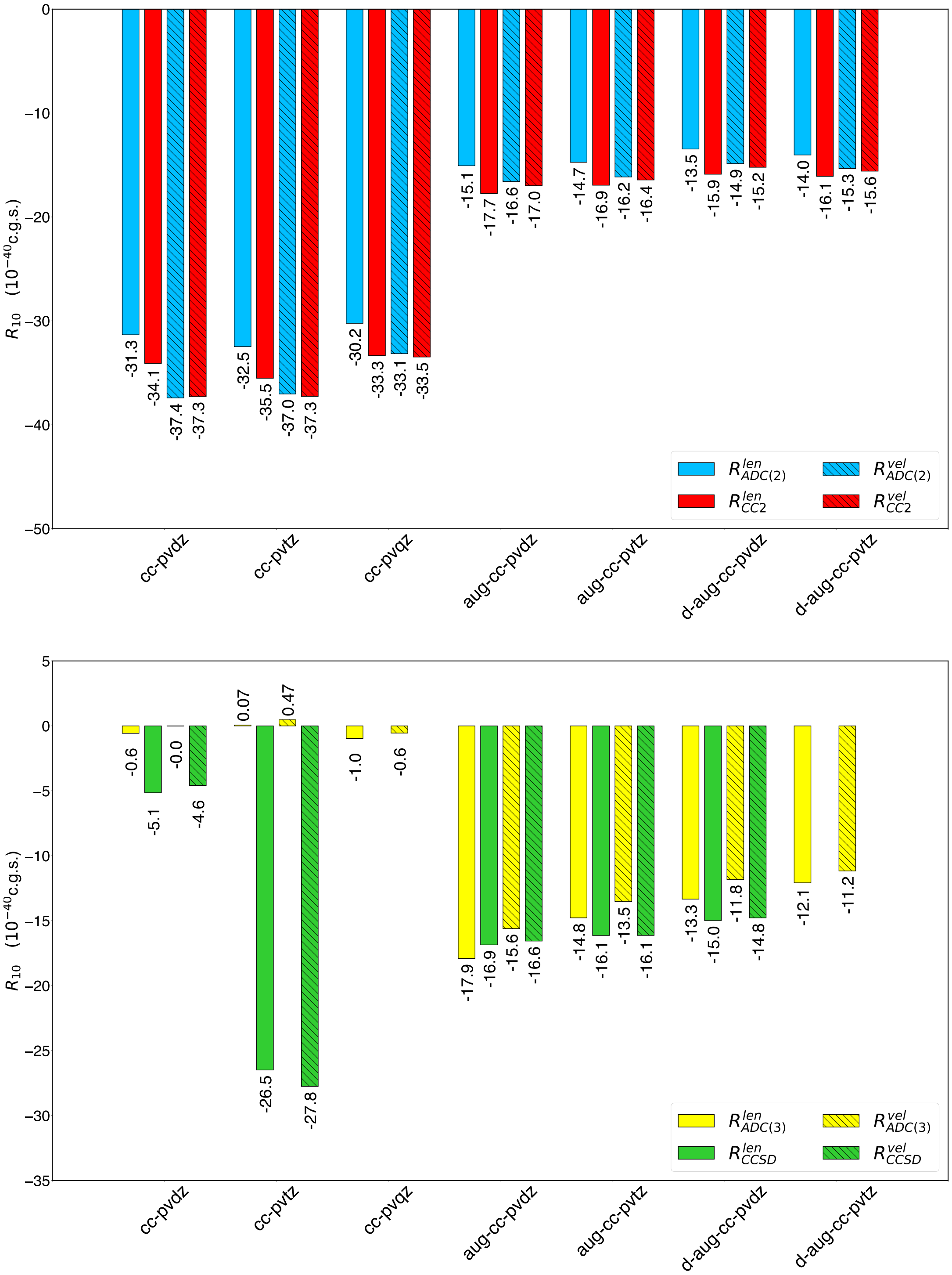

FIGURE 3.5: Rotatory strengths ($\times 10^{-40}$esu^2·cm^2) of the energetically lowest singlet electronic transition of R-methyloxirane calculated at the ADC(2), ADC(3), CC2 and CCSD levels of theory in length and velocity gauges using Dunning basis sets.

double to quadruple-zeta lowers the excitation energy to 7.51 eV and 7.54 eV for ADC(2) and CC2, respectively. However, the rotatory strength of the first transition is largely unaffected and is roughly overestimated by a factor of two compared to experiment. In this regard, one could counter that the reported rotatory strength in Ref. 164 is based on Equation 3.2 with the limits of integration determined by a low-level CI calculation which likely introduced errors. In general, careful analysis is always required when comparing computed and experimental rotatory strengths.

Turning to the singly-augmented, aug-cc-pVXZ series (X: D,T), aug-cc-pVDZ yields similar excitation energies for the first vertically excited state at ADC(2) and CC2 level, with 6.23 eV and 6.37 eV, respectively. Increasing the basis from double to triple-zeta improves the excitation energies, name 6.52 eV and 6.55 eV for ADC(2) and CC2, respectively. Evidently, the rotatory strengths are much more sensitive to augmentation of the basis set than the excitation energies. The rotatory strength of the first transition is within 20% of experiment, for aug-cc-pVDZ, and within 15% for aug-cc-pVTZ, which is overestimated by roughly 100% using non-augmented basis sets.

Moving to the doubly augmented d-aug-cc-pVXZ series (X: D,T), the rotatory strength of the first excited state is within 10% of experiment for both ADC(2) and CC2 using d-aug-cc-pVDZ, but the excitation energy (< 0.04 eV) is hardly affected. Going to d-aug-cc-pVTZ, the rotatory strength is largely unaffected while the excitation energy is increased as was the case for the singly augmented aug-cc-pVTZ basis. Moreover, double augmentation has substantial impact on the rotatory strengths of higher-lying excited states. For cc-pVXZ and aug-cc-pVXZ basis sets, the second vertically excited state has an incorrect positive sign of the rotatory strength at ADC(2) and CC2 levels of theory but is correctly described as negative using d-aug-cc-pVXZ basis sets. Higher-order methods like ADC(3), CCSD or CC3 reproduce the correct sign regardless of which basis set is employed. This illustrates the importance of diffuse functions, as well as the degree of electron correlation included for the correct assignment of higher excited states.

Overall, the differences between the length and velocity gauge rotatory strengths are relatively small for the first electronic transition, i.e. on the order of $\sim 20 \leftrightarrow 10\%$ for cc-pVXZ, $\sim 10 \leftrightarrow 8\%$ for the aug-cc-pVXZ, and $\sim 10 \leftrightarrow 7\%$ for d-aug-cc-pVXZ at ADC(2) and CC2 levels of theory. The difference is on the same order of magnitude for energetically higher-lying excited states with minor exceptions. The difference between the length and velocity forms of the oscillator strength is very similar to the one observed for the rotatory strengths.

Electronic circular dichroism spectra of *R*-methyloxirane.

The experimental gas-phase ECD spectrum of *R*-methyloxirane consists of three distinct band features, here labelled **A**, **B** and **C**.[164] The simulated ECD and UV/VIS spectra of *R*-methyloxirane at ADC and CC levels of theory using the d-aug-cc-pVDZ basis set comprising the energetically lowest 15 singlet excited states are shown in Figure 3.6. Numerical values for the excitation energies, oscillator and rotatory strengths are collected in Table A.1-A.2. At ADC(2) and CC2 levels of theory, similar spectra are produced, which are shifted to correspond to the experimental value of 7.10 eV for the energetically lowest band feature, **A**. The shifts required are +0.92 eV for ADC(2) and +0.78 eV for CC2, respectively. The **A** and **B**-bands of the experimental spectrum are well reproduced at the ADC(2) and CC2 levels of theory (Figure 3.6). Furthermore, at these

(a) ADC spectra of R-methyloxirane

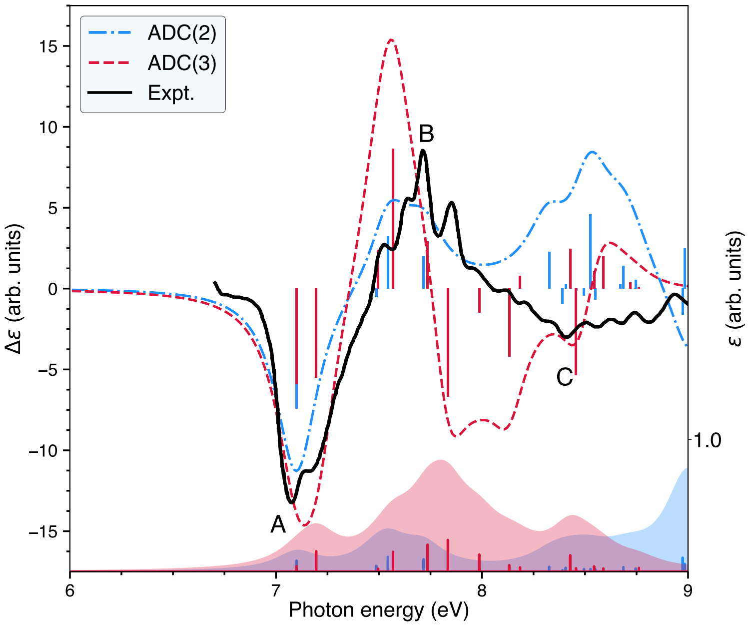

(b) CC spectra of R-methyloxirane

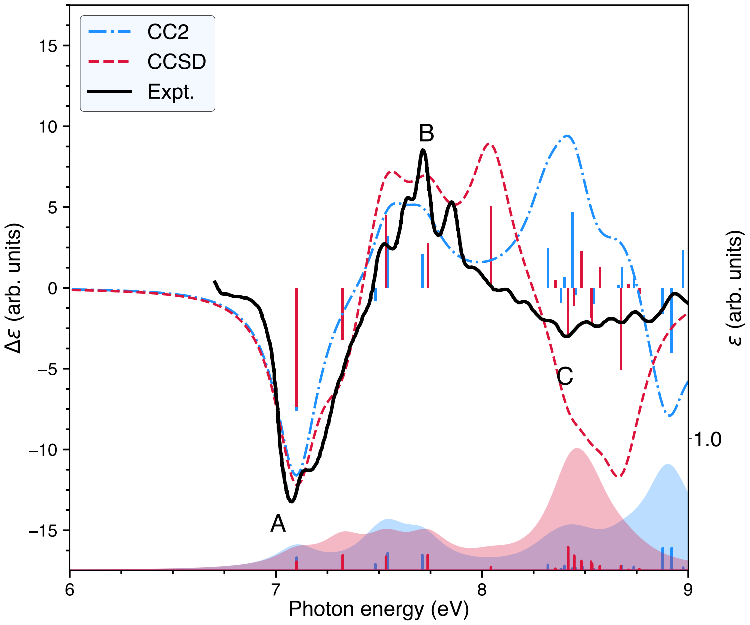

FIGURE 3.6: ECD (*top*) and UV/VIS (*bottom*) spectra of *R*-methyloxirane calculated with ADC(2), ADC(3), CC2 and CCSD in the velocity gauge using the d-aug-cc-pVDZ basis set. The spectra are shifted by +0.92 eV and −0.74 eV for ADC(2) and ADC(3), respectively, as well as +0.78 eV and −0.02 eV for CC2 and CCSD, respectively. The rotatory strength is scaled by a factor of 0.5. Experimental data (*black line*) are taken from Ref. 164.

levels of theory, **A-C** arise from oxygen lone-pair excitations to Rydberg orbitals. According to these calculations, the **A**-band is a convolution of two states of negative amplitude, and the **B**-band is a convolution of three states with an overall positive amplitude. Lastly, the **C**-band corresponds to a convolution of three states and is incorrectly predicted as positive by both methods.

The spectra calculated at ADC(3) and CCSD levels of theory are again shifted by -0.74 eV and -0.02 eV, respectively, for the first vertical excitation energy to match the experimental value. At these levels of theory, in addition to the **A** and **B**-bands being reproduced, the **C**-band is now correctly predicted as negative albeit red-shifted by ~ 0.5 eV for ADC(3).

Electronic circular dichroism spectra of *R*-methylthiirane.

Methylthiirane is the sulfur containing analog of methyloxirane for which high-quality experimental ECD gas-phase spectrum has been measured,[164,165] as well as experimental vibrational circular dichroism (VCD)[173] and Raman optical activity (ROA)[174] spectra. The ECD spectrum and the optical rotatory dispersion have also been addressed in theoretical studies.[175,176] The simulated ECD and UV/VIS spectra of *R*-methylthiirane at ADC and CC levels of theory using the d-aug-cc-pVDZ basis set comprising the energetically lowest 15 singlet excited states are shown in Figure 3.7. Numerical values for the excitation energies, oscillator and rotatory strengths are collected in Table A.3-A.4.

The experimental ECD spectrum of methylthiirane possesses three distinct band features, labelled **A**, **B** and **C** in analogy to methyloxirane. Using the d-aug-cc-pVDZ basis set, ADC(2) and CC2 yield very similar transition energies and rotatory strengths for the energetically lowest 15 computed states computed. All excited states correspond to electronic transitions from sulfur lone pair orbitals into Rydberg orbitals. ADC(2) and CC2 yield ECD spectra correctly predicting the signs of the **A**, **B** and **C**-bands. The excitation energies are red-shifted by roughly 0.4 eV in comparison to experiment. The first peak arises from a weakly absorbing state with a negative rotatory strength, which has also been experimentally observed but was not shown in the experimental spectrum as it was barely visible. The first significant feature of the experimental spectrum, the **A**-band, is a convolution of two peaks which are correctly predicted as negative but the amplitude is underestimated by a factor of two at these levels of theory. The **B** and **C**-bands correspond to convolutions of multiple states, the signs of which are correctly predicted using ADC(2) and CC2.

Proceeding to ADC(3), the excitation energies require no shift to align with the experimental spectrum and transition amplitudes likewise agree very well. The two electronic states constituting the spectral feature **A**, a_1 and a_2, lie within $\sim$0.02 eV of the experimental spectrum at the ADC(3) level, but, the rotatory strengths of these states appear to be swapped compared to experiment. Although, it cannot be excluded that these arise from vibrational effects. The improvement is of equal quality for CC2→CCSD, although slightly red-shifted compared to experiment. The **B**-band consist of four vibronic peaks in the experimental spectrum. At ADC(3) level two excited electronic states are computed exhibiting the correct excitation energies and signs of their corresponding rotatory strengths. The **C**-band is a convolution of several peaks in the experimental spectrum, and is incorrectly described as negative by at both ADC(3) and CCSD levels of theory.

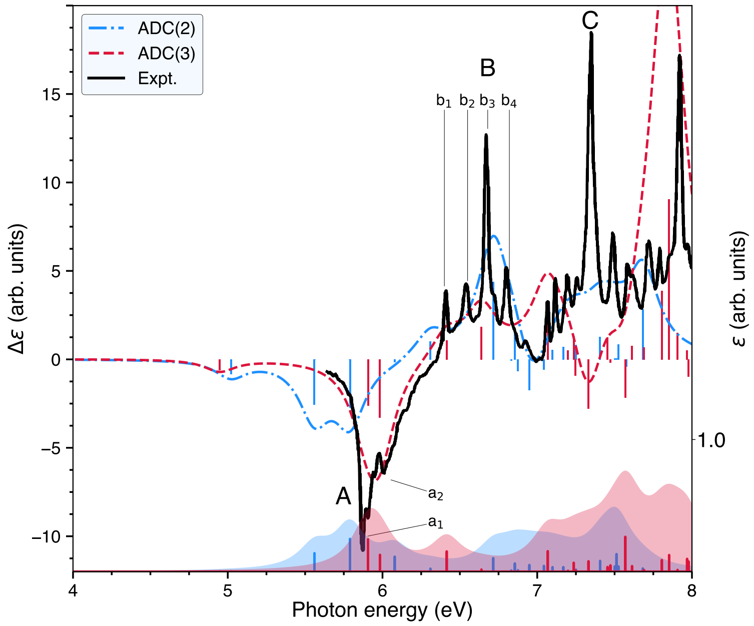
(a) ADC spectra of R-methylthiirane

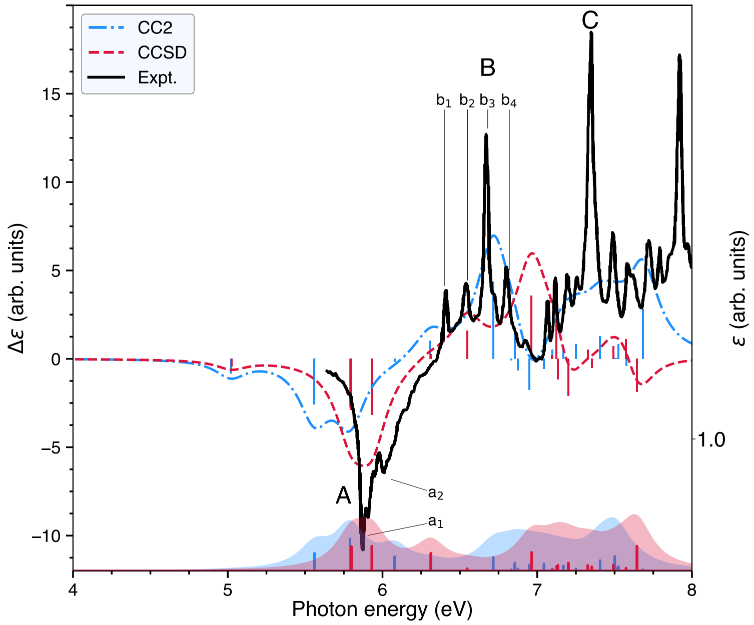
(b) CC spectra of R-methylthiirane

FIGURE 3.7: ECD (top) and UV/VIS (*bottom*) spectra of *R*-methylthiirane calculated with ADC(2), ADC(3), CC2, CCSD in the velocity gauge, using d-aug-cc-pVDZ. The rotatory strength is scaled by a factor of 0.5. Experimental data (*black line*) are taken from Ref. 164.

3.4.2 (*R*,*R*)-Dimethyloxirane and (*R*,*R*)-dimethylthiirane

As was the case for *R*-methyloxirane and *R*-methylthiirane, their dimethylated counterparts also have high-quality experimental gas phase ECD spectra recorded[164,165] which, unsurprisingly, show similar band features as those of methyloxirane and methylthiirane.

Electronic circular dichroism spectra of (*R*,*R*)-dimethyloxirane.

The simulated ECD and UV/VIS spectra of *R*-methylthiirane at ADC and CC levels of theory using the d-aug-cc-pVDZ basis set comprising the energetically lowest 15 singlet excited states are shown in Figure 3.8. Numerical values for the excitation energies, oscillator and rotatory strengths are collected in Table A.5-A.6. The experimental gas-phase ECD spectrum consists of four distinct band features, here labelled **A**, **B**, **C** and **D**. At the ADC(2) and CC2 levels of theory, similar spectra are produced for the energetically lowest 15 states, with the ADC(2) excitation energies red-shifted by $\sim 0.15 - 0.20$ eV compared to CC2. Both spectra in Figure 3.8 are shifted to correspond to the experimentally measured lowest singlet excited state at 7.0 eV (+0.92 eV for ADC(2) and +0.78 eV for CC2). At these levels of theory, the **A** to **D**-bands arise exclusively from lone-pair orbital excitations from the oxygen atom into Rydberg orbitals. The **A**-band arise solely from the energetically lowest transition with the excitation energy being red-shifted by $\sim$ 0.8 eV compared to experiment, and calculated to 6.08 eV and 6.22 eV for ADC(2) and CC2, respectively. The rotatory strength of this transition is in reasonable agreement with experiment, although it is roughly overestimated by 40% for both ADC(2) and CC2. The **B**-band, at ADC(2) and CC2 levels stems from the second excited state for which the excitation energy is calculated to 6.38 eV and 6.53 eV for ADC(2) and CC2, respectively, with both methods being red-shifted by $\sim$ 0.9 eV compared to experiment. The rotatory strength of this transition is overestimated by one order of magnitude. The third band, **C**, arises from a convolution of the third and fourth excited states, which are red-shifted by roughly 1 eV for both ADC(2) and CC2, compared to experiment. The **D**-band emerges from the fifth and sixth excited states, which are again red-shifted by roughly 1.1 eV.

The spectra of the higher order methods are likewise shifted to correspond to experiment (−0.81 eV for ADC(3) and −0.07 eV for CCSD). At ADC(3) level, the **A**-band arises from two states with negative rotatory strengths, separated by 0.10 eV. These peaks appear in good agreement with the experimental ECD spectrum, however, it is noteworthy that other studies have assigned these peaks to vibronic structures originating from up to two electronic states.[177] Furthermore, these two peaks are not reproduced in the CCSD spectrum which, alike ADC(2) and CC2, shows the **A**-band arising from a single excited electronic state whose width closely agrees with the experimental one. At ADC(3) level of theory, the **B**-band is a convolution of the third and fourth excited states with the former being sharply positive and latter negative. This results in a relatively weak positive feature, in reasonably good agreement with the measured spectrum. A similar convolution is observed at CCSD level, however, involving the second and third excited state. The larger energetic separation between these two states at CCSD level results in a more intensely positive **B**-band.The **C**-band is likewise a convolution of many states at ADC(3) level resulting in broad positive band, which is not present in the experimental spectrum, followed by a blue-shifted negative peak. CCSD correctly predicts the overall negative shape of the **C**-band which is originating from the fourth and fifth excited states, and clearly is in better agreement with experiment than at ADC(3) level. The **D**-band is correctly predicted as positive for both ADC(3) (arising from the tenth state) and CCSD (a convolution of many states).

(a) ADC spectra of (R,R)-dimethyloxirane

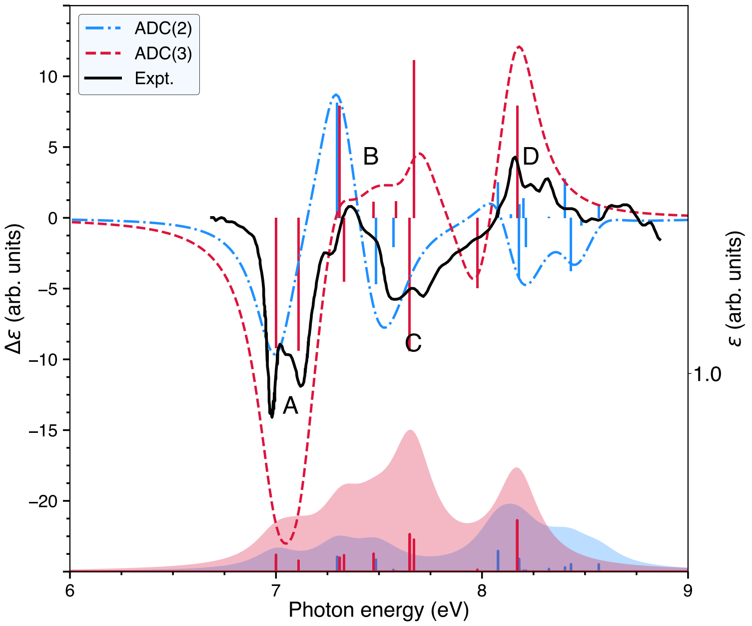

(b) CC spectra of (R,R)-dimethyloxirane

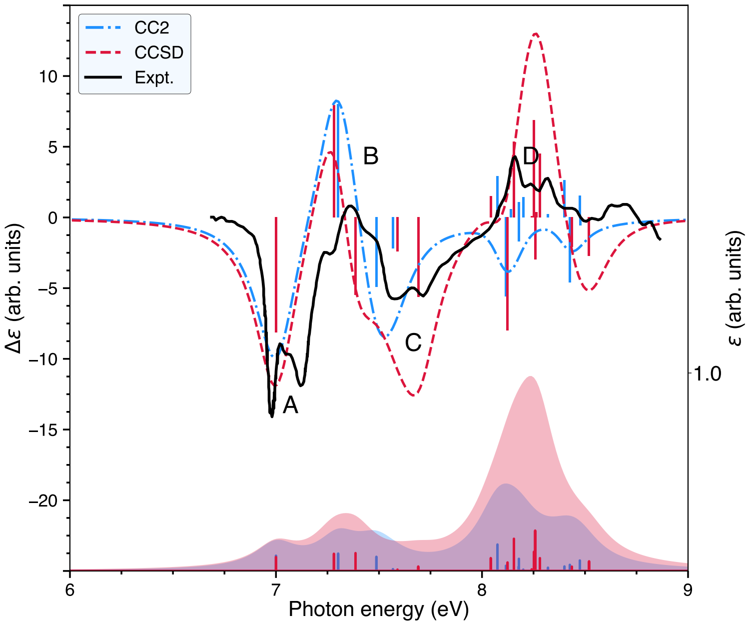

Figure 3.8: ECD (top) and UV/VIS (*bottom*) spectra of (*R*,*R*)-dimethyloxirane calculated with ADC(2), ADC(3), CC2 and CCSD in the velocity gauge using the d-aug-cc-pVDZ basis set. The spectra are shifted by +0.92 eV and −0.81 eV for ADC(2) and ADC(3), respectively, as well as +0.78 eV and −0.07 eV for CC2 and CCSD, respectively. The rotatory strength is scaled by a factor of 0.5. Experimental data (*black line*) for dimethyloxirane are taken from Ref. 164.

Electronic circular dichroism spectra of (*R*,*R*)-dimethylthiirane.

The simulated ECD and UV/VIS spectra of *(R,R)*-dimethylthiirane at ADC and CC levels of theory using the d-aug-cc-pVDZ basis set comprising the energetically lowest 15 singlet excited states are shown in Figure 3.9. Numerical values for the excitation energies, oscillator and rotatory strengths are collected in Table A.7-A.8) Three main band features, here labeled **A**, **B** and **C** are

(a) ADC spectra of (R,R)-dimethylthiirane

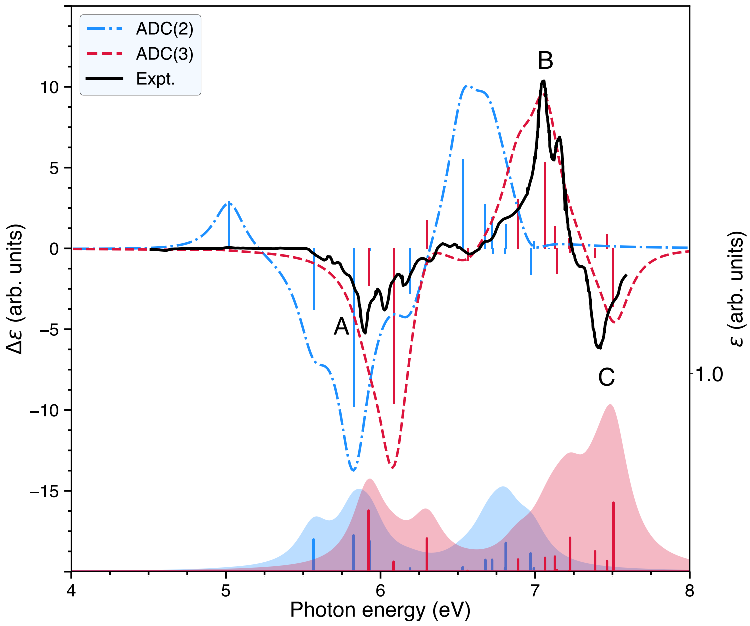

(b) CC spectra of (R,R)-dimethylthiirane

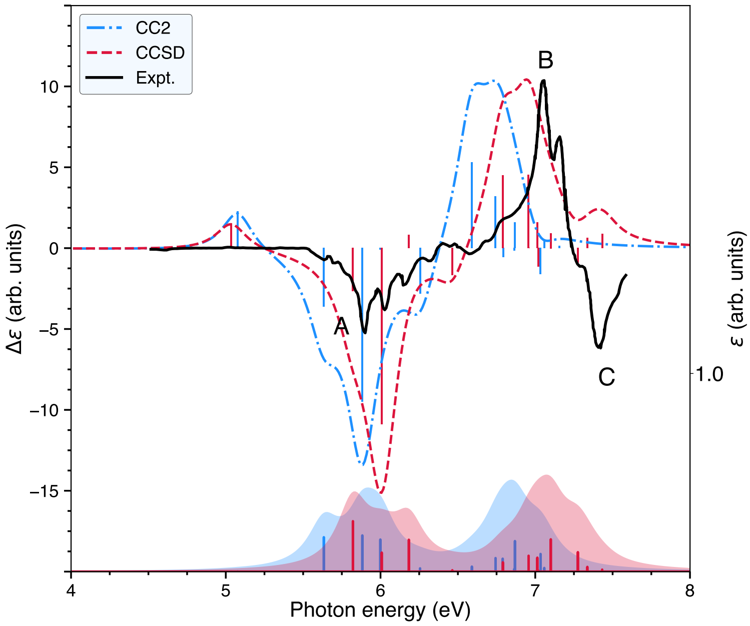

FIGURE 3.9: ECD (*top*) and UV/VIS (*bottom*) spectra in of (R,R)-dimethylthiirane calculated with ADC(2), ADC(3), CC2, CCSD in the velocity gauge using the d-aug-cc-pVDZ basis set. The spectra are shifted by +0.5 eV. The rotatory strength is scaled by a factor of 0.5. Experimental data (*black line*) are taken from Ref. 178

evident in the experimental gas-phase ECD spectrum of (R,R)-dimethylthiirane. These bands are again characterised by lone-pair excitations into Rydberg orbitals by both ADC(2) and CC2.

The spectra at ADC(2) and CC2 level are shifted (by +0.5 eV for each) to correspond to the experimentally measured lowest excited state at 4.5 eV.

The first rotatory strength exhibits an error of more than an order of magnitude, namely 5.7 ($\times 10^{-40}$ c.g.s.) and 4.3 ($\times 10^{-40}$ c.g.s.) for ADC(2) and CC2, respectively, compared to the experimental value of 0.1 ($\times 10^{-40}$ c.g.s.).[178] However, this is a weakly active state and as such experimental limitations may also play a role.

The energetically lowest feature, the **A**-band, is a convolution of the second to fifth excited states at the respective levels of theory. The **B**-band is a convolution of the sixth to eighth excited state, and the **C**-band arises from higher-lying excited states above the eighth state. It is interesting to recognize that the calculated spectra at ADC(2) and CC2 levels could be mistaken as that of a red-shifted (S,S)-dimethylthiirane, however, this is not the case for the higher order methods.

At the ADC(3) and CCSD levels of theory the lowest excitation energy remains mostly unaltered at 4.97 eV and 5.04 eV, respectively. For this transition, ADC(3) yields a rotatory strength of similar magnitude to that of the experiment, deviating by only $\sim$10%, however, the same transition is still overestimated by an order of magnitude using CCSD. For the **A**-**C** bands of the experimental spectrum, excellent agreement is achieved at ADC(3) level of theory with the **A**-band being overestimated by a factor of two. Notably, the last band feature, **C**, is correctly predicted as negative at ADC(3) level resulting from a convolution of several excited states but incorrectly predicted as positive using CCSD. For CCSD, however, more excited states may be needed to correctly reproduce this spectral region.

3.4.3 H_2O_2 and H_2S_2

Due to the small size and complex electronic structure, H_2O_2 and H_2S_2 have been the subject of benchmark calculations for various methods.[51,179,180] Previous studies have for instance shown that the optical rotatory strength depends heavily on the dihedral angle of H_2S_2 which has been studied at the CIS level of theory. Here, it was also shown that H_2S_2 has degenerate excited states at a dihedral angle of $\sim 90°$ which are poorly described using a HF wavefunction. Later work evaluated the performance of various density functionals in comparison to MRCI and CC2 calculations.[181] For both H_2O_2 and H_2S_2, CC3 and ADC(3) serve as the reference methods from which the spectral bands features are identified due to the lack of experimental reference spectra.

Electronic circular dichroism spectra of H_2O_2.

The simulated ECD and UV/VIS spectra of H_2O_2 at ADC and CC levels of theory using the d-aug-cc-pVTZ basis set comprising the energetically lowest 15 singlet excited states are shown in Figure 3.10. Numerical values for the excitation energies, oscillator and rotatory strengths are collected in Table A.9-A.10) Five distinct band features, labeled **A**, **B**, **C**, **D** and **E** are observed at ADC(3) and CC3 levels of theory all of which correspond to lone-pair excitations into Rydberg orbitals.

(a) ADC spectra of H_2O_2

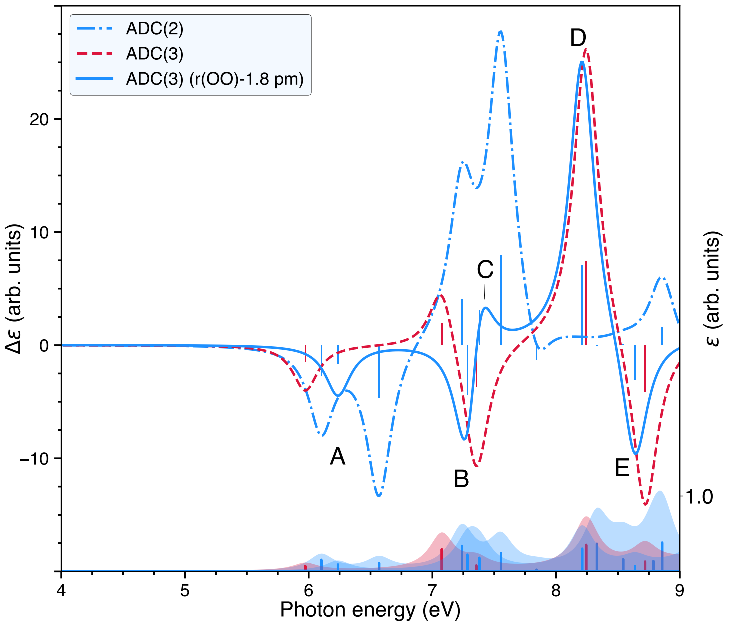

(b) CC spectra of H_2O_2

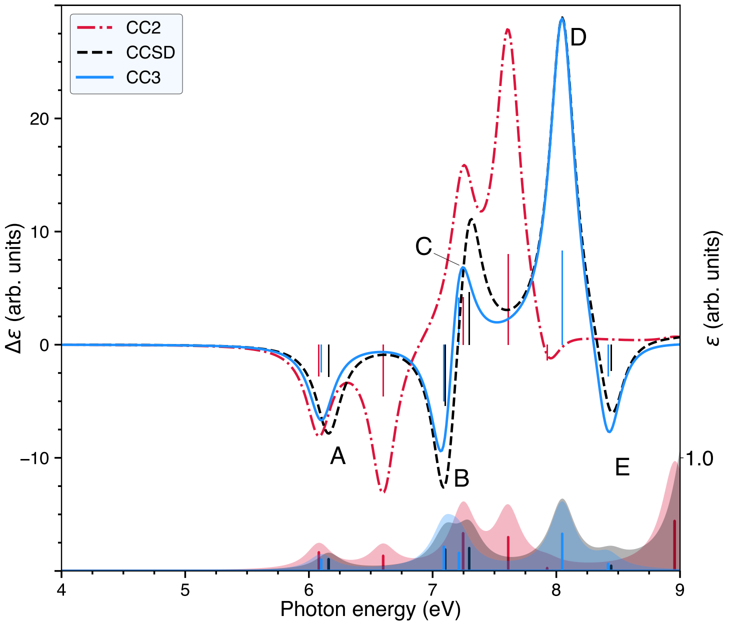

FIGURE 3.10: ECD (*top*) and UV/VIS (*bottom*) spectra of at ADC(2), ADC(3) (a), CC2, CCSD and CC3 (b) in the velocity gauge using the aug-cc-pVTZ basis set for CC3 and d-aug-cc-pVTZ for all others. The O-O bond has been contracted by 1.8 pm in (a) (*green line*).

At ADC(2) and CC2 levels, similar ECD spectra for the energetically lowest 15 singlet states are apparent. At these levels, the **A**-band arises from the first electronic excited state with the excitation energy and rotatory strengths calculated to within 0.03 eV and ∼ 15% of the corresponding CC3 values. The **B**-band arises from the second excited state and agrees well between both ADC(2) and CC2, however the spectra are red-shifted by ∼ 0.5 eV compared to

CC3. The rotatory strengths of this band at these levels of theory agree to within ∼ 10% with respect to CC3.The **C**-band stems from the third excited state with ADC(2) and CC2 yielding blue-shifted (∼ 0.04 eV) transition energies and rotatory strengths to within ∼10% to those at CC3 level. However, due to the larger energetic gap between the third and fourth excited state at the CC3 level, the **C**-band is overestimated by a factor of two at ADC(2) and CC2 levels. The **D**-band corresponds to the fourth excited state where ADC(2) and CC2 yield red-shifted transition energies (0.4 eV) with rotational strengths calculated to within ∼10% compared to CC3 level. Lastly, the **E**-band is caused by the fifth excitation and is red-shifted by ∼ 0.5 eV with rotatory strengths underestimated by ∼50% and ∼30% for ADC(2) and CC2, respectively, as compared with CC3. Noticeably, the **E**-band could be mistakenly interpreted as positive at the ADC(2) and CC2 levels due to the sixth excitation.

At ADC(3), CCSD and CC3 levels, the first excited state which comprises the **A**-band has

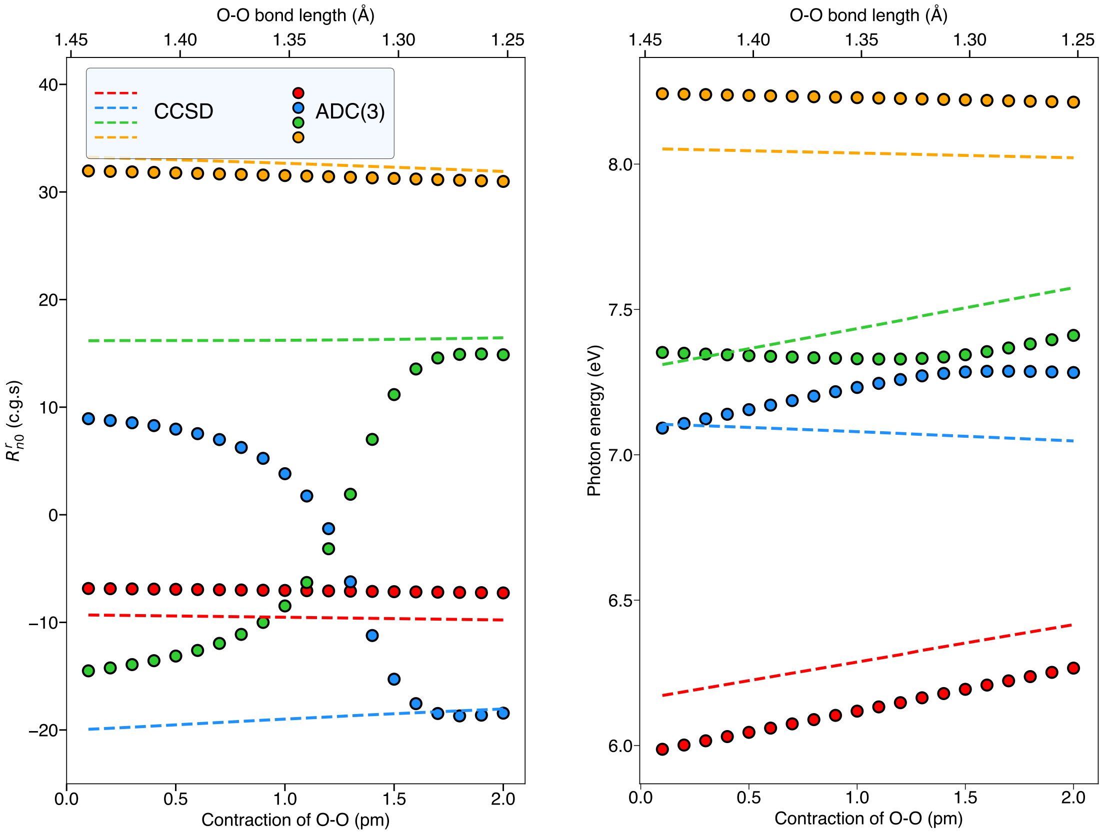

FIGURE 3.11: The four energetically lowest rotatory strengths of H_2O_2 calculated at the ADC(3) and CCSD levels of theory using the aug-cc-pVTZ basis set with a contraction of the O-O bond length.

an excitation energy of 5.95 eV, 6.14 eV and 6.08 eV, respectively. The **B**-band at ADC(3) and CCSD levels are blue-shifted by 0.5 eV, compared to ADC(2) and CC2. Conspicuously, at ADC(3) level, the sign of the transition is positive, whereas at CCSD and CC3 level the same band is negative. This sign-reversal can be explained by the sensitive dependence of the rotatory strength on structural parameters, specifically the length of the oxygen-oxygen bond. Contraction of this bond by 1.8 pm from its MP2 equilibrium geometry (1.452 Å) interchanges the second and third excitations, i.e. **B** ↔ **C**, at ADC(3) level, see Figure 3.11, which then fall directly into reasonable agreement with the CCSD and CC3 results (Figure 3.10). An identical contraction leaves CCSD and CC3 excited states relatively unaltered which clearly demonstrates the unique dependence on the structural parameters of H_2O_2 at ADC(3) level. The **D** and **E**-bands correspond to the same excited states as those calculated using ADC(2) and CC2, and agree well between ADC(3) and CC3, after contraction of the oxygen-oxygen bond.

Electronic circular dichroism spectra of H_2S_2.

The simulated ECD and UV/VIS spectra of H_2S_2 at ADC and CC levels of theory using the d-aug-cc-pVTZ basis set comprising the energetically lowest 15 singlet excited states are shown in Figure 3.10. Numerical values for the excitation energies, oscillator and rotatory strengths are collected in Table A.11-A.12. Four band features are present at ADC(3) level labelled **A**, **B**, **C** and **D**. At ADC(2) and CC2 levels, the simulated ECD spectra between both methods are very similar and all bands consist of near degenerate n-Rydberg excited states of alternating sign.

The **A**-band corresponds to the first and second excited state, the **B**-band arises from the third and fourth excited states, the **C**-band results from the fifth and sixth excited states, all separated by $\sim$ 0.02 eV. Lastly, the **D**-band is a convolution of multiple narrowly separated higher-lying states.

At ADC(3) and CCSD levels, the **A**-**D** bands remain mostly unaltered, with ADC(3) shifting **A**, **B**, **C** and **D** by -0.25 eV, -0.10 eV, -0.05 eV and $+0.01$ eV, respectively. In contrast, a smaller shift of opposite trend is observed for CCSD with **A**, **B**, **C** and **D** being shifted by $+0.02$ eV, -0.04 eV, -0.08 eV and -0.15 eV, respectively.

Of the four states converged at CC3 level, the excitation energy of the **A**-band is blue-shifted compared to ADC(3) and red-shifted compared with CCSD, both by 0.1 eV. The rotatory strength of the transition comprising the **A**-band is of equal quality for both ADC(3) and CCSD level with ADC(3) in slightly closer agreement. The CC3 energies of the **B**-band are blue-shifted by 0.02 eV from ADC(3) and red-shifted 0.09 eV from CCSD with similar rotatory strengths. Using the ADC(3) and CCSD spectra as references, ADC(2) and CC2 are shown to yield similar results in reproducing all bands.

3.4.4 (1*R*)-Camphor, (1*R*)-norcamphor and (1*R*)-fenchone

Camphor and its structurally related molecules, norcamphor and fenchone are often used as molecular standards for ECD calibrations[182–186] and their characteristic ECD and vibrational circular dichroism (VCD) spectra have been extensively explored.[148,187–190] Until this work these molecular systems had not been evaluated using high-level *ab initio* methods.[106] Numerical values for the excitation energies, oscillator and rotatory strengths calculated at the ADC(2) and ADC(3) levels of theory for the nine lowest excited states of (1*R*)-camphor, (1*R*)-norcamphor and (1*R*)-fenchone are collected in Table A.14-A.16.

(a) ADC spectra of H_2S_2

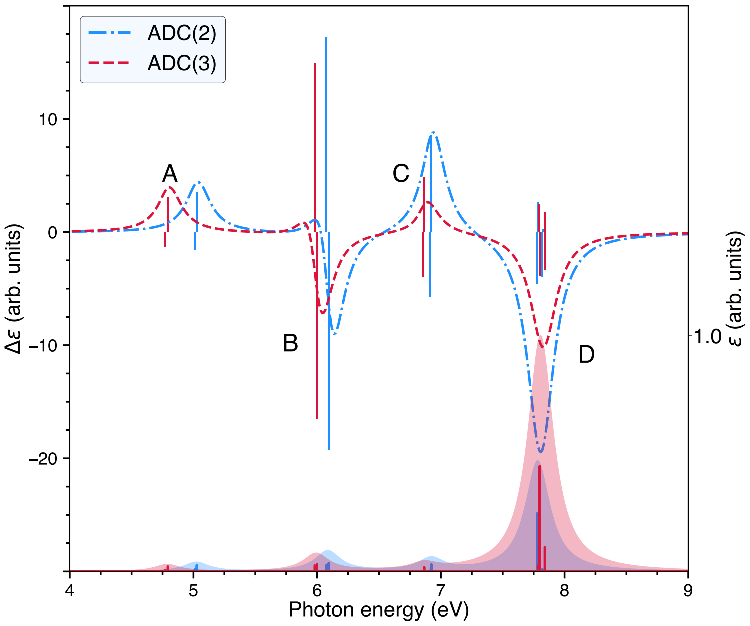

(b) CC spectra of H_2S_2

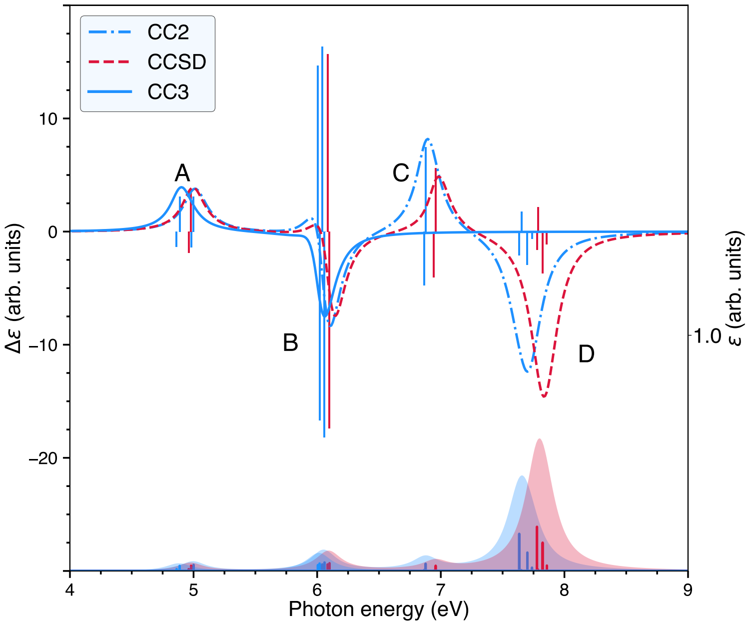

FIGURE 3.12: ECD (*top*) and UV/VIS (*bottom*) spectra of at ADC(2), ADC(3) (*a*), CC2, CCSD and CC3 (*b*) levels of theory in the velocity gauge using the aug-cc-pVTZ basis set for CC3 and d-aug-cc-pVTZ for all others. The rotatory and oscillator strength is scaled by a factor of 0.25 and 0.5 respectively.

Electronic circular dichroism spectra of (1*R*)-camphor.

The ECD spectrum of (1*R*)-camphor in gas phase is fully reproduced using ADC(3)/aug-cc-pVDZ with the ten lowest lying excited states, as seen in Figure 3.13. The signs of the three energetically lowest bands (**A**-**C**) of the experimental spectrum are all correctly predicted and the simulated ECD spectral amplitudes likewise are in good agreement.

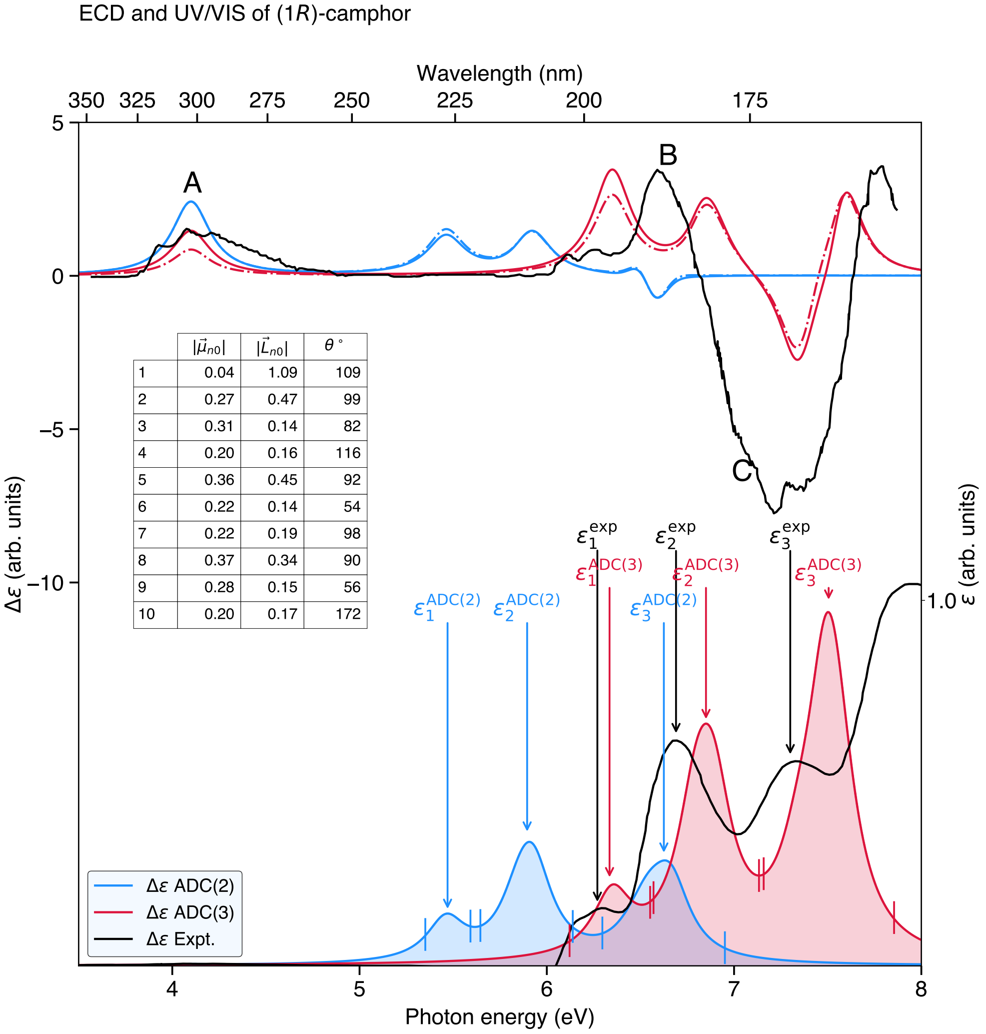

	$\lvert\vec{\mu}_{n0}\rvert$	$\lvert\vec{L}_{n0}\rvert$	θ°
1	0.04	1.09	109
2	0.27	0.47	99
3	0.31	0.14	82
4	0.20	0.16	116
5	0.36	0.45	92
6	0.22	0.14	54
7	0.22	0.19	98
8	0.37	0.34	90
9	0.28	0.15	56
10	0.20	0.17	172

FIGURE 3.13: ECD (*top*) and UV/VIS (*bottom*) spectra in the length (solid) and velocity (*dashed*) gauges of (1*R*)-camphor computed at ADC(3) and ADC(2) levels of theory using the aug-cc-pVDZ basis set. The ten energetically lowest states are used to plot the spectra. The ADC(3) and ADC(2) spectra have been shifted by -0.32 eV and -0.08 eV, respectively. The inset table shows the norm of the transition dipole moments and the angle, θ, between them. Experimental data (*black line*) are taken from Ref. 187; the UV/VIS spectra are in arbitrary units.

The simulated ECD spectrum are shifted by -0.32 eV to correspond with experiment. The **A**-band is caused by the energetically lowest excited state, although a dark state in the UV/VIS spectrum, it becomes visible in the ECD spectrum due to its large magnetic transition dipole moment. The rotatory strengths for this band are in excellent agreement with experiment. The **B**-band, appears as a vibrationally resolved peak in the experimental spectrum and is calculated as arising from the second to fifth excited electronic states which match closely in amplitude. The **C**-band is a convolution of the sixth to ninth excitations. All excited states correspond to n-Rydberg excitations.

At the ADC(2)/aug-cc-pVDZ level, **A**, **B** and **C** arise from the same states as those computed at ADC(3) level with identical signs. The simulated spectrum is shifted -0.08 eV to correspond with experiment. The rotatory strength of the peak comprising the **A**-band, at this level of theory, matches well with experiment and roughly overestimates ADC(3) by a factor of 2. The **B** and **C**-bands are both red-shifted with respect to experiment by ∼ 0.8 eV and ∼ 1 eV, respectively. The rotatory strength of **B** and **C** is calculated to roughly half and roughly one quarter, respectively, as those at ADC(3) level.

The UV/VIS spectra calculated at ADC(3) and ADC(2) levels are likewise in good agreement for the features corresponding to the **B**-band, labelled $\epsilon_1^{\mathrm{exp}}$ and $\epsilon_2^{\mathrm{exp}}$, as well as the **C**-band labelled $\epsilon_3^{\mathrm{exp}}$. Here, the relative amplitudes of these bands are excellently reproduced already at ADC(2) level, with ADC(3) producing a slightly overestimated $\epsilon_3^{\mathrm{ADC(3)}}$ as compared to experiment.

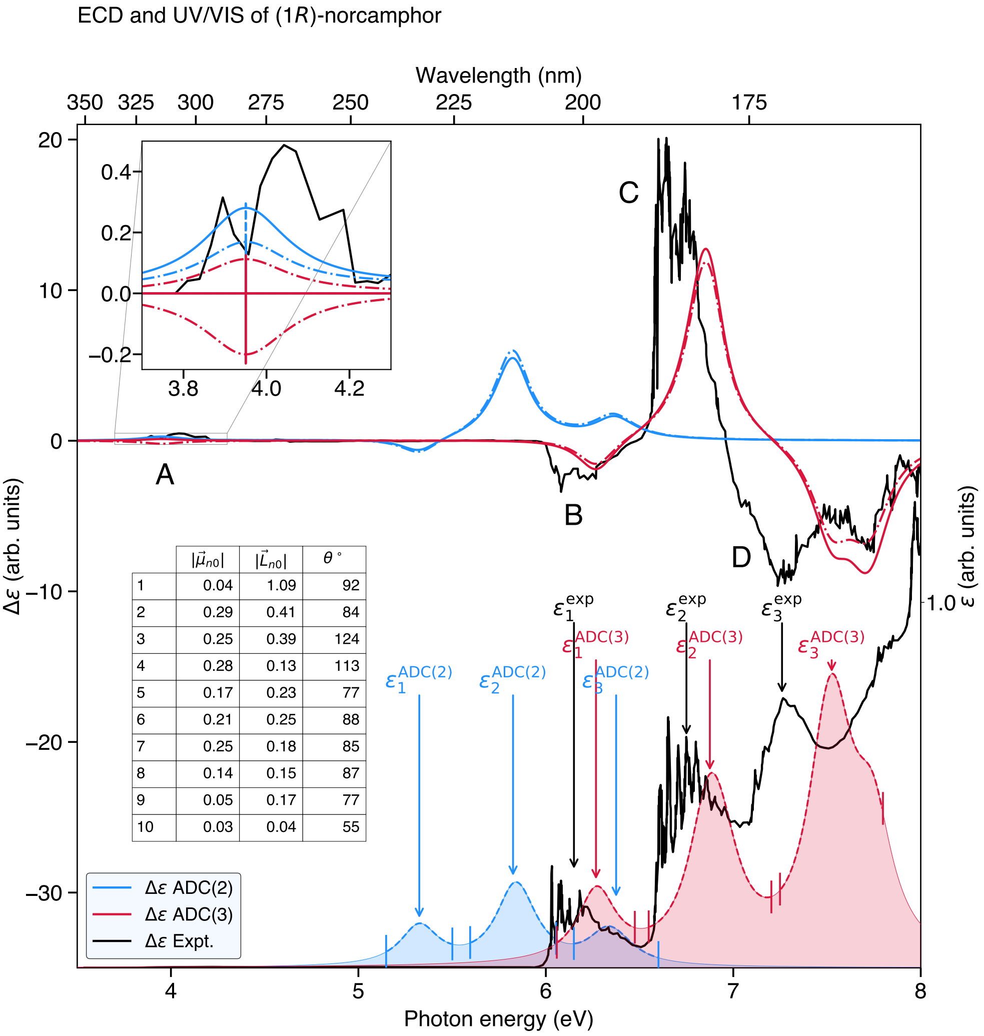

	$\lvert\vec{\mu}_{n0}\rvert$	$\lvert\vec{L}_{n0}\rvert$	$\theta\,^\circ$
1	0.04	1.09	92
2	0.29	0.41	84
3	0.25	0.39	124
4	0.28	0.13	113
5	0.17	0.23	77
6	0.21	0.25	88
7	0.25	0.18	85
8	0.14	0.15	87
9	0.05	0.17	77
10	0.03	0.04	55

FIGURE 3.14: ECD (*top*) and UV/VIS (*bottom*) spectra in the length (solid) and velocity (*dashed*) gauges of (1*R*)-norcamphor computed at ADC(3) and ADC(2) levels of theory using the d-aug-cc-pVDZ basis set. The ten lowest states are used to plot the spectra. The ADC(3) and ADC(2) spectra have been shifted by -0.40 eV and -0.14 eV, respectively. The inset table shows the norm of the transition dipole moments and the angle, θ, between them. Experimental data (*black line*) are taken from Ref. 187; the UV/VIS spectra are in arbitrary units.

Electronic circular dichroism spectra of (1*R*)-norcamphor.

Equally good results are found for (1*R*)-norcamphor, however, here, excitation energies are blue-shifted by roughly 0.4 eV, as seen in Figure 3.14. Noticeably, the first band feature **A** is weakly positive ($+0.3 \times 10^{-40}$ c.g.s.) in the length gauge and weakly negative (-0.5×10^{-40} c.g.s.) in the velocity gauge at the ADC(3)/d-aug-cc-pVDZ level of theory. This can be attributed to one-electron basis sets incompleteness as well as the overall small spectral intensity of the transition. The **A**-band arises from the first excited state which is again characterized by n-Rydberg character, as all other computed higher-lying states of norcamphor are as well. The **B**-band of the experimental ECD spectrum, is caused by the second vertical excited state and again aligns excellently with the experimental reference. The sharply positive **C**-band arises from a convolution of the third and fourth excited states with vibrational fine structure appearing in the experimental spectrum. Lastly the **D**-band arises from convolutions of the fifth to seventh excited states which are hard to separate.

At the ADC(2)/d-aug-cc-pVDZ level, the **A**- **B**- and **C**-bands are consistently reproduced as those at ADC(3) level. Here, a shift of -0.14 eV is applied to align with experiment. The **B**- and **C**-bands are both red-shifted by ~1.0 eV with rotatory strengths roughly half as those calculated at ADC(3) level. The **D**-band is not reproduced at the ADC(2) level from the lowest ten electronic excited states.

The UV/VIS spectra calculated at ADC(3) and ADC(2) levels are here in good agreement for the features corresponding to the **B**, **C** and **D**-bands; labelled $\epsilon_1^{\mathrm{exp}}$, $\epsilon_2^{\mathrm{exp}}$ and $\epsilon_3^{\mathrm{exp}}$, respectively. Here, the relative amplitudes of these bands are qualitatively reproduced at ADC(2) level, however, $\epsilon_3^{\mathrm{ADC(2)}}$ is slightly underestimated as compared to $\epsilon_3^{\mathrm{ADC(3)}}$.

Electronic circular dichroism spectra of (1*R*)-fenchone.

Lastly, we look at the ECD and UV/VIS spectra of (1*R*)-fenchone, the constitutional isomer of (1R)-camphor, shown in Figure 3.15. Unsurprisingly, all computed excited states of fenchone correspond again to transitions from lone-pair oxygen n-orbitals to Rydberg orbitals. Three main bands (**A**-**C**)are apparent in the experimental spectrum. The **A**-band is dark in the UV/VIS spectrum as was the case for (1R)-camphor, however, is clearly visible in the ECD spectrum, again arising from the energetically lowest excited state which is in good agreement with experiment. The **B**-band appears again as a vibrationally resolved peak with a slightly red-shifted shoulder, as was the case for camphor. At ADC(3) level this band arises from a convolution of the second to fifth excited states which are further blue-shifted by ~ 0.4 eV from experiment. The simulated (broadened and convoluted) ECD spectral amplitude of the **B**-band is in excellent agreement with experiment. The **C**-band arises from a convolution of the eighth excitation and upwards.

At ADC(2)/aug-cc-pVDZ level, the spectrum is shifted by +0.04 eV to align with experiment. At this level the **A**-, **B**- and **C**-bands are consistently reproduced as those calculated at ADC(3) level. The rotatory strength of the **A**-band is within 10% of those at ADC(3) level. The **B**- and **C**-bands are red-shifted by ~1.0 eV and the rotatory strengths are roughly half of those obtained at ADC(3) level.

The UV/VIS spectra calculated at ADC(3) and ADC(2), as was the case for (1*R*)-camphor

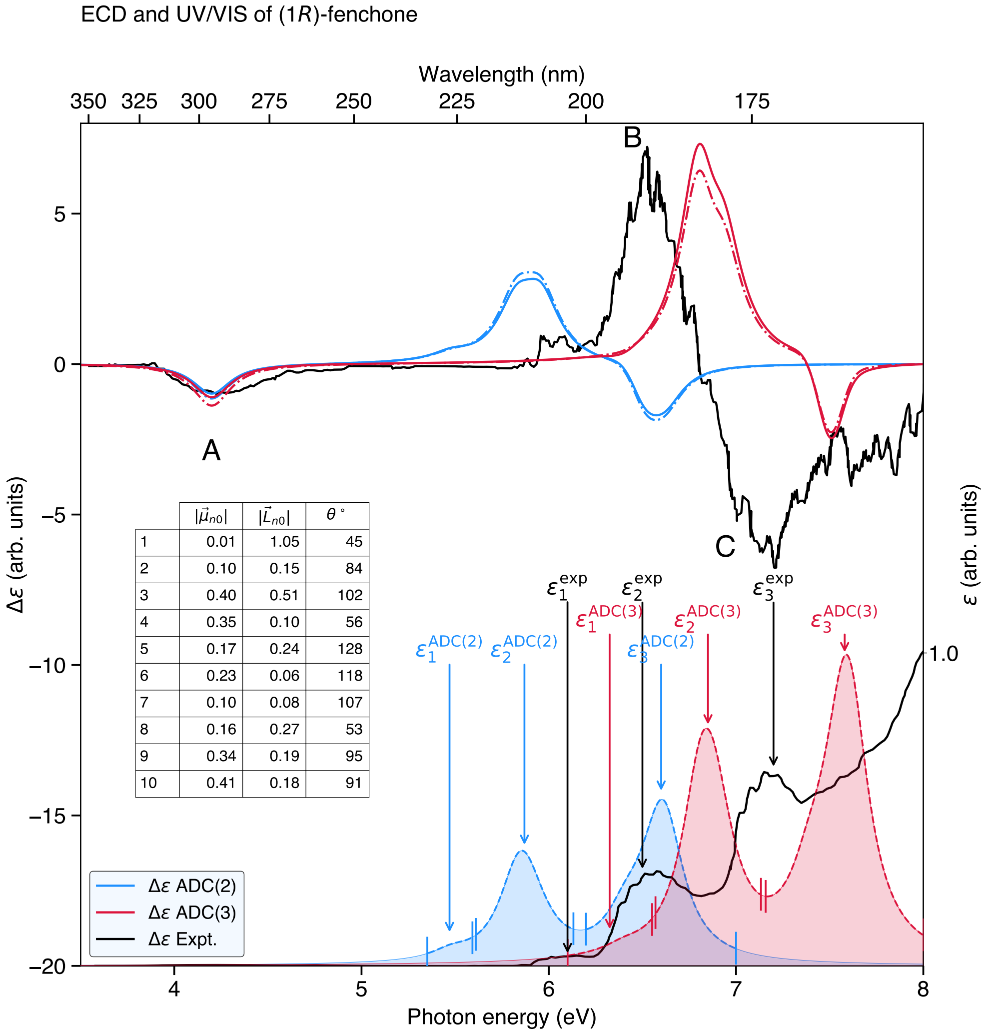

	$\lvert\vec{\mu}_{n0}\rvert$	$\lvert\vec{L}_{n0}\rvert$	θ°
1	0.01	1.05	45
2	0.10	0.15	84
3	0.40	0.51	102
4	0.35	0.10	56
5	0.17	0.24	128
6	0.23	0.06	118
7	0.10	0.08	107
8	0.16	0.27	53
9	0.34	0.19	95
10	0.41	0.18	91

FIGURE 3.15: ECD (*top*) and UV/VIS (*bottom*) spectra in the length (solid) and velocity (*dashed*) gauges of (1*R*)-fenchone computed at ADC(3) and ADC(2) levels of theory using the aug-cc-pVDZ basis set. The ten lowest states are used to plot the spectra. The ADC(3) and ADC(2) spectra have been shifted by -0.18 eV and +0.04 eV, respectively. The inset table shows the norm of the transition dipole moments and the angle, θ, between them. Experimental data (*black line*) are taken from Ref. 187; the UV/VIS spectra are in arbitrary units.

and (1*R*)-norcamphor, in excellent agreement for the features corresponding to the **B**, **C** and **D**-bands; labelled ϵ_1^{exp}, ϵ_2^{exp} and ϵ_3^{exp}, respectively. The relative amplitudes of the three bands are qualitatively reproduced at both ADC(2) and ADC(3) levels of theory as compared with experiment; with the energetic shifts that we're evident in the ECD spectra.

3.5 Inclusion of solvent effects

The *D*-enantiomer of epinephrine (commonly known as adrenaline) is biologically active yet organic synthesis produces a racemic mixture of both enantiomers.[191] An efficient method to obtain

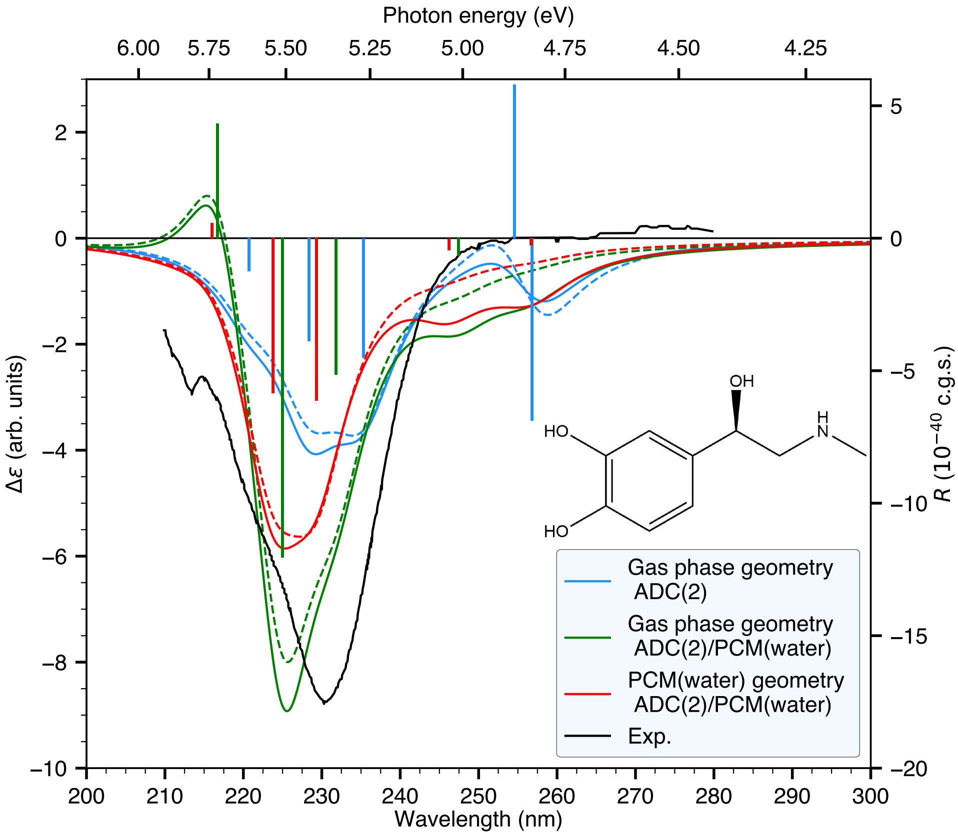

Figure 3.16: ECD spectra of *L*-epinephrine calculated with ADC(2) with and without PCM in the length (*solid spectrum*) and velocity (*dashed line*) gauges using the aug-cc-pVDZ basis set. Rotatory strengths are in the length gauge. The reference experimental data (*red spectrum*) was measured in water and is taken from Ref. 154.

isolated *D*-epinephrine is via HPLC separation in combination with ECD spectroscopy.[154] To demonstrate the general ability of this novel ADC implementation to calculate rotatory strengths for the simulation of ECD spectra of solvated molecules, the solution spectrum of *L*-epinephrine in water was computed using a conductor-like PCM for water.[192,193] To explore the solvent effects of solvated epinephrine thoroughly, one would obviously need to include explicit water to capture all interactions, however, as a proof-of-concept, the PCM approach suffices. To this end, the geometry of the *L*-epinephrine was optimized at CAM-B3LYP/cc-pVTZ level with and without PCM (the converged geometry in both cases corresponds to the AG1a conformer using the nomenclature adopted from Ref 194). The ECD spectra of these molecular systems were then computed at the ADC(2)/aug-cc-pVDZ/PCM(water) and ADC(2)/aug-cc-pVDZ levels of theory for the five energetically lowest excited states as shown in Figure 3.16. Numerical values for the excitation energies, oscillator and rotatory strengths are collected in Table A.13.

At these levels of theory, all states included in the spectra are dominated by $\pi\pi^*$ excitations with contributions from the oxygen/nitrogen lone pair into π^*- orbitals of the phenyl ring. Two bands, labeled **A** and **B** are seen in the experimental spectrum. The **A**-band is a weakly positive band centered around 270 nm and the **B**-band is a broad negative peak centered around 230 nm. However, the **A**-band is not unambiguously assignable in the experiment and may well correspond to noise. Using the gas-phase geometry at ADC(2)/aug-cc-pVDZ level, the **B**-band of the ECD spectrum is clearly reproduced as a convolution of the third to fifth vertically excited states. The **A**-band is a convolution of the first two excited states producing an overall negative band. Including the PCM for water solvation only for the calculation of the spectrum, leads to a blue-shift of the center of the **B**-band and drastically alters the computed rotatory strengths, which falls inline with the experimental spectrum, however, with the **A**-band again predicted as weakly negative. Using the PCM for both geometry optimization as well as the calculation of the ECD spectrum yields a very similar spectrum to that obtained using the gas-phase geometry, showing that the optimized geometry is only negligibly influenced by solvation. The difference between the length and velocity gauges for the energetically lowest excited states are as large as a factor of two but small in absolute terms, owing to the weak absorption, which can already originate from the incompleteness of the one-particle basis set. For energetically higher states with higher absorption, the gauges agree acceptably well, with deviations of $\sim$15%. For all states, the sign of the rotatory strength remains consistent.

3.6 Summary

Expressions for the calculation of rotatory strength in the length and velocity gauges have been implemented for the algebraic diagrammatic constructions scheme for the polarization propagator up to third order. The accuracy of the simulated ECD spectra using the ADC(2) and ADC(3) schemes has assessed by comparison to the corresponding coupled cluster schemes CC2, CCSD and, for the smaller systems, also CC3. For that objective, the gas phase ECD spectra of the *R*-enantiomers of methyloxirane, methylthiirane, dimethyloxirane, dimethylthiirane, hydrogenperoxid, hydrogendisulfide, camphor, norcamphor and fenchone have been computed. Furthermore, addressing the spectra of molecules in solution, the water spectrum of epinephrine was evaluated using ADC(2) in combination with the polarizable continuum model.

A strong basis set dependence of the computed rotatory strengths has been observed, in particular with respect to the inclusion of diffuse orbital functions. However, this owes to the n-Rydberg excitation character of all transitions studied here, and can be expected to be less prominent when other chiral organic molecules involving less diffuse $n-\pi^*$ and $\pi-\pi^*$ electronic transitions are investigated.

Not surprisingly, ADC(2) yields rotatory strengths and ECD spectra very similar to those obtained at the CC2 level. ADC(3) produces spectra similar in quality to CCSD which are both comparable to CC3. ADC(3) spectra are in better agreement with the experimental ones for the larger systems studied here, i.e. camphor, norcamphor and fenchone, than for the smaller molecules. For the purpose of assigning an ECD spectrum to one specific enantiomer, ADC(2) and ADC(3) are clearly sufficiently accurate. Together they represent an excellent complementary toolbox for the simulation of ECD spectra which holds promise that the same will also apply for other chiro-optical properties that will be the subject of future studies.

An important aspect in the simulation of experimental ECD spectra of medium-sized to large molecules is the influence of molecular environments, as has been shown for the solution spectrum of epinephrine where the application of PCM shifted the simulated spectrum. Within the ADC framework, further different solvation models are available, for example frozen density embedding,[195,196] effective fragment potentials[197] or polarizable embedding.[198,199] The suitability of these environment models in combination with ADC for the simulation of ECD spectra should be the focus of future work.

Chapter 4

Excited state electronic circular dichroism

This chapter deals with excited-state electronic circular dichroism ES-ECD implemented at the ADC(n) levels of theory. The simulated S_1-ES-ECD spectrum of norcamphor, calculated at ADC(3) level is compared to those calculated at TD-DFT level using various exchange-correlation functionals. The S_1-ES-ECD spectra of camphor and fenchone are also analysed at the ADC(3) level of theory. Lastly, the ground state ECD and the S_1-ES-ECD spectra of 1,1'-bis-2-naphthol (binol) is analysed at the ADC(2) and CAM-B3LYP levels of theory. This chapter has already been published as Mikael Scott, Dirk R. Rehn, Patrick Norman, and Andreas Dreuw. "Ab initio excited-state electronic circular dichroism spectra exploiting the third-order algebraic-diagrammatic construction scheme for the polarization propagator", The Journal of Physical Chemistry Letters, 12(21):5132–5137, 2021.[107]

4.1 Introduction

ECD spectroscopy can in principle be extended to the investigation of excited electronic states (ES-ECD), in analogy to pump-probe transient absorption spectroscopies, in which excited-state absorption is measured.[63] Such techniques allow for time-resolved ECD measurements of initially excited molecules on a sub-picosecond timescale.[60–63]

While experimental setups for probing ES-ECD are still in their infancy and remain technically quite involved, the theoretical simulation of ES-ECD spectra requires the evaluation of the Rosenfeld equation (2.86), with the corresponding excited-state wave function $\Psi_i, i \neq 0$, replacing the ground state wave function Ψ_0. When excited-state wave functions are directly accessible, the corresponding electric and magnetic transition moments can be calculated in a straightforward manner employing the Rosenfeld equation and the excited-state rotatory strength for $\Psi_i \rightarrow \Psi_f$ can thus be computed.

An general alternative approach is response theory, where the excited-state wave function are not required explicitly. The electric and magnetic moments between excited states can then be extracted from higher-order ground state response functions,[114] for example, as a double residue of the quadratic response function, which is usually employed within density functional theory, or alternatively the rotatory strength can be extracted directly from the triple residue of a cubic response function.[167]

To demonstrate the applicability of this ADC approach, the excited-state rotatory strengths from the S_1 state of the chiral molecules (1*R*)-camphor, (1*R*)-fenchone and (1*R*)-norcamphor are calculated, due to their excellent agreement of their ground state ECD spectra at ADC(2) and ADC(3) levels of theory with their reported experimental spectra, as was demonstrated in Section 3.4.4. Furthermore (*R*)-binol is chosen due to the strongly absorbing ground state experimental ECD spectra.

4.2 Computational details

Both the length and velocity gauge ground state and excited-state rotatory strengths at ADC(n) levels were implemented in a development version of Q-Chem 5.2,[155] as described in Section 2.6.2. For the TD-DFT rotatory strengths, a locally modified version of Dalton2018 was used.[156] Dunning basis sets were employed throughout this chapter.[157–160] The origin for the position operator was set to the center of charge for all calculations. To simulate the ECD spectra, the computed rotatory strengths are converted from a.u. to 10^{-40} c.g.s. using the conversion factor of 471.44 and subsequently broadened by a Lorentzian function according to

$$\begin{aligned}
\Delta\epsilon(\omega) &= \sum_n \Delta\epsilon_n \frac{\gamma_n}{(\omega-\omega_{n0})^2+\gamma_n^2} && (4.1)\\
\Delta\epsilon_n &= \frac{\omega R_{n0}}{22.94\pi} \times 10^{40}, && (4.2)
\end{aligned}$$

where $\Delta\epsilon_n$ is the peak intensity of the n-th transition given in L mol $^{-1}$ cm^{-1}, R_{n0} is the rotatory strength in 10^{-40} c.g.s., γ_n is the Lorentzian broadening factor, ω and ω_{n0} are the incident optical frequency and excitation energy in eV.

4.3 Comparison with DFT

This section will start with a comparison of ADC and density-functional theory (DFT) simulated ES-ECD spectra. Here, quadratic-response density functional theory (QR-DFT) was employed using Equation 2.101 and calculated using a locally modified version of Dalton2018a.[156] In order to get a measure of the accuracy of the simulated ES-ECD spectra at these levels of theory, the ground state ECD spectra is also analysed. Starting with an inspection of the ground state and S_1-ECD spectra of (1*R*)-norcamphor at different levels of theory, which have been computed at the equilibrium ground state geometry optimized at DFT/CAM-B3LYP/aug-cc-pVTZ level (Fig. 4.1). Numerical values for the excitation energies, oscillator and rotatory strengths of both the ground state and excited-state to excited-state transitions are collected in Table B.1.

The computed ground state ECD spectra at DFT levels show the typical shift of the main

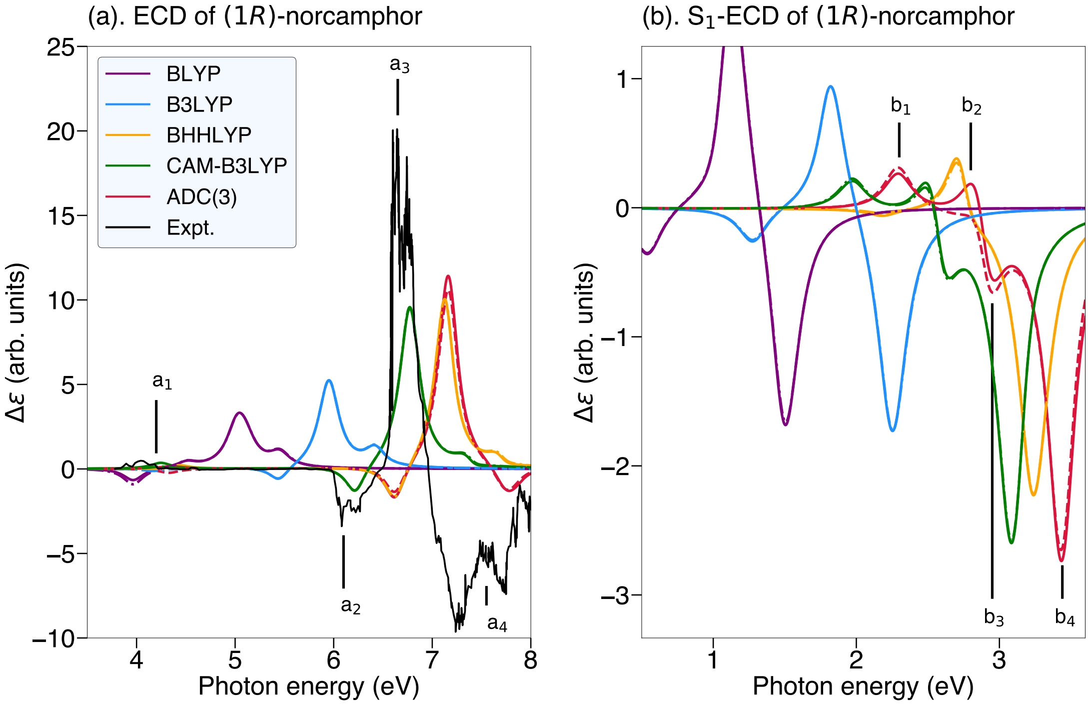

FIGURE 4.1: (a) Ground state ECD spectra and (b) S_1-ECD spectra of (1*R*)-norcamphor computed at TD-DFT level with various exchange-correlation functionals as well as the ADC(3) level using the d-aug-cc-pVDZ basis set. At ADC(3) level, the spectra have been computed in length (*dashed line*) and velocity gauge (*solid line*). The experimental ground state ECD spectrum (*red line*) from Ref.[187] is given for comparison. Lorentzian broadening with a half width at half maximum (HWHM) of 0.124 eV is used to simulate the spectra.

spectral features with varying amount of non-local orbital exchange from BLYP,[200] B3LYP,[201] to BHandHLYP[202] and CAM-B3LYP[161] exchange-correlation functionals.[203] The computed ECD spectra at the BHandHLYP and, in particular, CAM-B3LYP levels agree very favorably with the experimental one as well as with the one computed at ADC(3) level. The detailed analysis of the performance of ADC methods in the calculation of the ground state ECD spectra show ADC(3) can yield a near quantitative accuracy and to reproduce experimental spectral shapes reliably, as demonstrated in chapter 3.[106] The spectra (of camphor and its related structures) usually exhibit a small energetic offset, as it is the case for (1*R*)-norcamphor (Fig. 4.1), however all major spectral features are reproduced with the correct sign.

The S_1 excited state ECD spectrum (S_1-ECD) of (1*R*)-norcamphor computed with DFT employing different exchange-correlation (xc)-functionals as well as ADC(3) reveals a similar trend as observed for ground state ECD (Fig. 4.1). The S_1-ECD spectra are again blue-shifted at the DFT level with increasing amounts of non-local orbital exchange. However, the overall shape of the spectra, in particular, at DFT/CAM-B3LYP and ADC(3) level is very similar, even though they are energetically slightly shifted by about 0.4 eV. Owing to the fact that these two conceptually different theoretical methods (CAM-B3LYP and ADC(3)) in the description of the S_1-ECD spectrum of (1*R*)-norcamphor, as well as its established accuracy in the description of ground state ECD gives additional confidence in the accuracy of ADC(3) in the computation of S_1-ECD spectra of organic molecules.

4.4 S_1-ES-ECD of camphor, norcamphor and fenchone

To demonstrate the ability of the novel computational functionality, the S_1 excited-state ECD spectra of the related molecules (1*R*)-camphor and (1*R*)-fenchone were also computed at ADC(3)/aug-cc-pVDZ and QR-DFT/CAM-B3LYP/aug-cc-pVDZ level due to the overall good agreement between both methods of the ground state ECD and S_1-ECD spectra of (1*R*)-norcamphor. For further comparison the excited-state absorption (ESA) spectra at these levels of theory were also calculated.

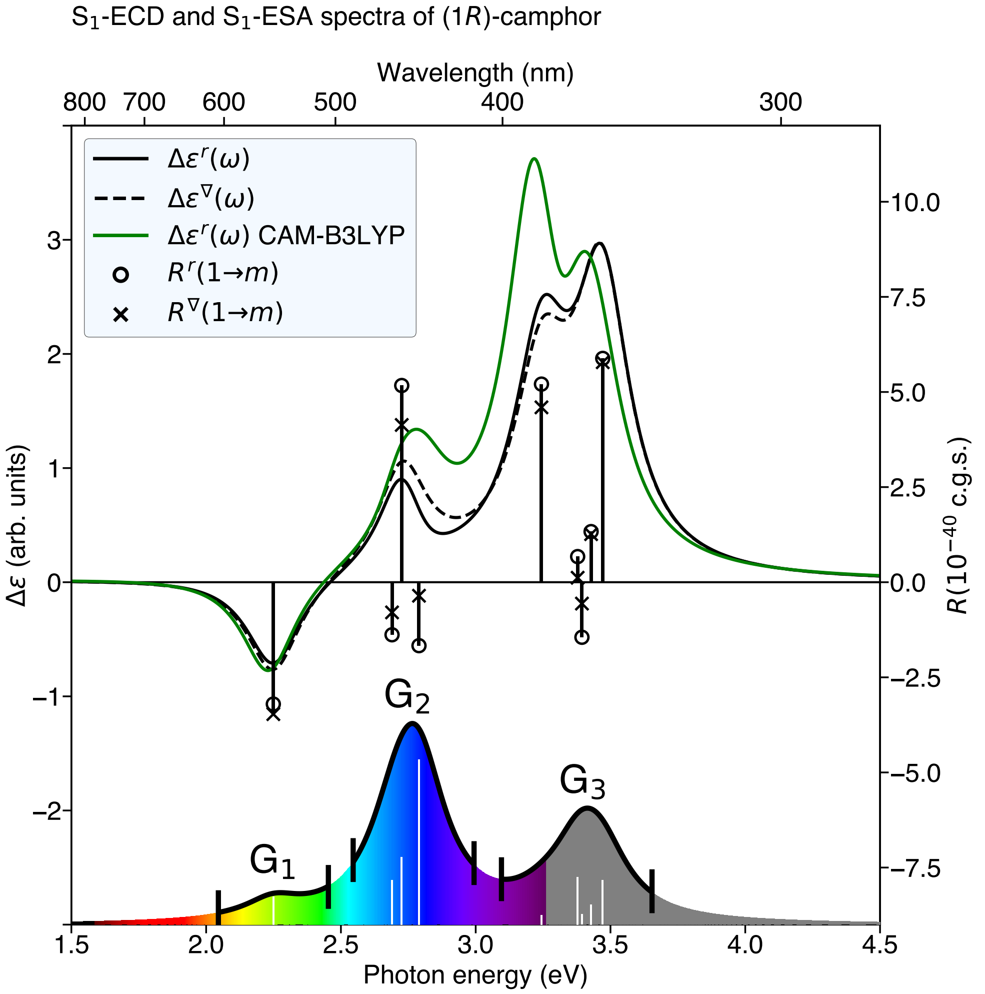

FIGURE 4.2: S_1-ECD and S_1-ESA spectra of (1*R*)-camphor calculated at the ADC(3) level in velocity (*dashed*) and length (*solid*) gauges. Lorentzian broadening with a HWHM of 0.124 eV is used to simulate the spectra. The ESA spectrum (*true color*) is calculated at ADC(3) level in the length gauge; simulated in arbitrary units. The CAM-B3LYP spectra have been shifted to correspond to the energetically lowest transition at the ADC(3) level.

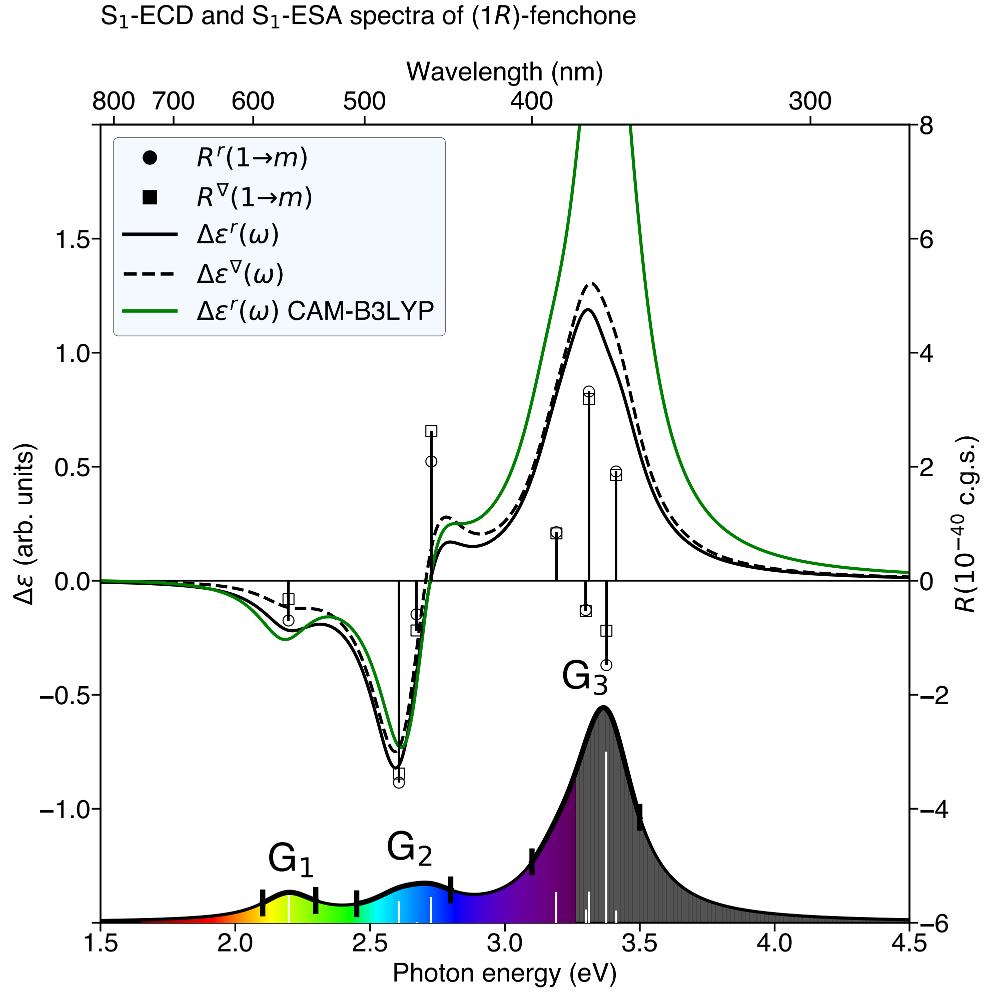

FIGURE 4.3: S$_1$-ECD and S$_1$-ESA spectra of (1R)-fenchone calculated at the ADC(3) level in velocity (*dashed*) and length (*solid*) gauges. Lorentzian broadening with a HWHM of 0.124 eV is used to simulate the spectra. The ESA spectrum (*true color*) is calculated at ADC(3) level in the length gauge; simulated in arbitrary units. The CAM-B3LYP spectra have been shifted to correspond to the energetically lowest transition at the ADC(3) level.

The S$_1$-ECD and S$_1$-ESA spectra comprising transitions into the nine energetically higher-lying excited states S$_n$ ($n = 2-10$) calculated at the ADC(3) and QR-DFT/CAM-B3LYP levels of theory; simulated using a Lorentzian with a HWHM of 0.124 eV of (1R)-camphor, (1R)-fenchone and (1R)-norcamphor are shown in Figure 4.2, 4.3 and 4.4, respectively. All rotatory and oscillator strengths for these transitions are shown in Table B.2-B.3. The electronic structure of these states were analyzed in Chapter 3 and were shown to correspond to electronic transitions into Rydberg orbitals. For all molecules, the simulated S$_1$-ECD spectra consist of three distinct regions (**G**), separated by ≈0.5 eV. The first group G$_1$ arises from the S$_1$ → S$_2$ transition and is energetically well separated in all spectra from the higher-energy features with an excitation energy of 2.2 eV. At this level of theory, the rotatory strength of the first feature is negative for (1R)-camphor and (1R)-fenchone and positive for (1R)-norcamphor. The energetically next higher distinct spectral feature is G$_2$ which consists of a convolution of three excitations out of

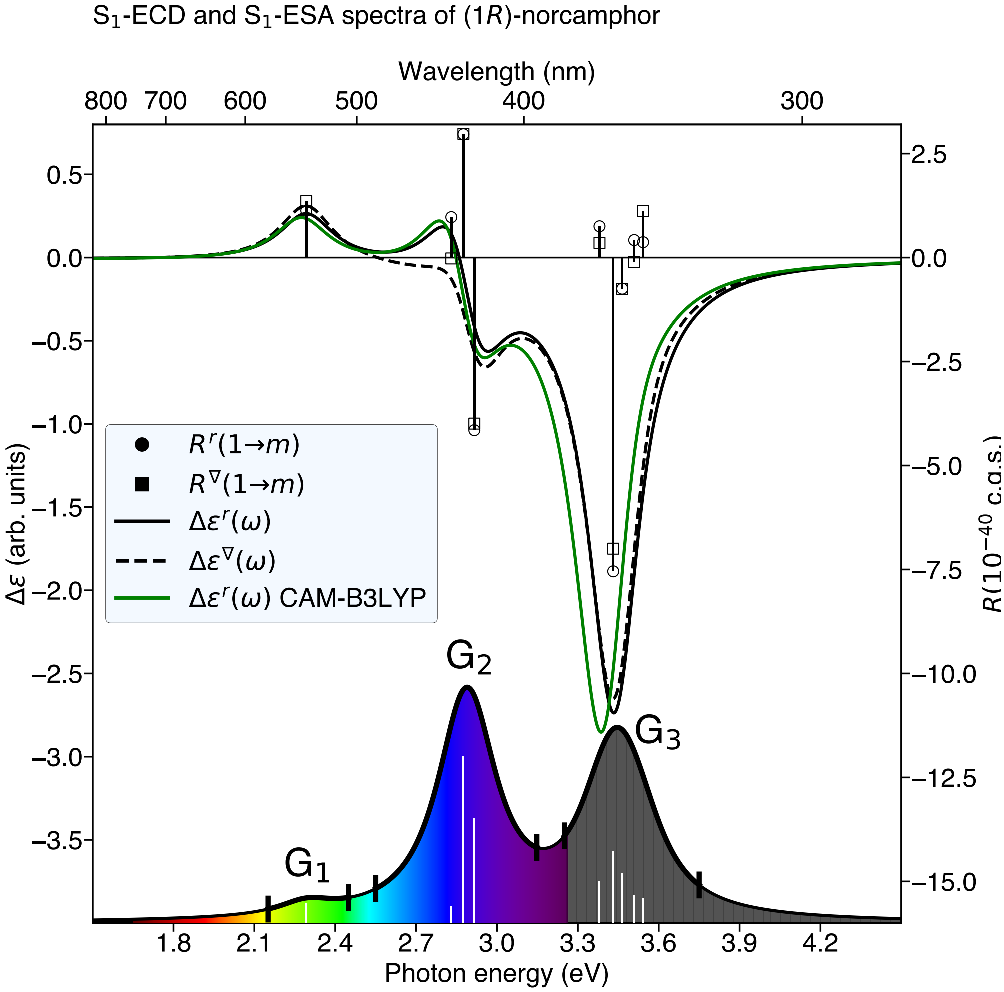

FIGURE 4.4: S_1-ECD and S_1-ESA spectra of (1R)-norcamphor calculated at the ADC(3) level in velocity (*dashed*) and length (*solid*) gauges. Lorentzian broadening with a HWHM of 0.124 eV is used to simulate the spectra. The ESA spectrum (*true color*) is calculated at ADC(3) level in the length gauge; simulated in arbitrary units. The CAM-B3LYP spectra have been shifted to correspond to the energetically lowest transition at the ADC(3) level.

S_1 into S_3, S_4 and S_5, respectively, with oscillating negative and positive rotatory strengths for (1R)-camphor, two negative and one positive for (1R)-fenchone and two positive and one negative for (1R)-norcamphor. In all three molecules, the maximum of G_2 is centered around ≈2.7 eV in the simulated S_1-ECD spectra. The third spectral feature centered around ≈ 3.5 eV consistent for all three molecules and labelled G_3 (Figure 4.2-4.4). It corresponds to a convolution of the electronic transition from S_1 into S_6 to S_{10}. While the individual electronic transitions have different signs in the S_1-ECD spectrum, for example, in (1R)-fenchone these transitions exhibit rotatory strengths of +0.9, -0.5, +3.3, -1.5, +1.9 (10^{-40} c.g.s.) the resulting convoluted peak has an overall clearly positive sign in the S_1-ECD spectrum of (1R)-fenchone. The same holds true for (1R)-camphor, in which the overall sign of G_3 is also positive, while it is negative for (1R)-norcamphor (Figure 4.4).

As explained in Section 2.4.2 and shown in Figure 3.3, calculated rotatory strengths using approximate quantum chemical methods and incomplete one-electron basis sets are well known to be gauge-variant (origin dependent in the length gauge).[167] For example, the ground state rotatory strength of the $S_0 \rightarrow S_1$ transition of (1*R*)-norcamphor calculated at ADC(3)/d-aug-cc-pVDZ level yields opposite signs in the length and velocity gauge owing to the incompleteness of the basis (Figure 3.13b). One may assume the gauge dependence to be amplified for ES-ECD, however, this is not the case, as the simulated S_1-ECD spectra in length and velocity gauges agree generally well (Figure 4.1-4.4). One noticeable and at the same time typical exception is the $S_1 \rightarrow S_3$ electronic transition of (1*R*)-norcamphor for which an overall very small and positive or negative sign is computed in the length and velocity gauge, respectively, which we also attribute to basis set incompleteness.In general, the differences between the length-velocity gauges is found to be on the same order of magnitude for the excited state (S_1) rotatory strength as for the ground state one.

4.5 S_1-ES-ECD of 1,1'-bis-2-naphthol (binol)

Another prominent test case for theoretical methods to simulate ECD spectra is 1,1'-bis-2-naphthol (binol), for which ground state as well as excited-state circular dichroism has been investigated earlier.[60,61,204] It has been observed experimentally and verified by calculations that the two naphtol moieties exhibit a significant rotational barrier making binol an axially chiral compound.[205] The enantiomers are called atropoisomers and specified by the stereodescriptors P/M or R_a/S_a. Interestingly, the binol enantiomers undergo a conformational change in the excited state, switching from an orthogonal conformation of the two moietes to a cisoid or transoid conformation with the transoid being slightly more preferred.[204] As starting point for the simulation of the ground state and S_1 excited-state ECD spectra, we optimized the structure of (R_a)-binol using standard DFT in combination with the CAM-B3LYP functional and the aug-cc-pVTZ basis set and a polarizable continuum model (PCM) for EtOH solution. We restricted ourselves to the energetically most favorable conformer (I1,R adopting the nomenclature used in Ref.[206]) and subsequently computed the 20 energetically lowest electronic excited states at the second-order ADC (ADC(2)) level and TDDFT/CAM-B3LYP using the cc-pVDZ basis set.

The rotatory strengths for the $S_0 \rightarrow S_n$ (n=1–20) and $S_1 \rightarrow S_n$ (n=2–20) transitions were calculated and the ground-state ECD and S_1 excite-state ECD spectra constructed using Lorentzian broadening with a half width at half maximum of 0.2 eV, shown in Figure 4.5 and 4.6, for the ground state and S_1-excited state spectra, respectively.

Again, the simulated ECD spectra at both levels of theory agree very favorably with the experimental spectrum measured in EtOH solution. The main features of the experimental ground-state ECD spectrum are clearly identifiable after a shift of -0.6 eV is applied to the calculated excitation energies.[207] For (R_a)-binol, a very small, only slightly positive band a_1 is visible in the low-energy region of the experimental spectrum. At both levels of theory this small positive feature is reproduced and identified to originate from the two energetically lowest excited states that are nearly degenerate with $\pi\pi^*$ character and which possess opposite rotatory

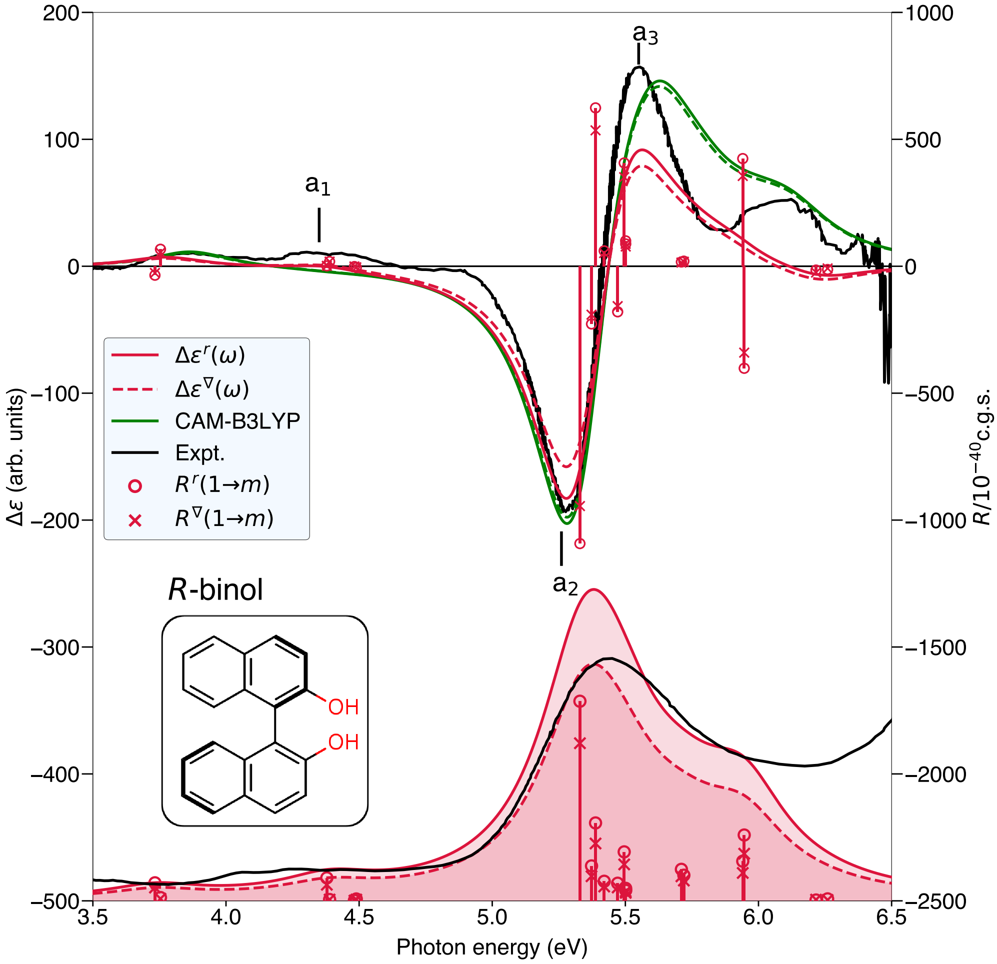

FIGURE 4.5: ECD (*top*) and UV/VIS spectrum (*bottom*) of (*R*)-binol computed at ADC(2)/cc-pVDZ (*black*) and CAM-B3LYP/cc-pVDZ (*green*) levels of theory in length (*solid*) and velocity (*dashed*) gauges. Lorentzian broadening of HWHM of 0.20 eV is applied to simulate the spectra. The UV/VIS spectrum is in arbitrary units and the experimental (*red*) line is from Ref.[61].

strengths. In the molecular orbital representation, the S_1 and S_2 states are best characterized as electronic transitions from the highest occupied molecular orbital (HOMO) to the lowest unoccupied molecular orbital (LUMO) as well as from the HOMO-1 to the LUMO+1, respectively (Figure 4.7).

The first significant feature of the experimental ECD spectrum is a sharp negative band a_2 at ≈ 5.25 eV. At both theoretical levels this feature is well reproduced. At ADC(2) level, it arises from a convolution of electronic transitions into S_7 and S_8, which both exhibit $\pi\pi^*$ character.

The rotatory strength of the $S_0 \rightarrow S_7$ and $S_0 \rightarrow S_8$ transitions are calculated to -1092 ($\times 10^{-40}$ c.g.s.) and -227 ($\times 10^{-40}$ c.g.s.) in the length gauge, respectively. The next band a_3 at ≈ 5.5 eV in the experimental spectrum is a rather sharp peak, which according to our calculations arises from a convolution of electronic transitions into S_9 and higher excited states with the most significant peak arising from the $S_0 \rightarrow S_{12}$ with a rotatory strength of 407 ($\times 10^{-40}$ c.g.s.) in the

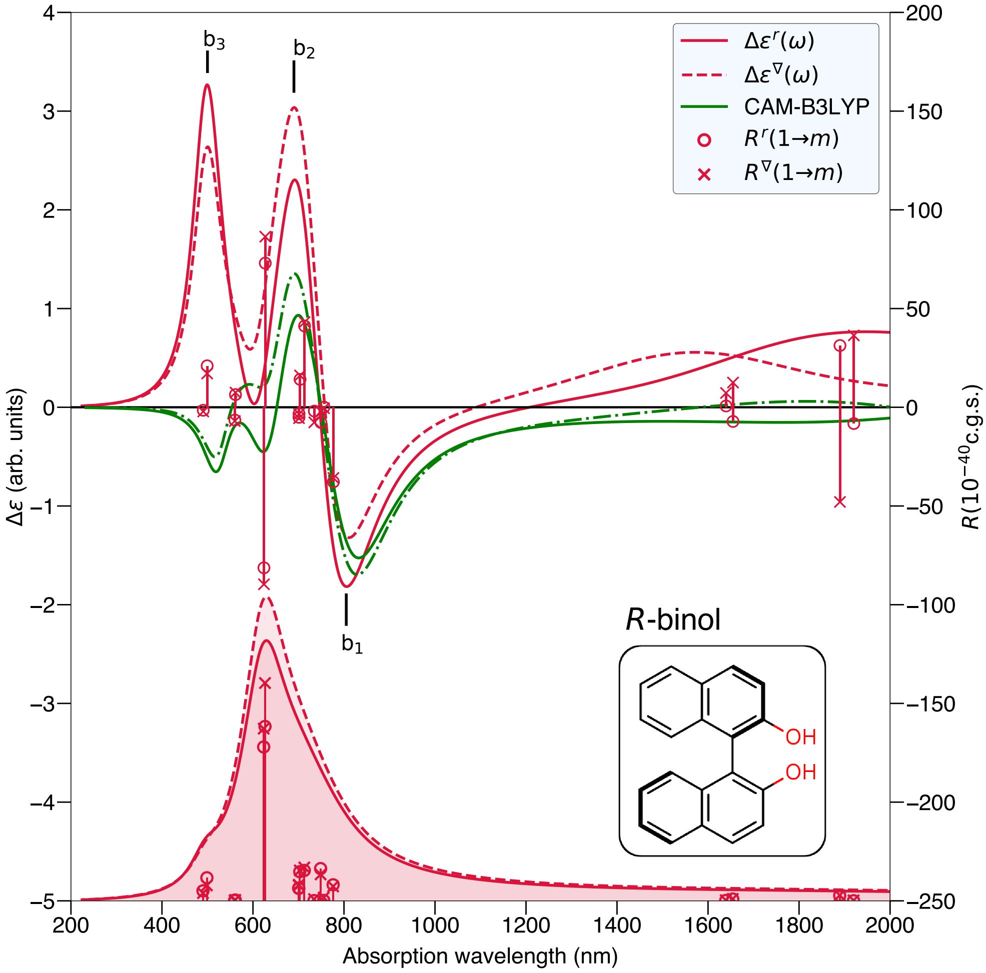

FIGURE 4.6: S_1-ECD (*top*) and corresponding ESA spectra (*bottom*) of (*R*)-binol computed at ADC(2)/cc-pVDZ (*black*) and CAM-B3LYP/cc-pVDZ (*green*) levels of theory in length (*solid*) and velocity (*dashed*) gauges. Lorentzian broadening of HWHM of 0.20 eV is applied to simulate the spectra. The ESA spectra are in arbitrary units.

length gauge.

The S_1-ECD spectrum has been simulated at ADC(2)/cc-pVDZ as well as TDDFT/CAM-B3LYP/cc-pVDZ level for the electronic transitions $S_1 \rightarrow S_n$ (n=2-20). The energetically lowest transition is of course $S_1 \rightarrow S_2$, which has an excitation energy of 0.02 eV, which corresponds to an absorption wavelength in the far-IR around 60 μm, owing to the near degeneracy of the S_1 and S_2 excited states. There are several other energetically low-lying transitions $S_1 \rightarrow S_n$ (n=3–6) with absorption wavelengths in the near IR region between 1000 and 2000 nm (Figure 4.6), which are responsible for the overall positive tail of the simulated S_1-ECD spectrum of (R_a)-binol in that spectral range. In the visible and UV region, it shows three distinct features. The first band b_1 with negative rotatory strength is centered around ≈775 nm, and results from the $S_1 \rightarrow S_7$ transition according to our ADC(2) as well as CAM-B3LYP calculations. The second band, b_2 arises from the $S_1 \rightarrow S_{11}$ and $S_1 \rightarrow S_{12}$ transitions with rotatory strengths of 41 ($\times 10^{-40}$ c.g.s.) and 14 ($\times 10^{-40}$ c.g.s.) and absorption wavelengths calculated as 713 nm and 703 nm respectively.

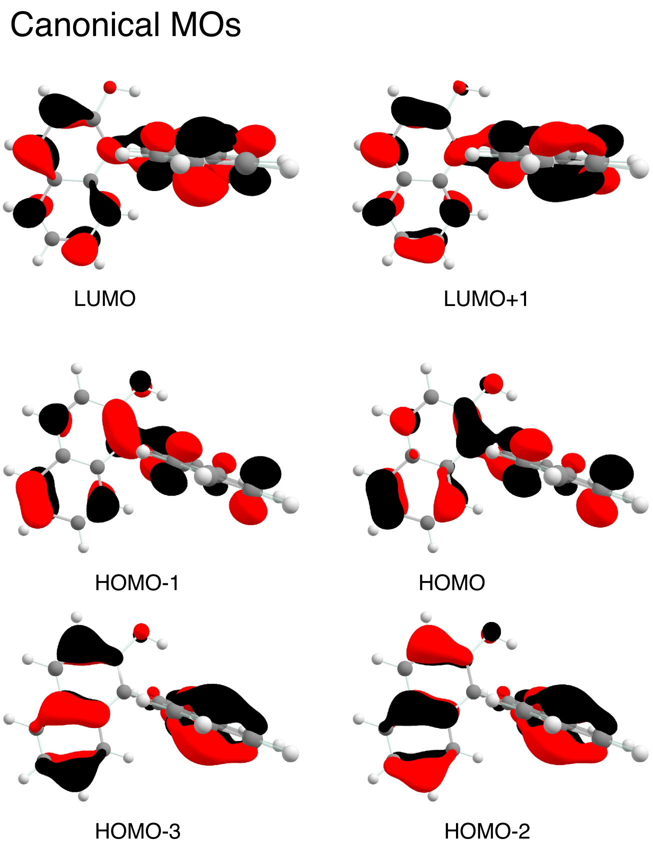

FIGURE 4.7: Canonical molecular orbitals of (R)-binol computed at Hartree-Fock/cc-pVDZ level of theory.

The third band b_3, a positive peak arise from a convolution of the transitions $S_1 \rightarrow S_n$ (n=13–20), with two sharp opposite-signed near-degenerate peaks $S_1 \rightarrow S_{15}$ and $S_1 \rightarrow S_{16}$ canceling out and producing an overall positive band.

A comparison of our simulated excited-state ECD spectra of (R_a)-binol to experimental ones would be highly desirable, however the existing experiments[60,61,204] demonstrate the usefulness of time-resolved ECD and report changes in ECD signal at selected absorption wavelengths only and not complete ES-ECD spectra. This renders a comparison to experiment impossible at present impossible.

4.6 Summary

In conclusion, it is reassuring that the results of the TD-DFT/CAM-B3LYP and ADC calculations agree well for the ES-ECD spectra of (R)-binol. This gives great confidence in the accuracy of both computational schemes which can, for organic compounds with single-reference electronic ground states, be expected to be similar to the one observed for ground-state ECD spectra. Furthermore, our findings emphasize the relevance of computational methods in the investigation of chiral compounds. They represent a straightforward means to determine the absolute configuration, but much more, with the help of the presented methodology time-resolved pump-probe experiments with circularly polarized light can be reliably simulated and chiral reaction paths followed. With this contribution we hope to trigger further experimental work in that direction.

Chapter 5

Two-photon circular dichroism

In this chapter, expressions for the two-photon rotatory strength within the ADC/ISR formalism as described in Section 2.6.3 are used to simulate the TPCD spectra of *S*-methyloxirane and *S*-methylthiirane at the ADC(2) level. These are then compared to those same spectra at CC2 level. Furthermore, the one- and two-photon circular dichroism spectra of twisted biphenyl are investigated at the ADC(2) level of theory. Lastly, the TPCD spectra of (1*R*)-norcamphor at ADC(2) and ADC(3) level is used to illustrate the impact different polarization and propagation configurations available to experimentalist.

5.1 Introduction

The linear ECD and its time-resolved nonlinear counterpart ES-ECD have been explored in Chapter 3 and Chapter 4, respectively. Similar to ECD, TPCD involves the absorption of circularly polarized light, however, here involving the simultaneous absorption of two photons with at least one being circularly polarized.[32] The interest in nonlinear optical processes and specifically those involving two photons has been increasing over the last few decades due to its applicability in prodrug activation where molecular systems function as carriers of inactive drugs which upon irradiation of two-photons, releases the drug making it bioactive. Several such molecular systems have been developed over the past decades and are referred to as two-photon caging compounds, or photo-removable protecting groups (PPGs).[208–215] Another major area where NLO and TPA in particular are employed is two-photon fluorescent probes where the aim is to develop diagnostic tools for Alzheimer's disease.[216] Beyond these medicinal applications, TPA is used in the manufacturing of computer components, e.g., optical data storage and 3D-microfabrication.[217–222] These applications exploit the high temporal and spatial resolution afforded by the TPA process and, in the case of *in vivo* applications, using "safe" radiation in the infra-red region. The extension to include chiroptical properties in addition naturally follows with TPCD spectroscopy where all the spatial and temporal benefits of TPA are combined with the absolute stereochemistry information carried over from ECD, yielding unique TPCD spectra for different enantiomers. As was the case for ECD, the TPCD rotatory strength also exhibits origin-dependence when using the length formulation, however, producing origin-independent TPCD rotatory strengths is even more complex owing to the NLO process. Instead of just one velocity gauge formulation, three origin-independent velocity gauge formulations have been developed, referred to as the ω_1, ω_3 and translationally invariant (TI) equation. All three formulations have been studied at the TD-HF level of theory,[78,79] and the TI equation has been employed at the CC2 level of theory.[83] Neither of the formulations have been used within the ADC/ISR scheme, which is the goal of this work. Specifically, the calculation of the TPCD rotatory strength has been implemented at the ADC(2) and ADC(3) levels of theory.

5.2 Computational details

The derivation of the ω_0, ω_1 and ω_3 formulation two-photon rotatory strengths within the ADC/ISR formalism, were presented in Section 2.6.3 which resulted in Equations 2.191-2.193. These three formulations were implemented in a development version of Q-Chem 5.2[155]. The rotatory strengths were convoluted using a Lorentzian or Gaussian function, $g(\omega)$, to simulate the spectra according to,

$$\Delta\epsilon(\omega) = 471.211 \cdot \omega \cdot g(\omega)^f R^{\text{OP}} \quad (10^{-40}\text{ c.g.s}), \tag{5.1}$$

$$\delta^{\text{TPCD}}(\omega) = 4.87555 \times 10^{-5} \cdot \omega^2 \cdot g(2\omega)^f R^{\text{TP}} \quad (\text{GM}). \tag{5.2}$$

Here R^{OP} and R^{TP} denote the one and two-photon rotatory strength of the f-excited state in atomic units. The ground state geometries of S-methyloxirane and S-methylthiirane are taken from Ref. 83. Biphenyl was optimized at the CAM-B3LYP/cc-pVTZ level and norcamphor at the CAM-B3LYP/aug-cc-pVTZ level. The origin of the position operator was set to the center of charge for all length gauge calculations.

5.3 Two-photon circular dichroism at ADC and CC levels

While TPCD has been explored at TD-HF, TD-DFT, CC2 and CCSD levels of theory, a relatively limited amount of molecular systems have been investigated.[78,79,83] For comparison purposes, the TPCD spectra at the ADC(2) level of theory of S-methyloxirane and S-methylthiirane were calculated and compared with the same spectra calculated at the CC2 level of theory.[83] Starting with S-methyloxirane, for the six energetically lowest singlet states computed at the ADC(2)/aug-cc-pVDZ level, there is excellent agreement with those reported in literature at the CC2/aug-cc-pVDZ level where the translation invariant (TI) formulation of the rotatory strength has been used, as seen in Figure 5.1. These spectra are convoluted using a Gaussian function with a HWHM of 0.02 eV; the peaks are well separated and the energies of each excited state are in close agreement between ADC(2) and CC2. The peaks labeled I_n $(n = 1, 2, 3, 4, 5)$ agree in sign for all gauges with the exception of I_5 which is calculated as negative in the ω_3 formulation. This good agreement between the three formulations indicates that aug-cc-pVDZ is an adequate basis set for methyloxirane (although, as seen in Section 3.4.4, extra diffuse functions are needed at the ADC(2) level of theory to correctly predict the sign of the rotatory strength of the second excited state). When comparing the ECD spectrum to the TPCD spectrum, there is an almost

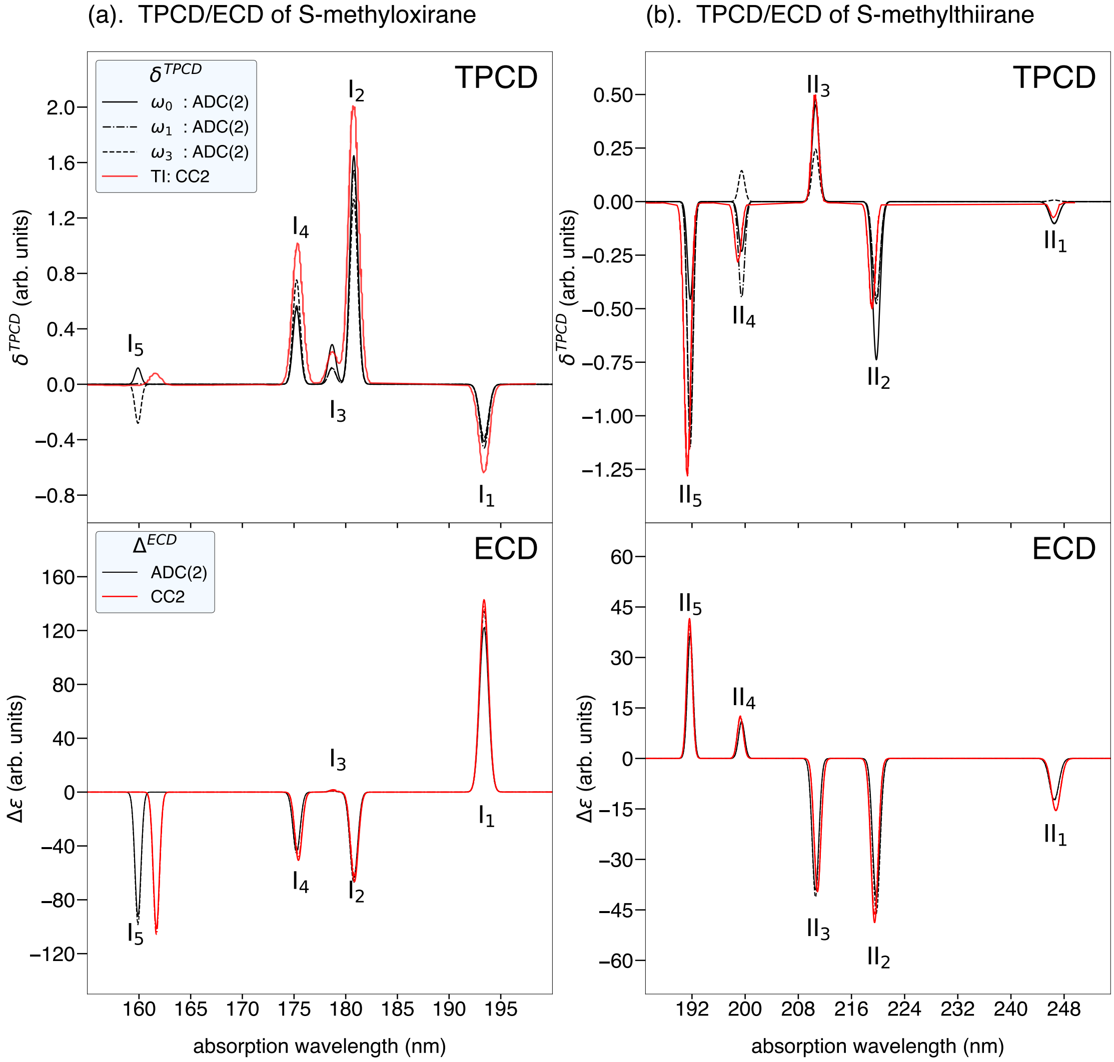

Figure 5.1: Simulated TPCD and ECD (*length gauge*) spectra of (a) S-methyloxirane and (b) S-methylthiirane. Computed at the ADC(2)/aug-cc-pVDZ level of theory in the ω_0, ω_1 and ω_3 formulations for the six energetically lowest singlet excited states and convoluted using a Gaussian function with a HWHM of 0.02 eV. The CC2-TI values were taken from Ref. 83. The ADC(2) spectra have been shifted to correspond to the energetically lowest excited state of CC2, +0.14 eV for methyloxirane and +0.06 eV for methylthiirane, respectively.

direct reversal of signs of the rotatory strengths. Furthermore, I_3 is a dark-state in ECD but is present as a small peak in the TPCD spectrum.

For S-methylthiirane, the results are equally consistent for the first five states which produce near identically two-photon rotatory strengths for ADC(2) and CC2, with the somewhat significant exception of II_1 and II_4 which deviate for the ω_3 formulation, as was the case for I_5 (ω_3) of methyloxirane. Beyond these exceptions, all three formulations are in good agreement which indicate that the aug-cc-pVDZ basis set is adequate to achieve consistency between the gauges (ω_0, ω_1, ω_3) concerning methylthiirane. Comparing the TPCD spectrum with the ECD spectrum reveal a reversal of rotatory strengths signs of the II_n ($n = 3, 4, 5$) peaks, although the ratio between the peaks remain mostly unaltered.

5.4 Two-photon circular dichroism of biphenyl chromophores

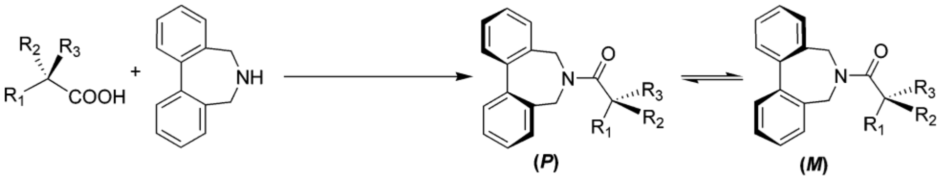

FIGURE 5.2: Biphenyl chromophores for carboxylic acids.

Biphenyl chromophores have been used as chirality probes for the assignment of the absolute configuration of 2-substituted chiral carboxylic acids by amide derivatization.[223] Attachment of biphenyl to a 2-substituted carboxylic acid, twists the phenyl moieties with a P/M torsion depending on the substituents on the C_α (O=C-C_α), with larger substituents being sterically hindered from approaching the phenyl ring and therefore leading to a specific torsion, illustrated in Figure 5.2. Furthermore, aromatic substituents are favorably attracted to the phenyl ring due to $\pi - \pi^*$ interactions. While direct assignment of an carboxylic acid enantiomer is in principle straightforward by ECD, the weak band arising from the $n - \pi^*$ transition introduces uncertainty in measurements. A benefit of this attachment approach is the strong absorbance and ECD signal in the 250 nm region (A-band) and the characteristic P/M torsional-dependent ECD spectra. The diphenyl moiety exhibits a low rotational barrier of around $\sim$ 14 kcal/mol, allowing for the thermodynamically most favorable conformation to be the major product at room temperature.[224]

Thus, to test this novel TPCD implementation within the ADC/ISR formalism, biphenyl in its application as a chirality probe represent an excellent starting point. To this end, the ground state geometry of biphenyl was optimized at the CAM-B3LYP/cc-pVTZ level of theory, resulting in an relaxed torsion angle of $\approx \pm 40°$ for the P and M conformer, respectively. Subsequently, using the optimized geometry of the M enantiomer as a starting point, the ECD spectra comprising the ten energetically lowest singlet excited states of biphenyl as a function of the torsional angle ($5° < \theta < 45°$) was computed in an unrelaxed scan, Figure 5.4. The spectra can be divided into two main regions, the **A**-band (200 - 250 nm) and the **B**-band (180 - 200 nm). At this level of theory, the **A**-band arises solely from the three energetically lowest singlet excited states. Moreover, there is a clear dependence on the torsional angle which impacts the intensity of the A-band in a linear manner up until 45°. The absorption maximum of this band is blue-shifted with increasing torsional angle. The energetically higher **B**-band, shows similar features to the A-band, namely the ECD signal is strongly dependent on the torsional angle, reaching a minimum around 40°, with the excitation energies likewise blue-shifted. While the **A**-band is clearly distinguishable in the ECD spectrum, one should keep in mind that due to the low rotational barrier, a mixture of P/M will always be present in the experimental spectra yielding weaker signals.

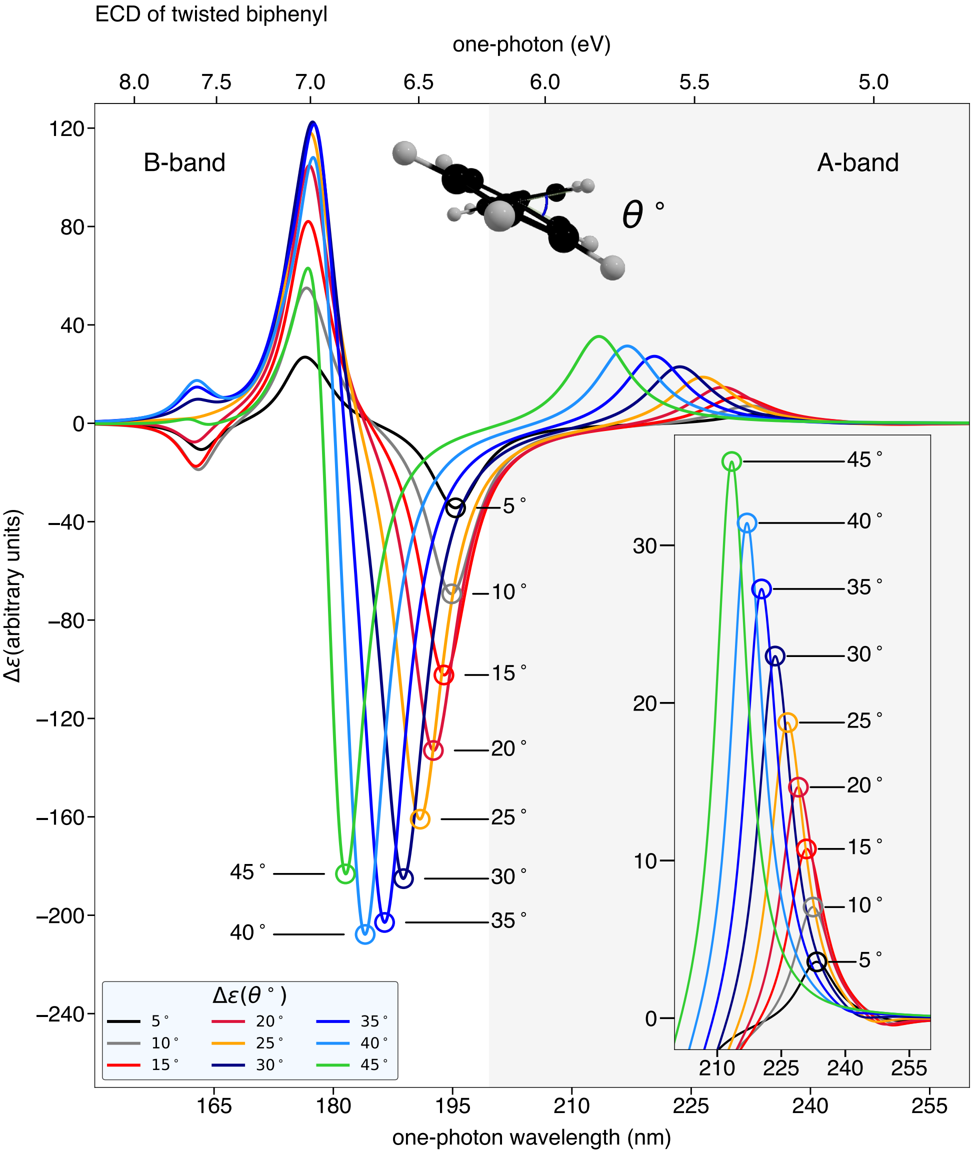

Figure 5.3: ECD spectra of biphenyl twisted along its torsional angle $5° < \phi < 45°$ (M) calculated at the ADC(2)/cc-pVDZ level of theory for the ten energetically lowest singlet excited states. The spectra are convoluted using a Lorentzian function with a HWHM 0.124 eV.

Next, the TPCD spectra were computed at ADC(2)/cc-pVDZ level of theory. Here, the **A**-band consist of a sinusoidal signal situated in the visible energy range, around 500 nm, with the energetically lowest peak reaching a maximum when the torsional angle is around 22.5°.The B-band is now centered at 350 nm with the TPCD signal increasing linearly with the torsional angle.

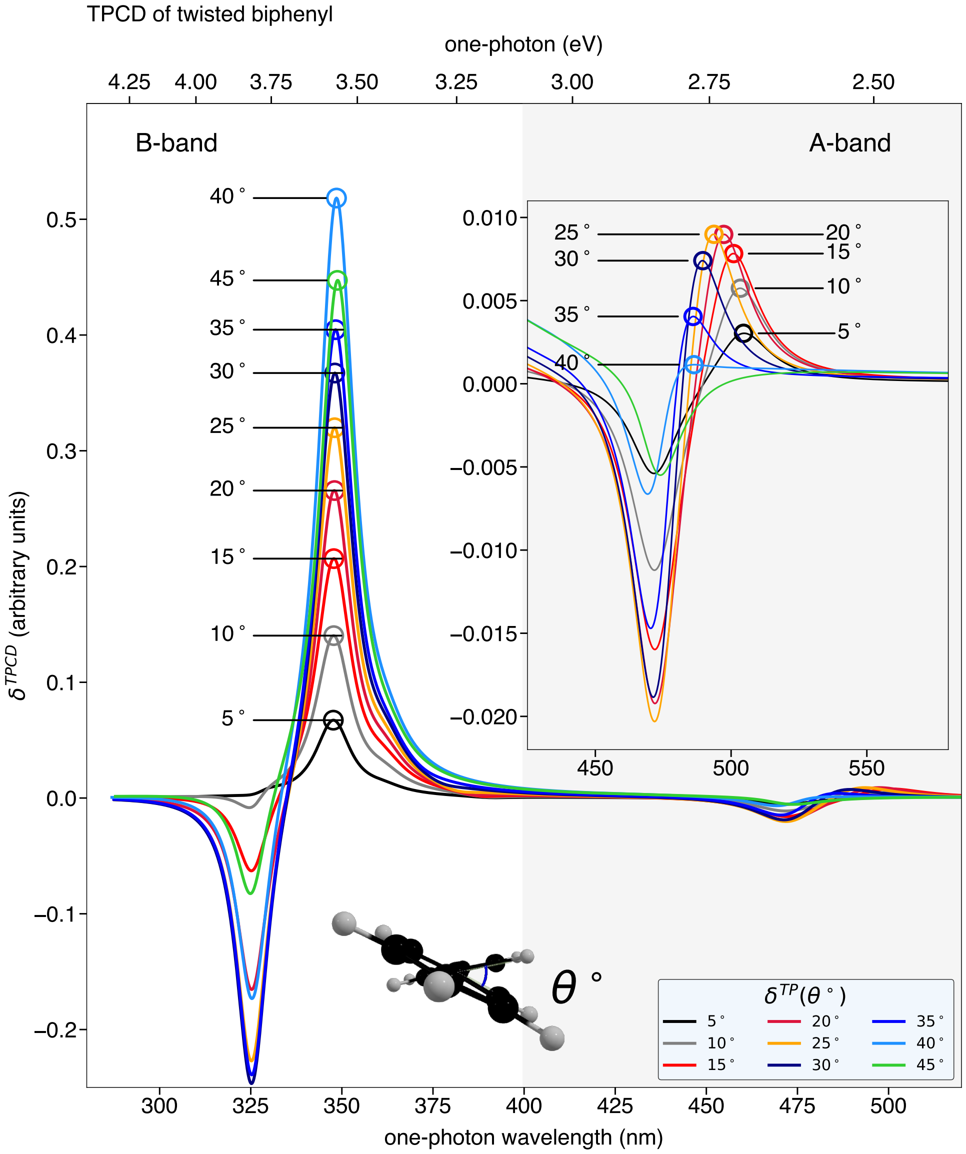

FIGURE 5.4: TPCD spectra of biphenyl twisted along its torsional angle $5° < \phi < 45°$ (M) calculated at the ADC(2)/cc-pVDZ level of theory for the ten energetically lowest singlet excited states. The spectra are convoluted using a Lorentzian function with a HWHM 0.124 eV.

5.5 Polarization-propagation impact on the two-photon rotatory strength

The ECD and ES-ECD spectra of norcamphor and its related compounds camphor and fenchone were intensively investigated at ADC(2) and ADC(3) levels of theory in Chapter 3 and 4.[106] Due to the overall excellent agreement with the experimental gas-phase ECD spectra and those calculated at ADC(3) level of theory, norcamphor represent a good model-system to evaluate TPCD spectra. Specifically, to illustrate the impact different setups have on the simulated TPCD

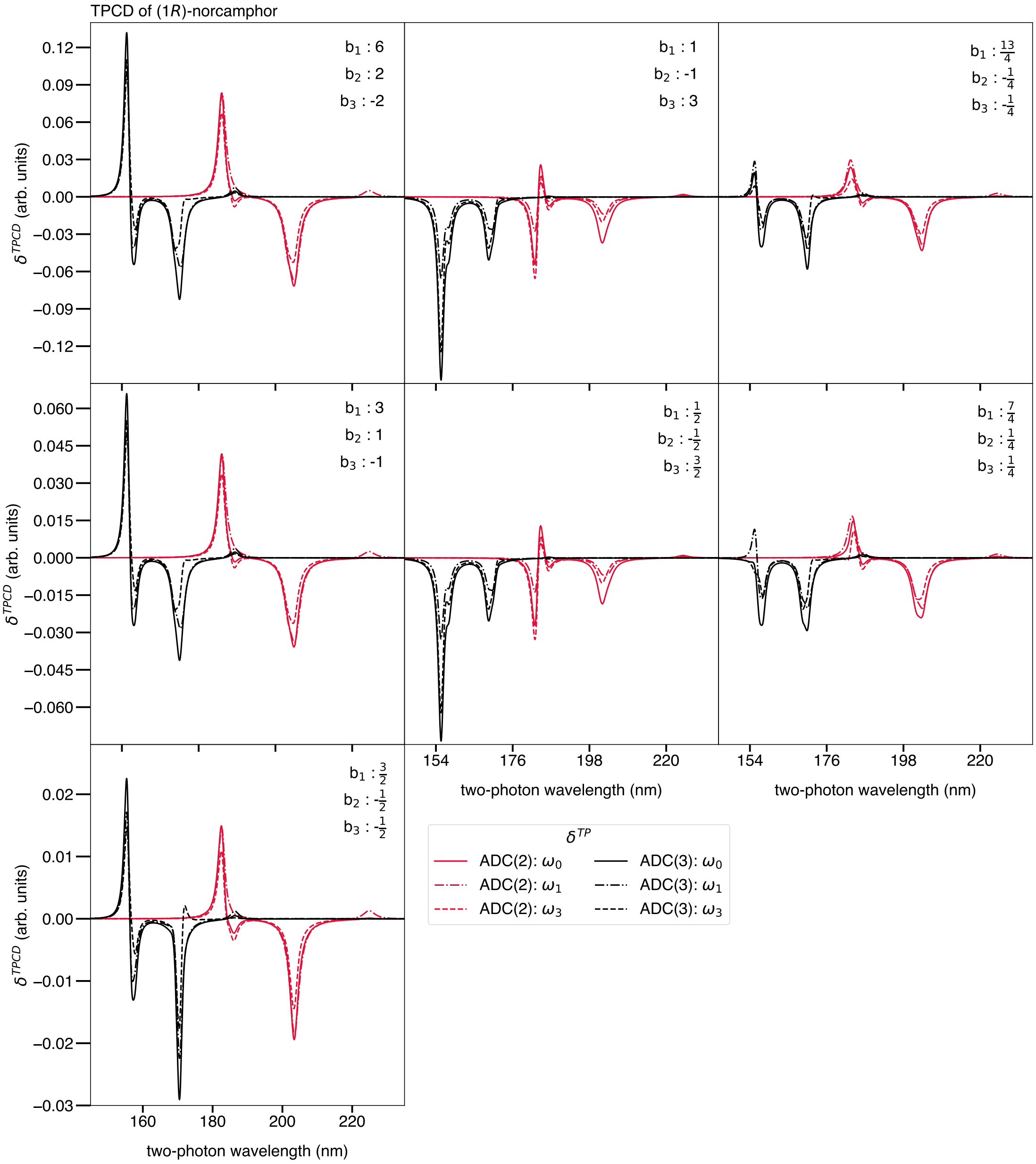

FIGURE 5.5: The impact of polarization and propagation (b_1, b_2 and b_3) on the TPCD spectra of (1*R*)-norcamphor at the ADC(2) and ADC(3) levels of theory using the aug-cc-pVDZ basis set simulated using a Lorentzian function with a HWHM of 0.124 eV.

spectra, the TPCD spectra of norcamphor comprising the eight energetically lowest singlet excited states was computed at the ADC(2) and ADC(3) levels of theory using the aug-cc-pVDZ basis set. The seven different polarization-propagation setups listed in Table 2.5 were then used to simulate the resulting TPCD spectra, shown in figure Figure 5.5. As seen in this figure, using the common setup of two left circularly polarized lightwaves propagating parallel produces the strongest absorbing ADC(2) and ADC(3) spectra (top-left). Using the same polarization but with the two photons propagating antiparallel (top-middle) produces spectra of similar two-photon absorption intensity, but with sign reversal of the last peak. Next, with the same polarization yet with the photons propagating perpendicular (top-right) yields a near identical spectra as for parallel propagation, but with an two-photon absorption intensity of roughly half the magnitude. The middle-left and middle-middle spectra are obviously just the same spectra as those of the top-left and top-middle at half the magnitude. The other middle-right and lower-left likewise exhibit the same features as those of top-left and top-right, respectively. The dominant terms in Equations. 2.139-2.156, for the majority of peaks in the spectra are the $\mathcal{B}_1$ and $\mathcal{B}_2$ terms, with small quadrupole-electric dipole interactions in the strongly absorbing at $\sim$ 180 nm.

5.6 Summary

The calculated TPCD spectra at the ADC(2) level compares favorably to those calculated at the CC2 level, as shown for the S-methyloxirane and S-methylthiirane molecules. Furthermore, biphenyl chromophores provides an interesting test case for experimental verification of computed TPCD spectra, as well as a promising area for further development of chirality probes using the TPCD process. As demonstrated at the ADC(2) level, biphenyl exhibit strongly absorbing TPCD bands in the one-photon visible range, thus accessible to standard spectroscopic measurement techniques. Furthermore, the use of different polarization and propagation configurations for the experiment can be easily included in the calculated two-photon rotatory strength. While TPCD remain experimentally challenging, this work extends the theoretical toolbox at an *ab initio* level for evaluation of two-photon rotatory strengths.

Chapter 6

Hyperpolarizability and higher harmonic generation

In this chapter the expressions for the static and dynamic first-order hyperpolarizability tensor within the ADC/ISR described in Section 2.6.4 are used to compute the static β at ADC(1), ADC(2) and ADC(3) levels of theory. Furthermore, these are then compared against those same quantities at CCS, CC2 and CCSD levels of theory for several small organic and inorganic molecules. Next, the dynamic first-order hyperpolarizability response or SHG signal of several small organic molecules calculated at ADC(n) levels are compared with experimentally measured values. Lastly, the dynamic HRS spectra of ammonia calculated at the ADC(2) and ADC(3) levels of theory are briefly discussed.

6.1 Introduction

The field of nonlinear optics NLO was pioneered by Maria Goeppert in the 1930s,[225] however experimental demonstration required high-intensity light and hence wasn't possible until the advent of the laser in the 1960s.[226] NLO has since grown into a promising field in physics which investigates the induced polarization in a material as the nonlinear response to an applied electric field. At the microscopic level, the interaction of a molecular system and an oscillating electromagnetic field may be described semi-classically, within the electric dipole approximation, the interaction Hamiltonian takes the form,[227]

$$H_{int} = \vec{\mu} \cdot \vec{E}, \tag{6.1}$$

where $\vec{\mu}$ is the molecular electric dipole moment. The induced dipole moment may then be expressed as a power series of the electric field strength where the perturbation is orders of magnitudes lower than the interatomic electric field,

$$\vec{\mu}_i = \vec{\mu}_i^0 + \vec{\alpha}_{ij}\vec{E}_j + \underbrace{\vec{\beta}_{ijk}\vec{E}_j\vec{E}_k + \vec{\gamma}_{ijkl}\vec{E}_j\vec{E}_k\vec{E}_l + \ldots}_{\textbf{NLO}}, \tag{6.2}$$

where $\vec{E}_j$ is the electric field strength, $\vec{\mu}_i^0$ is the static dipole moment, $\vec{\alpha}_{ij}$ is the linear polarizability (zeroth order hyperpolarizability), $\vec{\beta}_{ijk}$ is the first-order hyperpolarizability and $\vec{\gamma}_{ijkl}$ is the second-order hyperpolarizabilitiy. The first hyperpolarizability, β, incorporates SHG, differential frequency generation (DFG), sum-frequency generation (SFG) and optical retification (OR). Similarly, third harmonic generation (THG), two-photon absorption TPA and more are captured by the second-order hyperpolarizabilitiy, $\vec{\gamma}_{ijkl}$.

SHG has found wide use, of particular importance is the application of bio-imaging where SHG microscopy is used to investigate cancer, cardiovascular and fibrotic diseases.[228–232] A major benefit of using NLO in bio-imaging is the spatial and temporal resolution afforded by the method, as well as the minimal noise from bulk material. One method is to use organic dyes to enhance contrast in tissue imaging by exploiting SHG.[233] There is naturally a need to find and develop molecular system with large first-order hyperpolarizabilities suitable for this purpose as well as a general need of finding molecular systems with specific nonlinear optical properties for uses in other applications e.g. 3D data storage, signal processing and microfabrication, and other uses in biology.[98–104] The classical systems which demonstrates large first-order hyperpolarizabilities are those of a push-pull character, e.g. paranitro-aniline (pNA) where electron withdrawing and donating groups are positioned opposite on a phenylring.[234–248] Furthermore, a recent source of novel molecular systems that's starting to be exploited is that of marine natural products (MNP) which are produced by marine microorganisms for particular cellular functions that exhibit interesting nonlinear optical properties.[249–251]

The first-order hyperpolarizability, β, at SHG frequency conditions is commonly measured using the electric-field induced second harmonic electric-field-induced second-harmonic generation (EFISH) experimental method.[252] Another method which is frequently employed is measuring hyper-Rayleigh scattering HRS.[253–258] HRS generates a non-vanishing signal even in bulk, allowing for β to be measured in liquids.[259–269] The central differences of SHG and HRS is that the signal in the case of SHG is anisotropic, coherent and in phase, whereas for HRS the signal is isotropic, incoherent and dephasing with the exciton photon.[105]

The development of theoretical frameworks in the calculation of hyperpolarizabilities are important since they allow for the prediction of nonlinear optical properties *in silico*. In the pursuit of this aim several approaches to calculate the first-order hyperpolarizability are available with the common methods being the finite field finite field (FF) method,[270,271] sum-over-states (SOS) method and the response function (RF) formalism.[272,273] In the finite field method, molecular properties, e.g., the dipole moment, polarizability and first-order hyperpolarizability, are identified as derivatives of the total molecular energy in the presence of a static uniform electric field, which are evaluated at zero field strength. This method does not require a wave function and are thus accessible to electronic structure methods that only provide the energy, e.g. MP2, CASPT2 and CCSD(T) etc. These partial derivatives may then be computed using the finite difference formula. The SOS method can be applied to any quantum chemistry method where excited-state properties (dipole moments) as well as excitation energies are accessible. Here, the state-to-state transition elements and excitation energies are used to form the hyperpolarizability explicitly in the SOS expression. This approach has the benefit of revealing the individual contribution of each excited state to the hyperpolarizability at a given frequency. The SOS method is however computationally intractable for molecular systems with large numbers of excited states. Lastly, the RF formalism where a full diagonalization of the molecular Hamiltonian yields the equivalent to including all excited states in the SOS method. At the *ab initio* level the RF has been employed using CC to calculate static and dynamic first- and second-order hyperpolarizabilities at the CCS, CC2, CCSD, CCSD(T) and CC3 levels of theory.[59,64,274–287] For very large molecular systems density functionals have been employed, however early developed functionals were often inadequate in the description of hyperpolarizabilities.[288–306]

The RF formalism is employed in this ADC implementation that will be evaluated in the following sections.

6.2 Computational details

The first-order hyperpolarizability tensor, expressed within the ADC/ISR formalism, Equation 2.198, was solved using a DIIS algorithm as described by Equations 2.199-2.201 as implemented in a development version of Q-Chem 5.2.[155] The same quantities calculated at CC levels were performed in a locally modified version of Dalton2018a using the CC-QR module.[156] The Dunning basis sets were employed throughout this work.[157–160]

The geometries of the molecular systems investigated in the two following sections were optimized at different levels of theory depending on the system size. For the comparison of static first-order hyperpolarizabilities, the inorganic molecules were optimized at the CCSD/aug-cc-pVTZ level and for the organic molecules in the same section CCSD/cc-pVTZ was used. For the comparison of dynamic first-order hyperpolarizabilities (SHG) with experiment, CCSD/aug-cc-pVTZ was used. Furthermore, in the static case, the alignment of the molecules of their permanent dipole moment with the positive z-axis was not always performed, since here only methods are compared. As such, for the comparison of CC values, the sign of the isotropic hyperpolarizability should be viewed as not important. However, when the calculated β_{SHG} is compared with experiment, all molecules are aligned with the permanent dipole moment in the z-axis.

(Inorganic) HX

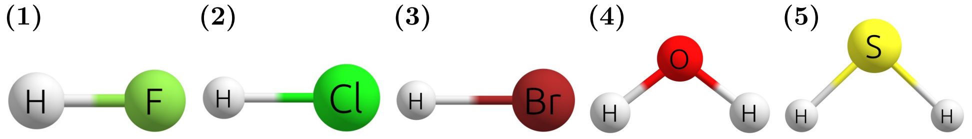

FIGURE 6.1: HF, HCl, HBr, H_2O and H_2S chemical sketches.

(Inorganic) NaX

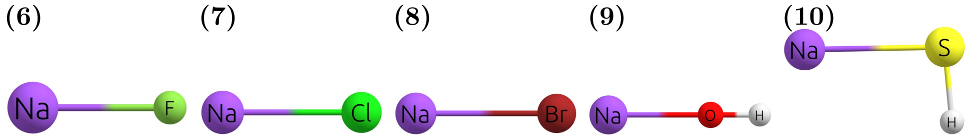

FIGURE 6.2: NaF, NaCl, NaBr, NaOH and NaSH chemical sketches.

(Inorganic) LiX

(11) **(12)** **(13)** **(14)** **(15)**

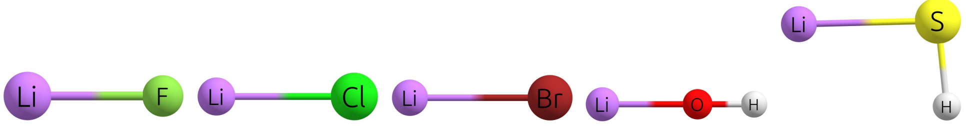

FIGURE 6.3: LiF, LiCl, LiBr, LiOH and LiSH chemical sketches.

(Inorganic) H_2SO_x

(16) **(17)** **(18)** **(19)**

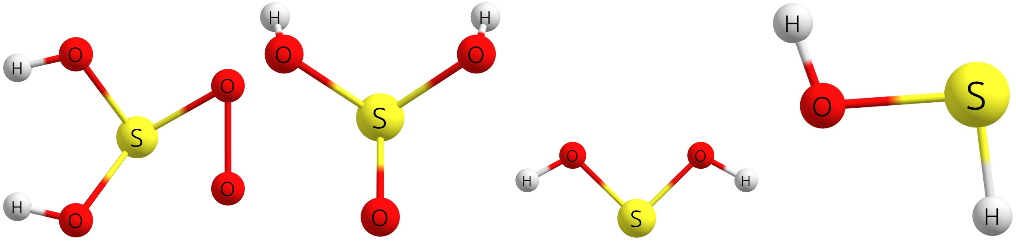

FIGURE 6.4: H_2SO_4, H_2SO_3, H_2SO_2, H_2SO, H_3BO_3 and H_3PO_4 chemical sketches.

(Inorganic) H_3PO_4 and H_3BO_3

(20) **(21)**

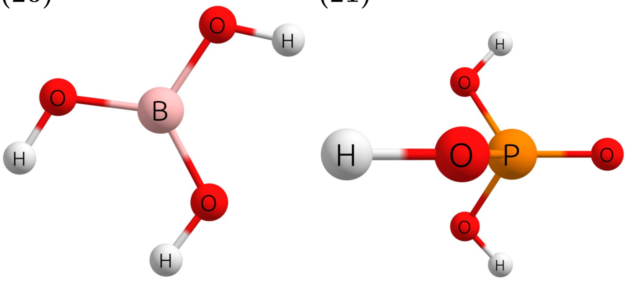

FIGURE 6.5: H_3BO_3 and H_3PO_4 chemical sketches.

(Inorganic) HNO_x and N_2O

(22) **(23)** **(24)** **(25)**

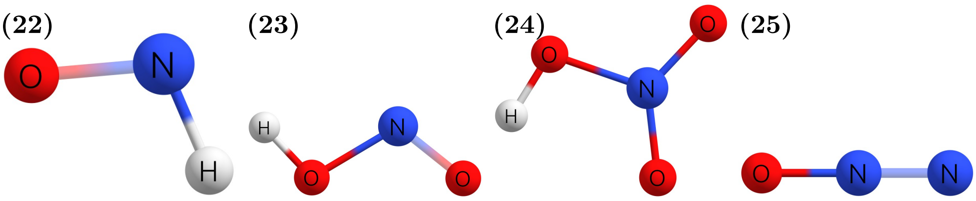

FIGURE 6.6: HNO, HNO_2, HNO_3 and N_2O chemical sketches.

(Inorganic) HNS_x and N_2O

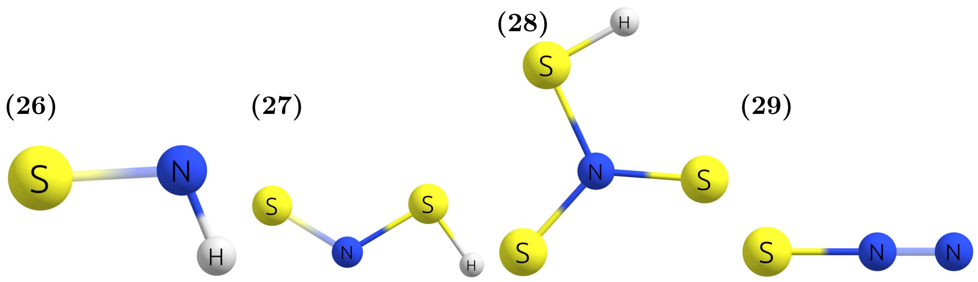
(26) **(27)** **(28)** **(29)**

FIGURE 6.7: HNS, HNS_2, HNS_3 and N_2S chemical sketches.

(Organic) Hydrocarbons ketones

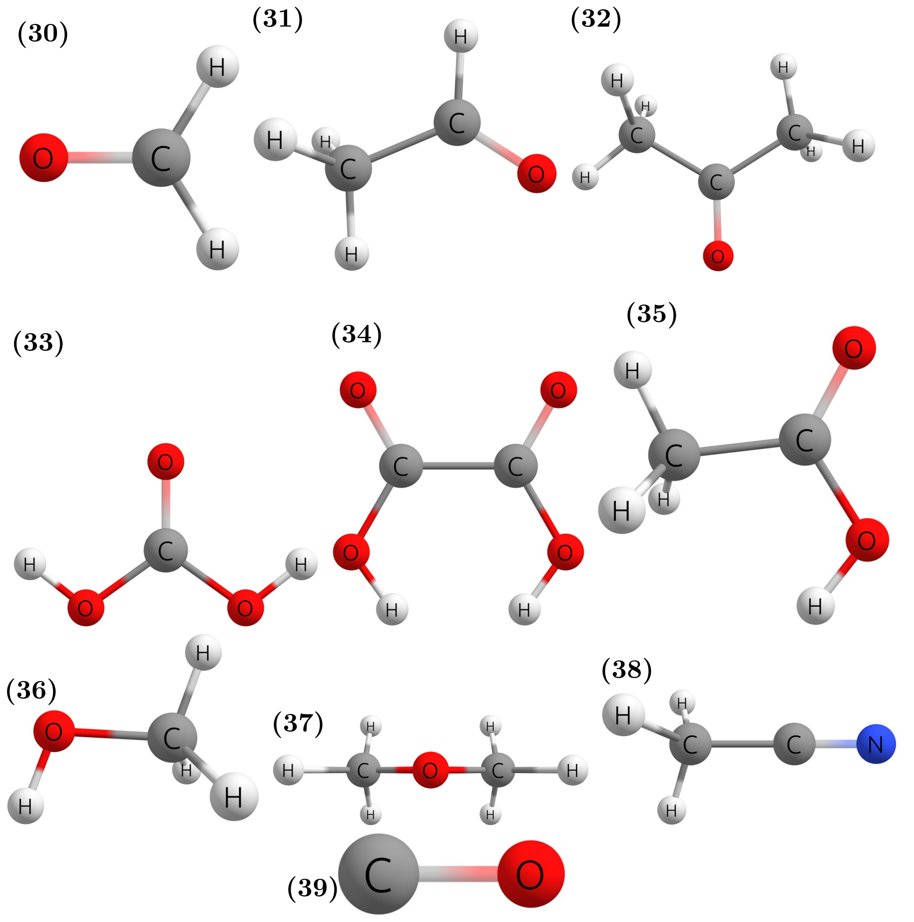
(30) **(31)** **(32)** **(33)** **(34)** **(35)** **(36)** **(37)** **(38)** **(39)**

FIGURE 6.8: H_2CO, H_5C_2O, H_6C_3O, H_2O_3C, $C_2O_4H_2$, $C_2O_2H_4$, COH_4, C_2OH_6, C_2NH_3 and CO chemical sketches.

(Organic) Heterocycles

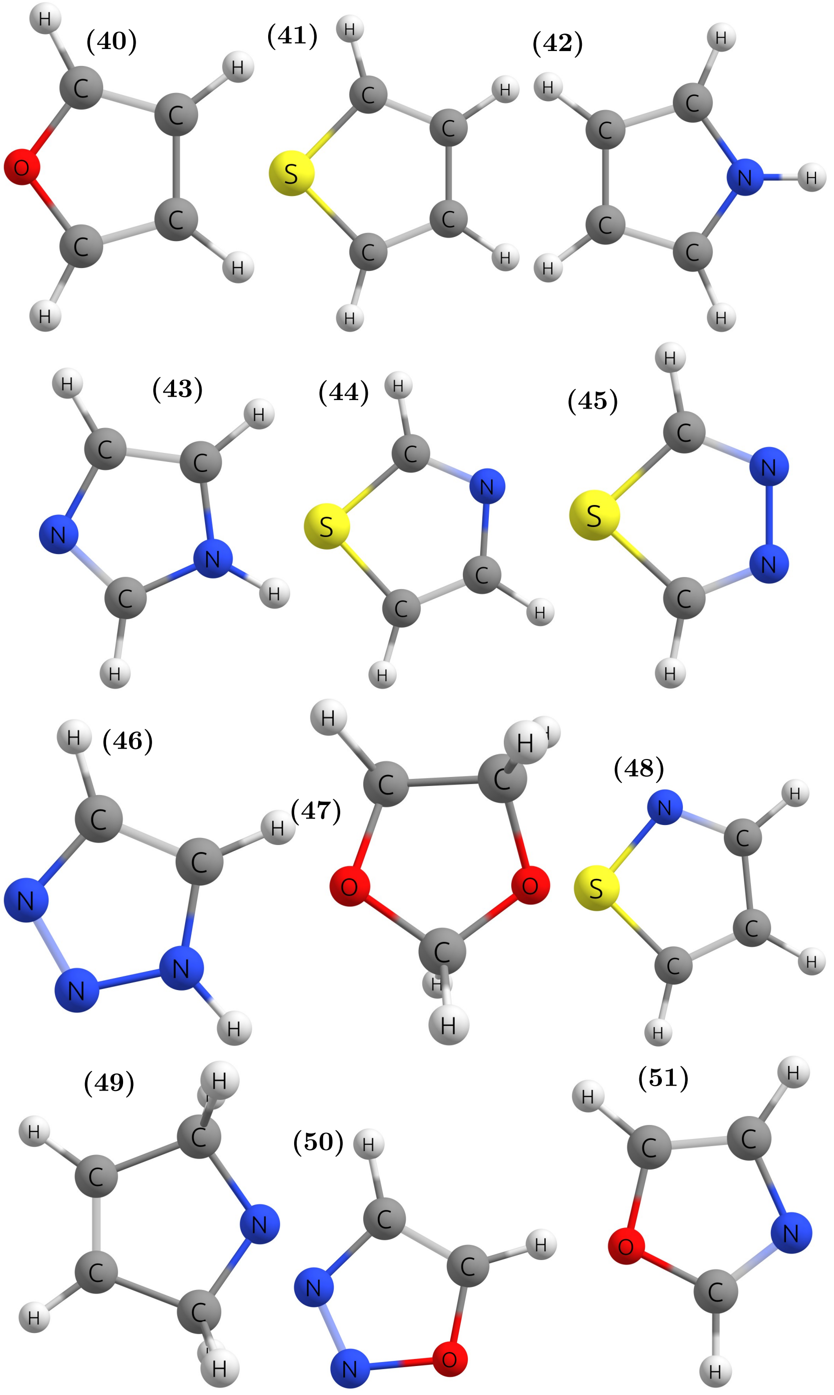

FIGURE 6.9: Furan, thiopenthene, pyrrole, imidazole, thiozole, thiadiazole, thiazole, dioxolane, isothiazole, 3-pyrroline, oxadiazole and oxazole chemical sketches.

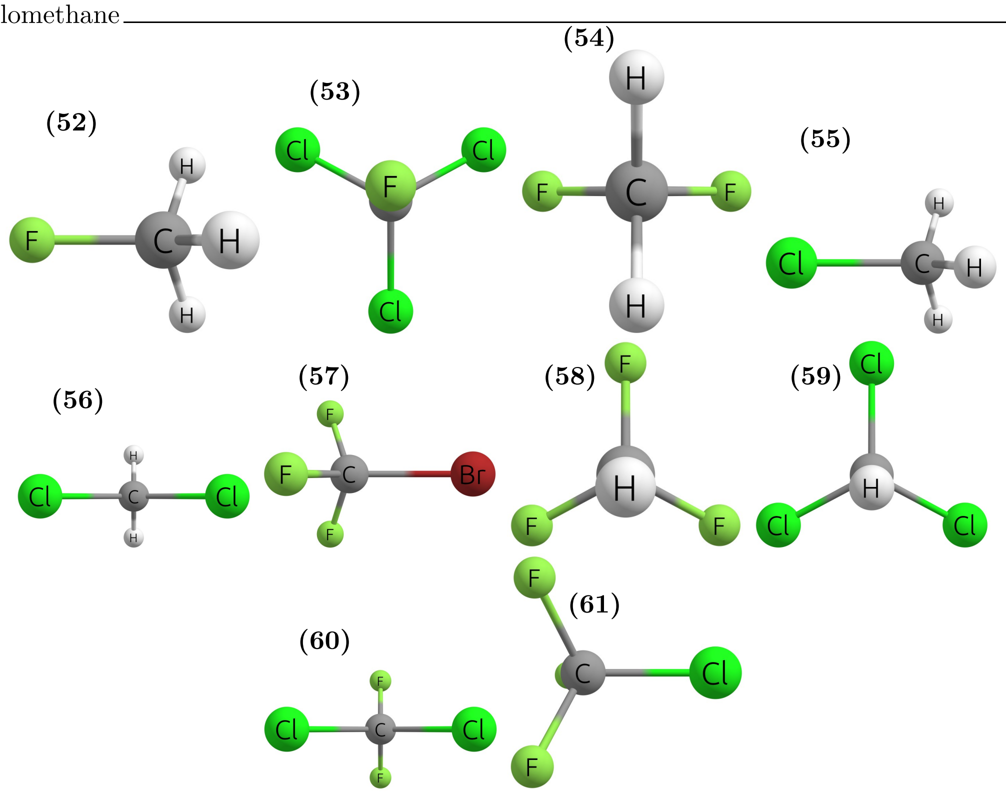

FIGURE 6.10: CFH_3, $CFCl_3$, CF_2H_2, CH_3Cl, CH_2Cl_2, CF_3Br, CF_3H, $CHCl_3$, CF_2Cl_2 and CF_3Cl chemical sketches.

6.3 Static first-order hyperpolarizability tensor at ADC and CC levels

The molecules examined below are divided into an inorganic and organic category.

6.3.1 Inorganic molecules

Starting with the inorganic series HX, X=(F, Cl, Br, OH, SH), at ADC and CC levels of theory using the aug-cc-pVTZ basis set. For all molecules, ADC(1), ADC(2), ADC(3) and CCS, CC2 and CCSD produce similar $\beta_{\alpha\beta\gamma}$ values, indicating that the first-order hyperpolarizability is already well described using a lower-order method, as seen in Figure 6.11.

For the series NaX, X=(F, Cl, Br, OH, SH), at ADC and CC levels using the aug-cc-pVTZ basis set, there is again good agreement between the pairs ADC(1)/CCS, ADC(2)/CC2 and ADC(3)/CCSD, as seen in Figure 6.12. However, the second-order methods heavily overestimate β for NaF and NaOH, and the lowest-order methods ADC(1) and CCS tend to underestimate these same components.

For the series LiX, X=(F, Cl, Br, OH, SH), at ADC and CC levels using the aug-cc-pVTZ basis set, the results are showing all the features evident for the NaX series, as could be expected, as seen in Figure 6.13.

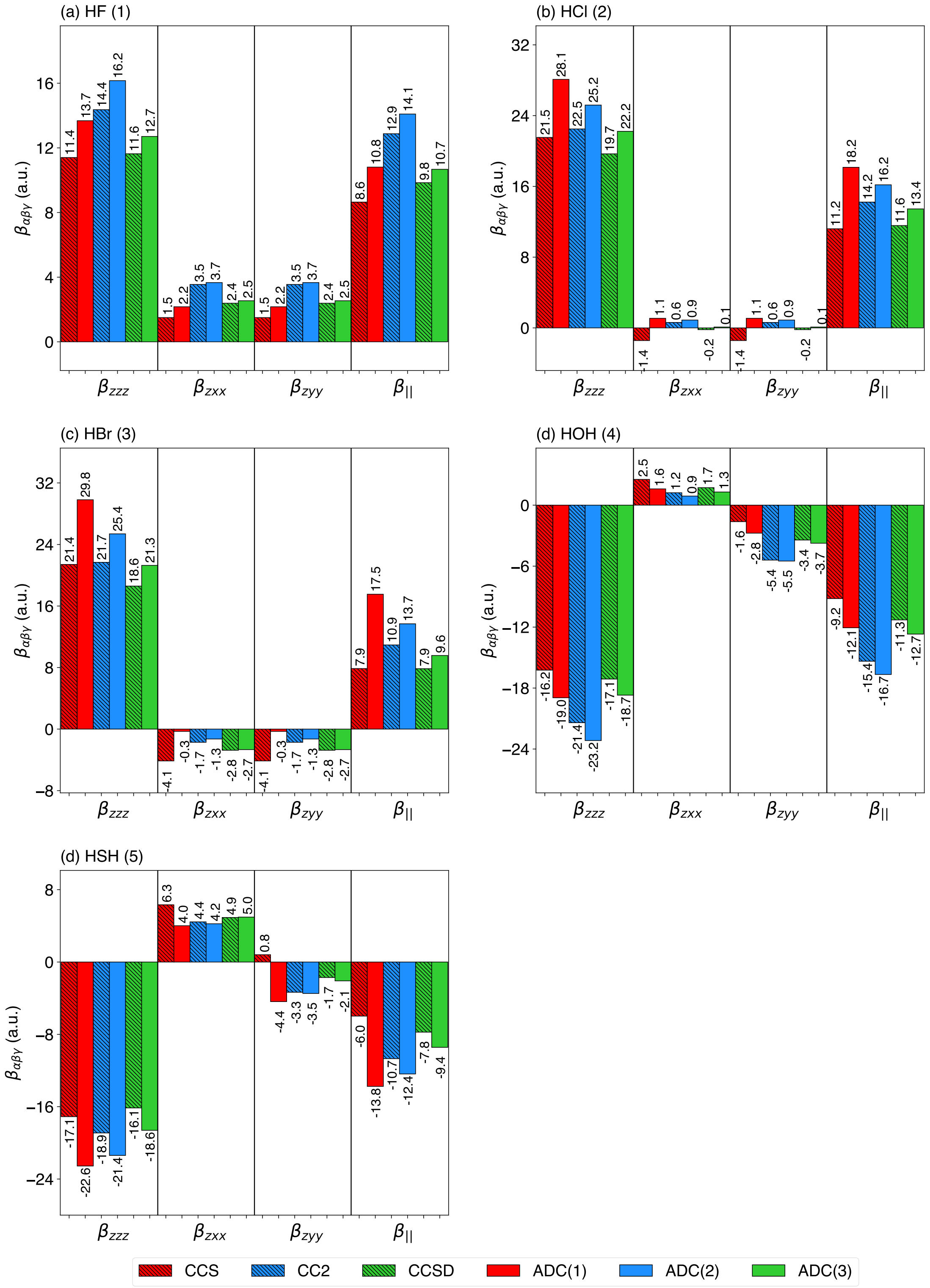

FIGURE 6.11: Components of static β at ADC and CC levels using the aug-cc-pVTZ basis set of HF, HCl, HBr, H_2O and H_2S (Fig. 6.1).

For the H_2SO_x, x=(1,2,3,4) series, ADC and CC methods compare favorably, with ADC(3) and CCSD producing near equivalent first-order hyperpolarizabilities for all systems included.

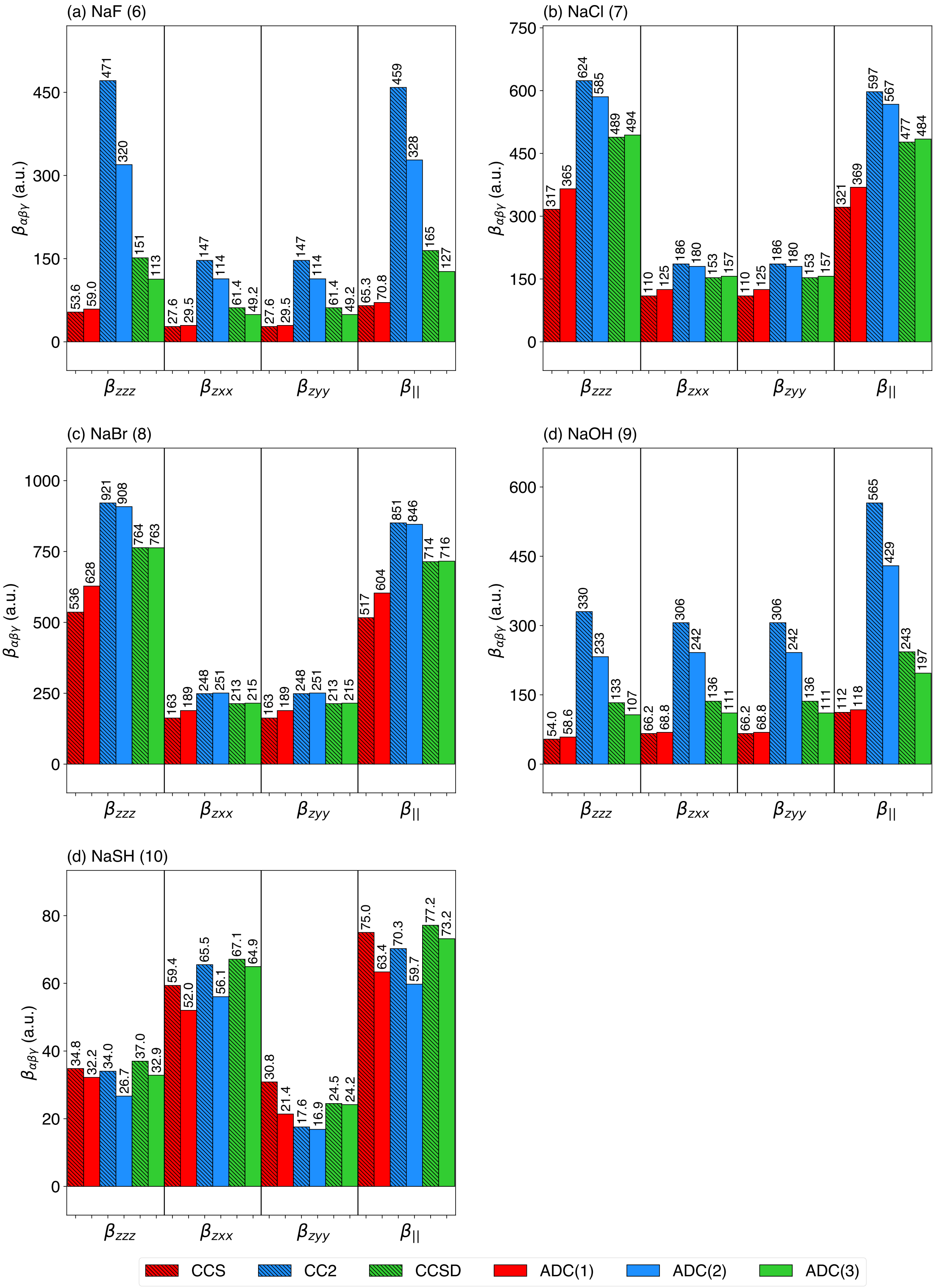

FIGURE 6.12: Components of static β at ADC and CC levels using the aug-cc-pVTZ basis set of NaF, NaCl, NaBr, NaOH and NaSH (Fig. 6.2).

For the series HNO$_x$, x=(1,2,3), there is equally good agreement between ADC and CC for the static β, as seen in Figure 6.15, with the somewhat noticeable exception of β_{zxx} of HNO$_2$ at

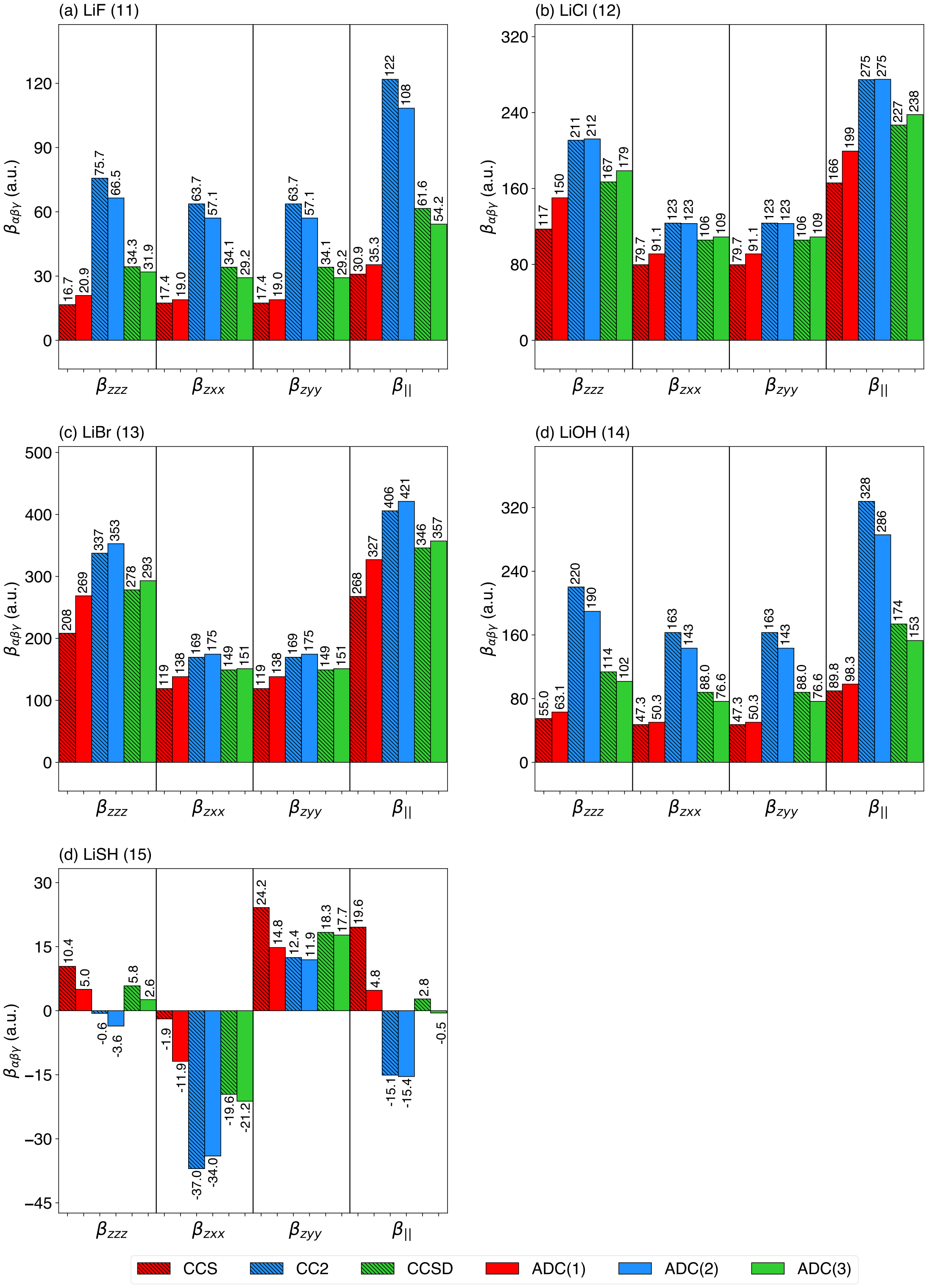

FIGURE 6.13: Components of static β at ADC and CC levels using the aug-cc-pVTZ basis set of LiF, LiCl, LiBr, LiOH and LiSH (Fig. 6.3).

ADC(2) level which is heavily overestimated (-17.7 a.u.) as compared to the same component at CC2 level (-3.4 a.u.). Although, when comparing the isotropic value at these same levels of

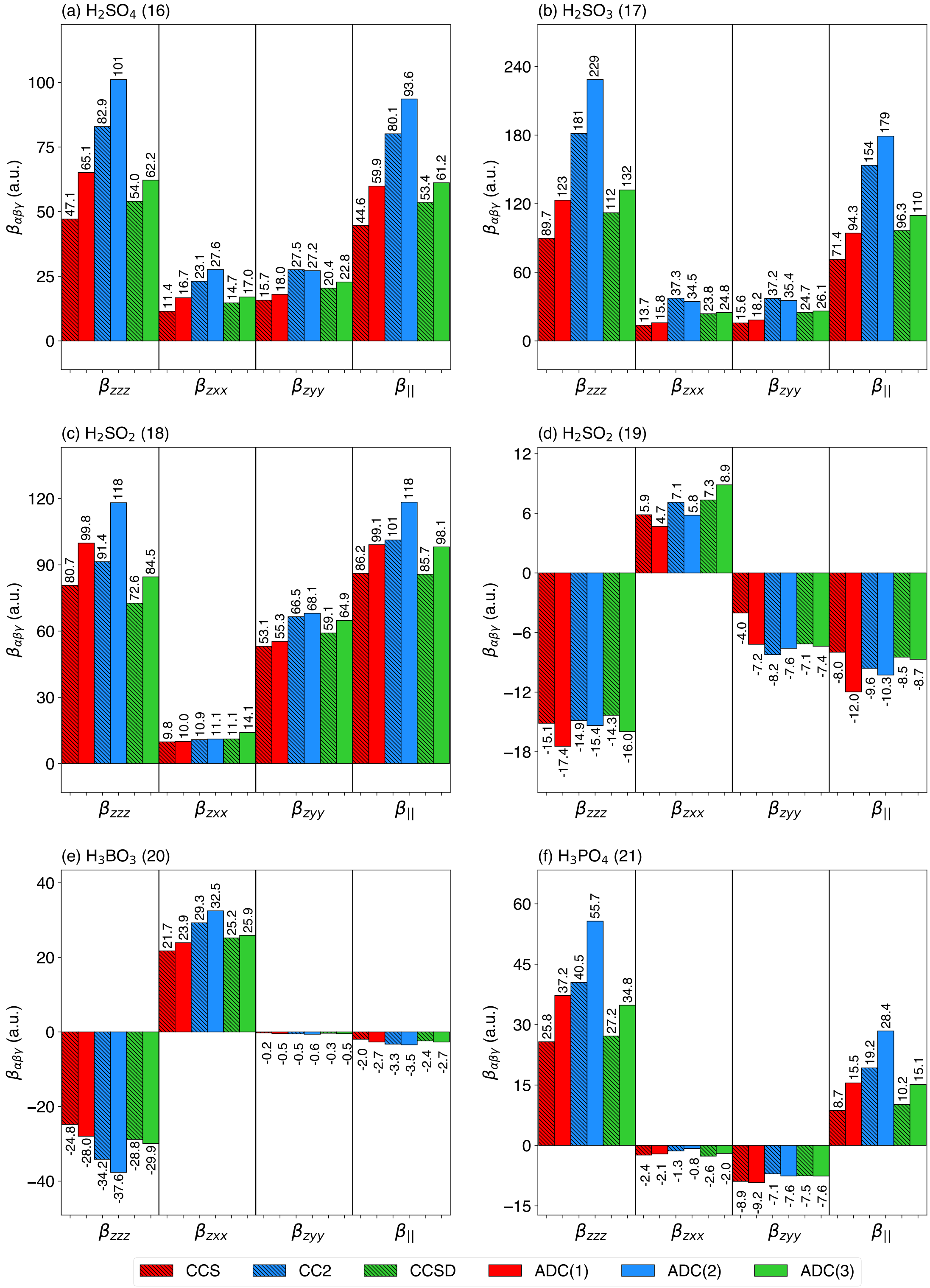

FIGURE 6.14: Components of static β at ADC and CC levels using the aug-cc-pVTZ basis set of H_2SO_4, H_2SO_3, H_2SO_2 and H_2SO, H_3BO_3 and H_3PO_4 (Fig. 6.4 and 6.5).

theory, ADC(2) is in closer agreement to both ADC(3) and CCSD as compared to CC2.

Another case is that of N_2O, where ADC(2) heavily overestimates β_{zzz}, calculating it to

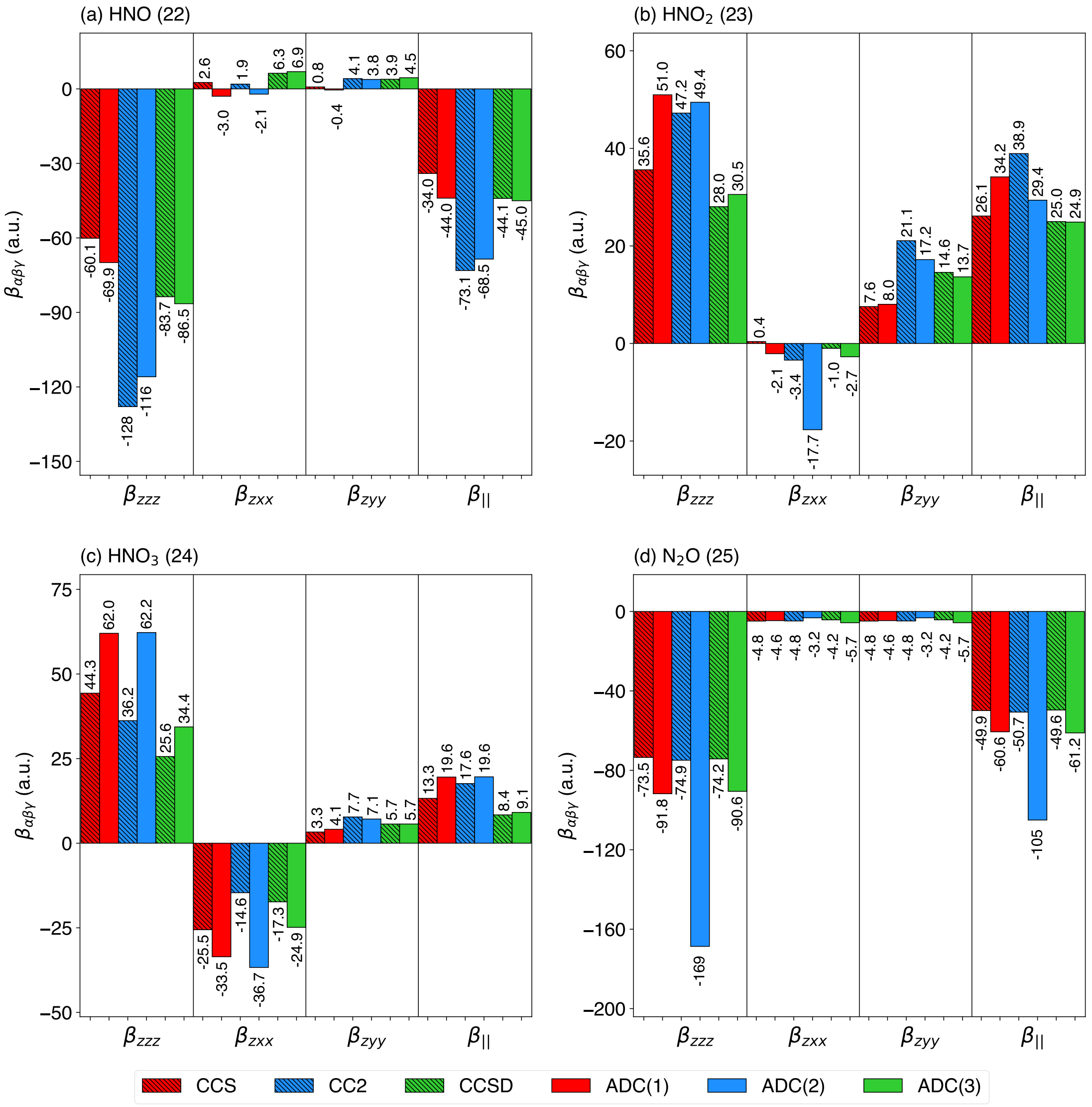

FIGURE 6.15: Components of static β at ADC and CC levels using the aug-cc-pVTZ basis set of HNO, HNO$_2$, HNO$_3$ and N$_2$O (Fig. 6.6).

about twice as large as the same value at CC2 level, resulting in an isotropic value that is likewise twice as large as at CC2 level.

For the similar series HNS$_x$, x=(1,2,3), near identical trends emerge, as seen in Figure 6.16. For HNS, ADC(2) β_{zzz} is roughly twice as large as at CC2 level, calculated to 53.6 a.u. compared to 24.7 a.u., although the isotropic values are in better agreement at 85.5 a.u. compared to 64 a.u. Overall, β at ADC levels of theory are slightly overestimated compared to the same values at corresponding CC levels. For HNS$_2$, there is good enough agreement between the methods to elude discussion.

For HNS$_3$, β at ADC levels is again overestimated compared with corresponding CC level. Here, β_{zzz} at CC2 level is calculated to 10.3 a.u., whereas at ADC(2) level it is calculated to -69.7 a.u. While this is clearly a nontrivial difference, the isotropic values are in fact in excellent agreement at 23.1 a.u. and 22.7 a.u. at CC2 and ADC(2) level, respectively.

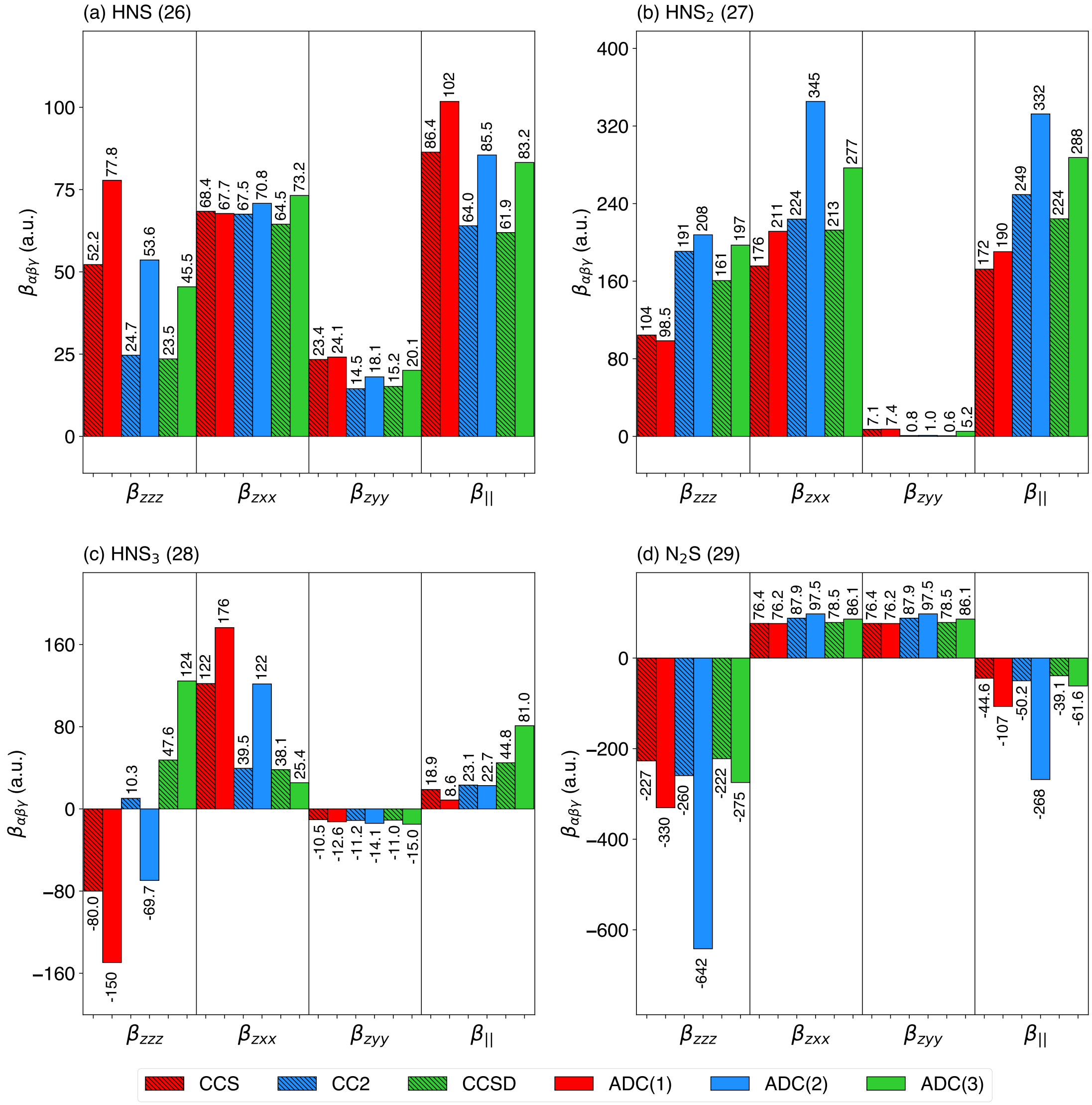

FIGURE 6.16: Components of static β at ADC and CC levels using the aug-cc-pVTZ basis set of HNS, HNS_2, HNS_3 and N_2S (Fig. 6.7).

As was the case N_2O, β of N_2S at ADC(2) level of theory is heavily overestimated, due to the similarity between the molecules.

6.3.2 Organic molecules

For the organic molecules, the trends are identical to those discovered for the inorganic molecules, i.e., the ADC method produces equivalent first-order hyperpolarizabilities as those at corresponding CC levels.

In summery, for most molecules, the trend ADC(1)-ADC(2)-ADC(3) mirrors the trend of the series CCS-CC2-CCSD for the calculated static $\beta_{\alpha\beta\gamma}$ component. As could be expected, the pairs ADC(1)/CCS, ADC(2)/CC2, ADC(3)/CCSD are generally in closest agreement, due to the

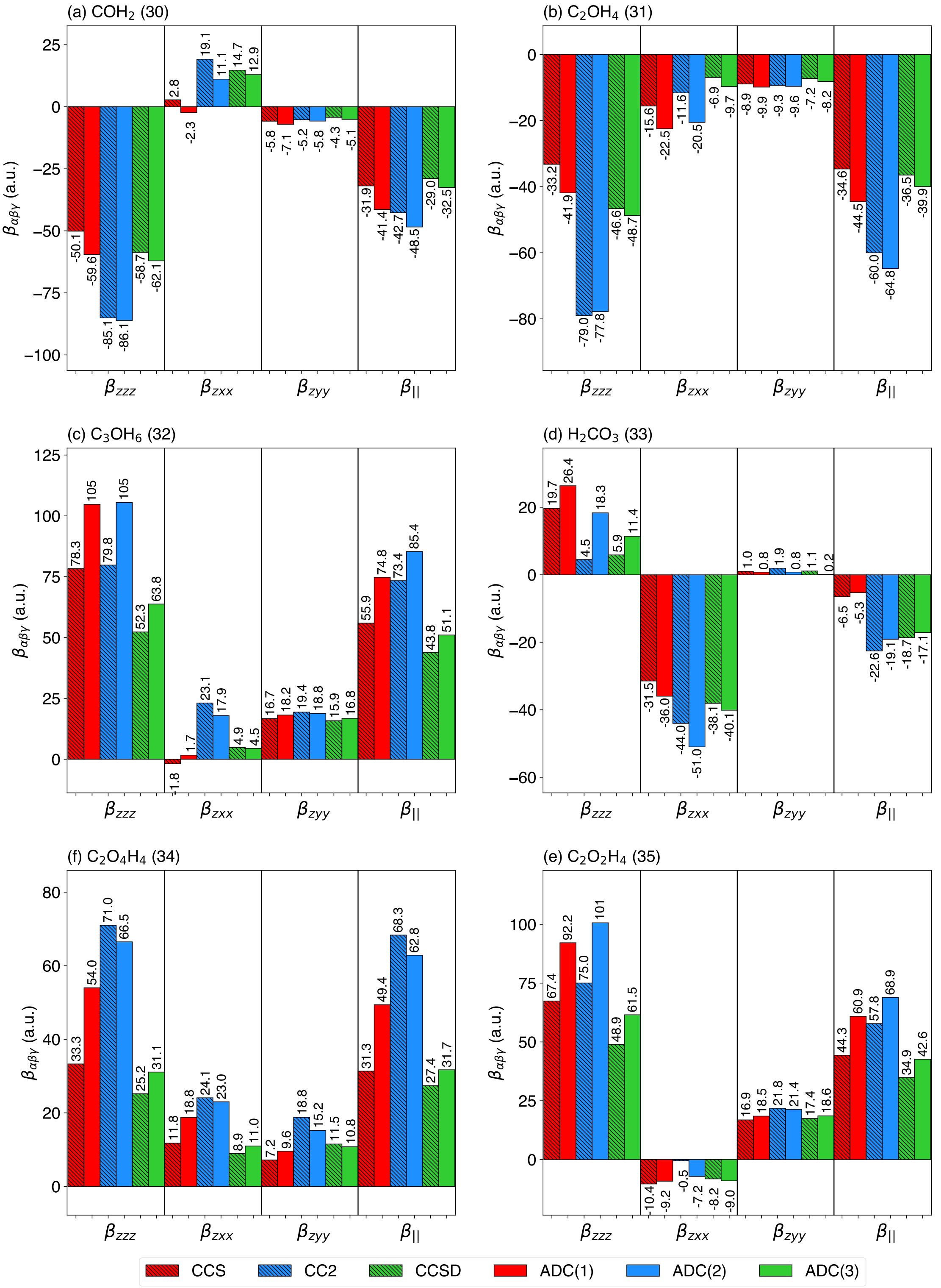

FIGURE 6.17: Components of β of organic molecules at ADC and CC levels using the aug-cc-pVTZ basis set, molecular sketches shown in Fig. 6.8

similarity between the methods. In all cases, the line drawn ADC(1)-ADC(3) is near parallel to the line CCS-CCSD which indicates similar convergence behaviour.

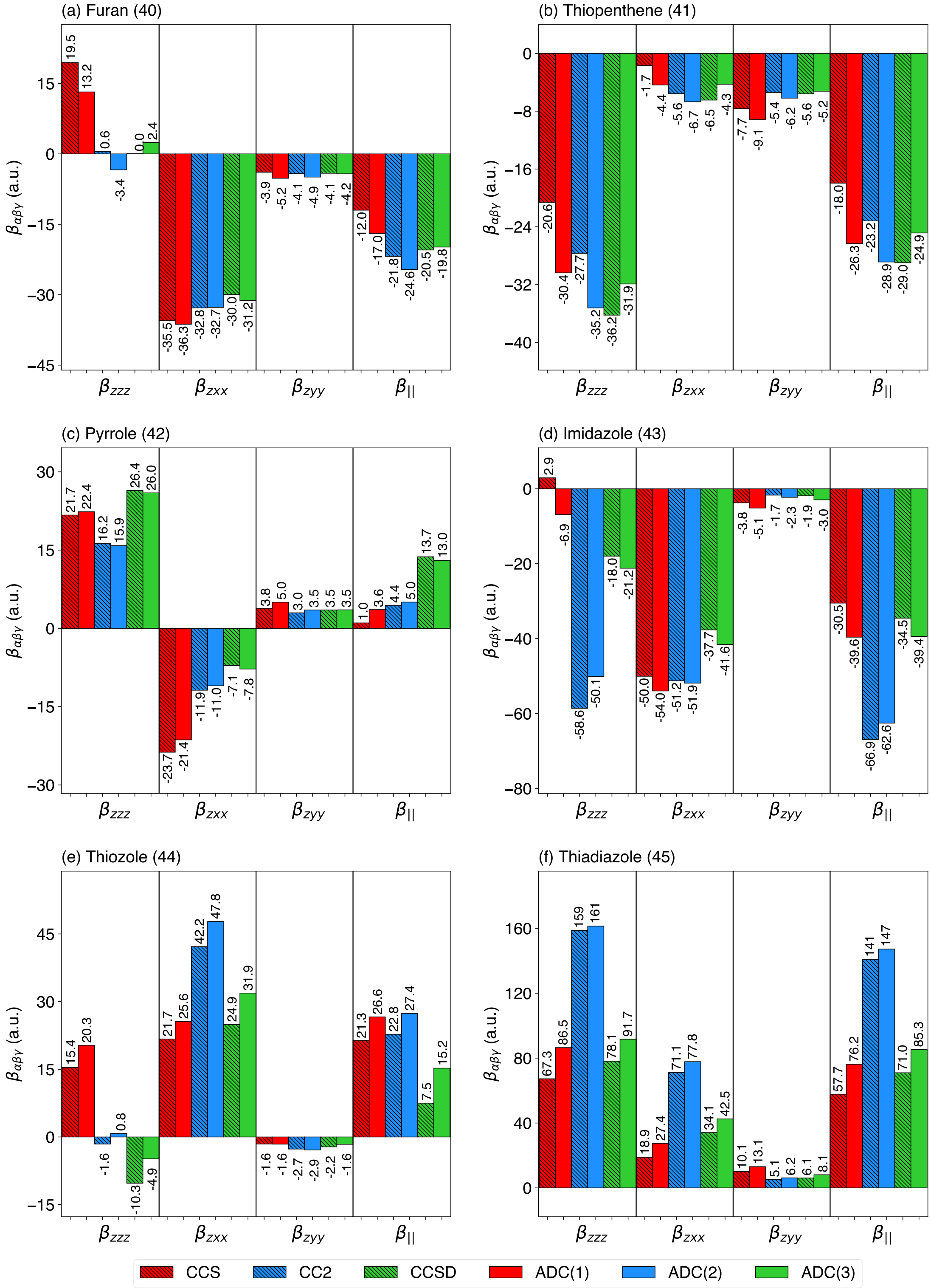

FIGURE 6.18: Components of β of organic molecules at ADC and CC levels using the aug-cc-pVTZ basis set, molecular sketches shown in Fig. 6.8

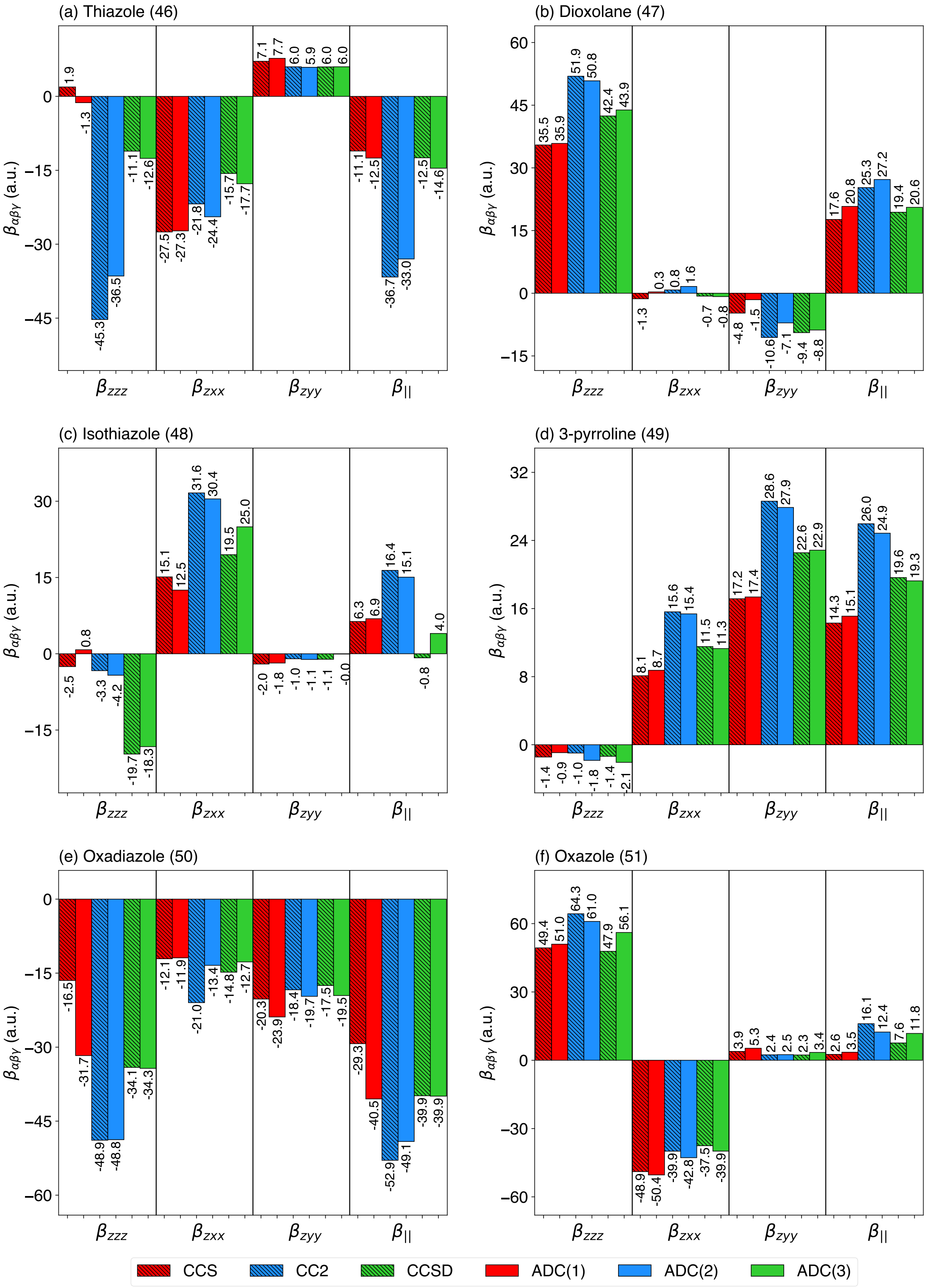

FIGURE 6.19: Components of β of organic molecules at ADC and CC levels using the aug-cc-pVTZ basis set, molecular sketches shown in Fig. 6.8

6.4 Dynamic first-order hyperpolarizability at ADC(n) levels compared with experiment

To gauge the accuracy of the frequency dependent first-order hyperpolarizability (at SHG conditions) afforded at the ADC(1), ADC(2) and ADC(3) levels of theory, β_{SHG} was calculated with a perturbation of 694.3 nm for the small organic molecules CO, HF, HCl, H_2O, H_2S and NH_3 using the j-aug-cc-pVXZ, j=s,d, X=T,Q basis sets and CH_3CN, CH_3F, $CFCl_3$, CH_2F_2, CH_3Cl, CH_2Cl_2, CH_3OH $(CH_3)_2O$, CF_3Br, CF_3H, $CHCl_3$, CF_2Cl_2 and CF_3Cl using the aug-cc-pVXZ, X=T,Q basis sets.

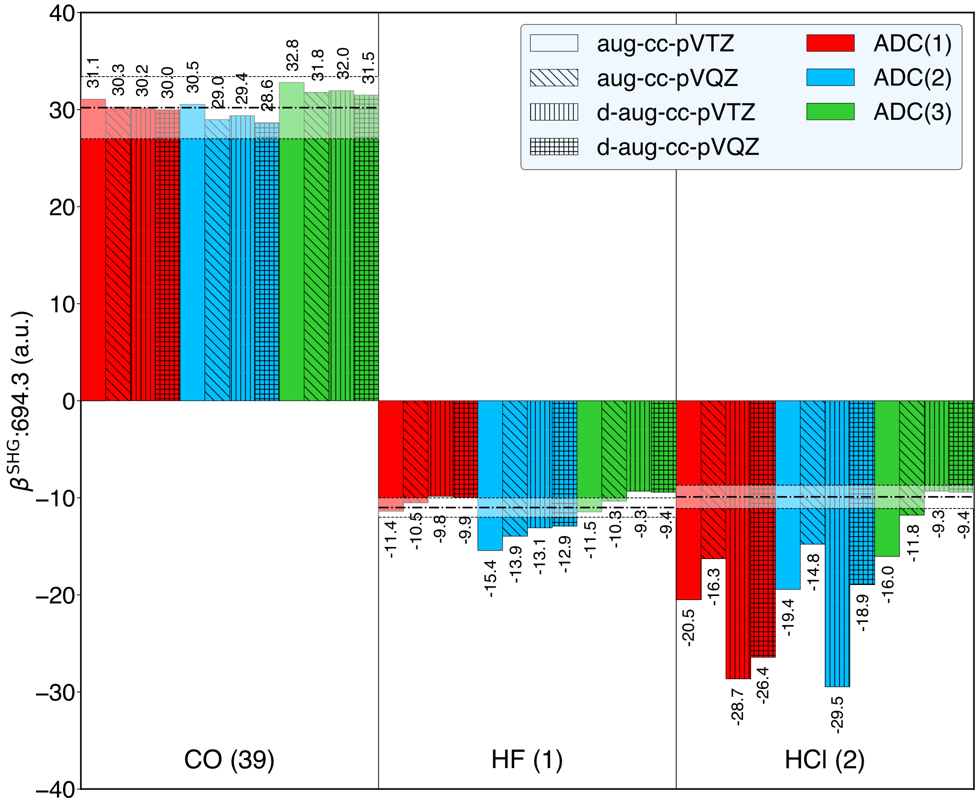

FIGURE 6.20: β_{SHG} (a.u.) at 694.3 nm of CO, HF, HCl at ADC levels using the Dunning basis sets. Experimental values are from Ref. 307.

For the linear diatomic molecules CO, HF and HCl, Figure 6.20, it is possible to approach the complete basis set limit using d-aug-cc-pVQZ at the higher end. Starting with CO, at the ADC(1)/d-aug-cc-pVQZ level of theory the theoretical β_{SHG} of 30.0 a.u. matches excellently with experiment (within $\sim$ 0.5% of 30.2 ± 3.2 a.u.) which is likely due to fortuitous error cancellation. At the ADC(2)/d-aug-cc-pVQZ and ADC(3)/d-aug-cc-pVQZ levels of theory, β_{SHG} is calculated to 28.6 a.u. (within $\sim$ 6% of experiment) and 31.5 a.u. (within $\sim$ 4% of experiment), which indicates a good convergence with increasing order.

For the HF molecule, at the ADC(1)/d-aug-cc-pVQZ level of theory the theoretical β_{SHG} of -9.9 a.u. again agrees favourably with experiment at -11.0 ± 1.0 a.u. (to within $\sim$ 11%), as before this is attributable to fortuitous error cancellation. At the ADC(2)/d-aug-cc-pVQZ and ADC(3)/d-aug-cc-pVQZ levels of theory, β_{SHG} is calculated to 12.9 a.u. and 9.4 a.u., respectively, both being within $\sim$ 17% of the experimental value.

For HCl, at the ADC(1)/d-aug-cc-pVQZ level of theory the theoretical β_{SHG} of -26.4 a.u.

which compared to the experimental value of -9.9 ± 1.2 a.u. is overestimated by a factor of ~ 2.5. At ADC(2)/d-aug-cc-pVQZ level β_{SHG} is calculated to -18.9 a.u., overestimating the measured value by a factor of ~ 2. Lastly, at ADC(3)/d-aug-cc-pVQZ level, β_{SHG} is calculated at -9.4 a.u. which excellently captures experiment to within $\sim 5\%$.

For the triatomic molecules H_2O and H_2S and NH_3, collected in Figure 6.21, starting with H_2O at ADC(1)/d-aug-cc-pVQZ level we see an excellent agreement with β_{SHG} calculated to -21.6 a.u., which is within $\sim 2\%$ of experiment at -22.0 ± 0.9 a.u. As was the case for CO and HF, this is attributable to fortuitous error cancellation. At ADC(2)/d-aug-cc-pVQZ level, β_{SHG} is overestimated by $\sim 50\%$ calculated at -33.2 a.u. and lastly at ADC(3)/d-aug-cc-pVQZ β_{SHG} is overestimated by $\sim 9.5\%$ calculated to -24.1 a.u.

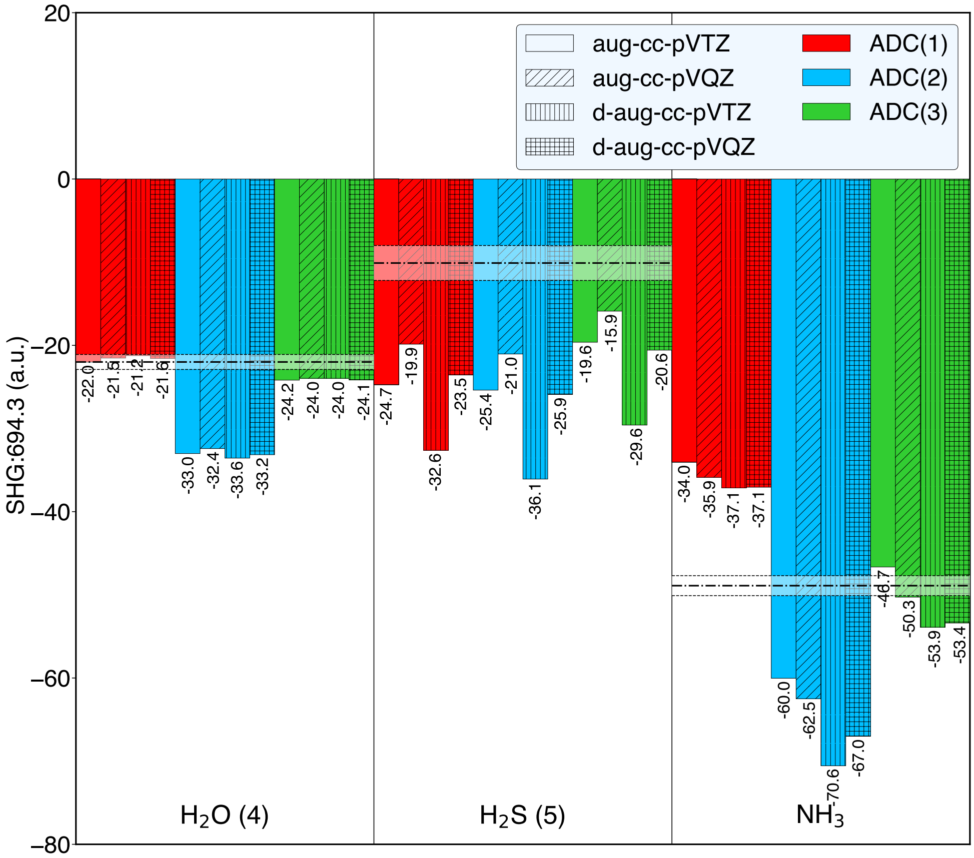

FIGURE 6.21: β_{SHG} (a.u.) at 694.3 nm of H_2O, H_2S and NH_3 at ADC levels using the Dunning basis sets. Experimental values are from Ref. 307.

For H_2S, at ADC(1)/d-aug-cc-pVQZ level β_{SHG} is overestimated by a factor of ~ 2.3, calculated to -23.5 a.u. compared with -10.1 ± 2.1 a.u. of experiment. Similar results occur at ADC(2)/d-aug-cc-pVQZ and ADC(3)/d-aug-cc-pVQZ levels where β_{SHG} is overestimated by a factor of ~ 2.6 (-25.9 a.u.) and ~ 2 (-20.6 a.u.) for ADC(2) and ADC(3), respectively.

For NH_3, at ADC(1)/d-aug-cc-pVQZ level, β_{SHG} is underestimated by $\sim 32\%$ calculated to 37.1 a.u. compared with experiment at 48.9 ± 1.2 a.u. At ADC(2)/d-aug-cc-pVQZ level, β_{SHG} is instead overestimated by $\sim 37\%$ at -67.0 a.u. and lastly at ADC(3)/d-aug-cc-pVQZ level, there is reasonably good agreement with experiment with β_{SHG} overestimated by $\sim 9\%$ calculated at

-53.4 a.u.

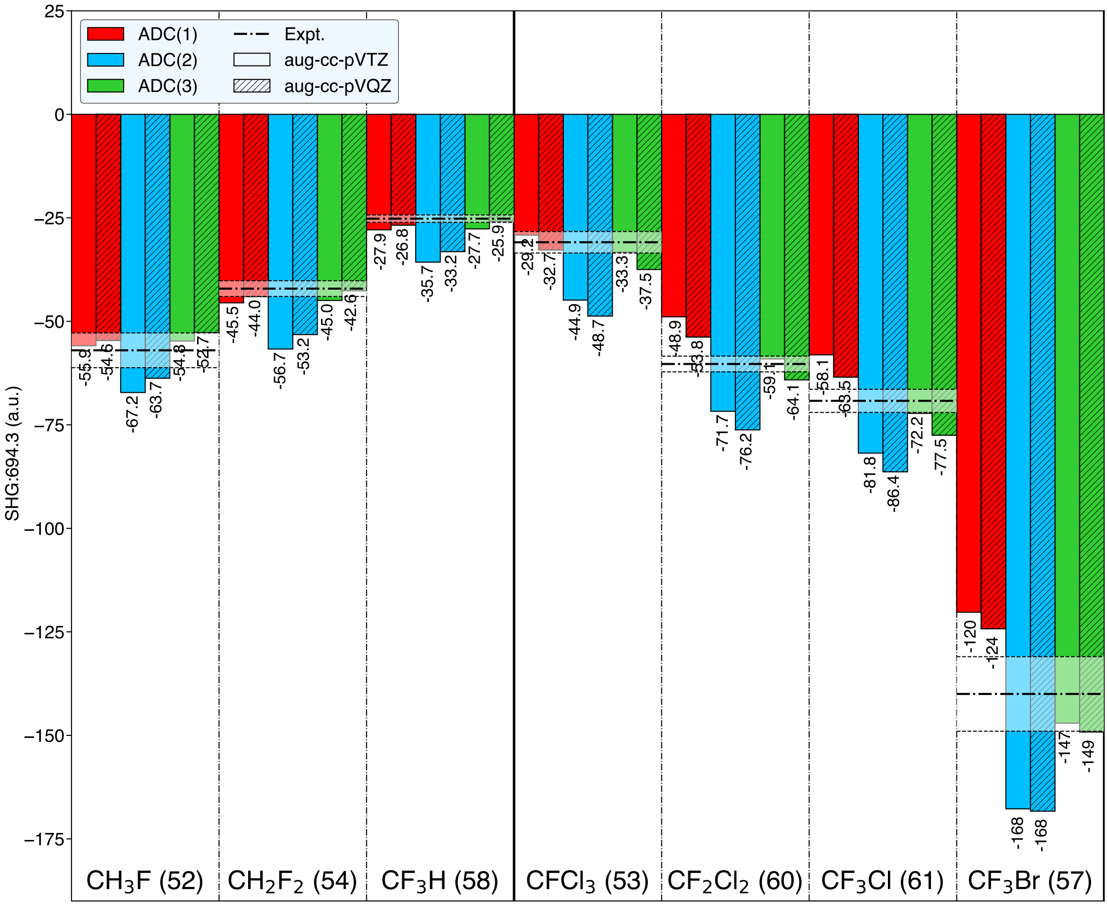

FIGURE 6.22: β_{SHG} (a.u.) at 694.3 nm of 13 organic molecules computed at ADC levels of theory using the aug-cc-pVTZ and aug-cc-pVQZ basis sets. Experimental values are from Ref. 307. Molecular sketches shown in Fig. 6.10

For the heavier molecules, Figure 6.23, we limit the basis set to aug-cc-pVQZ on the higher end and start at the flourinated methane series CH_nF_m, m=(1,2,3), n=4-m. Beginning with CH_3F, at ADC(1) level, the computed β_{SHG} of -54.6 a.u. is well within the error margins of the experimental β_{SHG} of 57.0 ± 4.2 a.u. which as for previous cases likely arise from the completeness of the one particle basis set and cancellation of terms. At ADC(2) level, β_{SHG} is overestimated by $\sim$ 12%, computed to -63.7 a.u. and falling slightly outside the margins of error. Finally, at ADC(3) level, the calculated β_{SHG} of -52.7 a.u. is slightly underestimated ($\sim$ 8%) with respect to measurement.

For CH_2F_2, unexpectedly identical trends emerge with the computed β_{SHG} of -44.0 a.u., -53.2 a.u., -42.6 a.u. at ADC(1), ADC(2) and ADC(3) levels of theory, respectively, which should be compared to the experimental β_{SHG} of -42.1 ± 1.9 a.u.

Similarly, for CHF_3, the computed β_{SHG} of -26.8 a.u., -33.2 a.u., -25.9 a.u. at ADC(1), ADC(2) and ADC(3) levels of theory, respectively, which when compared to the experimental

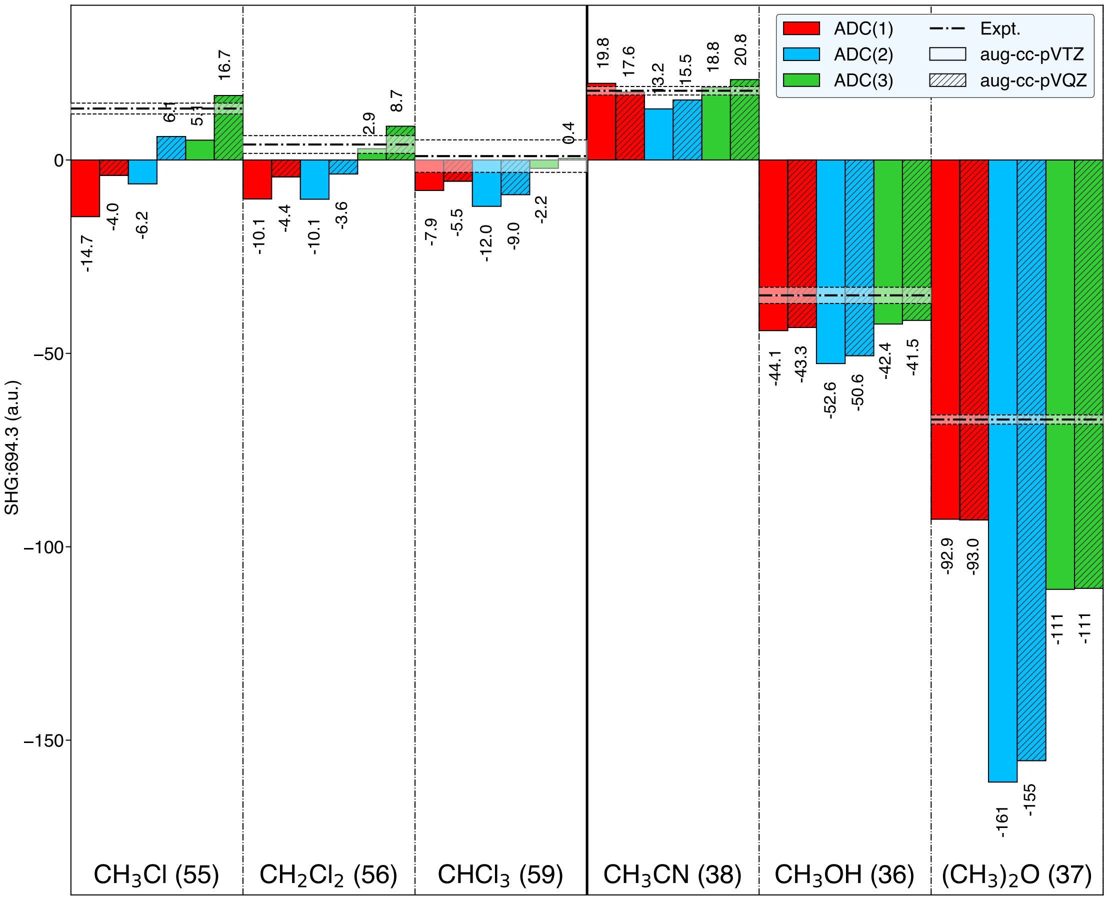

FIGURE 6.23: β_{SHG} (a.u.) at 694.3 nm of 13 organic molecules computed at ADC levels of theory using the aug-cc-pVTZ and aug-cc-pVQZ basis sets. Experimental values are from Ref. 307. Molecular sketches shown in Fig. 6.10

value of -25.2 ± 0.9 a.u. demonstrate the same behaviour as for CH_2F_2 and CH_3F.

For the series CF_nCl_m, m=(1,2,3), n=(4-m), starting with $CFCl_3$ at ADC(1) level the calculated β_{SHG} at -32.7 a.u. is within the margins of error of experiment measured at -30.9 ± 2.6 a.u. for identical reasons to the previous cases. At ADC(2) level the calculated β_{SHG} signal is overestimated by $\sim$ 58% at -48.7 a.u. and at ADC(3) level the calculated β_{SHG} is overestimated by $\sim$ 21% at -37.5 a.u. showing the expected convergence behaviour of ADC(2)-ADC(3).

For CF_2Cl_2, CF_3Cl and CF_3Br, identical trends are displayed as for $CFCl_3$ which is unsurprising due to the related structures. Starting with CF_2Cl_2 the computed β_{SHG} of -53.8 a.u., -76.2 a.u. and -64.1 a.u. at ADC(1), ADC(2) and ADC(3) levels, respectively, compares favorably to the experimental value of -60.3 ± 1.9 a.u. Furthermore, for CF_3Cl the computed β_{SHG} of -63.5 a.u., -86.4 a.u. and -77.5 a.u. at ADC(1), ADC(2) and ADC(3) levels, respectively, again agrees favorably to the experimental value of -69.2 ± 2.8 a.u. Lastly, for CF_3Br the computed β_{SHG} of -120 a.u., -168 a.u. and -149 a.u. at ADC(1), ADC(2) and ADC(3) levels, respectively, show the same trends as the previous cases with ADC(1) below, ADC(2) above and ADC(3) in close agreement with -140 ± 9.0 a.u measured.

For the series CH_nCl_m, m=(1,2,3), n=4-m, beginning with CH_3Cl, at the ADC(1) level of theory the sign of the β_{SHG} signal is incorrectly predicted as negative at -4.0 a.u., while at ADC(2) level the correct sign is obtained with β_{SHG} calculated to 6.1 a.u. and lastly at ADC(3) level reasonable agreement with experiment is achieved with β_{SHG} calculated to 16.7 a.u. In this case its clear that the aug-cc-pVTZ basis is inadequate and due to the large shift at higher basis its unclear whether aug-cc-pVQZ is close to the basis set limit.

For CH_2Cl_2, a similar trend is observed with β_{SHG} calculated to -4.4 a.u., -3.6 a.u. and 8.7 a.u. at ADC(1), ADC(2) and ADC(3) level, respectively which should be compared to 4.0 ± 2.3 a.u. of measurement. Likewise, large shifts are observed with increasing basis for this molecule with ADC(2) failing to predict the correct sign even at aug-cc-pVQZ.

Last in this series, $CHCl_3$, β_{SHG} is calculated as -5.5 a.u., -9.0 a.u. and 0.4 a.u. at ADC(1), ADC(2) and ADC(3) level, respectively. Here ADC(3) is in reasonable agreement with 1.2 ± 2.6 a.u. of experiment, though for such a small measured value its hard to make qualitative statements.

For CH_3CN, already at ADC(1) level β_{SHG} is calculated to 17.6 a.u. which is within $\sim 2\%$ of experiment at 17.9 ± 1.1 a.u., likely due to cancellation of terms. At ADC(2) level β_{SHG} is calculated to 15.5 a.u., which underestimates the measured value by $\sim 15\%$ and lastly at ADC(3) level β_{SHG} is overestimated by $\sim 16\%$ calculated to 20.8 a.u.

For CH_3OH, β_{SHG} is calculated to -43.3 a.u., -50.6 a.u. and -41.5 a.u. at ADC(1), ADC(2) and ADC(3) level, respectively with ADC(3) approaching closest to the experimental value of -35 ± 2.1 a.u.

For $(CH_3)_2O$, β_{SHG} is calculated to -92.9 a.u., -155 a.u. and -111 a.u. at ADC(1), ADC(2) and ADC(3) level, respectively. Here ADC(2) heavily overestimates β_{SHG} by a factor of ~ 2.3 compared with experiment at -67.1 ± 1.2 a.u..

6.5 Dynamic β_{HRS} of NH_3

As a proof-of-concept the dynamic β_{HRS} signal above the first two-photon absorption resonance energy of ammonia, NH_3, was calculated at ADC(2)/aug-cc-pVTZ and ADC(3)/aug-cc-pVTZ level of theory using a damping factor of 0.124 eV. The spectra, consisting of both the real and imaginary part of β_{HRS} are collected in Figure 6.24b and Figure 6.24c. The real and dispersive part, $\beta_{\text{HRS}}^{\text{Re}}$, steadily increases towards $\frac{1}{2}\omega_{01}$, as expected, reaching a local minimum of ~ 483 a.u. at 394 nm, then sharply decreases when passing through the two-photon absorption point at ω_{21} =and subsequently increasing again reaching the second local minimum of 550 a.u. at ~ 379 nm, showing the typical behaviour passing through resonance. At the same time the imaginary and absorptive part $\beta_{\text{HRS}}^{\text{Im}}$ shows the expected local maximum at $\frac{1}{2}\omega_{01}$, reaching a value of 1025 a.u. at ~ 386.5 nm. At ADC(3) level the same features are observed, with the two dispersive maxima occurring at 382 nm and 367 nm with 290 a.u. and 356 a.u. and the absorptive part reaching a local maximum of 635 a.u. at the two-photon absorption point of 374 nm.

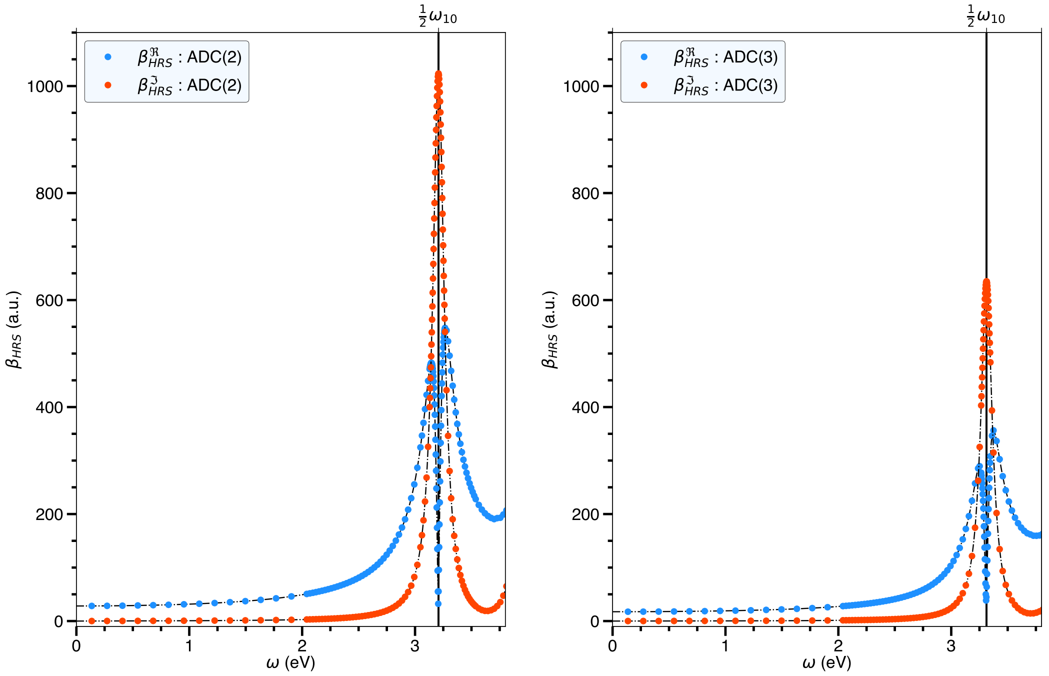

FIGURE 6.24: HRS spectra of ammonia, NH_3, at the ADC(2) and ADC(3) levels of theory using the aug-cc-pVTZ basis set with a damping constant of $\Gamma = 1000\ \text{cm}^{-1}$.

6.6 Summary

In the calculation of first-order hyperpolarizabilities with both static and dynamic perturbations, ADC(n) provides a hierarchy of *ab initio* methods that prove highly capable. For the several organic and inorganic molecules evaluated in this work, the static β at ADC(n) levels of theory are directly comparable with CC methods of similar scaling. Furthermore, the trend of ADC(1)→ADC(2)→ADC(3) mirror that of CCS→CC2→CCSD, indicating consistent convergence behaviour.

With a perturbation of 694.3 nm, β_{SHG} for the di- and tri-atomic molecules CO, HF, HCl, H_2O, H_2S and NH_3 calculated at ADC(1), ADC(2) and ADC(3) levels agree favorably with those same quantities measured experimentally. Here, ADC(1) and ADC(3) often produce close β_{SHG} values which can be attributed to fortuitous cancellation of terms. For the heavier molecules CH_3F, CH_2F_2, CF_3H, $CFCl_3$, CF_2Cl_2, CF_3Cl, CF_3Br, CH_3Cl, CH_2Cl_2, $CHCl_3$m CH_3CN, CH_3OH and $(CH_3)O$, β_{SHG} calculated at ADC(1) and ADC(3) again agree excellently with measurement. For these molecules a very large one-electron basis set was often required to get the correct sign of β_{SHG}, with even the aug-cc-pVTZ basis set not being sufficient. In most cases, ADC(2) overestimates the β_{SHG} signal by $\sim 10\%$. Furthermore, the hyper-Rayleigh scattering of NH_3 computed at the ADC(2) and ADC(3) levels of theory demonstrated the ability to calculate first-order hyperpolarizabilities in the two-photon resonant region. Here, the typical dispersion/absorption behaving passing through resonance was observed.

This chapter concludes with another property obtainable at the ADC(1), ADC(2) and ADC(3) levels of theory. An obvious future extension to this work is the inclusion of solvent effects, which are very important when simulating HRS spectra, commonly measured in solution.

Chapter 7

Conclusion

In this dissertation, five spectroscopies, ECD, ES-ECD, TPCD, SHG and HRS, have been theoretically described and implemented at the ADC(n) levels of theory.

In Chapter 3, expressions for the rotatory strength in the length and velocity gauges within the ADC/ISR formalism as described in Section 2.6.2, were used to simulate the ECD spectra of *R*-methyloxirane, *R*-methylthiirane and their dimethylated counterparts as well as H_2O_2 and H_2S_2. These simulated spectra were then compared to the same spectra calculated at CC levels of theory and with experimental gas-phase ECD spectra. At ADC levels of theory, these spectra were shown to be of similar quality to corresponding the CC level. Furthermore, for the majority of these molecular systems, ADC(2) was shown to adequately reproduce all major bands in the experimental gas-phase ECD spectra, with the exception of dimethylthiirane. Next, simulation of solvent effects by employment of PCM was demonstrated for the water solvated L-epinephrine enantiomer. Here, inclusion of PCM in the simulated ECD spectrum at the ADC(2) level, greatly improved the theoretical description of the spectral features of the experimental solution ECD spectrum, thus exemplifying one available method to account for solvent effects in the calculation of chiroptical properties using ADC(n). Lastly, the ECD spectra of the bicyclic ketones (1*R*)-camphor, (1*R*)-norcamphor and (1*R*)-fenchone, were simulated at ADC(2) and ADC(3) level. For all three molecules, a remarkably good agreement between the calculated spectra and experimentally measured gas-phase ECD spectra was observed. Moreover, at ADC(2) level, all major spectral features were reproduced, albeit energetically shifted. The origin-dependence of the length-gauge formulation of the rotatory strength at the ADC(1), ADC(2) and ADC(3) levels of theory were shown to be of similar sensitivity as those of CCS, CC2 and CCSD levels of theory, as demonstrated for the case of *R*-methyloxirane. To summarize this chapter, the ADC(n) method has been shown to be excellent in reproducing the ECD spectra of small to medium-sized chiral molecules in both gas-phase and solution environments.

In Chapter 4, expressions for excited-state to excited-state rotatory strength in both the length and velocity gauges as described in Section 2.6.2 were used to simulate the S_1-ES-ECD spectrum of (1*R*)-norcamphor at the ADC(3) level of theory. This spectrum was then compared to those calculated at TD-DFT level using varying exchange-correlation functionals which showed good agreement between ADC(3) and CAM-B3LYP. Furthermore, the S_1-ES-ECD spectra of

(1R)-camphor and (1R)-fenchone were calculated at the ADC(3) level of theory and compared to those same spectra calculated at TD-DFT/CAM-B3LYP level, showing equally good agreement. Next, ground state ECD spectra of (R)-Binol were calculated at the ADC(3) and TD-DFT/CAM-B3LYP levels of theory. At both these levels, all major spectral features were reproduced. The S_1-ES-ECD spectra of (R)-Binol was then computed at these same levels of theory. Here, both methods revealed the same spectral features, as one should expect from the good agreement of the ground state ECD spectra. The absolute difference between the excited-state to excited-state length and velocity gauge rotatory strengths of these molecules was shown to be on the same order as for the ground state rotatory strengths of these same molecules. To summarize this chapter, comparison of ground state ecd spectra using the ADC(2), ADC(3) and TD-DFT/CAM-B3LYP methods, showed good agreement, similarly good agreement was found for the S_1-ES-ECD spectra, which indicates the robustness of the ADC(2) and ADC(3) methods in the prediction of excited-state to excited-state rotatory strengths. While experimental ES-ECD methods are still in their infancy, the theoretical groundwork has been clearly presented in this work using the ADC/ISR formalism.

In Chapter 5, three expressions for the two-photon rotatory strength within ADC/ISR as described in Section 2.6.3 were used to simulate the TPCD spectra of S-methyloxirane and S-methylthiirane at the ADC(2) level of theory. These spectra where then compared to those calculated at the CC2 level of theory using the equivalent TI-formulation of the rotatory strength. Here, all three formulations at ADC(2) level were shown to yield similar spectra as those calculated at CC2 level. Furthermore, the ECD and TPCD spectra of a twisted-biphenyl molecule with varying torsional angle was calculated at the ADC(2) levels of theory. A potential application is to use this molecular system as a chirality probe of amino acids, using TPCD. The ECD spectra showed a strong dependence on the torsional angle for the magnitude of the energetically lowest band feature (A-band). In close proximity to this same energetic region, the TPCD spectra showed a similar band feature, with a magnitude exhibiting a similar dependence on the torsional angle. This demonstrates that TPCD can be used in absolute configuration assignment of carboxylic acids with this amide derivation method. Next, the impact of various polarization and propagation configurations of the two photons absorbed, was calculated at ADC(2) and ADC(3) levels of theory and demonstrated with the TPCD spectra of R-norcamphor. here, reversal of several band features were evident, as impacted by the different polarization and propagation setups. To summarize the chapter, while experimentally challenging, ADC(n) has been added as an *ab initio* method, to the theoretical toolbox to calculate TPCD spectra.

Lastly, in Chapter 6, expressions for the first-order hyperpolarizability within ADC/ISR as described in Section 2.6.4 were used to calculate the static first-order hyperpolarizabilities of several small organic molecules at ADC(n) levels of theory. These quantities were subsequently compared to those same quantities calculated at the corresponding CC levels. For the overwhelming majority of cases, the components of the first-order hyperpolarizability tensor at ADC(n) level consistently matched with those at the corresponding CC level. Two noticeable exceptions were evident, namely HNO_2 and N_2O, where the molecular systems where poorly described using a single HF reference. Next, the dynamic first-order hyperpolarizability, with SHG frequency conditions, was calculated at ADC levels of theory for several organic molecules. Here, it was shown that the

ADC(1) and ADC(3) methods produce hyperpolarizabilities, with consistently good agreement to those measured experimentally, while ADC(2) often overestimate these same quantities. The fact that ADC(1), in contrast to ADC(2), produces first-order hyperpolarizabilities in good agreement with experiment, can be attributed to fortuitous cancellation of terms. As a proof-of-concept, the HRS signal of NH_3 was calculated in the two-photon resonance region at the ADC(2) and ADC(3) levels of theory. Here, the expected absorption/dispersion behaviour was observed passing through resonance. To summarize this chapter, the ADC(n) methods were shown to be excellent in the prediction of static and dynamic first-order hyperpolarizabilities. Predicting similar static hyperpolarizabilities as corresponding CC levels, as well as dynamic first-order hyperpolarizabilities that can be directly compared with experiment .

In conclusion, this dissertation covers several chiroptical properties that where previously novel to the ADC method. The ground state and excited-state optical rotatory strength in both the length and velocity gauges are now accessible at the ADC(n) level. This allows for the simulation of ECD and ES-ECD spectroscopies. The simultaneous absorption of two photons where one is circularly polarized can likewise be evaluated at the ADC(n) level of theory for the three formulations of the two-photon rotatory strength described. This allows for the simulation of TPCD spectroscopy. The first-order hyperpolarizability tensor can now also be evaluated at ADC(n) levels of theory. Here, for dynamic fields, ADC(n) has been used to simulate the SHG and HRS spectroscopies.

Appendices

Appendix A

Ground to excited-state rotatory and oscillator strengths

The excitation energies, rotatory and oscillator strengths of all calculations discussed in chapter 3. For R-methyloxirane, R-methylthiirane, (R,R)-dimethyloxirane, (R,R)-dimethylthiirane, H2O_2, H_2S_2, (1R)-camphor, (1R)-norcamphor and (1R)-fenchone the oxygen or sulfur atom was used as the origin of the position operator.

A.1 *R*-Methyloxirane

Table A.1: Transition energy, ω (eV), optical rotatory strength, R ($\times$ 10^{-40}esu$^2\cdot$cm^2) and oscillator strength ($\times 10^{-3}$) of the lowest singlet excitations of *R*-methyloxirane calculated at the ADC(2) level of theory using the d-aug-cc-pVDZ basis set.

	ADC(2)/d-aug-cc-pVDZ					ADC(3)/d-aug-cc-pVDZ				
n	ω_{n0}	R^{r}_{n0}	R^{∇}_{n0}	f^{r}_{n0}	f^{∇}_{n0}	ω_{n0}	R^{r}_{n0}	R^{∇}_{n0}	f^{r}_{n0}	f^{∇}_{n0}
1	6.18	-13.5	-14.9	11.7	13.4	7.84	-13.3	-11.8	5.8	4.4
2	6.56	-0.8	-1.1	6.2	8.0	7.93	-12.8	-11.0	21.7	16.1
3	6.62	5.8	6.5	15.7	18.9	8.23	5.6	4.8	3.2	3.2
4	6.79	3.6	4.0	13.2	15.4	8.30	20.5	17.3	21.1	15.5
5	7.40	4.1	4.6	5.2	5.5	8.47	6.5	5.8	28.7	25.2
6	7.47	-1.8	-1.9	1.6	1.9	8.57	-15.5	-13.4	33.6	25.8
7	7.48	0.4	0.5	4.2	4.8	8.72	-3.4	-2.9	18.2	17.2
8	7.54	-0.3	-0.3	1.8	1.9	8.87	-8.6	-8.4	6.9	6.7
9	7.57	-0.8	-0.9	2.8	2.9	8.92	4.2	1.6	4.6	3.3
10	7.60	8.4	9.2	2.8	3.1	9.16	5.4	4.9	17.4	14.3
11	7.63	-1.3	-1.4	2.4	2.7	9.19	-11.8	-10.7	3.6	3.2
12	7.75	0.6	0.5	0.4	0.4	9.28	2.2	2.2	5.7	4.7
13	7.76	2.6	2.8	4.8	5.6	9.33	4.5	4.0	3.4	3.0
14	7.82	1.0	1.1	3.4	3.7	9.46	0.9	0.8	0.2	0.2
15	8.05	-3.2	-3.2	14.8	13.0	9.50	-0.3	0.2	4.0	3.6
16	8.06	4.7	5.0	8.2	8.3					
17	8.09	-8.4	-8.6	27.2	25.2					
18	8.11	0.8	0.9	2.0	2.5					
19	8.18	0.9	0.9	0.6	0.6					
20	8.21	0.7	0.9	1.7	1.9					
21	8.21	-6.8	-6.9	3.7	3.9					
22	8.25	-0.5	-0.5	2.5	2.6					
23	8.28	0.2	0.1	1.1	1.4					
24	8.38	2.6	2.6	2.0	1.9					
25	8.48	-0.2	-0.2	0.5	0.6					

TABLE A.2: Transition energy, ω (eV), optical rotatory strength, R ($\times$ 10^{-40}esu^2·cm^2) and oscillator strength ($\times 10^{-3}$) of the lowest singlet excitations of methyloxirane calculated at the CC2, CCSD and CC3 levels of theory using the d-aug-cc-pVDZ and aug-cc-pVDZ basis sets.

	CC2/d-aug-cc-pVDZ					CCSD/d-aug-cc-pVDZ				
n	ω_{n0}	R^r_{n0}	R^{∇}_{n0}	f^r_{n0}	f^{∇}_{n0}	ω_{n0}	R^r_{n0}	R^{∇}_{n0}	f^r_{n0}	f^{∇}_{n0}
1	6.32	-15.9	-15.2	14.1	12.9	7.12	-15.0	-14.8	9.6	9.0
2	6.70	-1.3	-1.5	7.0	6.9	7.35	-5.9	-6.4	16.5	18.8
3	6.76	6.5	6.4	18.7	17.9	7.56	9.1	9.0	15.0	14.6
4	6.93	4.4	4.1	16.8	15.9	7.76	5.6	5.6	16.9	17.1
5	7.54	5.0	4.9	6.3	5.6	8.07	9.8	10.2	4.1	4.3
6	7.61	-2.1	-1.9	1.9	1.8	8.38	0.8	0.9	2.2	2.1
7	7.62	1.1	1.3	5.2	4.8	8.44	-6.4	-5.9	25.3	23.9
8	7.66	8.5	9.3	2.7	2.	8.47	-1.7	-2.2	16.1	14.9
9	7.68	-0.9	-0.8	3.1	2.8	8.50	4.5	4.6	10.5	10.9
10	7.71	-0.1	0.0	3.5	3.2	8.55	-3.3	-3.7	9.7	9.4
11	7.76	-2.0	-2.0	1.8	1.7	8.56	-4.5	-4.6	7.5	7.3
12	7.88	0.6	0.4	0.3	0.3	8.59	2.5	2.6	4.9	4.7
13	7.90	2.6	2.5	5.1	4.9	8.70	-10.1	-10.2	5.1	5.4
14	7.96	1.3	1.2	4.2	4.0	8.73	0.3	0.4	1.0	0.8
15	8.10	-3.2	-3.3	24.0	21.2	8.79	-0.7	-0.7	1.8	2.0
16	8.14	-8.2	-8.1	24.2	21.8					
17	8.20	4.7	4.7	3.4	3.3					
18	8.25	1.4	1.5	1.9	1.9					
19	8.26	-6.7	-6.7	4.3	4.4					
20	8.31	1.3	1.2	0.9	0.9					

	CC3/aug-cc-pVDZ				
n	ω_{n0}	R^r_{n0}	R^{∇}_{n0}	f^r_{n0}	f^{∇}_{n0}
1	7.18	-19.4	-18.8	13.5	12.7
2	7.47	-3.8	-4.0	12.8	12.8
3	7.65	10.5	10.1	18.4	16.9

A.2 ***R*-Methylthiirane**

TABLE A.3: Transition energy, ω (eV), optical rotatory strength, R ($\times$ 10^{-40}esu^2·cm^2) and oscillator strength ($\times 10^{-3}$) of the lowest singlet excitations of methylthiirane calculated at the ADC(2) level of theory using the d-aug-cc-pVDZ basis set.

	ADC(2)/d-aug-cc-pVDZ					ADC(3)/d-aug-cc-pVDZ				
n	ω_{n0}	R^{r}_{n0}	R^{∇}_{n0}	f^{r}_{n0}	f^{∇}_{n0}	ω_{n0}	R^{r}_{n0}	R^{∇}_{n0}	f^{r}_{n0}	f^{∇}_{n0}
1	5.02	-1.8	-1.7	0.3	0.3	4.95	-1.2	-1.2	0.2	0.2
2	5.56	-4.7	-5.1	18.9	19.5	5.91	-5.2	-5.2	34.3	29.7
3	5.79	-5.3	-5.5	33.9	37.8	5.98	-6.9	-6.6	17.8	17.2
4	6.08	-0.3	-0.3	15.3	15.6	6.41	2.3	2.1	21.5	19.1
5	6.31	2.1	2.0	3.5	3.5	6.64	3.7	3.7	2.2	2.1
6	6.72	8.3	8.7	14.5	13.3	7.07	5.6	5.4	21.7	17.6
7	6.83	-0.1	-0.2	1.5	1.3	7.20	1.1	1.0	1.0	0.9
8	6.86	3.5	3.5	8.6	8.8	7.24	2.8	2.6	9.4	8.2
9	6.88	-1.2	-1.3	2.3	1.7	7.25	-1.9	-1.8	1.0	0.9
10	6.95	-3.7	-3.5	6.3	6.7	7.33	-5.7	-5.6	11.0	10.6
11	7.04	-1.0	-1.1	7.6	6.0	7.45	2.6	2.5	4.9	4.6
12	7.10	1.2	1.1	2.2	4.9	7.47	-0.1	-0.4	6.7	6.0
13	7.17	1.5	1.4	5.4	4.5	7.57	-4.9	-4.3	36.9	29.7
14	7.25	1.7	1.7	2.2	2.1	7.61	1.7	1.5	6.0	4.9
15	7.41	2.1	2.6	11.1	10.5	7.69	1.4	1.4	1.8	1.6
16	7.50	-0.1	0.1	15.6	4.9	7.81	8.8	7.7	12.3	10.3
17	7.51	-0.7	0.1	2.9	15.8	7.85	20.7	18.1	17.6	13.7
18	7.52	1.8	1.7	4.7	5.4	7.91	2.7	3.0	1.8	1.7
19	7.57	-0.6	-0.8	0.2	0.2	7.97	0.5	1.0	13.6	11.1
20	7.68	6.7	5.6	1.5	2.6	7.98	-1.8	-2.0	10.8	8.4
21	7.70	9.9	8.2	1.6	6.9					
22	7.76	2.6	3.0	0.4	2.0					
23	7.91	4.4	4.1	9.6	7.3					
24	7.93	-8.5	-8.4	1.1	10.1					
25	7.94	2.0	2.3	10.0	4.2					

Table A.4: Transition energy, ω (eV), optical rotatory strength, R ($\times$ 10^{-40}esu^2·cm^2) and oscillator strength ($\times 10^{-3}$) of the lowest singlet excitations of methylthiirane calculated at the CC2 level of theory using the d-aug-cc-pVDZ basis set.

	CC2/d-aug-cc-pVDZ					CCSD/d-aug-cc-pVDZ				
n	ω_{n0}	R^r_{n0}	R^∇_{n0}	f^r_{n0}	f^∇_{n0}	ω_{n0}	R^r_{n0}	R^∇_{n0}	f^r_{n0}	f^∇_{n0}
1	5.07	-2.2	-2.1	0.3	0.3	5.02	-1.2	-0.9	0.3	0.3
2	5.62	-5.7	-5.2	20.1	18.9	5.80	-5.6	-5.8	26.1	24.6
3	5.84	-5.4	-5.3	34.9	33.9	5.93	-6.1	-6.3	26.5	29.5
4	6.14	0.0	0.0	17.2	15.3	6.31	0.6	0.5	19.0	18.3
5	6.37	2.5	2.3	3.7	3.5	6.55	3.2	3.2	2.5	2.5
6	6.77	8.3	8.6	15.2	14.5	6.96	6.9	7.2	19.9	17.5
7	6.89	0.2	0.2	1.5	1.5	7.10	0.6	0.4	1.4	1.3
8	6.92	4.0	3.9	9.1	8.6	7.13	5.1	4.9	5.3	4.9
9	6.93	-1.2	-1.2	2.4	2.3	7.13	-2.3	-2.3	6.1	6.2
10	6.99	-3.7	-3.4	7.1	6.3	7.20	-4.3	-4.2	8.6	8.4
11	7.10	-2.0	-1.9	7.9	7.6	7.33	1.2	1.1	6.1	6.0
12	7.13	1.4	1.4	2.4	2.8	7.35	-0.9	-1.0	4.6	4.5
13	7.23	1.6	1.5	6.1	5.4	7.49	1.5	1.5	6.3	5.8
14	7.31	2.0	1.9	2.3	2.2	7.57	2.3	2.3	3.2	3.1
15	7.46	3.0	3.0	11.5	11.1	7.64	-4.8	-3.7	26.4	21.4
16	7.53	-3.6	-3.2	18.4	15.6					
17	7.55	2.8	2.8	3.2	2.9					
18	7.59	1.00	0.9	5.0	4.7					
19	7.60	0.2	0.1	0.2	0.2					
20	7.62	-0.6	-0.6	1.7	1.5					

	CC3/ aug-cc-pVDZ				
n	ω_{n0}	R^r_{n0}	R^∇_{n0}	f^r_{n0}	f^∇_{n0}
1	4.99	-1.5	-1.5	0.2	0.3
2	5.80	-8.5	-8.5	18.9	17.7

A.3 (*R*,*R*)-Dimethyloxirane

Table A.5: Transition energy, ω (eV), optical rotatory strength, R ($\times$ 10^{-40}esu^2·cm^2) and oscillator strength ($\times 10^{-3}$) of the lowest singlet excitations of dimethyloxirane calculated at the ADC(2) level of theory using the d-aug-cc-pVDZ basis set.

	ADC(2)/d-aug-cc-pVDZ					ADC(3)/d-aug-cc-pVDZ				
n	ω_{n0}	R^r_{n0}	R^{∇}_{n0}	f^r_{n0}	f^{∇}_{n0}	ω_{n0}	R^r_{n0}	R^{∇}_{n0}	f^r_{n0}	f^{∇}_{n0}
1	6.08	-12.6	-14.0	8.0	10.4	7.81	-20.0	-18.4	12.0	10.1
2	6.38	14.6	16.3	10.6	13.3	7.92	-18.5	-18.8	7.8	8.0
3	6.57	-8.5	-9.3	8.6	10.7	8.12	20.4	15.9	10.0	6.0
4	6.65	-3.8	-4.1	1.2	1.5	8.14	-10.3	-9.0	11.7	7.7
5	7.16	4.6	5.0	14.7	15.9	8.28	2.6	2.3	12.7	11.8
6	7.22	0.3	0.5	0.0	0.0	8.39	1.6	2.3	0.2	0.5
7	7.26	-8.2	-8.6	9.1	9.8	8.46	-21.8	-18.9	26.6	19.9
8	7.27	1.8	1.9	2.4	3.0	8.48	23.0	22.3	22.7	21.1
9	7.29	2.6	2.8	0.8	0.9	8.79	-8.8	-10.0	1.4	1.8
10	7.30	-4.6	-4.1	0.8	0.6	8.98	17.0	15.9	36.4	31.7
11	7.41	0.1	0.2	1.9	2.3	9.07	3.1	2.5	13.9	9.6
12	7.49	5.2	5.5	3.1	3.5	9.07	0.0	-0.1	1.1	1.2
13	7.52	-6.9	-7.5	5.3	6.5	9.11	3.9	3.7	5.8	5.2
14	7.57	-1.0	-1.1	0.2	0.2	9.12	3.6	3.9	1.8	2.1
15	7.65	2.2	1.9	5.2	4.6	9.18	-16.1	-15.0	10.5	8.9

Table A.6: Transition energy, ω (eV), optical rotatory strength, R ($\times$ 10^{-40}esu^2·cm^2) and oscillator strength ($\times 10^{-3}$) of the lowest singlet excitations of dimethyloxirane calculated at the CC2 level of theory using the d-aug-cc-pVDZ basis set.

	CC2/d-aug-cc-pVDZ					CCSD/d-aug-cc-pVDZ				
n	ω_{n0}	R^{r}_{n0}	R^{∇}_{n0}	f^{r}_{n0}	f^{∇}_{n0}	ω_{n0}	R^{r}_{n0}	R^{∇}_{n0}	f^{r}_{n0}	f^{∇}_{n0}
1	6.22	-15.0	-14.2	10.8	10.1	7.07	-16.3	-16.3	9.8	10.3
2	6.53	16.5	16.0	12.3	11.6	7.35	16.2	15.9	12.2	11.7
3	6.71	-9.8	-9.8	10.0	10.0	7.46	-10.1	-11.0	12.6	14.2
4	6.79	-4.1	-4.4	1.3	1.5	7.66	-4.8	-4.8	1.0	0.9
5	7.30	5.9	5.8	18.7	17.1	7.76	-11.1	-11.2	3.2	3.2
6	7.34	-12.4	-11.1	3.7	3.0	8.12	3.5	3.0	9.1	8.5
7	7.37	0.8	1.2	0.1	0.2	8.20	-16.4	-16.0	6.0	5.7
8	7.40	2.2	2.2	3.2	3.3	8.23	10.6	10.7	22.8	22.8
9	7.40	-3.6	-3.4	8.6	7.6	8.31	0.2	0.2	1.2	1.1
10	7.42	3.0	2.9	0.9	0.9	8.33	13.1	13.7	13.6	13.6
11	7.54	0.4	0.5	2.3	2.2	8.33	-6.1	-5.9	28.6	26.9
12	7.62	5.5	5.2	3.2	2.9	8.34	0.6	0.8	0.1	0.1
13	7.65	-9.1	-9.1	4.3	4.5	8.35	9.0	9.0	9.1	9.3
14	7.70	3.4	3.1	7.4	6.5	8.51	-3.7	-4.1	3.1	3.7
15	7.70	-1.0	-1.1	0.2	0.2	8.59	-5.4	-5.5	6.8	7.5

A.4 (*R*,*R*)-Dimethylthiirane

TABLE A.7: Transition energy, ω (eV), optical rotatory strength, R ($\times$ 10^{-40}esu^2·cm^2) and oscillator strength ($\times 10^{-3}$) of the lowest singlet excitations of dimethylthiirane calculated at the ADC(2) level of theory using the d-aug-cc-pVDZ basis set.

	ADC(2)/d-aug-cc-pVDZ					ADC(3)/d-aug-cc-pVDZ				
n	ω_{n0}	R^{r}_{n0}	R^{∇}_{n0}	f^{r}_{n0}	f^{∇}_{n0}	ω_{n0}	R^{r}_{n0}	R^{∇}_{n0}	f^{r}_{n0}	f^{∇}_{n0}
1	5.02	5.1	5.8	0.2	0.2	4.97	0.7	0.1	0.0	0.0
2	5.57	-6.9	-7.6	22.8	23.0	5.92	-3.9	-4.7	43.2	38.6
3	5.83	-19.1	-19.6	25.6	27.7	6.08	-20.1	-19.3	7.0	6.7
4	5.93	-0.3	-0.3	21.3	21.4	6.30	3.8	3.6	23.4	20.4
5	6.19	-5.2	-5.6	2.3	2.7	6.56	-2.2	-1.6	0.6	0.3
6	6.53	10.3	11.0	3.1	2.9	6.89	6.1	6.1	8.6	6.6
7	6.68	5.5	5.4	8.4	8.3	7.06	11.3	10.7	9.8	8.9
8	6.72	3.8	3.8	8.4	8.4	7.13	2.9	2.7	10.7	9.1
9	6.73	-1.1	-0.6	0.2	0.1	7.14	-2.9	-3.2	1.2	1.4
10	6.80	0.0	-0.7	2.3	2.0	7.22	1.4	1.3	0.2	0.2
11	6.81	3.0	3.0	20.4	20.3	7.23	-0.6	-0.6	24.0	21.5
12	6.97	-3.2	-3.3	12.9	13.4	7.39	-0.9	-1.2	14.3	12.8
13	6.99	1.0	0.9	2.4	2.2	7.47	2.0	1.8	7.6	6.1
14	7.09	0.3	0.1	0.0	0.0	7.51	-8.2	-7.3	48.8	38.7
15	7.21	3.5	3.6	7.2	6.3	7.57	-9.8	-8.6	12.9	9.8

TABLE A.8: Transition energy, ω (eV), optical rotatory strength, R ($\times$ 10^{-40}esu^2·cm^2) and oscillator strength ($\times 10^{-3}$) of the lowest singlet excitations of dimethylthiirane calculated at the CC2 level of theory using the d-aug-cc-pVDZ basis set.

	CC2/d-aug-cc-pVDZ					CCSD/d-aug-cc-pVDZ				
n	ω_{n0}	R^{r}_{n0}	R^{∇}_{n0}	f^{r}_{n0}	f^{∇}_{n0}	ω_{n0}	R^{r}_{n0}	R^{∇}_{n0}	f^{r}_{n0}	f^{∇}_{n0}
1	5.08	4.4	4.5	0.1	0.1	5.04	2.4	3.1	0.0	0.1
2	5.63	-8.0	-7.2	24.3	23.2	5.82	-5.2	-5.3	35.6	34.9
3	5.88	-19.6	-19.0	25.6	24.5	6.01	-21.0	-21.7	13.5	15.4
4	6.00	-0.2	-0.2	22.7	20.4	6.18	1.7	1.6	22.5	21.7
5	6.26	-5.5	-5.6	2.3	2.4	6.46	-3.4	-3.4	1.0	0.9
6	6.59	10.6	10.6	3.6	3.6	6.79	8.6	9.0	6.6	5.2
7	6.74	6.6	6.4	9.6	9.0	6.96	9.5	9.1	11.2	10.4
8	6.79	4.3	4.2	9.1	8.8	7.01	3.2	3.2	9.9	9.3
9	6.79	-1.4	-1.1	0.3	0.2	7.02	-2.3	-2.3	0.7	0.7
10	6.86	-0.5	-0.3	1.9	1.8	7.10	0.4	-0.1	0.5	0.4
11	6.87	3.3	3.2	21.6	20.2	7.10	1.9	1.9	22.8	22.7
12	7.03	-3.3	-3.2	12.5	11.8	7.28	-1.8	-1.8	13.8	13.8
13	7.06	1.1	1.0	2.6	2.2	7.34	1.4	1.3	3.3	3.0
14	7.16	0.5	0.3	0.0	0.0	7.43	2.0	1.8	1.4	1.1
15	7.27	3.8	3.8	8.5	8.3	7.55	1.0	1.1	10.1	9.1

A.5 H_2O_2

TABLE A.9: Transition energy, ω (eV), optical rotatory strength, R ($\times$ 10^{-40}esu^2$\cdot$cm^2) and oscillator strength ($\times 10^{-3}$) of the lowest singlet excitations of H_2O_2 calculated at the ADC(2) level of theory using the d-aug-cc-pVDZ basis set.

	ADC(2)/d-aug-cc-pVDZ					ADC(3)/d-aug-cc-pVDZ				
n	ω_{n0}	R^r_{n0}	R^∇_{n0}	f^r_{n0}	f^∇_{n0}	ω_{n0}	R^r_{n0}	R^∇_{n0}	f^r_{n0}	f^∇_{n0}
1	6.10	-9.9	-10.9	6.2	7.5	5.97	-6.8	-6.1	2.9	2.3
2	6.57	-15.9	-18.6	4.4	5.4	7.08	9.1	7.8	11.8	8.3
3	7.24	15.9	16.3	13.6	11.3	7.35	-14.7	-14.7	3.2	3.3
4	7.55	29.0	31.8	9.7	11.8	8.24	32.0	29.6	14.1	12.1
5	7.84	-5.8	-5.2	0.9	0.8	8.72	-17.8	-16.3	5.3	4.4
6	8.33	-0.1	-0.1	14.7	16.0	9.66	13.7	12.6	21.6	18.8
7	8.54	0.3	0.3	6.5	6.8	10.06	1.0	-0.1	136.0	127.1
8	8.79	0.1	0.0	5.6	5.7	10.06	0.1	0.1	0.2	0.1
9	8.86	6.9	6.3	15.3	14.2	10.30	2.3	2.1	12.6	10.6
10	9.10	-2.2	-2.1	0.4	0.4	10.45	-13.2	-11.7	44.2	33.6
11	9.15	-2.1	-2.1	1.5	1.6	10.81	1.7	3.0	1.6	2.1
12	9.25	-1.4	-1.0	0.9	0.8	10.95	-9.7	-9.1	7.9	7.0
13	9.29	0.0	0.0	0.8	0.6	11.22	-5.6	-5.2	5.5	4.9
14	9.40	3.2	3.7	0.7	0.9	11.36	0.6	0.6	4.3	4.4
15	9.41	4.4	4.5	1.4	1.4	11.37	3.3	3.5	13.1	15.2
16	9.46	-0.1	-0.2	1.7	2.0					
17	9.59	-6.4	-6.5	13.2	13.9					
18	9.84	-0.9	-0.6	15.2	13.9					
19	9.86	2.7	3.1	0.2	0.3					
20	9.97	1.8	1.7	4.8	4.5					

Table A.10: Transition energy, ω (eV), optical rotatory strength, R ($\times$ 10^{-40}esu$^2\cdot$cm^2) and oscillator strength ($\times10^{-3}$) of the lowest singlet excitations of H_2O_2 calculated at the CC2, CCSD and CC3 levels of theory using the d-aug-cc-pVTZ and aug-cc-pVDZ basis sets set.

	CC2/d-aug-cc-pVDZ					CCSD/d-aug-cc-pVDZ				
n	ω_{n0}	R^r_{n0}	$R^{\boldsymbol{\nabla}}_{n0}$	f^r_{n0}	$f^{\boldsymbol{\nabla}}_{n0}$	ω_{n0}	R^r_{n0}	$R^{\boldsymbol{\nabla}}_{n0}$	f^r_{n0}	$f^{\boldsymbol{\nabla}}_{n0}$
1	6.10	-11.4	-11.3	6.6	6.5	6.16	-9.3	-11.4	4.2	6.4
2	6.60	-18.4	-18.4	5.4	4.9	7.10	-20.0	-21.6	7.6	8.2
3	7.24	16.9	16.9	13.4	11.2	7.30	16.0	18.6	8.1	8.0
4	7.59	32.4	32.1	12.0	11.8	8.05	32.1	32.8	13.0	13.5
5	7.87	-6.3	-5.5	1.1	0.8	8.44	-10.0	-9.3	1.9	1.6
6	8.36	0.3	0.4	17.7	16.0	9.06	-0.6	-0.6	20.7	21.1
7	8.57	0.7	0.7	7.3	7.1	9.27	-0.3	-0.3	10.1	9.6
8	8.82	0.1	-0.2	5.9	5.3	9.40	12.5	12.3	24.6	23.9
9	8.89	7.4	6.8	16.9	13.7	9.64	1.1	0.6	2.3	2.1
10	9.14	-2.0	-1.9	0.3	0.3	9.90	0.0	0.0	0.0	0.0
11	9.18	-2.6	-2.4	1.7	1.6	9.95	-5.7	-5.5	2.8	2.6
12	9.28	-1.3	-1.0	1.2	0.9	10.05	-4.4	-4.0	6.8	6.4
13	9.32	0.0	0.0	0.7	0.6	10.09	0.3	0.3	0.5	0.5
14	9.43	3.7	3.9	0.9	0.9	10.19	5.7	5.8	7.6	7.2
15	9.44	5.3	5.1	1.9	1.7	10.21	-0.5	-0.5	0.0	0.0
16	9.49	-0.3	-0.3	1.8	1.7	10.26	-13.0	-13.0	35.0	34.1
17	9.62	-7.2	-7.0	14.8	14.3	10.27	4.0	3.9	5.5	5.4
18	9.87	-0.9	-0.5	16.3	13.4	10.62	2.4	2.7	48.5	43.7
19	9.89	2.7	2.8	0.2	0.2	10.68	3.8	4.3	0.4	0.5
20	10.00	2.0	1.9	5.1	4.6	10.79	0.9	0.9	8.1	7.4
21	10.20	1.6	1.0	0.5	0.3	10.84	0.0	-0.8	31.9	28.1
22	10.23	-2.4	-2.4	6.9	6.0	10.97	0.5	0.3	0.6	0.5
23	10.23	-0.4	-0.3	0.0	0.0	10.99	0.1	0.1	0.0	0.0
24	10.26	-0.5	-0.5	10.9	9.7	11.02	-7.3	-7.2	22.4	22.0
25	10.35	-1.8	-1.8	2.1	2.1	11.03	-7.1	-7.0	2.0	2.0

	CC3/aug-cc-pVDZ				
n	ω_{n0}	R^r_{n0}	$R^{\boldsymbol{\nabla}}_{n0}$	f^r_{n0}	$f^{\boldsymbol{\nabla}}_{n0}$
1	6.10	-9.5	-9.8	4.1	4.3
2	7.09	-20.0	-20.0	8.6	8.5
3	7.21	16.1	16.6	6.4	6.6
4	8.05	33.3	33.2	13.2	13.1
5	8.42	-11.4	-11.3	2.5	2.5

A.6 H_2S_2

TABLE A.11: Transition energy, ω (eV), optical rotatory strength, R ($\times$ 10^{-40}esu$^2\cdot$cm^2) and oscillator strength ($\times 10^{-3}$) of the lowest singlet excitations of H_2S_2 calculated at the ADC(2) level of theory using the d-aug-cc-pVDZ basis set.

	ADC(2)/d-aug-cc-pVDZ					ADC(3)/d-aug-cc-pVDZ				
n	ω_{n0}	R^r_{n0}	R^∇_{n0}	f^r_{n0}	f^∇_{n0}	ω_{n0}	R^r_{n0}	R^∇_{n0}	f^r_{n0}	f^∇_{n0}
1	5.01	-5.5	-6.4	4.4	5.8	4.77	-5.0	-5.3	3.3	3.7
2	5.03	14.4	14.1	13.3	12.3	4.79	13.8	12.5	10.5	8.4
3	6.08	65.1	69.0	14.0	15.7	5.98	57.7	59.6	12.8	13.7
4	6.09	-73.2	-77.0	18.1	19.7	6.00	-64.3	-66.0	15.2	15.9
5	6.91	-20.6	-22.8	2.1	2.6	6.86	-13.9	-15.9	0.7	1.0
6	6.92	31.4	34.5	15.2	16.2	6.87	17.0	19.4	8.8	8.4
7	7.78	-19.0	-18.5	124.0	117.8	7.79	10.3	9.9	14.0	13.0
8	7.78	11.1	10.5	6.8	6.1	7.80	-16.3	-15.6	223.4	203.6
9	7.82	-16.9	-15.9	4.7	4.2	7.84	8.0	7.2	51.1	45.9
10	7.83	1.0	1.0	0.4	0.6	7.84	-14.1	-13.2	4.1	3.6
11	7.90	2.8	2.9	54.6	49.4	7.85	-5.8	-5.6	11.6	11.9
12	7.99	-2.6	-2.7	0.1	0.1	8.02	-4.6	-4.7	0.4	0.4
13	8.10	-41.2	-40.3	42.5	40.9	8.09	1.0	0.8	44.2	33.5
14	8.12	39.7	38.9	28.4	27.3	8.19	-27.7	-27.5	20.7	21.0
15	8.24	23.6	21.5	127.3	107.5	8.20	48.0	47.0	35.3	33.9

Table A.12: Transition energy, ω (eV), optical rotatory strength, R ($\times$ 10^{-40}esu$^2\cdot$cm^2) and oscillator strength ($\times 10^{-3}$) of the lowest singlet excitations of H_2S_2 calculated at the CC2, CCSD and CC3 levels of theory using the d-aug-cc-pVDZ basis set.

	CC2/d-aug-cc-pVDZ					CCSD/d-aug-cc-pVDZ				
n	ω_{n0}	R^r_{n0}	R^{∇}_{n0}	f^r_{n0}	f^{∇}_{n0}	ω_{n0}	R^r_{n0}	R^{∇}_{n0}	f^r_{n0}	f^{∇}_{n0}
1	4.98	-5.8	-5.6	4.6	4.2	4.96	-6.3	-7.4	3.9	5.4
2	5.00	13.6	12.3	13.0	10.1	4.98	14.0	14.1	11.1	10.6
3	6.04	64.4	65.4	14.0	14.5	6.08	60.6	62.8	13.9	14.9
4	6.06	-72.5	-72.7	18.1	17.9	6.10	-67.7	-69.7	16.5	17.4
5	6.87	-20.6	-19.1	2.1	1.8	6.94	-14.2	-16.3	0.8	1.0
6	6.88	31.7	29.9	15.4	14.6	6.96	20.1	22.4	11.1	11.2
7	7.63	-8.7	-8.5	78.8	74.3	7.78	-6.4	-6.4	93.7	92.9
8	7.65	7.7	7.1	1.7	1.5	7.79	8.9	8.7	2.7	2.6
9	7.70	-12.5	-11.8	39.1	35.4	7.82	-15.1	-14.7	60.1	57.2
10	7.74	-2.6	-2.5	7.1	6.8	7.86	-4.8	-4.6	11.5	10.5
11	7.76	10.1	10.0	12.0	11.3	7.89	10.5	10.2	15.9	14.8
12	7.78	-10.7	-10.5	3.3	3.2	7.93	-8.3	-8.0	1.9	1.7
13	8.02	-36.8	-36.8	23.8	24.1	8.17	-8.5	-9.1	128.2	113.3
14	8.03	43.7	43.6	23.9	23.8	8.20	-18.8	-18.6	14.7	13.9
15	8.18	22.5	20.0	127.6	109.4	8.21	45.3	44.4	30.0	28.8
16	8.24	11.5	11.6	25.4	21.4	8.36	22.4	21.7	7.0	6.2
17	8.24	-43.3	-42.4	17.2	16.5	8.36	-40.9	-39.5	13.6	12.6
18	8.37	1.4	1.4	1.9	1.8	8.56	1.5	1.5	4.9	4.8
19	8.42	5.9	5.6	9.4	7.6	8.60	9.7	9.5	4.8	4.2
20	8.43	3.9	3.7	16.8	14.5	8.63	2.6	2.5	6.7	6.1
21	8.44	0.0	-0.1	0.0	0.0	8.65	-0.1	-0.1	0.1	0.1
22	8.46	-3.1	-3.0	1.1	1.0	8.67	-4.9	-4.8	2.9	2.8
23	8.48	-2.1	-1.9	12.4	10.9	8.69	-1.6	-1.5	11.1	10.2
24	8.67	2.6	2.6	33.0	31.0	8.85	-17.3	-17.1	64.0	62.2
25	8.68	-1.4	-1.3	24.4	22.1	8.91	1.6	1.5	23.7	22.1

	CC3/aug-cc-pVDZ				
n	ω_{n0}	R^r_{n0}	R^{∇}_{n0}	f^r_{n0}	f^{∇}_{n0}
1	4.86	-6.0	-5.4	3.9	3.2
2	4.89	13.1	12.4	10.8	9.7
3	6.01	59.3	58.6	12.6	12.3
4	6.02	-67.3	-66.8	15.9	15.7

A.7 *L*-Epinephrine

TABLE A.13: Transition energy, ω (eV), optical rotatory strength, R ($\times$ 10^{-40}esu^2·cm^2) and oscillator strength ($\times 10^{-3}$) of the lowest singlet excitations of L-epinephrine calculated at the ADC(2) level of theory using the d-aug-cc-pVDZ basis set.

	ADC(2) - gas phase geometry				
n	ω_{n0}	R^{r}_{n0}	R^{∇}_{n0}	f^{r}_{n0}	f^{∇}_{n0}
1	4.828	−4.3	−6.9	42.4	33.5
2	4.871	3.1	5.8	17.1	16.2
3	5.268	−4.3	−4.5	0.7	0.9
4	5.430	−4.6	−3.9	3.7	3.3
5	5.617	−1.4	−1.3	1.8	1.7

	ADC(2)/PCM - gas phase geometry				
n	ω_{n0}	R^{r}_{n0}	R^{∇}_{n0}	f^{r}_{n0}	f^{∇}_{n0}
1	4.831	−1.1	−0.3	59.1	47.1
2	5.010	−1.6	−0.7	2.1	5.3
3	5.348	−4.9	−5.1	1.3	1.7
4	5.510	−13.6	−12.1	6.0	5.0
5	5.722	4.4	4.3	15.9	13.8

	ADC(2)/PCM - PCM geometry				
n	ω_{n0}	R^{r}_{n0}	R^{∇}_{n0}	f^{r}_{n0}	f^{∇}_{n0}
1	4.830	−1.4	−0.3	59.1	47.1
2	5.036	−1.5	−0.4	2.0	5.1
3	5.406	−5.5	−6.1	2.0	2.6
4	5.541	−6.7	−5.8	1.5	1.2
5	5.740	0.6	0.6	0.9	0.7

A.8 (1*R*)-camphor, (1*R*)-norcamphor, (1*R*)-fenchone

(1*R*)-camphor

Table A.14: Transition energy, ω (eV), optical rotatory strength, R ($\times$ 10^{-40}esu^2$\cdot$cm^2) and oscillator strength ($\times 10^{-3}$) of the lowest singlet excitations of *(1R)*-camphor calculated at the ADC(2) level of theory using the aug-cc-pVDZ basis set.

	ADC(2)/aug-cc-pVDZ					ADC(3)/aug-cc-pVDZ				
n	ω_{n0}	R^{r}_{n0}	R^{∇}_{n0}	f^{r}_{n0}	f^{∇}_{n0}	ω_{n0}	R^{r}_{n0}	R^{∇}_{n0}	f^{r}_{n0}	f^{∇}_{n0}
1	4.18	5.2	5.2	0.2	0.2	4.42	3.2	1.8	0.1	0.1
2	5.54	2.0	2.3	9.6	11.8	6.67	4.7	3.6	12.3	9.7
3	5.92	-0.4	-0.4	6.5	6.5	7.11	-1.4	-1.3	16.6	15.4
4	5.97	1.0	0.9	5.4	5.9	7.14	3.4	3.0	7.1	6.0
5	6.01	1.5	1.4	15.4	17.3	7.21	1.3	1.2	23.5	18.8
6	6.52	-0.7	-0.7	0.9	1.2	7.66	-4.3	-4.1	9.0	8.4
7	6.59	3.1	3.3	3.2	3.7	7.80	1.4	1.3	9.4	7.7
8	6.63	-0.9	-1.0	4.2	4.6	7.81	-0.1	1.1	26.1	19.8
9	6.65	-2.6	-2.8	2.6	3.2	7.85	-5.4	-4.6	14.8	10.7
10	6.74	0.6	0.9	13.4	15.5	7.89	7.6	6.2	7.5	4.9

(1*R*)-norcamphor

Table A.15: Transition energy, ω (eV), optical rotatory strength, R ($\times$ 10^{-40}esu^2$\cdot$cm^2) and oscillator strength ($\times 10^{-3}$) of the lowest singlet excitations of *(1R)*-norcamphor calculated at the ADC(2) level of theory using the d-aug-cc-pVDZ basis set.

	ADC(2)/d-aug-cc-pVDZ					ADC(3)/d-aug-cc-pVDZ				
n	ω_{n0}	R^{r}_{n0}	R^{∇}_{n0}	f^{r}_{n0}	f^{∇}_{n0}	ω_{n0}	R^{r}_{n0}	R^{∇}_{n0}	f^{r}_{n0}	f^{∇}_{n0}
1	4.09	0.6	0.3	0.2	0.1	4.33	0.3	-0.5	0.2	0.1
2	5.47	-1.6	-1.8	9.4	11.9	6.65	-3.3	-2.8	14.3	11.3
3	5.97	10.0	10.8	12.3	14.0	7.23	15.0	13.6	12.5	9.8
4	5.99	-0.3	-0.2	2.9	2.9	7.27	3.7	3.9	15.5	15.1
5	6.03	-1.6	-1.8	3.1	3.4	7.33	-2.1	-2.0	7.9	6.4
6	6.46	0.2	0.4	4.8	5.6	7.86	-1.0	-1.2	12.9	10.3
7	6.51	2.0	2.2	2.0	2.5	7.91	-5.9	-5.1	29.0	24.7
8	6.53	-0.2	-0.5	0.7	0.9	7.98	0.0	-0.3	3.8	3.9
9	6.57	0.0	-0.1	0.1	0.1	8.07	-4.2	-3.0	2.2	1.2
10	6.60	0.2	0.2	0.2	0.2	8.13	-4.7	-3.5	18.6	12.9

(1*R*)-fenchone

TABLE A.16: Transition energy, ω (eV), optical rotatory strength, R ($\times$ 10^{-40}esu^2·cm^2) and oscillator strength ($\times 10^{-3}$) of the lowest singlet excitations of *(1R)*-fenchone calculated at the ADC(2) level of theory using the aug-cc-pVDZ basis set.

	ADC(2)/aug-cc-pVDZ					ADC(3)/aug-cc-pVDZ				
n	ω_{n0}	R^{r}_{n0}	R^{∇}_{n0}	f^{r}_{n0}	f^{∇}_{n0}	ω_{n0}	R^{r}_{n0}	R^{∇}_{n0}	f^{r}_{n0}	f^{∇}_{n0}
1	4.16	-2.1	-2.5	0.0	0.0	4.38	-2.4	-3.0	0.0	0.0
2	5.44	0.4	0.3	2.2	1.9	6.58	-0.4	-0.2	1.5	2.0
3	5.79	2.9	3.3	14.6	15.7	6.99	10.2	9.2	27.9	21.7
4	5.84	-0.4	-0.4	12.7	13.8	7.05	-4.5	-4.3	21.0	17.6
5	5.92	3.0	3.2	2.1	2.3	7.11	5.9	5.2	5.2	4.0
6	6.37	0.9	0.9	7.2	6.8	7.57	1.5	1.4	9.5	8.4
7	6.47	-0.2	-0.4	1.8	1.9	7.68	0.6	0.5	1.8	1.5
8	6.48	-1.6	-1.6	0.6	0.6	7.69	-5.9	-5.6	4.7	4.2
9	6.54	0.0	-0.1	8.8	9.4	7.75	1.4	1.4	22.0	18.8
10	6.58	-1.4	-1.4	25.2	26.7	7.79	0.4	0.4	31.7	27.8

Appendix B

Excited-state to excited-state rotatory and oscillator strengths

B.1 Camphor, norcamphor and fenchone

Table B.1: Transition energy, ω (eV) and optical rotatory strength R ($\times 10^{-40}$esu^2·cm^2) of the energetically lowest singlet excitations of (1R)-norcamphor calculated at the ADC(3), BLYP, B3LYP, BHandHLYP and CAM-B3LYP levels using the d-aug-cc-pVDZ basis set.

	ADC(3)/d-aug-cc-pVDZ					
n	ω_{n0}	R^{r}_{n0}	R^{∇}_{n0}	ω_{n1}	R^{r}_{n1}	R^{∇}_{n1}
1	4.33	0.28	-0.50			
2	6.62	-3.00	-2.51	2.29	1.13	1.36
3	7.16	12.96	11.75	2.83	0.97	-0.02
4	7.20	3.35	3.45	2.88	2.96	2.97
5	7.24	-2.12	-2.04	2.92	-4.15	-3.99
6	7.71	-0.50	-0.68	3.38	0.75	0.35
7	7.76	-0.87	-0.70	3.43	-7.54	-7.00
8	7.79	-0.26	-0.47	3.46	-0.75	-0.75
9	7.84	-0.46	-0.16	3.51	0.42	-0.11
10	7.87	-0.15	-0.09	3.54	0.37	1.12

	BLYP/d-aug-cc-pVDZ						B3LYP/d-aug-cc-pVDZ					
n	ω_{n0}	R^{r}_{n0}	R^{∇}_{n0}	ω_{n1}	R^{r}_{n1}	R^{∇}_{n1}	ω_{n0}	R^{r}_{n0}	R^{∇}_{n0}	ω_{n1}	R^{r}_{n1}	R^{∇}_{n1}
1	3.97	-1.64	-2.20				4.17	0.18	-0.30			
2	4.51	0.66	0.72	0.54	-3.25	-3.20	5.44	-1.44	-1.45	1.28	-0.98	-0.94
3	5.01	3.02	2.95	1.04	-3.96	-3.93	5.94	5.22	5.15	1.77	-1.42	-1.41
4	5.05	1.68	1.69	1.09	5.52	5.47	5.98	3.04	3.12	1.81	3.77	3.70
5	5.11	1.67	1.71	1.15	5.13	5.22	6.01	-0.34	-0.34	1.85	0.18	0.23
6	5.42	0.33	0.32	1.45	0.89	0.85	6.40	0.25	0.25	2.23	-0.44	-0.39
7	5.44	0.13	0.11	1.48	-0.67	-0.54	6.43	1.50	1.54	2.26	-3.82	-3.72
8	5.47	1.07	1.15	1.50	-6.03	-5.89	6.44	-0.35	-0.37	2.28	0.23	0.20
9	5.50	-0.05	-0.03	1.53	0.92	0.81	6.46	0.45	0.48	2.29	0.43	0.37
10	5.51	-0.12	-0.11	1.54	-0.57	-0.64	6.48	-0.37	-0.38	2.31	0.04	-0.02

	BHandHLYP/d-aug-cc-pVDZ						CAM-B3LYP/d-aug-cc-pVDZ					
n	ω_{n0}	R^{r}_{n0}	R^{∇}_{n0}	ω_{n1}	R^{r}_{n1}	R^{∇}_{n1}	ω_{n0}	R^{r}_{n0}	R^{∇}_{n0}	ω_{n1}	R^{r}_{n1}	R^{∇}_{n1}
1	4.44	0.41	0.03			4.25	0.73	0.25				
2	6.62	-2.95	-2.99	2.18	-0.11	-0.07	6.22	-2.48	-2.51	1.97	-0.11	-0.07
3	7.13	13.27	13.37	2.69	-1.15	-1.20	6.77	10.34	10.52	2.52	-1.15	-1.20
4	7.16	1.25	1.25	2.72	3.24	3.20	6.81	3.44	3.35	2.56	3.24	3.20
5	7.20	-2.38	-2.40	2.76	-1.47	-1.44	6.84	-1.16	-1.17	2.60	-1.47	-1.44
6	7.63	0.16	0.15	3.19	-0.02	-0.01	7.29	0.19	0.17	3.04	-0.02	-0.01
7	7.67	1.78	1.81	3.24	-2.96	-2.90	7.34	0.40	0.46	3.09	-2.96	-2.90
8	7.69	-1.23	-1.24	3.25	0.19	0.17	7.36	0.43	0.40	3.11	0.19	0.17
9	7.72	0.01	0.07	3.28	-0.20	-0.26	7.40	-0.42	-0.34	3.16	-0.20	-0.26
10	7.75	-0.26	-0.25	3.31	-0.17	-0.15	7.44	-0.24	-0.23	3.19	-0.17	-0.15

Table B.2: Transition energy, ω (eV) and optical rotatory strength R ($\times$ 10^{-40}esu^2·cm^2) of the energetically lowest singlet excitations of (1R)-camphor and (1R)-fenchone calculated at the ADC(3) level using the aug-cc-pVDZ basis set.

	(1R)-camphor					(1R)-fenchone				
n	ω_{n1}	R^{r}_{n1}	R^{∇}_{n1}	f^{r}_{n1}	f^{∇}_{n1}	ω_{n1}	R^{r}_{n1}	R^{∇}_{n1}	f^{r}_{n1}	f^{∇}_{n1}
2	2.25	−3.20	−3.47	2.20	4.25	2.20	−0.70	−0.32	3.21	0.78
3	2.69	−1.38	−0.79	3.48	1.83	2.61	−3.54	−3.38	1.71	2.86
4	2.73	5.17	4.13	5.30	4.25	2.67	−0.59	−0.87	0.04	0.10
5	2.79	−1.67	−0.36	12.94	13.57	2.73	2.09	2.63	2.00	3.01
6	3.24	5.21	4.60	0.75	0.73	3.19	0.85	0.83	2.42	2.13
7	3.38	0.67	0.12	3.74	3.31	3.30	−0.51	−0.53	1.02	0.82
8	3.39	−1.45	−0.56	0.81	0.77	3.31	3.32	3.19	2.44	2.04
9	3.43	1.33	1.26	1.57	1.79	3.38	−1.48	−0.88	13.42	11.95
10	3.47	5.88	5.78	3.47	3.31	3.41	1.92	1.86	0.95	1.74

Table B.3: Transition energy, ω (eV) and optical rotatory strength R ($\times$ 10^{-40}esu^2·cm^2) of the energetically lowest singlet excitations of (1R)-camphor and (1R)-fenchone calculated at the CAM-B3LYP level using the d-aug-cc-pVDZ basis set.

	(1R)-camphor			(1R)-fenchone			(1R)-norcamphor		
n	ω_{n1}	R^{r}_{n1}	R^{∇}_{n1}	ω_{n1}	R^{r}_{n1}	R^{∇}_{n1}	ω_{n1}	R^{r}_{n1}	R^{∇}_{n1}
2	1.99	−1.80	−1.80	1.96	−0.50	−0.52	1.97	0.52	0.57
3	2.43	−0.90	−0.87	2.42	−1.83	−1.82	2.52	0.78	0.71
4	2.46	1.81	1.79	2.44	−0.40	−0.43	2.56	1.51	1.49
5	2.56	0.94	1.03	2.50	1.31	1.35	2.60	−2.34	−2.32
6	2.97	5.14	4.94	2.95	0.56	0.57	3.04	−0.43	−0.41
7	3.07	−2.03	−1.91	3.08	−0.62	−0.60	3.09	−3.63	−3.58
8	3.13	1.61	1.40	3.10	1.70	1.78	3.11	−0.09	−0.11
9	3.17	0.93	0.82	3.17	2.37	2.42	3.16	−0.12	−0.15
10	3.20	1.24	1.54	3.20	0.38	0.40	3.19	0.73	0.74

B.2 Binol

Table B.4: Transition energy, ω (eV) and optical rotatory strength R ($\times$ 10^{-40}esu^2$\cdot$cm^2) of the energetically lowest singlet excitations of BINOL calculated at the ADC(2) and CAM-B3LYP levels using the aug-cc-pVDZ basis set.

	ADC(2)/aug-cc-pVDZ					CAM-B3LYP/aug-cc-pVDZ			
n	ω_{n0}	R^r_{n0}	R^{∇}_{n0}	f^r_{n0}	f^{∇}_{n0}	ω_{n0}	R^r_{n0}	R^{∇}_{n0}	f^r_{n0}
1	4.33	-35.28	-26.54	0.10	0.07	4.41	-24.95	-23.20	1.34
2	4.35	66.97	53.81	0.02	0.01	4.45	71.94	66.59	0.15
3	4.98	1.53	1.62	0.13	0.09	4.83	-1.94	-0.96	0.73
4	4.99	18.55	18.37	0.01	0.01	4.84	0.37	0.49	0.00
5	5.08	-1.34	-0.82	0.00	0.00	5.01	-0.41	-0.48	0.02
6	5.09	-5.26	-4.26	0.01	0.01	5.01	-2.46	-2.35	0.04
7	5.93	-1092.48	-944.74	1.12	0.89	5.93	-1178.02	-1147.75	7.03
8	5.97	-227.32	-190.81	0.20	0.14	6.00	280.78	271.21	1.66
9	5.99	623.88	535.31	0.44	0.32	6.00	14.23	8.88	0.51
10	6.02	60.66	51.86	0.11	0.08	6.03	196.38	199.60	0.62
11	6.07	-179.52	-157.15	0.10	0.08	6.05	-210.80	-206.01	0.70
12	6.10	406.91	350.91	0.28	0.20	6.08	679.36	667.31	2.78
13	6.10	100.06	88.29	0.07	0.05	6.12	-314.80	-314.20	1.68
14	6.10	87.87	77.75	0.06	0.05	6.21	361.86	356.86	1.53
15	6.31	16.87	14.48	0.18	0.14	6.38	21.89	16.86	0.18
16	6.32	20.05	17.78	0.14	0.11	6.39	55.65	52.56	0.94
17	6.54	424.09	355.61	0.22	0.16	6.55	-239.47	-240.55	0.96
18	6.55	-402.01	-340.34	0.37	0.27	6.55	272.07	271.67	0.83
19	6.82	-15.11	-24.87	0.00	0.01	6.71	49.45	44.29	0.18
20	6.86	-12.88	-8.56	0.01	0.01	6.73	26.14	29.99	0.01

TABLE B.5: Transition energy, ω (nm) and optical rotatory strength R ($\times 10^{-40}$esu^2·cm^2) of the energetically lowest singlet excitations of BINOL calculated at the ADC(2) and CAM-B3LYP level using the d-aug-cc-pVDZ basis set.

	ADC(2)/aug-cc-pVDZ					CAM-B3LYP/aug-cc-pVDZ			
n	ω_{n1}	R^{r}_{n1}	R^{∇}_{n1}	f^{r}_{n1}	f^{∇}_{n1}	ω_{n1}	R^{r}_{n1}	R^{∇}_{n1}	f^{r}_{n1}
2	59753	-1.00	-7.67	0.16	4.85	27328	-0.94	-2.17	148.18
3	1920	-8.24	36.38	0.03	0.16	2945	10.82	25.51	2.95
4	1890	31.28	-47.95	1.77	1.90	2851	-0.89	-39.24	22.46
5	1655	-7.19	12.51	0.62	0.67	2062	-3.29	3.42	58.74
6	1640	0.66	7.24	0.12	0.22	2041	-0.77	3.62	26.14
7	777	-37.80	-35.80	5.41	4.87	813	-11.00	-11.15	39.16
8	756	0.06	-0.46	0.15	1.14	779	0.33	-0.36	107.83
9	749	-7.70	-2.09	10.89	8.93	775	-0.50	-0.98	31.95
10	735	-1.94	-7.66	0.08	0.56	762	-1.92	-2.29	39.41
11	713	41.16	43.14	10.26	11.27	756	1.50	1.80	24.86
12	703	14.14	16.11	9.85	10.28	741	2.32	1.76	23.62
13	701	-3.27	-3.41	4.18	5.19	724	2.27	1.29	21.03
14	701	-5.11	-5.54	4.31	5.43	687	8.06	10.81	134.18
15	627	73.01	86.41	58.89	73.55	630	-29.71	-33.62	496.83
16	624	-81.32	-89.65	51.96	58.14	626	23.70	29.33	304.42
17	562	6.43	7.46	0.29	0.31	579	0.23	0.22	405.20
18	560	-6.47	-6.98	0.12	0.14	577	0.29	0.21	559.27
19	499	21.00	17.10	7.79	5.20	538	8.87	8.41	106.72
20	491	-1.52	-2.14	3.37	2.62	533	-10.32	-9.76	101.64

Appendix C

First-order hyperpolarizability tensor

C.1 Static first-order hyperpolarizability tensor

Table C.1: Components of static β at ADC and CC levels of theory of HF (1), HCl (2), HBr (3), HOH (4), and HSH (5) using the aug-cc-pVTZ basis set.

Molecule	Method	β_{zzz}	β_{zxx}	β_{zyy}	$\beta_{\|\|}$
HF (1)	ADC(1)	13.68	2.17	2.17	10.81
	ADC(2)	16.16	3.66	3.66	14.09
	ADC(3)	12.71	2.54	2.54	10.68
	CCS	11.40	1.50	1.50	8.64
	CC2	14.36	3.55	3.55	12.88
	CCSD	11.63	2.39	2.39	9.85
HCl (2)	ADC(1)	28.09	1.08	1.08	18.15
	ADC(2)	25.19	0.88	0.88	16.17
	ADC(3)	22.22	0.10	0.10	13.45
	CCS	21.53	−1.43	−1.43	11.20
	CC2	22.49	0.61	0.61	14.22
	CCSD	19.68	−0.20	−0.20	11.57
HBr (3)	ADC(1)	29.81	−0.30	−0.30	17.53
	ADC(2)	25.38	−1.28	−1.28	13.69
	ADC(3)	21.28	−2.67	−2.67	9.57
	CCS	21.40	−4.14	−4.14	7.87
	CC2	21.67	−1.72	−1.72	10.94
	CCSD	18.60	−2.75	−2.75	7.85
HOH (4)	ADC(1)	−18.95	1.60	−2.76	−12.07
	ADC(2)	−23.17	0.89	−5.50	−16.66
	ADC(3)	−18.70	1.29	−3.75	−12.69
	CCS	−16.23	2.53	−1.63	−9.20
	CC2	−21.40	1.22	−5.41	−15.36
	CCSD	−17.11	1.72	−3.43	−11.29
HSH (5)	ADC(1)	−22.56	4.01	−4.38	−13.75
	ADC(2)	−21.39	4.23	−3.47	−12.38
	ADC(3)	−18.61	4.97	−2.09	−9.44
	CCS	−17.10	6.32	0.81	−5.98
	CC2	−18.91	4.44	−3.34	−10.68
	CCSD	−16.14	4.92	−1.72	−7.76

Table C.2: Components of static β at ADC and CC levels of theory of NaF (6), NaCl (7), NaBr (8), NaOH (9), and NaSH (10) using the aug-cc-pVTZ basis set.

Molecule	Method	β_{zzz}	β_{zxx}	β_{zyy}	$\beta_{\|\|}$
NaF (6)	ADC(1)	59.01	29.53	29.53	70.85
	ADC(2)	319.54	113.54	113.54	327.98
	ADC(3)	113.01	49.16	49.16	126.80
	CCS	53.59	27.60	27.60	65.28
	CC2	471.03	146.82	146.82	458.80
	CCSD	151.48	61.41	61.41	164.58
NaCl (7)	ADC(1)	365.45	124.87	124.87	369.12
	ADC(2)	585.29	180.10	180.10	567.30
	ADC(3)	493.94	156.58	156.58	484.26
	CCS	316.54	109.61	109.61	321.45
	CC2	623.79	185.87	185.87	597.32
	CCSD	488.76	153.15	153.15	477.04
NaBr (8)	ADC(1)	628.23	188.82	188.82	603.53
	ADC(2)	908.34	250.70	250.70	845.85
	ADC(3)	763.17	215.01	215.01	715.92
	CCS	536.07	162.51	162.51	516.65
	CC2	921.36	248.50	248.50	851.02
	CCSD	763.56	213.35	213.35	714.16
NaOH (9)	ADC(1)	58.60	68.75	68.75	117.66
	ADC(2)	232.57	241.61	241.61	429.47
	ADC(3)	106.82	110.69	110.69	196.92
	CCS	54.02	66.21	66.21	111.86
	CC2	330.18	306.11	306.11	565.44
	CCSD	132.85	136.14	136.14	243.07
NaSH (10)	ADC(1)	32.21	52.02	21.38	63.37
	ADC(2)	26.67	56.05	16.86	59.75
	ADC(3)	32.86	64.94	24.17	73.18
	CCS	34.83	59.38	30.85	75.03
	CC2	34.03	65.50	17.56	70.26
	CCSD	36.99	67.12	24.48	77.16

TABLE C.3: Components of static β at ADC and CC levels of theory of LiF (11), LiCl (12), LiBr (13), LiOH (14), and LiSH (15) using the aug-cc-pVTZ basis set.

Molecule	Method	β_{zzz}	β_{zxx}	β_{zyy}	$\beta_{\|\|}$
LiF (11)	ADC(1)	20.93	18.95	18.95	35.30
	ADC(2)	66.45	57.09	57.09	108.38
	ADC(3)	31.92	29.24	29.24	54.24
	CCS	16.65	17.42	17.42	30.90
	CC2	75.69	63.70	63.70	121.86
	CCSD	34.35	34.14	34.14	61.57
Molecule	Method	β_{zzz}	β_{zxx}	β_{zyy}	$\beta_{\|\|}$
LiCl (12)	ADC(1)	150.16	91.08	91.08	199.39
	ADC(2)	212.19	123.09	123.09	275.02
	ADC(3)	178.65	108.92	108.92	237.89
	CCS	117.17	79.66	79.66	165.89
	CC2	210.85	123.49	123.49	274.70
	CCSD	166.91	105.57	105.57	226.84
Molecule	Method	β_{zzz}	β_{zxx}	β_{zyy}	$\beta_{\|\|}$
LiBr (13)	ADC(1)	268.69	138.21	138.21	327.07
	ADC(2)	352.83	174.54	174.54	421.14
	ADC(3)	293.03	151.11	151.11	357.15
	CCS	208.29	118.95	118.95	267.72
	CC2	337.45	169.47	169.47	405.83
	CCSD	278.32	149.18	149.18	346.01
Molecule	Method	β_{zzz}	β_{zxx}	β_{zyy}	$\beta_{\|\|}$
LiOH (14)	ADC(1)	63.13	50.31	50.31	98.26
	ADC(2)	189.65	143.36	143.36	285.83
	ADC(3)	101.71	76.60	76.60	152.95
	CCS	55.01	47.33	47.33	89.80
	CC2	220.23	163.04	163.04	327.79
	CCSD	113.61	87.97	87.97	173.74
Molecule	Method	β_{zzz}	β_{zxx}	β_{zyy}	$\beta_{\|\|}$
LiSH (15)	ADC(1)	5.00	−11.85	14.80	4.77
	ADC(2)	−3.60	−34.03	11.93	−15.42
	ADC(3)	2.59	−21.20	17.72	−0.53
	CCS	10.39	−1.92	24.15	19.57
	CC2	−0.62	−36.98	12.45	−15.09
	CCSD	5.83	−19.59	18.35	2.75

Table C.4: Components of static β at ADC and CC levels of theory of H_2SO_4 (16), H_2SO_3 (17), H_2SO_2 (18), H_2SO_2 (19), and H_3BO_3 (20) using the aug-cc-pVTZ basis set.

Molecule	Method	β_{zzz}	β_{zxx}	β_{zyy}	$\beta_{\|\|}$
H_2SO_4 (16)	ADC(1)	65.11	16.67	18.02	59.88
	ADC(2)	101.14	27.64	27.16	93.56
	ADC(3)	62.19	16.96	22.78	61.16
	CCS	47.12	11.45	15.74	44.58
	CC2	82.92	23.06	27.54	80.12
	CCSD	53.99	14.68	20.38	53.43
Molecule	Method	β_{zzz}	β_{zxx}	β_{zyy}	$\beta_{\|\|}$
H_2SO_3 (17)	ADC(1)	123.09	15.79	18.22	94.26
	ADC(2)	228.71	34.48	35.40	179.15
	ADC(3)	132.05	24.77	26.10	109.76
	CCS	89.67	13.66	15.65	71.39
	CC2	181.45	37.34	37.23	153.61
	CCSD	112.09	23.76	24.70	96.33
Molecule	Method	β_{zzz}	β_{zxx}	β_{zyy}	$\beta_{\|\|}$
H_2SO_2 (18)	ADC(1)	99.84	10.04	55.32	99.12
	ADC(2)	118.12	11.11	68.06	118.38
	ADC(3)	84.55	14.09	64.86	98.10
	CCS	80.67	9.84	53.12	86.18
	CC2	91.42	10.87	66.51	101.28
	CCSD	72.63	11.15	59.11	85.73
Molecule	Method	β_{zzz}	β_{zxx}	β_{zyy}	$\beta_{\|\|}$
H_2SO_2 (19)	ADC(1)	−17.45	4.68	−7.19	−11.97
	ADC(2)	−15.37	5.81	−7.58	−10.28
	ADC(3)	−15.98	8.87	−7.38	−8.69
	CCS	−15.14	5.85	−4.02	−7.98
	CC2	−14.87	7.11	−8.22	−9.59
	CCSD	−14.33	7.34	−7.13	−8.47
Molecule	Method	β_{zzz}	β_{zxx}	β_{zyy}	$\beta_{\|\|}$
H_3BO_3 (20)	ADC(1)	−27.98	23.94	−0.46	−2.70
	ADC(2)	−37.64	32.48	−0.62	−3.47
	ADC(3)	−29.94	25.90	−0.47	−2.71
	CCS	−24.78	21.74	−0.24	−1.97
	CC2	−34.18	29.27	−0.52	−3.26
	CCSD	−28.84	25.20	−0.34	−2.39

TABLE C.5: Components of static β at ADC and CC levels of theory of HNO (22), HNO_2 (23), HNO_3 (24), and N_2O (25) using the aug-cc-pVTZ basis set.

Molecule	Method	β_{zzz}	β_{zxx}	β_{zyy}	$\beta_{\|\|}$
HNO (22)	ADC(1)	−69.92	−2.95	−0.44	−43.99
	ADC(2)	−115.92	−2.10	3.81	−68.53
	ADC(3)	−86.49	6.94	4.49	−45.04
	CCS	−60.11	2.58	0.79	−34.04
	CC2	−127.91	1.92	4.11	−73.13
	CCSD	−83.69	6.30	3.89	−44.10
Molecule	Method	β_{zzz}	β_{zxx}	β_{zyy}	$\beta_{\|\|}$
HNO_2 (23)	ADC(1)	50.98	−2.09	8.03	34.15
	ADC(2)	49.45	−17.68	17.20	29.38
	ADC(3)	30.55	−2.73	13.66	24.89
	CCS	35.60	0.39	7.57	26.14
	CC2	47.23	−3.41	21.07	38.93
	CCSD	28.04	−0.98	14.58	24.98
Molecule	Method	β_{zzz}	β_{zxx}	β_{zyy}	$\beta_{\|\|}$
HNO_3 (24)	ADC(1)	62.01	−33.54	4.12	19.55
	ADC(2)	62.24	−36.70	7.14	19.61
	ADC(3)	34.35	−24.86	5.67	9.10
	CCS	44.33	−25.54	3.31	13.25
	CC2	36.21	−14.62	7.74	17.60
	CCSD	25.62	−17.33	5.67	8.38
Molecule	Method	β_{zzz}	β_{zxx}	β_{zyy}	$\beta_{\|\|}$
N_2O (25)	ADC(1)	−91.77	−4.60	−4.60	−60.58
	ADC(2)	−168.65	−3.19	−3.19	−105.02
	ADC(3)	−90.59	−5.67	−5.67	−61.15
	CCS	−73.50	−4.84	−4.84	−49.91
	CC2	−74.91	−4.78	−4.78	−50.68
	CCSD	−74.25	−4.22	−4.22	−49.61

Table C.6: Components of static β at ADC and CC levels of theory of HNS (26), HNS_2 (27), HNS_3 (28), and N_2S (29) using the aug-cc-pVTZ basis set.

Molecule	Method	β_{zzz}	β_{zxx}	β_{zyy}	$\beta_{\|\|}$
HNS (26)	ADC(1)	77.81	67.73	24.10	101.79
	ADC(2)	53.60	70.82	18.08	85.50
	ADC(3)	45.46	73.21	20.06	83.24
	CCS	52.20	68.39	23.36	86.37
	CC2	24.66	67.53	14.47	64.00
	CCSD	23.54	64.48	15.18	61.92

Molecule	Method	β_{zzz}	β_{zxx}	β_{zyy}	$\beta_{\|\|}$
HNS_2 (27)	ADC(1)	98.53	211.41	7.40	190.40
	ADC(2)	207.80	345.34	0.95	332.45
	ADC(3)	197.17	276.82	5.19	287.51
	CCS	104.44	175.75	7.13	172.39
	CC2	190.76	223.96	0.79	249.30
	CCSD	160.57	212.63	0.60	224.28

Molecule	Method	β_{zzz}	β_{zxx}	β_{zyy}	$\beta_{\|\|}$
HNS_3 (28)	ADC(1)	−149.53	176.44	−12.56	8.61
	ADC(2)	−69.67	121.59	−14.08	22.70
	ADC(3)	124.47	25.44	−14.96	80.97
	CCS	−80.04	121.97	−10.50	18.86
	CC2	10.27	39.46	−11.25	23.09
	CCSD	47.57	38.14	−10.97	44.84

Molecule	Method	β_{zzz}	β_{zxx}	β_{zyy}	$\beta_{\|\|}$
N_2S (29)	ADC(1)	−330.43	76.21	76.21	−106.80
	ADC(2)	−641.86	97.46	97.46	−268.16
	ADC(3)	−274.77	86.06	86.06	−61.58
	CCS	−227.11	76.35	76.35	−44.64
	CC2	−259.50	87.92	87.92	−50.20
	CCSD	−222.14	78.50	78.50	−39.08

Table C.7: Components of static β at ADC and CC levels of theory of COH_2 (30), C_2OH_4 (31), C_3OH_6 (32), H_2CO_3 (33), and $C_2O_4H_4$ (34) using the aug-cc-pVTZ basis set.

Molecule	Method	β_{zzz}	β_{zxx}	β_{zyy}	$\beta_{\|\|}$
COH_2 (30)	ADC(1)	−59.56	−2.32	−7.08	−41.38
	ADC(2)	−86.11	11.12	−5.78	−48.46
	ADC(3)	−62.09	12.95	−5.08	−32.54
	CCS	−50.15	2.81	−5.82	−31.90
	CC2	−85.08	19.13	−5.21	−42.70
	CCSD	−58.71	14.72	−4.26	−28.95
C_2OH_4 (31)	ADC(1)	−41.89	−22.46	−9.86	−44.53
	ADC(2)	−77.79	−20.54	−9.64	−64.78
	ADC(3)	−48.71	−9.69	−8.16	−39.94
	CCS	−33.23	−15.59	−8.90	−34.63
	CC2	−79.05	−11.61	−9.34	−60.00
	CCSD	−46.62	−6.94	−7.24	−36.48
C_3OH_6 (32)	ADC(1)	104.70	1.71	18.19	74.76
	ADC(2)	105.49	17.95	18.83	85.37
	ADC(3)	63.78	4.48	16.84	51.06
	CCS	78.29	−1.80	16.73	55.94
	CC2	79.78	23.14	19.39	73.39
	CCSD	52.31	4.85	15.86	43.81
H_2CO_3 (33)	ADC(1)	26.38	−35.98	0.78	−5.30
	ADC(2)	18.34	−51.00	0.80	−19.12
	ADC(3)	11.40	−40.14	0.16	−17.15
	CCS	19.69	−31.48	0.99	−6.48
	CC2	4.51	−44.04	1.94	−22.55
	CCSD	5.88	−38.10	1.11	−18.66
$C_2O_4H_4$ (34)	ADC(1)	54.01	18.76	9.57	49.41
	ADC(2)	66.50	23.01	15.22	62.84
	ADC(3)	31.08	10.98	10.79	31.71
	CCS	33.30	11.76	7.18	31.34
	CC2	71.01	24.10	18.78	68.33
	CCSD	25.20	8.93	11.52	27.39

Table C.8: Components of static β at ADC and CC levels of theory of $C_2O_2H_4$ (35), Furan (40), Thiopenthene (41), Pyrrole (42), and Imidazole (43) using the aug-cc-pVTZ basis set.

Molecule	Method	β_{zzz}	β_{zxx}	β_{zyy}	$\beta_{\|\|}$
$C_2O_2H_4$ (35)	ADC(1)	92.18	−9.20	18.46	60.86
	ADC(2)	100.65	−7.17	21.36	68.90
	ADC(3)	61.55	−9.04	18.56	42.64
	CCS	67.40	−10.38	16.86	44.32
	CC2	75.03	−0.51	21.80	57.79
	CCSD	48.88	−8.21	17.45	34.87
Molecule	Method	β_{zzz}	β_{zxx}	β_{zyy}	$\beta_{\|\|}$
Furan (40)	ADC(1)	13.19	−36.29	−5.19	−16.98
	ADC(2)	−3.41	−32.69	−4.93	−24.62
	ADC(3)	2.42	−31.24	−4.24	−19.84
	CCS	19.46	−35.53	−3.91	−11.99
	CC2	0.55	−32.80	−4.14	−21.84
	CCSD	0.01	−30.00	−4.13	−20.47
Molecule	Method	β_{zzz}	β_{zxx}	β_{zyy}	$\beta_{\|\|}$
Thiopenthene (41)	ADC(1)	−30.37	−4.38	−9.13	−26.33
	ADC(2)	−35.22	−6.69	−6.19	−28.86
	ADC(3)	−31.91	−4.27	−5.24	−24.85
	CCS	−20.60	−1.67	−7.66	−17.96
	CC2	−27.67	−5.58	−5.41	−23.19
	CCSD	−36.23	−6.46	−5.60	−28.97
Molecule	Method	β_{zzz}	β_{zxx}	β_{zyy}	$\beta_{\|\|}$
Pyrrole (42)	ADC(1)	22.35	−21.36	5.01	3.60
	ADC(2)	15.85	−11.00	3.52	5.02
	ADC(3)	25.96	−7.79	3.54	13.02
	CCS	21.71	−23.73	3.76	1.04
	CC2	16.23	−11.86	2.97	4.41
	CCSD	26.42	−7.11	3.53	13.70
Molecule	Method	β_{zzz}	β_{zxx}	β_{zyy}	$\beta_{\|\|}$
Imidazole (43)	ADC(1)	−6.91	−53.97	−5.15	−39.62
	ADC(2)	−50.11	−51.87	−2.29	−62.56
	ADC(3)	−21.22	−41.57	−2.96	−39.44
	CCS	2.93	−50.05	−3.75	−30.52
	CC2	−58.60	−51.25	−1.71	−66.93
	CCSD	−18.00	−37.67	−1.88	−34.53

TABLE C.9: Components of static β at ADC and CC levels of theory of Thiozole (44), Thiadiazole (45), Thiazole (46), Dioxolane (47), and Isothiazole (48) using the aug-cc-pVTZ basis set.

Molecule	Method	β_{zzz}	β_{zxx}	β_{zyy}	$\beta_{\|\|}$
Thiozole (44)	ADC(1)	20.32	25.63	-1.59	26.61
	ADC(2)	0.79	47.76	-2.89	27.39
	ADC(3)	-4.85	31.89	-1.63	15.25
	CCS	15.42	21.71	-1.56	21.34
	CC2	-1.58	42.19	-2.68	22.76
	CCSD	-10.26	24.94	-2.20	7.49
Molecule	Method	β_{zzz}	β_{zxx}	β_{zyy}	$\beta_{\|\|}$
Thiadiazole (45)	ADC(1)	86.48	27.45	13.08	76.21
	ADC(2)	161.37	77.81	6.16	147.21
	ADC(3)	91.65	42.50	8.09	85.34
	CCS	67.26	18.85	10.10	57.72
	CC2	158.64	71.07	5.07	140.87
	CCSD	78.09	34.10	6.08	70.96
Molecule	Method	β_{zzz}	β_{zxx}	β_{zyy}	$\beta_{\|\|}$
Thiazole (46)	ADC(1)	-1.28	-27.29	7.72	-12.51
	ADC(2)	-36.46	-24.44	5.90	-33.00
	ADC(3)	-12.58	-17.73	6.01	-14.58
	CCS	1.91	-27.52	7.13	-11.09
	CC2	-45.28	-21.83	6.01	-36.66
	CCSD	-11.12	-15.65	5.99	-12.47
Molecule	Method	β_{zzz}	β_{zxx}	β_{zyy}	$\beta_{\|\|}$
Dioxolane (47)	ADC(1)	35.85	0.32	-1.55	20.78
	ADC(2)	50.84	1.62	-7.09	27.22
	ADC(3)	43.86	-0.80	-8.80	20.56
	CCS	35.48	-1.32	-4.75	17.64
	CC2	51.93	0.78	-10.57	25.29
	CCSD	42.43	-0.69	-9.43	19.39
Molecule	Method	β_{zzz}	β_{zxx}	β_{zyy}	$\beta_{\|\|}$
Isothiazole (48)	ADC(1)	0.79	12.52	-1.82	6.89
	ADC(2)	-4.22	30.45	-1.11	15.07
	ADC(3)	-18.26	24.96	-0.05	3.99
	CCS	-2.52	15.11	-2.02	6.35
	CC2	-3.32	31.63	-0.99	16.39
	CCSD	-19.73	19.49	-1.08	-0.79

TABLE C.10: Components of static β at ADC and CC levels of theory of 3-pyrroline (49) , Oxadiazole (50), and Oxazole (51) using the aug-cc-pVTZ basis set.

Molecule	Method	β_{zzz}	β_{zxx}	β_{zyy}	$\beta_{\|\|}$
3-pyrroline (49)	ADC(1)	−0.93	8.75	17.36	15.11
	ADC(2)	−1.83	15.38	27.88	24.85
	ADC(3)	−2.07	11.30	22.86	19.25
	CCS	−1.44	8.11	17.15	14.30
	CC2	−0.97	15.61	28.61	25.95
	CCSD	−1.36	11.54	22.56	19.64
Molecule	Method	β_{zzz}	β_{zxx}	β_{zyy}	$\beta_{\|\|}$
Oxadiazole (50)	ADC(1)	−31.71	−11.90	−23.88	−40.49
	ADC(2)	−48.75	−13.42	−19.70	−49.12
	ADC(3)	−34.30	−12.72	−19.54	−39.94
	CCS	−16.49	−12.08	−20.25	−29.30
	CC2	−48.87	−20.98	−18.38	−52.94
	CCSD	−34.11	−14.81	−17.51	−39.86
Molecule	Method	β_{zzz}	β_{zxx}	β_{zyy}	$\beta_{\|\|}$
Oxazole (51)	ADC(1)	50.99	−50.38	5.26	3.53
	ADC(2)	60.97	−42.80	2.47	12.38
	ADC(3)	56.12	−39.92	3.43	11.78
	CCS	49.37	−48.92	3.85	2.58
	CC2	64.34	−39.93	2.35	16.05
	CCSD	47.86	−37.54	2.31	7.58

C.2 Dynamic first-order hyperpolarizability tensor

Table C.11: $\beta_{\alpha\beta\gamma}$ components at 693.1 nm perturbation of CO, H_2O, H_2S and NH_3 at ADC levels of theory with the aug-cc-pVTZ and aug-cc-pVQZ basis sets.

	β_{zzz}		β_{zxx}		β_{xzx}		β_{yzy}		$\beta_{\|\|}$	
CO (39)	TZ	QZ	TZ	QZ	TZ	QZ	TZ	QZ	TZ	QZ
ADC(1)	48.2	48.2	2.4	2.4	0.5	0.5	0.5	0.5	30.3	30.3
ADC(2)	39.8	38.9	6.4	5.5	5.1	4.3	5.1	4.3	30.5	29.0
ADC(3)	38.7	38.2	9.1	8.4	7.5	6.8	7.5	6.8	32.8	31.8

	β_{zzz}		β_{zxx}		β_{xzx}		β_{yzy}		$\beta_{\|\|}$	
H_2O (4)	TZ	QZ	TZ	QZ	TZ	QZ	TZ	QZ	TZ	QZ
ADC(1)	−16.4	−16.6	−14.6	−13.7	−14.9	−13.9	−6.1	−6.0	−22.0	−21.5
ADC(2)	−24.1	−25.0	−18.3	−16.6	−18.2	−16.4	−14.3	−13.7	−33.0	−32.4
ADC(3)	−17.5	−18.3	−14.7	−13.4	−14.8	−13.4	−9.0	−9.0	−24.2	−24.0

	β_{zzz}		β_{zxx}		β_{xzx}		β_{yzy}		$\beta_{\|\|}$	
H_2S (5)	TZ	QZ	TZ	QZ	TZ	QZ	TZ	QZ	TZ	QZ
ADC(1)	−10.1	−6.3	−20.1	−15.5	−21.8	−17.2	−13.1	−12.8	−24.7	−19.9
ADC(2)	−9.9	−7.2	−20.9	−16.2	−21.5	−16.6	−14.1	−13.5	−25.4	−21.0
ADC(3)	−5.2	−2.7	−19.1	−14.7	−19.8	−15.2	−11.0	−11.0	−19.6	−15.9

	β_{zzz}		β_{zxx}		β_{xzx}		β_{yzy}		$\beta_{\|\|}$	
NH_3	TZ	QZ	TZ	QZ	TZ	QZ	TZ	QZ	TZ	QZ
ADC(1)	−33.5	−36.1	−11.7	−12.0	−11.5	−11.8	−11.5	−11.8	−34.0	−35.9
ADC(2)	−69.0	−72.8	−17.1	−17.1	−14.8	−15.0	−14.8	−15.0	−60.0	−62.5
ADC(3)	−52.4	−57.6	−13.5	−14.0	−12.2	−12.7	−12.2	−12.7	−46.7	−50.3

TABLE C.12: $\beta_{\alpha\beta\gamma}$ components at 693.1 nm perturbation of CO, H_2O, H_2S and NH_3 at ADC levels of theory with the aug-cc-pVTZ and aug-cc-pVQZ basis sets.

	β_{zzz}		β_{zxx}		β_{xzx}		β_{yzy}		$\beta_{\|\|}$	
CH_3F (52)	TZ	QZ	TZ	QZ	TZ	QZ	TZ	QZ	TZ	QZ
ADC(1)	−47.5	−47.1	−22.8	−21.9	−22.9	−22.0	−22.9	−22.0	−55.9	−54.6
ADC(2)	−56.6	−55.1	−27.5	−25.4	−27.8	−25.6	−27.8	−25.6	−67.2	−63.7
ADC(3)	−42.2	−42.2	−24.4	−24.4	−24.6	−24.6	−24.6	−24.6	−54.8	−54.8

	β_{zzz}		β_{zxx}		β_{xzx}		β_{yzy}		$\beta_{\|\|}$	
CH_2F_2 (54)	TZ	QZ	TZ	QZ	TZ	QZ	TZ	QZ	TZ	QZ
ADC(1)	−34.6	−32.5	−23.8	−22.9	−23.8	−22.9	−17.5	−17.8	−45.5	−44.0
ADC(2)	−42.7	−38.6	−28.7	−26.7	−28.9	−26.8	−22.8	−23.2	−56.7	−53.2
ADC(3)	−34.0	−34.0	−25.5	−25.5	−25.6	−25.6	−15.3	−15.3	−45.0	−45.0

	β_{zzz}		β_{zxx}		β_{xzx}		β_{yzy}		$\beta_{\|\|}$	
CF_3H (58)	TZ	QZ	TZ	QZ	TZ	QZ	TZ	QZ	TZ	QZ
ADC(1)	−28.5	−26.8	−9.1	−9.0	−9.0	−8.9	−9.0	−8.9	−27.9	−26.8
ADC(2)	−34.6	−31.0	−12.6	−12.3	−12.4	−12.1	−12.4	−12.1	−35.7	−33.2
ADC(3)	−29.0	−29.0	−8.7	−8.7	−8.5	−8.5	−8.5	−8.5	−27.7	−27.7

	β_{zzz}		β_{zxx}		β_{xzx}		β_{yzy}		$\beta_{\|\|}$	
$CFCl_3$ (53)	TZ	QZ	TZ	QZ	TZ	QZ	TZ	QZ	TZ	QZ
ADC(1)	−51.0	−58.0	1.2	1.6	1.2	1.7	1.2	1.7	−29.2	−32.7
ADC(2)	−69.7	−77.6	−2.2	−1.5	−2.7	−1.9	−2.7	−1.9	−44.9	−48.7
ADC(3)	−49.7	−49.7	−2.5	−2.5	−3.1	−3.1	−3.1	−3.1	−33.3	−33.3

	β_{zzz}		β_{zxx}		β_{xzx}		β_{yzy}		$\beta_{\|\|}$	
CF_2Cl_2 (60)	TZ	QZ	TZ	QZ	TZ	QZ	TZ	QZ	TZ	QZ
ADC(1)	−50.2	−57.5	−23.2	−25.0	−22.4	−24.2	−8.4	−7.5	−48.9	−53.8
ADC(2)	−68.9	−76.2	−32.8	−34.5	−32.3	−34.0	−18.2	−16.7	−71.7	−76.2
ADC(3)	−55.1	−55.1	−26.2	−26.2	−26.1	−26.1	−17.4	−17.4	−59.1	−59.1

TABLE C.13: $\beta_{\alpha\beta\gamma}$ components at 693.1 nm perturbation of CO, H_2O, H_2S and NH_3 at ADC levels of theory with the aug-cc-pVTZ and aug-cc-pVQZ basis sets.

	β_{zzz}		β_{zxx}		β_{xzx}		β_{yzy}		$\beta_{\parallel}$	
CF_3Cl (61)	TZ	QZ	TZ	QZ	TZ	QZ	TZ	QZ	TZ	QZ
ADC(1)	−45.8	−48.4	−26.4	−29.6	−25.1	−28.2	−25.1	−28.2	−58.1	−63.5
ADC(2)	−70.6	−71.8	−33.7	−36.8	−32.5	−35.7	−32.5	−35.7	−81.8	−86.4
ADC(3)	−64.1	−64.1	−28.8	−28.8	−27.9	−27.9	−27.9	−27.9	−72.2	−72.2

	β_{zzz}		β_{zxx}		β_{xzx}		β_{yzy}		$\beta_{\parallel}$	
CF_3Br (57)	TZ	QZ	TZ	QZ	TZ	QZ	TZ	QZ	TZ	QZ
ADC(1)	−1069	−1103	−49.0	−50.6	−45.6	−47.3	−45.6	−47.3	−1203	−1242
ADC(2)	−1601	−1600	−61.9	−62.3	−58.7	−59.3	−58.7	−59.3	−1677	−1683
ADC(3)	−1389	−1389	−54.6	−54.6	−52.4	−52.4	−52.4	−52.4	−1471	−1471
CH_3Cl (55)	TZ	QZ	TZ	QZ	TZ	QZ	TZ	QZ	TZ	QZ
ADC(1)	−32.8	−26.3	5.3	11.0	3.6	9.3	3.6	9.3	−14.7	−4.0
ADC(2)	−25.0	−16.9	8.2	14.2	6.9	13.1	6.9	13.1	−6.2	6.1
ADC(3)	−8.7	−1.9	9.2	15.3	8.3	14.6	8.3	14.6	5.1	16.7

	β_{zzz}		β_{zxx}		β_{xzx}		β_{yzy}		$\beta_{\parallel}$	
CH_2Cl_2 (56)	TZ	QZ	TZ	QZ	TZ	QZ	TZ	QZ	TZ	QZ
ADC(1)	1.9	11.4	−0.3	1.4	−1.4	0.4	−18.1	−19.8	−10.1	−4.4
ADC(2)	0.5	11.4	1.1	2.8	0.8	2.6	−18.2	−20.1	−10.1	−3.6
ADC(3)	6.7	6.7	5.4	5.4	5.2	5.2	−7.0	−7.0	2.9	2.9

	β_{zzz}		β_{zxx}		β_{xzx}		β_{yzy}		$\beta_{\parallel}$	
$CHCl_3$ (59)	TZ	QZ	TZ	QZ	TZ	QZ	TZ	QZ	TZ	QZ
ADC(1)	10.6	16.1	−11.6	−12.3	−12.0	−12.7	−12.0	−12.7	−7.9	−5.5
ADC(2)	12.0	18.5	−16.4	−17.1	−15.7	−16.5	−15.7	−16.5	−12.0	−9.0
ADC(3)	15.6	15.6	−9.9	−9.9	−9.4	−9.4	−9.4	−9.4	−2.2	−2.2

Table C.14: $\beta_{\alpha\beta\gamma}$ components at 693.1 nm perturbation of CO, H_2O, H_2S and NH_3 at ADC levels of theory with the aug-cc-pVTZ and aug-cc-pVQZ basis sets.

	β_{zzz}		β_{zxx}		β_{xzx}		β_{yzy}		$\beta_{\|\|}$	
CH_3CN (38)	TZ	QZ	TZ	QZ	TZ	QZ	TZ	QZ	TZ	QZ
ADC(1)	−14.7	−14.3	−8.3	−6.6	−9.6	−8.0	−9.6	−8.0	−19.8	−17.6
ADC(2)	28.0	29.2	−2.1	−0.7	−3.5	−2.1	−3.5	−2.1	13.2	15.5
ADC(3)	35.0	35.0	−1.2	−1.2	−2.2	−2.2	−2.2	−2.2	18.8	18.8

	β_{zzz}		β_{zxx}		β_{xzx}		β_{yzy}		$\beta_{\|\|}$	
CH_3OH (36)	TZ	QZ	TZ	QZ	TZ	QZ	TZ	QZ	TZ	QZ
ADC(1)	−36.5	−35.8	−13.2	−12.9	−13.6	−13.3	−23.8	−23.4	−44.1	−43.3
ADC(2)	−41.8	−40.6	−19.6	−18.6	−20.0	−18.8	−26.6	−25.4	−52.6	−50.6
ADC(3)	−34.8	−34.8	−11.5	−11.5	−11.9	−11.9	−24.5	−24.5	−42.4	−42.4

	β_{zzz}		β_{zxx}		β_{xzx}		β_{yzy}		$\beta_{\|\|}$	
$(CH_3)_2O$ (37)	TZ	QZ	TZ	QZ	TZ	QZ	TZ	QZ	TZ	QZ
ADC(1)	−71.7	−72.1	−22.3	−22.4	−22.5	−22.7	−61.1	−60.9	−92.9	−93.0
ADC(2)	−1132	−1106	−54.8	−52.2	−52.0	−49.8	−1036	−98.9	−1608	−1553
ADC(3)	−79.9	−80.5	−30.0	−29.7	−29.2	−29.0	−76.5	−75.6	−1110	−1107

Bibliography

[1] Pavia, D.; Lampman, G.; Kriz, G.; Vyvyan, J. *Introduction to Spectroscopy*; Cengage Learning, 2008.

[2] Woody, R. W. Circular dichroism. *Methods in enzymology* **1995**, *246*, 34–71.

[3] Hansen, A. Natural chiroptical spectroscopy: theory and computations. **1980**,

[4] Polavarapu, P. L. *Chiroptical spectroscopy: fundamentals and applications*; Crc Press, 2016.

[5] Fasman, G. D. *Circular dichroism and the conformational analysis of biomolecules*; Springer Science & Business Media, 2013.

[6] Berova, N.; Nakanishi, K.; Woody, R. W. *Circular dichroism: principles and applications*; John Wiley & Sons, 2000.

[7] Meierhenrich, U. J.; Filippi, J.-J.; Meinert, C.; Bredehöft, J. H.; Takahashi, J.-i.; Nahon, L.; Jones, N. C.; Hoffmann, S. V. Circular Dichroism of Amino Acids in the Vacuum-Ultraviolet Region. *Angewandte Chemie International Edition* **2010**, *49*, 7799–7802.

[8] Rodger, A.; Nordén, B., et al. *Circular dichroism and linear dichroism*; Oxford University Press, 1997; Vol. 1.

[9] Yang, J. T.; Wu, C.-S. C.; Martinez, H. M. Calculation of protein conformation from circular dichroism. *Methods in enzymology* **1986**, *130*, 208–269.

[10] Griffiths, D. J. *Introduction to Quantum Mechanics (2nd Edition)*, 2nd ed.; Pearson Prentice Hall, 2004.

[11] Schrödinger, E. An Undulatory Theory of the Mechanics of Atoms and Molecules. *Phys. Rev.* **1926**, *28*, 1049–1070.

[12] Dirac, P. A. M. *The principles of quantum mechanics*; Oxford university press, 1981.

[13] Von Neumann, J. *Mathematische grundlagen der quantenmechanik*; Springer-Verlag, 2013; Vol. 38.

[14] Schrödinger, E. Quantisierung als Eigenwertproblem. *Annalen der Physik* **1926**, *384*, 361–376.

[15] Szabo, A.; Ostlund, N. *Modern Quantum Chemistry: Introduction to Advanced Electronic Structure Theory*; Dover Books on Chemistry; Dover Publications, 1996.

[16] Fock, V. Näherungsmethode zur Lösung des quantenmechanischen Mehrkörperproblems. *Zeitschrift für Physik* **1930**, *61*, 126–148.

[17] Fock, V. „Selfconsistent field“ mit Austausch für Natrium. *Zeitschrift für Physik* **1930**, *62*, 795–805.

[18] Hartree, D. R.; Hartree, W. Self-consistent field, with exchange, for beryllium. *Proceedings of the Royal Society of London. Series A - Mathematical and Physical Sciences* **1935**, *150*, 9–33.

[19] Slater, J. C. The Self Consistent Field and the Structure of Atoms. *Phys. Rev.* **1928**, *32*, 339–348.

[20] Slater, J. C. Note on Hartree's Method. *Phys. Rev.* **1930**, *35*, 210–211.

[21] Møller, C.; Plesset, M. S. Note on an Approximation Treatment for Many-Electron Systems. *Phys. Rev.* **1934**, *46*, 618–622.

[22] Head-Gordon, M.; Pople, J. A.; Frisch, M. J. MP2 energy evaluation by direct methods. *Chemical Physics Letters* **1988**, *153*, 503–506.

[23] Knowles, P. J.; Andrews, J. S.; Amos, R. D.; Handy, N. C.; Pople, J. A. Restricted Møller—Plesset theory for open-shell molecules. *Chemical Physics Letters* **1991**, *186*, 130–136.

[24] Murray, C.; Davidson, E. R. Perturbation theory for open shell systems. *Chemical Physics Letters* **1991**, *187*, 451–454.

[25] Lee, T. J.; Jayatilaka, D. An open-shell restricted Hartree—Fock perturbation theory based on symmetric spin orbitals. *Chemical Physics Letters* **1993**, *201*, 1–10.

[26] Kozlowski, P.; Davidson, E. Construction of open shell perturbation theory invariant with respect to orbital degeneracy. *Chemical Physics Letters* **1994**, *226*, 440–446.

[27] Amos, R. D.; Andrews, J. S.; Handy, N. C.; Knowles, P. J. Open-shell Mller—Plesset perturbation theory. *Chemical Physics Letters* **1991**, *185*, 256–264.

[28] David Sherrill, C.; Schaefer, H. F. In *The Configuration Interaction Method: Advances in Highly Correlated Approaches*; Löwdin, P.-O., Sabin, J. R., Zerner, M. C., Brändas, E., Eds.; Advances in Quantum Chemistry; Academic Press, 1999; Vol. 34; pp 143–269.

[29] Schirmer, J. Beyond the random-phase approximation: A new approximation scheme for the polarization propagator. *Physical Review A* **1982**, *26*, 2395.

[30] Schirmer, J. *Many-Body Methods for Atoms, Molecules and Clusters*; Springer, 2018.

[31] Dreuw, A.; Wormit, M. The algebraic diagrammatic construction scheme for the polarization propagator for the calculation of excited states. *Wiley Interdisciplinary Reviews: Computational Molecular Science* **2015**, *5*, 82–95.

[32] Barron, L. D. *Molecular Light Scattering and Optical Activity*; Cambridge University Press, 2004.

[33] Whitmore, L.; Wallace, B. A. Protein secondary structure analyses from circular dichroism spectroscopy: Methods and reference databases. *Biopolymers* **2008**, *89*, 392–400.

[34] Greenfield, N. J. Using circular dichroism spectra to estimate protein secondary structure. *Nature protocols* **2006**, *1*, 2876–2890.

[35] Kelly, S. M.; Jess, T. J.; Price, N. C. How to study proteins by circular dichroism. *Biochimica et Biophysica Acta (BBA)-Proteins and Proteomics* **2005**, *1751*, 119–139.

[36] Greenfield, N. J.; Fasman, G. D. Computed circular dichroism spectra for the evaluation of protein conformation. *Biochemistry* **1969**, *8*, 4108–4116.

[37] Bertucci, C.; Pistolozzi, M.; De Simone, A. Circular dichroism in drug discovery and development: an abridged review. *Analytical and Bioanalytical Chemistry* **2010**, *398*, 155–166.

[38] Allenmark, S. Induced circular dichroism by chiral molecular interaction. *Chirality: The Pharmacological, Biological, and Chemical Consequences of Molecular Asymmetry* **2003**, *15*, 409–422.

[39] Saeva, F.; Wysocki, J. Induced circular dichroism in cholesteric liquid crystals. *Journal of the American Chemical Society* **1971**, *93*, 5928–5929.

[40] Gawroński, J.; Grajewski, J. The significance of induced circular dichroism. *Organic letters* **2003**, *5*, 3301–3303.

[41] Shimizu, H.; Kaito, A.; Hatano, M. Induced circular dichroism of β-cyclodextrin complexes with substituted benzenes. *Bulletin of the Chemical Society of Japan* **1979**, *52*, 2678–2684.

[42] Kodaka, M. A general rule for circular dichroism induced by a chiral macrocycle. *Journal of the American Chemical Society* **1993**, *115*, 3702–3705.

[43] Liu, J.; Su, H.; Meng, L.; Zhao, Y.; Deng, C.; Ng, J. C.; Lu, P.; Faisal, M.; Lam, J. W.; Huang, X., et al. What makes efficient circularly polarised luminescence in the condensed phase: aggregation-induced circular dichroism and light emission. *Chemical Science* **2012**, *3*, 2737–2747.

[44] Polavarapu, P. Ab initio molecular optical rotations and absolute configurations. *Molecular Physics* **1997**, *91*, 551–554.

[45] Bondo Pedersen, T.; Hansen, A. E. Ab initio calculation and display of the rotary strength tensor in the random phase approximation. Method and model studies. *Chemical Physics Letters* **1995**, *246*, 1–8.

[46] Hansen, A. E.; Bak, K. L. Ab initio calculations and display of enantiomeric and nonenantiomeric anisotropic circular dichroism: The lowest $\pi \rightarrow \pi^*$ excitation in butadiene, cyclohexadiene, and methyl-substituted cyclohexadienes. *Journal of Physical Chemistry A* **2000**, *104*, 11362–11370.

[47] Bouř, P. Simulation of Electronic Circular Dichroism with Rigid KohnSham Orbitals: A Computational Experiment. *The Journal of Physical Chemistry A* **1999**, *103*, 5099–5104.

[48] Cheeseman, J. R.; Frisch, M. J.; Devlin, F. J.; Stephens, P. J. HartreeFock and Density Functional Theory ab Initio Calculation of Optical Rotation Using GIAOs: Basis Set Dependence. *The Journal of Physical Chemistry A* **2000**, *104*, 1039–1046.

[49] Stephens, P. J.; Devlin, F. J.; Cheeseman, J. R.; Frisch, M. J. Calculation of Optical Rotation Using Density Functional Theory. *The Journal of Physical Chemistry A* **2001**, *105*, 5356–5371.

[50] Stephens, P.; McCann, D.; Cheeseman, J.; Frisch, M. Determination of absolute configurations of chiral molecules using ab initio time-dependent Density Functional Theory calculations of optical rotation: How reliable are absolute configurations obtained for molecules with small rotations? *Chirality* **2005**, *17*, S52–S64.

[51] Pecul, M.; Ruud, K. *Advances in Quantum Chemistry*; 2005; Vol. 50; pp 185–212.

[52] Norman, P.; Bishop, D. M.; Jensen, H. J. A.; Oddershede, J. Nonlinear response theory with relaxation: The first-order hyperpolarizability. *The Journal of Chemical Physics* **2005**, *123*, 194103.

[53] Helmich-Paris, B. CASSCF linear response calculations for large open-shell molecules. *The Journal of Chemical Physics* **2019**, *150*, 174121.

[54] Kowalczyk, T. D.; Abrams, M. L.; Crawford, T. D. Ab Initio Optical Rotatory Dispersion and Electronic Circular Dichroism Spectra of (S)-2-Chloropropionitrile. *The Journal of Physical Chemistry A* **2006**, *110*, 7649–7654.

[55] Crawford, T. D.; Tam, M. C.; Abrams, M. L. The problematic case of (*S*)-methylthiirane: electronic circular dichroism spectra and optical rotatory dispersion. *Molecular Physics* **2007**, *105*, 2607–2617.

[56] Pedersen, T. B.; Koch, H.; Ruud, K. Coupled cluster response calculation of natural chiroptical spectra. *The Journal of Chemical Physics* **1999**, *110*, 2883–2892.

[57] Ruud, K.; Stephens, P. J.; Devlin, F. J.; Taylor, P. R.; Cheeseman, J. R.; Frisch, M. J. Coupled-cluster calculations of optical rotation. *Chemical Physics Letters* **2003**, *373*, 606–614.

[58] Tam, M. C.; Russ, N. J.; Crawford, T. D. Coupled cluster calculations of optical rotatory dispersion of (S)-methyloxirane. *The Journal of Chemical Physics* **2004**, *121*, 3550–3557.

[59] Kongsted, J.; Hansen, A. E.; Pedersen, T. B.; Osted, A.; Mikkelsen, K. V.; Christiansen, O. A coupled cluster study of the oriented circular dichroism of the n$\rightarrow\pi$ electronic transition in cyclopropanone and natural optical active related structures. *Chemical Physics Letters* **2004**, *391*, 259–266.

[60] Niezborala, C.; Hache, F. Conformational Changes in Photoexcited (R)-(+)-1,1′-Bi-2-naphthol Studied by Time-Resolved Circular Dichroism. *J. Am. Chem. Soc.* **2008**, *130*, 12783–12786.

[61] Hache, F. Application of Time-Resolved Circular Dichroism to the Study of Conformational Changes in Photochemical and Photobiological Processes. *J. Photochem. Photobiol. A: Chem.* **2009**, *204*, 137–143.

[62] Hiramatsu, K.; Nagata, T. Communication: Broadband and Ultrasensitive Femtosecond Time-Resolved Circular Dichroism Spectroscopy. *J. Chem. Phys.* **2015**, *143*, 121102.

[63] Stadnytskyi, V.; Orf, G. S.; Blankenship, R. E.; Savikhin, S. Near Shot-Noise Limited Time-Resolved Circular Dichroism Pump-Probe Spectrometer. *Rev. Sci. Inst.* **2018**, *89*, 033104.

[64] Rizzo, A.; Coriani, S.; Fernández, B.; Christiansen, O. A coupled cluster response study of the electric dipole polarizability, first and second hyperpolarizabilities of HCl. *Physical Chemistry Chemical Physics* **2002**, *4*, 2884–2890.

[65] Göppert-Mayer, M. Über Elementarakte mit zwei Quantensprüngen. *Annalen der Physik* **1931**, *401*, 273–294.

[66] Denk, W.; Strickler, J. H.; Webb, W. W. Two-Photon Laser Scanning Fluorescence Microscopy. *Science* **1990**, *248*, 73–76.

[67] Xu, C.; Webb, W. W. Measurement of two-photon excitation cross sections of molecular fluorophores with data from 690 to 1050 nm. *JOSA B* **1996**, *13*, 481–491.

[68] Kogej, T.; Beljonne, D.; Meyers, F.; Perry, J.; Marder, S.; Brédas, J.-L. Mechanisms for enhancement of two-photon absorption in donor–acceptor conjugated chromophores. *Chemical Physics Letters* **1998**, *298*, 1–6.

[69] Tinoco Jr, I. Two-photon circular dichroism. *The Journal of Chemical Physics* **1975**, *62*, 1006–1009.

[70] Power, E. Two-photon circular dichroism. *The Journal of Chemical Physics* **1975**, *63*, 1348–1350.

[71] Toro, C.; De Boni, L.; Lin, N.; Santoro, F.; Rizzo, A.; Hernandez, F. E. Two-photon absorption circular dichroism: a new twist in nonlinear spectroscopy. *Chemistry* **2010**, *16*, 3504–3509.

[72] Rizzo, A.; Lin, N.; Ruud, K. Ab initio study of the one-and two-photon circular dichroism of R-(+)-3-methyl-cyclopentanone. *The Journal of chemical physics* **2008**, *128*, 164312.

[73] Jansík, B.; Rizzo, A.; Ågren, H. Response theory calculations of two-photon circular dichroism. *Chemical physics letters* **2005**, *414*, 461–467.

[74] Jansík, B.; Rizzo, A.; Ågren, H.; Champagne, B. Strong two-photon circular dichroism in helicenes: a theoretical investigation. *Journal of chemical theory and computation* **2008**, *4*, 457–467.

[75] Jansík, B.; Rizzo, A.; Ågren, H. Ab initio study of the two-photon circular dichroism in chiral natural amino acids. *The Journal of Physical Chemistry B* **2007**, *111*, 446–460.

[76] Guillaume, M.; Ruud, K.; Rizzo, A.; Monti, S.; Lin, Z.; Xu, X. Computational study of the one-and two-photon absorption and circular dichroism of (L)-tryptophan. *The Journal of Physical Chemistry B* **2010**, *114*, 6500–6512.

[77] Diaz, C.; Lin, N.; Toro, C.; Passier, R.; Rizzo, A.; Hernandez, F. E. The Effect of the π-Electron Delocalization Curvature on the Two-Photon Circular Dichroism of Molecules with Axial Chirality. *The journal of physical chemistry letters* **2012**, *3*, 1808–1813.

[78] Rizzo, A.; Jansík, B.; Pedersen, T. B.; Ågren, H. Origin invariant approaches to the calculation of two-photon circular dichroism. *The Journal of Chemical Physics* **2006**, *125*, 064113.

[79] Rizzo, A.; Lin, N.; Ruud, K. Ab initio study of the one- and two-photon circular dichroism of R-(+)-3-methyl-cyclopentanone. *The Journal of Chemical Physics* **2008**, *128*, 164312.

[80] Kaiser, W.; Garrett, C. G. B. Two-Photon Excitation in CaF_2: Eu^{2+}. *Phys. Rev. Lett.* **1961**, *7*, 229–231.

[81] Braunstein, R.; Ockman, N. Optical Double-Photon Absorption in CdS. *Phys. Rev.* **1964**, *134*, A499–A507.

[82] Mertins, F.; Schirmer, J. Algebraic propagator approaches and intermediate-state representations. I. The biorthogonal and unitary coupled-cluster methods. *Phys. Rev. A* **1996**, *53*, 2140–2152.

[83] Friese, D. H.; Hättig, C.; Rizzo, A. Origin-independent two-photon circular dichroism calculations in coupled cluster theory. *Physical Chemistry Chemical Physics* **2016**, *18*, 13683–13692.

[84] Kleinman, D. Theory of second harmonic generation of light. *Physical Review* **1962**, *128*, 1761.

[85] Miller, R. C. Optical second harmonic generation in piezoelectric crystals. *Applied Physics Letters* **1964**, *5*, 17–19.

[86] Bloembergen, N.; Chang, R. K.; Jha, S.; Lee, C. Optical second-harmonic generation in reflection from media with inversion symmetry. *Physical Review* **1968**, *174*, 813.

[87] Chen, C.; de Castro, A. R. B.; Shen, Y. Surface-enhanced second-harmonic generation. *Physical Review Letters* **1981**, *46*, 145.

[88] Guyot-Sionnest, P.; Chen, W.; Shen, Y. General considerations on optical second-harmonic generation from surfaces and interfaces. *Physical Review B* **1986**, *33*, 8254.

[89] Guyot-Sionnest, P.; Shen, Y. Bulk contribution in surface second-harmonic generation. *Physical Review B* **1988**, *38*, 7985.

[90] Shen, Y. Optical second harmonic generation at interfaces. *Annual Review of Physical Chemistry* **1989**, *40*, 327–350.

[91] Fejer, M. M.; Magel, G.; Jundt, D. H.; Byer, R. L. Quasi-phase-matched second harmonic generation: tuning and tolerances. *IEEE Journal of quantum electronics* **1992**, *28*, 2631–2654.

[92] Lüpke, G. Characterization of semiconductor interfaces by second-harmonic generation. *Surface Science Reports* **1999**, *35*, 75–161.

[93] Chen, X.; Nadiarynkh, O.; Plotnikov, S.; Campagnola, P. J. Second harmonic generation microscopy for quantitative analysis of collagen fibrillar structure. *Nature protocols* **2012**, *7*, 654–669.

[94] Cox, G.; Kable, E.; Jones, A.; Fraser, I.; Manconi, F.; Gorrell, M. D. 3-dimensional imaging of collagen using second harmonic generation. *Journal of structural biology* **2003**, *141*, 53–62.

[95] Stoller, P.; Reiser, K. M.; Celliers, P. M.; Rubenchik, A. M. Polarization-modulated second harmonic generation in collagen. *Biophysical journal* **2002**, *82*, 3330–3342.

[96] Campagnola, P. J.; Lewis, A.; Loew, L. M., et al. High-resolution nonlinear optical imaging of live cells by second harmonic generation. *Biophysical journal* **1999**, *77*, 3341–3349.

[97] Brown, E.; McKee, T.; Pluen, A.; Seed, B.; Boucher, Y.; Jain, R. K., et al. Dynamic imaging of collagen and its modulation in tumors in vivo using second-harmonic generation. *Nature medicine* **2003**, *9*, 796–800.

[98] Squirrell, J. M.; Wokosin, D. L.; White, J. G.; Bavister, B. D. Long-term two-photon fluorescence imaging of mammalian embryos without compromising viability. *Nature biotechnology* **1999**, *17*, 763–767.

[99] Velusamy, M.; Shen, J.-Y.; Lin, J. T.; Lin, Y.-C.; Hsieh, C.-C.; Lai, C.-H.; Lai, C.-W.; Ho, M.-L.; Chen, Y.-C.; Chou, P.-T., et al. A New Series of Quadrupolar Type Two-Photon Absorption Chromophores Bearing 11, 12-Dibutoxydibenzo [a, c]-phenazine Bridged Amines; Their Applications in Two-Photon Fluorescence Imaging and Two-Photon Photodynamic Therapy. *Advanced Functional Materials* **2009**, *19*, 2388–2397.

[100] Bhawalkar, J.; He, G.; Prasad, P. Nonlinear multiphoton processes in organic and polymeric materials. *Reports on Progress in Physics* **1996**, *59*, 1041.

[101] Cumpston, B. H.; Ananthavel, S. P.; Barlow, S.; Dyer, D. L.; Ehrlich, J. E.; Erskine, L. L.; Heikal, A. A.; Kuebler, S. M.; Lee, I.-Y. S.; McCord-Maughon, D., et al. Two-photon polymerization initiators for three-dimensional optical data storage and microfabrication. *Nature* **1999**, *398*, 51–54.

[102] Zhou, W.; Kuebler, S. M.; Braun, K. L.; Yu, T.; Cammack, J. K.; Ober, C. K.; Perry, J. W.; Marder, S. R. An efficient two-photon-generated photoacid applied to positive-tone 3D microfabrication. *science* **2002**, *296*, 1106–1109.

[103] Correa, D. S.; Cardoso, M. R.; Tribuzi, V.; Misoguti, L.; Mendonca, C. R. Femtosecond laser in polymeric materials: microfabrication of doped structures and micromachining. *IEEE Journal of Selected Topics in Quantum Electronics* **2011**, *18*, 176–186.

[104] Divochiy, A.; Marsili, F.; Bitauld, D.; Gaggero, A.; Leoni, R.; Mattioli, F.; Korneev, A.; Seleznev, V.; Kaurova, N.; Minaeva, O., et al. Superconducting nanowire photon-number-resolving detector at telecommunication wavelengths. *Nature Photonics* **2008**, *2*, 302–306.

[105] Vivas, M. G.; da Silva, D. L.; Mendonca, C. R.; De Boni, L. *Molecular and Laser Spectroscopy*; Elsevier, 2020; pp 275–314.

[106] Scott, M.; Rehn, D. R.; Coriani, S.; Norman, P.; Dreuw, A. Electronic Circular Dichroism Spectra Using the Algebraic Diagrammatic Construction Schemes of the Polarization Propagator up to Third Order. *J. Chem. Phys.* **2021**, *154*, 064107.

[107] Scott, M.; Rehn, D. R.; Norman, P.; Dreuw, A. Ab Initio Excited-State Electronic Circular Dichroism Spectra Exploiting the Third-Order Algebraic-Diagrammatic Construction Scheme for the Polarization Propagator. *The Journal of Physical Chemistry Letters* **2021**, *12*, 5132–5137.

[108] Dirac, P. A. M.; Bohr, N. H. D. The quantum theory of the emission and absorption of radiation. *Proceedings of the Royal Society of London. Series A, Containing Papers of a Mathematical and Physical Character* **1927**, *114*, 243–265.

[109] Beer, Bestimmung der Absorption des rothen Lichts in farbigen Flüssigkeiten. *Annalen der Physik* **1852**, *162*, 78–88.

[110] Demtröder, W. Widths and Profiles of Spectral Lines. *Laser Spectroscopy* **2004**, *120*, 61–98.

[111] Thulstrup, E. W.; Michl, J. *Elementary polarization spectroscopy*; John Wiley & Sons, 1989.

[112] Autschbach, J.; Ziegler, T.; van Gisbergen, S. J. A.; Baerends, E. J. Chiroptical properties from time-dependent density functional theory. I. Circular dichroism spectra of organic molecules. *The Journal of Chemical Physics* **2002**, *116*, 6930–6940.

[113] Rosenfeld, L. Quantenmechanische Theorie der natürlichen optischen Aktivität von Flüssigkeiten und Gasen. *Zeitschrift für Physik* **1929**, *52*, 161–174.

[114] Olsen, J.; Jørgensen, P. Linear and Nonlinear Response Functions for an Exact State and for an MCSCF State. *J. Chem. Phys.* **1985**, *82*, 3235–3264.

[115] Christiansen, O.; Jørgensen, P.; Hättig, C. Response functions from Fourier component variational perturbation theory applied to a time-averaged quasienergy. *International Journal of Quantum Chemistry* **1998**, *68*, 1–52.

[116] Norman, P.; Ruud, K.; Saue, T. *Principles and Practices of Molecular Properties*; John Wiley & Sons, Ltd: Chichester, UK, 2018.

[117] Olsen, J.; Jørgensen, P. *Time-dependent response theory with applications to self-consistent field and multiconfigurational self-consistent field wave functions*; pp 857–990.

[118] Sasagane, K.; Aiga, F.; Itoh, R. Higher-order response theory based on the quasienergy derivatives: The derivation of the frequency-dependent polarizabilities and hyperpolarizabilities. *The Journal of Chemical Physics* **1993**, *99*, 3738–3778.

[119] Pedersen, T. B.; Koch, H. Gauge invariance of the coupled cluster oscillator strength. *Chemical Physics Letters* **1998**, *293*, 251–260.

[120] Ruud, K.; Helgaker, T.; Jørgensen, P.; Bak, K. L. Theoretical calculations of the magnetizability of some small fluorine-containing molecules using London atomic orbitals. *Chemical Physics Letters* **1994**, *223*, 12–18.

[121] Ruud, K.; Helgaker, T.; Kobayashi, R.; Jo/rgensen, P.; Bak, K. L.; Jensen, H. J. A. Multiconfigurational self-consistent field calculations of nuclear shieldings using London atomic orbitals. *The Journal of Chemical Physics* **1994**, *100*, 8178–8185.

[122] Lee, A. M.; Handy, N. C.; Colwell, S. M. The density functional calculation of nuclear shielding constants using London atomic orbitals. *The Journal of Chemical Physics* **1995**, *103*, 10095–10109.

[123] Helgaker, T.; Wilson, P. J.; Amos, R. D.; Handy, N. C. Nuclear shielding constants by density functional theory with gauge including atomic orbitals. *Journal of Chemical Physics* **2000**, *113*, 2983–2989.

[124] Helgaker, T.; Ruud, K.; Bak, K. L.; Jørgensen, P.; Olsen, J. Vibrational Raman optical activity calculations using London atomic orbitals. *Faraday Discuss.* **1994**, *99*, 165–180.

[125] Gauss, J.; Ruud, K.; Helgaker, T. Perturbation-dependent atomic orbitals for the calculation of spin-rotation constants and rotational g tensors. *The Journal of Chemical Physics* **1996**, *105*, 2804–2812.

[126] Bak, K. L.; Jørgensen, P.; Helgaker, T.; Ruud, K.; Jo/rgen Aa. Jensen, H. Basis set convergence of atomic axial tensors obtained from self-consistent field calculations using London atomic orbitals. *The Journal of Chemical Physics* **1994**, *100*, 6620–6627.

[127] Bak, K. L.; Hansen, A. E.; Ruud, K.; Helgaker, T.; Olsen, J.; Jørgensen, P. Ab initio calculation of electronic circular dichroism fortrans-cyclooctene using London atomic orbitals. *Theoretica Chimica Acta* **1995**, *90*, 441–458.

[128] Kleinman, D. A. Theory of Second Harmonic Generation of Light. *Phys. Rev.* **1962**, *128*, 1761–1775.

[129] Monson, P. R.; McClain, W. M. Polarization Dependence of the Two-Photon Absorption of Tumbling Molecules with Application to Liquid 1-Chloronaphthalene and Benzene. *The Journal of Chemical Physics* **1970**, *53*, 29–37.

[130] McClain, W. M. Excited State Symmetry Assignment Through Polarized Two-Photon Absorption Studies of Fluids. *The Journal of Chemical Physics* **1971**, *55*, 2789–2796.

[131] Tinoco, I. Two-photon circular dichroism. *The Journal of Chemical Physics* **1975**, *62*, 1006–1009.

[132] Schirmer, J.; Cederbaum, L.; Walter, O. New approach to the one-particle Green's function for finite Fermi systems. *Physical Review A* **1983**, *28*, 1237.

[133] Oddershede, J.; Jørgensen, P.; Yeager, D. L. Polarization propagator methods in atomic and molecular calculations. *Computer Physics Reports* **1984**, *2*, 33–92.

[134] Oddershede, J. *Propagator methods*; John Wiley & Sons: London, UK, 1987; Vol. 2.

[135] Ortiz, J. V. Electron propagator theory: an approach to prediction and interpretation in quantum chemistry. *Wiley Interdisciplinary Reviews: Computational Molecular Science* **2013**, *3*, 123–142.

[136] Oddershede, J. *Advances in quantum chemistry*; Elsevier, 1978; Vol. 11; pp 275–352.

[137] Hodecker, M.; Rehn, D. R.; Dreuw, A.; Höfener, S. Similarities and Differences of the Lagrange Formalism and the Intermediate State Representation in the Treatment of Molecular Properties. *J. Chem. Phys.* **2019**, *150*, 164125.

[138] Harbach, P. H. P.; Wormit, M.; Dreuw, A. The third-order algebraic diagrammatic construction method (ADC(3)) for the polarization propagator for closed-shell molecules: Efficient implementation and benchmarking. *The Journal of Chemical Physics* **2014**, *141*, 064113.

[139] Cronstrand, P.; Luo, Y.; Ågren, H. *Advances in Quantum Chemistry*; 2005; Vol. 50; pp 1–21.

[140] Trofimov, A. B.; Krivdina, I. L.; Weller, J.; Schirmer, J. Algebraic-diagrammatic construction propagator approach to molecular response properties. *Chemical Physics* **2006**, *329*, 1–10.

[141] Knippenberg, S.; Rehn, D. R.; Wormit, M.; Starcke, J. H.; Rusakova, I. L.; Trofimov, A. B.; Dreuw, A. Calculations of nonlinear response properties using the intermediate state representation and the algebraic-diagrammatic construction polarization propagator approach: Two-photon absorption spectra. *The Journal of Chemical Physics* **2012**, *136*, 064107.

[142] Fransson, T.; Rehn, D. R.; Dreuw, A.; Norman, P. Static polarizabilities and C6 dispersion coefficients using the algebraic-diagrammatic construction scheme for the complex polarization propagator. *The Journal of Chemical Physics* **2017**, *146*, 094301.

[143] Knippenberg, S.; Rehn, D.; Wormit, M.; Starcke, J.; Rusakova, I.; Trofimov, A.; Dreuw, A. Calculations of nonlinear response properties using the intermediate state representation and the algebraic-diagrammatic construction polarization propagator approach: Two-photon absorption spectra. *The Journal of chemical physics* **2012**, *136*, 064107.

[144] Greenfield, N. J. Using circular dichroism spectra to estimate protein secondary structure. *Nature Protocols* **2006**, *1*, 2876–2890.

[145] Allenmark, S. Induced circular dichroism by chiral molecular interaction. *Chirality* **2003**, *15*, 409–422.

[146] Grimme, S.; Peyerimhoff, S.; Bartram, S.; Vögtle, F.; Breest, A.; Hormes, J. Experimental and theoretical study of the circular dichroism spectra of oxa- and thia- [2.2] metacyclophane. *Chemical Physics Letters* **1993**, *213*, 32–40.

[147] Hansen, A. E.; Bouman, T. D. *Natural Chiroptical Spectroscopy: Theory and Computations*; 2007; Vol. XL; pp 545–644.

[148] Morita, H. E.; Kodama, T. S.; Tanaka, T. Chirality of camphor derivatives by density functional theory. *Chirality* **2006**, *18*, 783–789.

[149] Bouř, P.; McCann, J.; Wieser, H. Measurement and Calculation of Absolute Rotational Strengths for Camphor, α-Pinene, and Borneol. *The Journal of Physical Chemistry A* **1998**, *102*, 102–110.

[150] Debie, E.; Jaspers, L.; Bultinck, P.; Herrebout, W.; Veken, B. V. D. Induced solvent chirality: A VCD study of camphor in CDCl3. *Chemical Physics Letters* **2008**, *450*, 426–430.

[151] Devlin, F. J.; Stephens, P. J. Ab Initio Calculation of Vibrational Circular Dichroism Spectra of Chiral Natural Products Using MP2 Force Fields: Camphor. *Journal of the American Chemical Society* **1994**, *116*, 5003–5004.

[152] Devlin, F. J.; Stephens, P. J.; Cheeseman, J. R.; Frisch, M. J. Ab Initio Prediction of Vibrational Absorption and Circular Dichroism Spectra of Chiral Natural Products Using Density Functional Theory: Camphor and Fenchone. *The Journal of Physical Chemistry A* **1997**, *101*, 6322–6333.

[153] BROWN, H. F.; DIFRANCESCO, D.; NOBLE, S. J. How does adrenaline accelerate the heart? *Nature* **1979**, *280*, 235–236.

[154] Kirkpatrick, D.; Yang, J.; Trehy, M. Determination of the enantiomeric purity of epinephrine by HPLC with circular dichroism detection. *Journal of Liquid Chromatography & Related Technologies* **2017**, *40*, 556–563.

[155] Shao, Y. et al. Advances in molecular quantum chemistry contained in the Q-Chem 4 program package. *Molecular Physics* **2015**, *113*, 184–215.

[156] Aidas, K. et al. The Dalton quantum chemistry program system. *WIREs Comput. Mol. Sci.* **2014**, *4*, 269–284.

[157] Woon, D. E.; Dunning, T. H. Gaussian basis sets for use in correlated molecular calculations. V. Core-valence basis sets for boron through neon. *The Journal of Chemical Physics* **1995**, *103*, 4572–4585.

[158] Kendall, R. A.; Dunning, T. H.; Harrison, R. J. Electron affinities of the first-row atoms revisited. Systematic basis sets and wave functions. *The Journal of Chemical Physics* **1992**, *96*, 6796–6806.

[159] Kendall, R. A.; Dunning, T. H.; Harrison, R. J. Electron affinities of the first-row atoms revisited. Systematic basis sets and wave functions. *The Journal of Chemical Physics* **1992**, *96*, 6796–6806.

[160] Woon, D. E.; Dunning, T. H. Gaussian basis sets for use in correlated molecular calculations. V. Core-valence basis sets for boron through neon. *The Journal of Chemical Physics* **1995**, *103*, 4572–4585.

[161] Yanai, T.; Tew, D. P.; Handy, N. C. A new hybrid exchange–correlation functional using the Coulomb-attenuating method (CAM-B3LYP). *Chemical Physics Letters* **2004**, *393*, 51–57.

[162] Jiemchooroj, A.; Norman, P. Electronic circular dichroism spectra from the complex polarization propagator. *The Journal of Chemical Physics* **2007**, *126*, 134102.

[163] Crawford, T. D.; Tam, M. C.; Abrams, M. L. The current state of ab initio calculations of optical rotation and electronic circular dichroism spectra. *Journal of Physical Chemistry A* **2007**, *111*, 12057–12068.

[164] Breest, A.; Ochmann, P.; Pulm, F.; Gödderz, K.; Carnell, M.; Hormes, J. Experimental circular dichroism and VUV spectra of substituted oxiranes and thiiranes. *Molecular Physics* **1994**, *82*, 539–551.

[165] Carnell, M.; Peyerimhoff, S.; Breest, A.; Gödderz, K.; Ochmann, P.; Hormes, J. Experimental and quantum-theoretical investigation of the circular dichroism spectrum of R-methyloxirane. *Chemical Physics Letters* **1991**, *180*, 477–481.

[166] Kongsted, J.; Pedersen, T. B.; Strange, M.; Osted, A.; Hansen, A. E.; Mikkelsen, K. V.; Pawlowski, F.; Jørgensen, P.; Hättig, C. Coupled cluster calculations of the optical rotation of S-propylene oxide in gas phase and solution. *Chemical Physics Letters* **2005**, *401*, 385–392.

[167] Rizzo, A.; Vahtras, O. Ab initio study of excited state electronic circular dichroism. Two prototype cases: Methyl oxirane and R-(+)-1,1 -bi(2-naphthol). *The Journal of Chemical Physics* **2011**, *134*, 244109.

[168] Lipparini, F.; Egidi, F.; Cappelli, C.; Barone, V. The Optical Rotation of Methyloxirane in Aqueous Solution: A Never Ending Story? *Journal of Chemical Theory and Computation* **2013**, *9*, 1880–1884.

[169] Mukhopadhyay, P.; Zuber, G.; Goldsmith, M.-R.; Wipf, P.; Beratan, D. N. Solvent Effect on Optical Rotation: A Case Study of Methyloxirane in Water. *ChemPhysChem* **2006**, *7*, 2483–2486.

[170] Šebestík, J.; Bouř, P. Raman Optical Activity of Methyloxirane Gas and Liquid. *The Journal of Physical Chemistry Letters* **2011**, *2*, 498–502.

[171] Egidi, F.; Carnimeo, I.; Cappelli, C. Optical rotatory dispersion of methyloxirane in aqueous solution: assessing the performance of density functional theory in combination with a fully polarizable QM/MM/PCM approach. *Optical Materials Express* **2015**, *5*, 196.

[172] Wiberg, K. B.; Wang, Y.-g.; Vaccaro, P. H.; Cheeseman, J. R.; Trucks, G.; Frisch, M. J. Optical Activity of 1-Butene, Butane, and Related Hydrocarbons. *The Journal of Physical Chemistry A* **2004**, *108*, 32–38.

[173] Dothe, H.; Lowe, M. A.; Alper, J. S. Vibrational circular dichroism of methylthiirane. *The Journal of Physical Chemistry* **1988**, *92*, 6246–6249.

[174] Bose, P. K.; Barron, L. D.; Polavarapu, P. L. Ab initio and experimental vibrational Raman optical activity in (+)-(R)-methylthiirane. *Chemical Physics Letters* **1989**, *155*, 423–429.

[175] Shcherbin, D.; Ruud, K. The use of Coulomb-attenuated methods for the calculation of electronic circular dichroism spectra. *Chemical Physics* **2008**, *349*, 234–243.

[176] Miyahara, T.; Hasegawa, J.-y.; Nakatsuji, H. Circular Dichroism and Absorption Spectroscopy for Three-Membered Ring Compounds Using Symmetry-Adapted Cluster-Configuration Interaction (SAC-CI) Method. *Bulletin of the Chemical Society of Japan* **2009**, *82*, 1215–1226.

[177] Neugebauer, J.; Jan Baerends, E.; Nooijen, M.; Autschbach, J. Importance of vibronic effects on the circular dichroism spectrum of dimethyloxirane. *The Journal of Chemical Physics* **2005**, *122*, 234305.

[178] Carnell, M.; Peyerimhoff, S. Ab initio investigation of the circular dichroism spectra of methylthiirane and trans-2,3-dimethylthiirane. *Chemical Physics* **1994**, *183*, 37–44.

[179] Rauk, A. Chiroptical properties of disulfides. Ab initio studies of dihydrogen disulfide and dimethyl disulfide. *Journal of the American Chemical Society* **1984**, *106*, 6517–6524.

[180] Ha, T.-K.; Cencek, W. Ab initio CI study of the optical rotatory strengths of HSSH. *Chemical Physics Letters* **1991**, *182*, 519–523.

[181] Diedrich, C.; Grimme, S. Systematic Investigation of Modern Quantum Chemical Methods to Predict Electronic Circular Dichroism Spectra. *The Journal of Physical Chemistry A* **2003**, *107*, 2524–2539.

[182] Cassim, J. Y.; Yang, J. T. A computerized calibration of the circular dichrometer. *Biochemistry* **1969**, *8*, 1947–1951.

[183] Yamada, T.; Yamamoto, A.; Matsunaga, A.; Watanabe, T.; Nakazawa, H. An Alternative Method for CD Measurement by a Conventional Spectrophotometer. *Analytical Sciences* **2000**, *16*, 325–327.

[184] Hennessey, J. P.; Johnson, W. Experimental errors and their effect on analyzing circular dichroism spectra of proteins. *Analytical Biochemistry* **1982**, *125*, 177–188.

[185] Venyaminov SY, Y. J. In *Circular Dichroism and the Conformational Analysis of Biomolecules*; Fasman, G. D., Ed.; Springer US: Boston, MA, 1996.

[186] Miles, A. J.; Wien, F.; Wallace, B. Redetermination of the extinction coefficient of camphor-10-sulfonic acid, a calibration standard for circular dichroism spectroscopy. *Analytical Biochemistry* **2004**, *335*, 338–339.

[187] Pulm, F.; Schramm, J.; Hormes, J.; Grimme, S.; Peyerimhoff, S. D. Theoretical and experimental investigations of the electronic circular dichroism and absorption spectra of bicyclic ketones. *Chemical Physics* **1997**, *224*, 143–155.

[188] Stener, M.; Di Tommaso, D.; Fronzoni, G.; Decleva, P.; Powis, I. Theoretical study on the circular dichroism in core and valence photoelectron angular distributions of camphor enantiomers. *The Journal of Chemical Physics* **2006**, *124*, 024326.

[189] Kongsted, J.; Mennucci, B.; Coutinho, K.; Canuto, S. Solvent effects on the electronic absorption spectrum of camphor using continuum, discrete or explicit approaches. *Chemical Physics Letters* **2010**, *484*, 185–191.

[190] Sousa, I.; Heerdt, G.; Ximenes, V.; de Souza, A.; Morgon, N. TD-DFT Analysis of the Dissymmetry Factor in Camphor. *Journal of the Brazilian Chemical Society* **2020**, *31*, 613–618.

[191] Szulczewski, D. H.; Hong, W.-h. *Epinephrine*; 1978; pp 193–229.

[192] Lange, A. W.; Herbert, J. M. A smooth, nonsingular, and faithful discretization scheme for polarizable continuum models: The switching/Gaussian approach. *The Journal of Chemical Physics* **2010**, *133*, 244111.

[193] Lange, A. W.; Herbert, J. M. Symmetric versus asymmetric discretization of the integral equations in polarizable continuum solvation models. *Chemical Physics Letters* **2011**, *509*, 77–87.

[194] van Mourik, T. The shape of neurotransmitters in the gas phase: A theoretical study of adrenaline, pseudoadrenaline, and hydrated adrenalineElectronic supplementary information (ESI) available: Relative energies of all adrenaline and pseudoadrenaline conformers studied. *Physical Chemistry Chemical Physics* **2004**, *6*, 2827.

[195] Prager, S.; Zech, A.; Aquilante, F.; Dreuw, A.; Wesolowski, T. A. First time combination of frozen density embedding theory with the algebraic diagrammatic construction scheme for the polarization propagator of second order. *The Journal of Chemical Physics* **2016**, *144*, 204103.

[196] Prager, S.; Zech, A.; Wesolowski, T. A.; Dreuw, A. Implementation and Application of the Frozen Density Embedding Theory with the Algebraic Diagrammatic Construction Scheme for the Polarization Propagator up to Third Order. *Journal of Chemical Theory and Computation* **2017**, *13*, 4711–4725.

[197] Sen, R.; Dreuw, A.; Faraji, S. Algebraic diagrammatic construction for the polarisation propagator in combination with effective fragment potentials. *Physical Chemistry Chemical Physics* **2019**, *21*, 3683–3694.

[198] Scheurer, M.; Herbst, M. F.; Reinholdt, P.; Olsen, J. M. H.; Dreuw, A.; Kongsted, J. Polarizable Embedding Combined with the Algebraic Diagrammatic Construction: Tackling Excited States in Biomolecular Systems. *Journal of Chemical Theory and Computation* **2018**, *14*, 4870–4883.

[199] Marefat Khah, A.; Karbalaei Khani, S.; Hättig, C. Analytic Excited State Gradients for the QM/MM Polarizable Embedded Second-Order Algebraic Diagrammatic Construction for the Polarization Propagator PE-ADC(2). *Journal of Chemical Theory and Computation* **2018**, *14*, 4640–4650.

[200] Lee, C.; Yang, W.; Parr, R. G. Development of the Colle-Salvetti Correlation-Energy Formula into a Functional of the Electron Density. *Phys. Rev. B* **1988**, *37*, 785–789.

[201] Becke, A. D. Density-Functional Thermochemistry. III. The Role of Exact Exchange. *J. Chem. Phys.* **1993**, *98*, 5648–5652.

[202] Becke, A. D. A New Mixing of Hartree–Fock and Local Density-Functional Theories. *J. Chem. Phys.* **1993**, *98*, 1372–1377.

[203] Harbach, P. H. P.; Dreuw, A. The Art of Choosing the Right Quantum Chemical Excited-State Method for Large Molecular Systems. *Modeling of Molecular Properties* **2011**, 29–47.

[204] Schmid, M.; Martinez-Fernandez, L.; Markovitsi, D.; Santoro, F.; Hache, F.; Improta, R.; Changenet, P. Unveiling Excited-State Chirality of Binaphthols by Femtosecond Circular Dichroism and Quantum Chemical Calculations. *J. Phys. Chem. Lett.* **2019**, *10*, 4089–4094.

[205] Kranz, M.; Clark, T.; Schleyer, P. v. R. Rotational Barriers of 1,1′-Binaphthyls: a Computational Study. *J. Org. Chem.* **1993**, *58*, 3317–3325.

[206] Sahnoun, R.; Koseki, S.; Fujimura, Y. Theoretical Investigation of 1,1′-Bi-2-Naphthol Isomerization. *J. Mol. Struct.* **2005**, *735-736*, 315–324.

[207] Banerjee, S.; Riggs, B.; Zakharov, L.; Blakemore, P. Synthesis, Properties, and Enantiomerization Behavior of Axially Chiral Phenolic Derivatives of 8-(Naphth-1-yl)quinoline and Comparison to 7,7′-Dihydroxy-8,8′-biquinolyl and 1,1′-Bi-2-naphthol. *Synthesis* **2015**, *47*, 4008–4016.

[208] Herrmann, A. Using photolabile protecting groups for the controlled release of bioactive volatiles. *Photochem. Photobiol. Sci.* **2012**, *11*, 446–459.

[209] Kramer, R. H.; Chambers, J. J.; Trauner, D. Photochemical tools for remote control of ion channels in excitable cells. *Nature Chemical Biology* **2005**, *1*, 360–365.

[210] Lee, H.-M.; Larson, D. R.; Lawrence, D. S. Illuminating the Chemistry of Life: Design, Synthesis, and Applications of "Caged" and Related Photoresponsive Compounds. *ACS Chemical Biology* **2009**, *4*, 409–427.

[211] Lin, C.-C.; Anseth, K. S. PEG Hydrogels for the Controlled Release of Biomolecules in Regenerative Medicine. *Pharmaceutical Research* **2009**, *26*, 631–643.

[212] Puliti, D.; Warther, D.; Orange, C.; Specht, A.; Goeldner, M. Small photoactivatable molecules for controlled fluorescence activation in living cells. *Bioorganic Medicinal Chemistry* **2011**, *19*, 1023–1029.

[213] Shigeri, Y.; Tatsu, Y.; Yumoto, N. Synthesis and application of caged peptides and proteins. *Pharmacology Therapeutics* **2001**, *91*, 85–92.

[214] Specht, A.; Bolze, F.; Donato, L.; Herbivo, C.; Charon, S.; Warther, D.; Gug, S.; Nicoud, J.-F.; Goeldner, M. The donor–acceptor biphenyl platform: A versatile chromophore for the engineering of highly efficient two-photon sensitive photoremovable protecting groups. *Photochemical Photobiological Sciences* **2012**, *11*, 578.

[215] Zhao, H.; Sterner, E. S.; Coughlin, E. B.; Theato, P. o -Nitrobenzyl Alcohol Derivatives: Opportunities in Polymer and Materials Science. *Macromolecules* **2012**, *45*, 1723–1736.

[216] Kim, D.; Baik, S. H.; Kang, S.; Cho, S. W.; Bae, J.; Cha, M.-Y.; Sailor, M. J.; Mook-Jung, I.; Ahn, K. H. Close correlation of monoamine oxidase activity with progress of Alzheimer's disease in mice, observed by in vivo two-photon imaging. *ACS central science* **2016**, *2*, 967–975.

[217] Deubel, M.; von Freymann, G.; Wegener, M.; Pereira, S.; Busch, K.; Soukoulis, C. M. Direct laser writing of three-dimensional photonic-crystal templates for telecommunications. *Nature Materials* **2004**, *3*, 444–447.

[218] Li, J.; Jia, B.; Gu, M. Engineering stop gaps of inorganic-organic polymeric 3D woodpile photonic crystals with post-thermal treatment. *Optics Express* **2008**, *16*, 20073.

[219] Carlotti, M.; Mattoli, V. Functional Materials for Two-Photon Polymerization in Microfabrication. *Small* **2019**, *15*, 1902687.

[220] Hribar, K. C.; Soman, P.; Warner, J.; Chung, P.; Chen, S. Light-assisted direct-write of 3D functional biomaterials. *Lab Chip* **2014**, *14*, 268–275.

[221] Coenjarts, C. A.; Ober, C. K. Two-Photon Three-Dimensional Microfabrication of Poly(Dimethylsiloxane) Elastomers. *Chemistry of Materials* **2004**, *16*, 5556–5558.

[222] Carlotti, M.; Mattoli, V. Functional Materials for Two-Photon Polymerization in Microfabrication. *Small* **2019**, *15*, 1902687.

[223] Superchi, S.; Bisaccia, R.; Casarini, D.; Laurita, A.; Rosini, C. Flexible Biphenyl Chromophore as a Circular Dichroism Probe for Assignment of the Absolute Configuration of Carboxylic Acids. *Journal of the American Chemical Society* **2006**, *128*, 6893–6902.

[224] Superchi, S.; Casarini, D.; Laurita, A.; Bavoso, A.; Rosini, C. Induction of a Preferred Twist in a Biphenyl Core by Stereogenic Centers: A Novel Approach to the Absolute Configuration of 1,2- and 1,3-Diols. *Angewandte Chemie International Edition* **2001**, *40*, 451–454.

[225] Göppert-Mayer, M. Über Elementarakte mit zwei Quantensprüngen. *Annalen der Physik* **1931**, *401*, 273–294.

[226] Franken, e. P.; Hill, A. E.; Peters, C.; Weinreich, G. Generation of optical harmonics. *Physical Review Letters* **1961**, *7*, 118.

[227] Orr, B.; Ward, J. Perturbation theory of the non-linear optical polarization of an isolated system. *Molecular Physics* **1971**, *20*, 513–526.

[228] Campagnola, P. Second Harmonic Generation Imaging Microscopy: Applications to Diseases Diagnostics. *Analytical Chemistry* **2011**, *83*, 3224–3231.

[229] Reeve, J. E.; Anderson, H. L.; Clays, K. Dyes for biological second harmonic generation imaging. *Physical Chemistry Chemical Physics* **2010**, *12*, 13484.

[230] López-Duarte, I.; Reeve, J. E.; Pérez-Moreno, J.; Boczarow, I.; Depotter, G.; Fleischhauer, J.; Clays, K.; Anderson, H. L. "Push-no-pull" porphyrins for second harmonic generation imaging. *Chemical Science* **2013**, *4*, 2024.

[231] Ladj, R.; Magouroux, T.; Eissa, M.; Dubled, M.; Mugnier, Y.; Dantec, R. L.; Galez, C.; Valour, J.-P.; Fessi, H.; Elaissari, A. Aminodextran-coated potassium niobate (KNbO3) nanocrystals for second harmonic bio-imaging. *Colloids and Surfaces A: Physicochemical and Engineering Aspects* **2013**, *439*, 131–137.

[232] Nuriya, M.; Fukushima, S.; Momotake, A.; Shinotsuka, T.; Yasui, M.; Arai, T. Multimodal two-photon imaging using a second harmonic generation-specific dye. *Nature Communications* **2016**, *7*, 11557.

[233] Bouevitch, O.; Lewis, A.; Pinevsky, I.; Wuskell, J.; Loew, L. Probing membrane potential with nonlinear optics. *Biophysical Journal* **1993**, *65*, 672–679.

[234] Cesaretti, A.; Foggi, P.; Fortuna, C. G.; Elisei, F.; Spalletti, A.; Carlotti, B. Uncovering Structure–Property Relationships in Push–Pull Chromophores: A Promising Route to Large Hyperpolarizability and Two-Photon Absorption. *The Journal of Physical Chemistry C* **2020**, *124*, 15739–15748.

[235] Bishop, D. M.; Champagne, B.; Kirtman, B. Relationship between static vibrational and electronic hyperpolarizabilities of π-conjugated push–pull molecules within the two-state valence-bond charge-transfer model. *The Journal of Chemical Physics* **1998**, *109*, 9987–9994.

[236] Castiglioni, C.; Del Zoppo, M.; Zerbi, G. Molecular first hyperpolarizability of push-pull polyenes: Relationship between electronic and vibrational contribution by a two-state model. *Physical Review B* **1996**, *53*, 13319–13325.

[237] Castro, M. C. R.; Belsley, M.; Raposo, M. M. M. Synthesis and characterization of push–pull bithienylpyrrole NLOphores with enhanced hyperpolarizabilities. *Dyes and Pigments* **2016**, *131*, 333–339.

[238] Chafin, A. P.; Lindsay, G. A. A Pattern for Increasing the First Hyperpolarizability of a PushPull Polyene Dye as Indicated from DFT Calculations. *The Journal of Physical Chemistry C* **2008**, *112*, 7829–7835.

[239] Champagne, B.; Kirtman, B. Evaluation of alternative sum-over-states expressions for the first hyperpolarizability of push-pull π-conjugated systems. *The Journal of Chemical Physics* **2006**, *125*, 024101.

[240] de Wergifosse, M.; Champagne, B. Electron correlation effects on the first hyperpolarizability of push–pull π-conjugated systems. *The Journal of Chemical Physics* **2011**, *134*, 074113.

[241] Jacquemin, D.; Champagne, B.; Hättig, C. Correlated frequency-dependent electronic first hyperpolarizability of small push–pull conjugated chains. *Chemical Physics Letters* **2000**, *319*, 327–334.

[242] Karki, L.; Vance, F. W.; Hupp, J. T.; LeCours, S. M.; Therien, M. J. Electronic Stark Effect Studies of a Porphyrin-Based PushPull Chromophore Displaying a Large First Hyperpolarizability: State-Specific Contributions to β. *Journal of the American Chemical Society* **1998**, *120*, 2606–2611.

[243] LeCours, S. M.; Guan, H.-W.; DiMagno, S. G.; Wang, C. H.; Therien, M. J. PushPull Arylethynyl Porphyrins: New Chromophores That Exhibit Large Molecular First-Order Hyperpolarizabilities. *Journal of the American Chemical Society* **1996**, *118*, 1497–1503.

[244] Liu, Z.-B.; Zhou, Z.-J.; Li, Y.; Li, Z.-R.; Wang, R.; Li, Q.-Z.; Li, Y.; Jia, F.-Y.; Wang, Y.-F.; Li, Z.-J.; Cheng, J.-B.; Sun, C.-C. Push–pull electron effects of the complexant in a Li atom doped molecule with electride character: a new strategy to enhance the first hyperpolarizability. *Physical Chemistry Chemical Physics* **2010**, *12*, 10562.

[245] Marder, S. R.; Cheng, L.-T.; Tiemann, B. G.; Friedli, A. C.; Blanchard-Desce, M.; Perry, J. W.; Skindhoj, J. Large First Hyperpolarizabilities in Push-Pull Polyenes by Tuning of the Bond Length Alternation and Aromaticity. *Science* **1994**, *263*, 511–514.

[246] Mohammed, N.; Wiles, A. A.; Belsley, M.; Fernandes, S. S. M.; Cariello, M.; Rotello, V. M.; Raposo, M. M. M.; Cooke, G. Synthesis and characterisation of push–pull flavin dyes with efficient second harmonic generation (SHG) properties. *RSC Advances* **2017**, *7*, 24462–24469.

[247] Priyadarshy, S.; Therien, M. J.; Beratan, D. N. Acetylenyl-Linked, Porphyrin-Bridged, DonorAcceptor Molecules: A Theoretical Analysis of the Molecular First Hyperpolarizability in Highly Conjugated PushPull Chromophore Structures. *Journal of the American Chemical Society* **1996**, *118*, 1504–1510.

[248] Bartkowiak, W.; Misiaszek, T. Solvent effect on static vibrational and electronic contribution of first-order hyperpolarizability of π-conjugated push–pull molecules: quantum-chemical calculations. *Chemical Physics* **2000**, *261*, 353–357.

[249] Carroll, A. R.; Copp, B. R.; Davis, R. A.; Keyzers, R. A.; Prinsep, M. R. Marine natural products. *Natural Product Reports* **2020**, *37*, 175–223.

[250] Milne, B. F.; Norman, P.; Nogueira, F.; Cardoso, C. Marine natural products from the deep Pacific as potential non-linear optical chromophores. *Physical Chemistry Chemical Physics* **2013**, *15*, 14814.

[251] Milne, B. F.; Norman, P. Resonant-Convergent PCM Response Theory for the Calculation of Second Harmonic Generation in Makaluvamines A–V: Pyrroloiminoquinone Marine Natural Products from Poriferans of Genus Zyzzya. *The Journal of Physical Chemistry A* **2015**, *119*, 5368–5376.

[252] Dworczak, R.; Kieslinger, D. Electric field induced second harmonic generation (EFISH) experiments in the swivel cell: New aspects of an established method. *Physical Chemistry Chemical Physics* **2000**, *2*, 5057–5064.

[253] Clays, K.; Persoons, A. Hyper-Rayleigh scattering in solution. *Physical review letters* **1991**, *66*, 2980.

[254] Clays, K.; Persoons, A. Hyper-Rayleigh scattering in solution. *Review of Scientific Instruments* **1992**, *63*, 3285–3289.

[255] Clays, K.; Persoons, A. Hyper-Rayleigh scattering in solution with tunable femtosecond continuous-wave laser source. *Review of Scientific Instruments* **1994**, *65*, 2190–2194.

[256] Flipse, M. C.; de Jonge, R.; Woudenberg, R. H.; Marsman, A. W.; van Walree, C. A.; Jenneskens, L. W. The determination of first hyperpolarizabilities β using hyper-Rayleigh scattering: a caveat. *Chemical Physics Letters* **1995**, *245*, 297–303.

[257] Clays, K.; Hendrickx, E.; Triest, M.; Persoons, A. Second-order nonlinear optics in isotropic liquids: Hyper-Rayleigh scattering in solution. *Journal of Molecular Liquids* **1995**, *67*, 133–155.

[258] Morrison, I. D.; Denning, R. G.; Laidlaw, W. M.; Stammers, M. A. Measurement of first hyperpolarizabilities by hyper-Rayleigh scattering. *Review of Scientific Instruments* **1996**, *67*, 1445–1453.

[259] Hao, E. C.; Schatz, G. C.; Johnson, R. C.; Hupp, J. T. Hyper-Rayleigh scattering from silver nanoparticles. *The Journal of Chemical Physics* **2002**, *117*, 5963–5966.

[260] Olbrechts, G.; Strobbe, R.; Clays, K.; Persoons, A. High-frequency demodulation of multi-photon fluorescence in hyper-Rayleigh scattering. *Review of Scientific Instruments* **1998**, *69*, 2233–2241.

[261] Russier-Antoine, I.; Jonin, C.; Nappa, J.; Bénichou, E.; Brevet, P.-F. Wavelength dependence of the hyper Rayleigh scattering response from gold nanoparticles. *The Journal of Chemical Physics* **2004**, *120*, 10748–10752.

[262] Itoh, T.; Ozaki, Y.; Yoshikawa, H.; Ihama, T.; Masuhara, H. Hyper-Rayleigh scattering and hyper-Raman scattering of dye-adsorbed silver nanoparticles induced by a focused continuous-wave near-infrared laser. *Applied Physics Letters* **2006**, *88*, 084102.

[263] Darvin, M.; König, K.; Kellner-Hoefer, M.; Breunig, H.; Werncke, W.; Meinke, M.; Patzelt, A.; Sterry, W.; Lademann, J. Safety Assessment by Multiphoton Fluorescence/Second Harmonic Generation/Hyper-Rayleigh Scattering Tomography of ZnO Nanoparticles Used in Cosmetic Products. *Skin Pharmacology and Physiology* **2012**, *25*, 219–226.

[264] Ohnoutek, L.; Cho, N. H.; Allen Murphy, A. W.; Kim, H.; Răsădean, D. M.; Pantoş, G. D.; Nam, K. T.; Valev, V. K. Single Nanoparticle Chiroptics in a Liquid: Optical Activity in Hyper-Rayleigh Scattering from Au Helicoids. *Nano Letters* **2020**, *20*, 5792–5798.

[265] Ray, P. C. Diagnostics of Single Base-Mismatch DNA Hybridization on Gold Nanoparticles by Using the Hyper-Rayleigh Scattering Technique. *Angewandte Chemie* **2006**, *118*, 1169–1172.

[266] Franzen, P. L.; Misoguti, L.; Zilio, S. C. Hyper-Rayleigh scattering with picosecond pulse trains. *Applied Optics* **2008**, *47*, 1443.

[267] Darbha, G. K.; Rai, U. S.; Singh, A. K.; Ray, P. C. Gold-Nanorod-Based Sensing of Sequence Specific HIV-1 Virus DNA by Using Hyper-Rayleigh Scattering Spectroscopy. *Chemistry - A European Journal* **2008**, *14*, 3896–3903.

[268] Das, P. K. Chemical Applications of Hyper-Rayleigh Scattering in Solution. *The Journal of Physical Chemistry B* **2006**, *110*, 7621–7630.

[269] El Harfouch, Y.; Benichou, E.; Bertorelle, F.; Russier-Antoine, I.; Jonin, C.; Lascoux, N.; Brevet, P.-F. Hyper-Rayleigh Scattering from Gold Nanorods. *The Journal of Physical Chemistry C* **2014**, *118*, 609–616.

[270] Bartlett, R. J.; Purvis, G. D. Molecular hyperpolarizabilities. I. Theoretical calculations including correlation. *Phys. Rev. A* **1979**, *20*, 1313–1322.

[271] Kirtman, B.; Luis, J. M.; Bishop, D. M. Simple finite field method for calculation of static and dynamic vibrational hyperpolarizabilities: Curvature contributions. *The Journal of Chemical Physics* **1998**, *108*, 10008–10012.

[272] Bishop, D. M.; Kirtman, B.; Champagne, B. Differences between the exact sum-over-states and the canonical approximation for the calculation of static and dynamic hyperpolarizabilities. *The Journal of Chemical Physics* **1997**, *107*, 5780–5787.

[273] Luo, Y.; Ågren, H.; Jørgensen, P.; Mikkelsen, K. V. In *Response Theory and Calculations of Molecular Hyperpolarizabilities*; Löwdin, P.-O., Ed.; Advances in Quantum Chemistry; Academic Press, 1995; Vol. 26; pp 165–237.

[274] Httig, C.; Jrgensen, P. Dispersion coefficients for first hyperpolarizabilities using coupled cluster quadratic response theory. *Theoretical Chemistry Accounts: Theory, Computation, and Modeling (Theoretica Chimica Acta)* **1998**, *100*, 230–240.

[275] Sałek ¶, P.; Helgaker *, T.; Vahtras, O.; Ågren, H.; Jonsson , D.; Gauss, J. A comparison of density-functional-theory and coupled-cluster frequency-dependent polarizabilities and hyperpolarizabilities. *Molecular Physics* **2005**, *103*, 439–450.

[276] O'Neill, D. P.; Kállay, M.; Gauss, J. Calculation of frequency-dependent hyperpolarizabilities using general coupled-cluster models. *The Journal of Chemical Physics* **2007**, *127*, 134109.

[277] Beaujean, P.; Champagne, B. Coupled cluster evaluation of the frequency dispersion of the first and second hyperpolarizabilities of water, methanol, and dimethyl ether. *The Journal of Chemical Physics* **2016**, *145*, 044311.

[278] Beaujean, P.; Champagne, B. Coupled cluster investigation of the vibrational and electronic second and third harmonic scattering hyperpolarizabilities of the water molecule. *The Journal of Chemical Physics* **2019**, *151*, 064303.

[279] Gauss, J.; Christiansen, O.; Stanton, J. F. Triple excitation effects in coupled-cluster calculations of frequency-dependent hyperpolarizabilities. *Chemical Physics Letters* **1998**, *296*, 117–124.

[280] Hammond, J. R.; Kowalski, K. Parallel computation of coupled-cluster hyperpolarizabilities. *The Journal of Chemical Physics* **2009**, *130*, 194108.

[281] Klimenko, T. A.; Ivanov, V. V.; Adamowicz, L. Dipole polarizabilities and hyperpolarizabilities of the small conjugated systems in the π-electron coupled cluster theory. *Molecular Physics* **2009**, *107*, 1729–1737.

[282] Larsen, H.; Olsen, J.; Hättig, C.; Jø rgensen, P.; Christiansen, O.; Gauss, J. Polarizabilities and first hyperpolarizabilities of HF, Ne, and BH from full configuration interaction and coupled cluster calculations. *The Journal of Chemical Physics* **1999**, *111*, 1917–1925.

[283] Maroulis, G. Electric dipole hyperpolarizability and quadrupole polarizability of methane from finite-field coupled cluster and fourth-order many-body perturbation theory calculations. *Chemical Physics Letters* **1994**, *226*, 420–426.

[284] Maroulis, G. On the accurate theoretical determination of the static hyperpolarizability of trans -butadiene. *The Journal of Chemical Physics* **1999**, *111*, 583–591.

[285] Maroulis, G. Static hyperpolarizability of the water dimer and the interaction hyperpolarizability of two water molecules. *The Journal of Chemical Physics* **2000**, *113*, 1813–1820.

[286] Sauer, S. P. A. Second-order polarization propagator approximation with coupled-cluster singles and doubles amplitudes - SOPPA(CCSD): the polarizability and hyperpolarizability of. *Journal of Physics B: Atomic, Molecular and Optical Physics* **1997**, *30*, 3773–3780.

[287] Sekino, H.; Bartlett, R. J. Frequency-dependent hyperpolarizabilities in the coupled-cluster method: the Kerr effect for molecules. *Chemical Physics Letters* **1995**, *234*, 87–93.

[288] Calaminici, P.; Jug, K.; Köster, A. M. Density functional calculations of molecular polarizabilities and hyperpolarizabilities. *The Journal of Chemical Physics* **1998**, *109*, 7756–7763.

[289] de Wergifosse, M.; Grimme, S. Nonlinear-response properties in a simplified time-dependent density functional theory (sTD-DFT) framework: Evaluation of the first hyperpolarizability. *The Journal of Chemical Physics* **2018**, *149*, 024108.

[290] Jacquemin, D.; Perpète, E. A.; Medved', M.; Scalmani, G.; Frisch, M. J.; Kobayashi, R.; Adamo, C. First hyperpolarizability of polymethineimine with long-range corrected functionals. *The Journal of Chemical Physics* **2007**, *126*, 191108.

[291] Sebastian, S.; Sundaraganesan, N.; Manoharan, S. Molecular structure, spectroscopic studies and first-order molecular hyperpolarizabilities of ferulic acid by density functional study. *Spectrochimica Acta Part A: Molecular and Biomolecular Spectroscopy* **2009**, *74*, 312–323.

[292] Sekino, H.; Maeda, Y.; Kamiya, M.; Hirao, K. Polarizability and second hyperpolarizability evaluation of long molecules by the density functional theory with long-range correction. *The Journal of Chemical Physics* **2007**, *126*, 014107.

[293] Suponitsky, K. Y.; Tafur, S.; Masunov, A. E. Applicability of hybrid density functional theory methods to calculation of molecular hyperpolarizability. *The Journal of Chemical Physics* **2008**, *129*, 044109.

[294] van Gisbergen, S. J. A.; Snijders, J. G.; Baerends, E. J. Time-dependent Density Functional Results for the Dynamic Hyperpolarizability of C_60. *Physical Review Letters* **1997**, *78*, 3097–3100.

[295] van Gisbergen, S. J. A.; Snijders, J. G.; Baerends, E. J. Accurate density functional calculations on frequency-dependent hyperpolarizabilities of small molecules. *The Journal of Chemical Physics* **1998**, *109*, 10657–10668.

[296] Yan, L.; Yang, G.; Guan, W.; Su, Z.; Wang, R. Density Functional Theory Study on the First Hyperpolarizabilities of Organoimido Derivatives of Hexamolybdates. *The Journal of Physical Chemistry B* **2005**, *109*, 22332–22336.

[297] Sałek, P.; Vahtras, O.; Helgaker, T.; Ågren, H. Density-functional theory of linear and nonlinear time-dependent molecular properties. *The Journal of Chemical Physics* **2002**, *117*, 9630–9645.

[298] Fominykh, O. D.; Sharipova, A. V.; Yu. Balakina, M. The choice of appropriate density functional for the calculation of static first hyperpolarizability of azochromophores and stacking dimers. *International Journal of Quantum Chemistry* **2016**, *116*, 103–112.

[299] Wang, F.; Yam, C. Y.; Chen, G. Time-dependent density-functional theory/localized density matrix method for dynamic hyperpolarizability. *The Journal of Chemical Physics* **2007**, *126*, 244102.

[300] Ding, F.; Van Kuiken, B. E.; Eichinger, B. E.; Li, X. An efficient method for calculating dynamical hyperpolarizabilities using real-time time-dependent density functional theory. *The Journal of Chemical Physics* **2013**, *138*, 064104.

[301] Sophy, K. B.; Calaminici, P.; Pal, S. Density Functional Static Dipole Polarizability and First-Hyperpolarizability Calculations of Na n (n = 2, 4, 6, 8) Clusters Using an Approximate CPKS Method and its Comparison with MP2 Calculations. *Journal of Chemical Theory and Computation* **2007**, *3*, 716–727.

[302] Lu, S.-I.; Chiu, C.-C.; Wang, Y.-F. Density functional theory calculations of dynamic first hyperpolarizabilities for organic molecules in organic solvent: Comparison to experiment. *The Journal of Chemical Physics* **2011**, *135*, 134104.

[303] Millefiori, S.; Alparone, A. (Hyper) polarizability of chalcogenophenes C4H4X (X= O, S, Se, Te) conventional ab initio and density functional theory study. *Journal of Molecular Structure: theochem* **1998**, *431*, 59–78.

[304] Chen, W.; Li, Z.-R.; Wu, D.; Li, Y.; Li, R.-Y.; Sun, C.-C. Inverse Sodium Hydride: Density Functional Theory Study of the Large Nonlinear Optical Properties. *The Journal of Physical Chemistry A* **2005**, *109*, 2920–2924.

[305] Matsuzawa, N.; Dixon, D. A. Density functional theory predictions of polarizabilities and first-and second-order hyperpolarizabilities for molecular systems. *The Journal of Physical Chemistry* **1994**, *98*, 2545–2554.

[306] Azhagiri, S.; Jayakumar, S.; Gunasekaran, S.; Srinivasan, S. Molecular structure, Mulliken charge, frontier molecular orbital and first hyperpolarizability analysis on 2-nitroaniline and 4-methoxy-2-nitroaniline using density functional theory. *Spectrochimica Acta Part A: Molecular and Biomolecular Spectroscopy* **2014**, *124*, 199–202.

[307] Shelton, D. P.; Rice, J. E. Measurements and calculations of the hyperpolarizabilities of atoms and small molecules in the gas phase. *Chemical Reviews* **1994**, *94*, 3–29.

Publication List

- Mikael Scott, Dirk R. Rehn, Patrick Norman, and Andreas Dreuw, "Ab Initio Excited-State Electronic Circular Dichroism Spectra Exploiting the Third-Order Algebraic-Diagrammatic Construction Scheme for the Polarization Propagator", The Journal of Physical Chemistry Letters, 12(21), 5132–5137. https://doi.org/10.1021/acs.jpclett.1c00839
- Mikael Scott, Dirk R. Rehn, Sonia Coriani, Patrick Norman, and Andreas Dreuw, "Electronic circular dichroism spectra using the algebraic diagrammatic construction schemes of the polarization propagator up to third order", The Journal of Chemical Physics 154, 064107 (2021) https://doi.org/10.1063/5.0038315
- Karan Ahmadzadeh, Mikael Scott, Manuel Brand, Olav Vahtras, Xin Li, Zilvinas Rinkevicius, and Patrick Norman , "Efficient implementation of isotropic cubic response functions for two-photon absorption cross sections within the self-consistent field approximation", J. Chem. Phys. 154, 024111 (2021) https://doi.org/10.1063/5.0031851
- Rinkevicius, Z, Li, X, Vahtras, O, et al. "VeloxChem: A Python-driven density-functional theory program for spectroscopy simulations in high-performance computing environments". WIREs Comput Mol Sci. 2020; 10:e1457. https://doi.org/10.1002/wcms.1457

Manuscripts Submitted for Publication or in Preparation

- Mikael Scott, Dirk R. Rehn, Patrick Norman, and Andreas Dreuw "First-order hyperpolarizabilities exploiting the Algebraic-Diagrammatic Construction scheme for the polarization propagator"
- Mikael Scott, Dirk R. Rehn, Patrick Norman, and Andreas Dreuw, "Two-photon circular dichroism by the Algebraic-Diagrammatic Construction scheme up to third order"
- Daniil A. Fedotov, Mikael Scott, Dirk R. Rehn, Andreas Dreuw and Sonia Coriani "Magnetic circular dichroism within the Algebraic Diagrammatic Construction scheme of the polarisation propagator up to third order"

Acknowledgement

This dissertation was made possible by financial support from the Marie Skłodowska-Curie European Training Network COSINE, grant no. 765739 and VR 2018-4343. Computational resources from the Swedish National Infrastructure for Computing (SNIC), are also acknowledged. I acknowledge the good supervision of Prof. Andreas Dreuw and thank him for letting me be part of his group, as well as the support and collaboration with Prof. Patrick Norman. Prof. Antonio Rizzo provided valuable insight of several of the methods developed in this dissertation. The help and guidance provided by Dr. Manuel Hodecker affected my work in a very positive way and helped illuminate several tricky aspects of the ADC method. Dr. Marvin Hoffmann likewise was an ideal coworker who always provided valuable insight and support. Dr. Dirk Rehn is acknowledged for the excellent knowledge provided in the code-intensive parts of this work. Dr. Thomas Fransson is likewise acknowledged for help, support and friendship during my work. Dr. Maximilien Ambroise further helped with implementation and coding as well as fun times during travels. MSc. Karan Ahmadzadeh is acknowledged as the excellent collaborator during my secondment in Prof. Patrick Norman's group. Others who supported me in various ways are Nils Oberhof, Felix Zeller, Prof. Xin Li, Sebastian Thielen, Dr. Maximilian Scheurer, Benjamin Thomitzni, Dr. Adrian Dempwolff, Brigitte Schierloh and Nader Sani. Lastly, I thank my parents Inger and Alf Scott and my sister Åsa.

Eidesstattliche Versicherung gemäß § 8 der Promotionsordnung für die Naturwissenschaftlich-Mathematische Gesamtfakultät der Universität Heidelberg

1. Bei der eingereichten Dissertation zu dem Thema
   “Linear and nonlinear spectroscopies exploiting the algebraic-diagrammatic construction scheme”
   handelt es sich um meine eigenständig erbrachte Leistung.

2. Ich habe nur die angegebenen Quellen und Hilfsmittel benutzt und mich keiner unzulässigen Hilfe Dritter bedient. Insbesondere habe ich wörtlich oder sinngemäß aus anderen Werken übernommene Inhalte als solche kenntlich gemacht.

3. Die Arbeit oder Teile davon habe ich bislang nicht an einer Hochschule des In- oder Auslands als Bestandteil einer Prüfungs- oder Qualifikationsleistung vorgelegt.

4. Die Richtigkeit der vorstehenden Erklärungen bestätige ich.

5. Die Bedeutung der eidesstattlichen Versicherung und die strafrechtlichen Folgen einer unrichtigen oder unvollständigen eidesstattlichen Versicherung sind mir bekannt.

Ich versichere an Eides statt, dass ich nach bestem Wissen die reine Wahrheit erklärt und nichts verschwiegen habe.

Ort/Datum	Unterschrift